②

Bulletin 52
(Part 2 of 5 Parts)

THE SHOCK AND VIBRATION BULLETIN

Part 2

Invited Papers, Space Shuttle Loads and Dynamics, Space Shuttle Data Systems,
Shock Testing, Shock Analysis
Space Shuttle Thermal Protection Systems

MAY 1982

A Publication of
THE SHOCK AND VIBRATION
INFORMATION CENTER
Naval Research Laboratory, Washington, D.C.

DEPARTMENT OF DEFENSE
UNITED STATES OF AMERICA

Office of
The Under Secretary of Defense
for Research and Engineering

SYMPOSIUM MANAGEMENT

THE SHOCK AND VIBRATION INFORMATION CENTER

Henry C. Pusey, Director
Rudolph H. Volin
J. Gordan Showalter
Jessica Hileman
Elizabeth A. McLaughlin

Bulletin Production

Publications Branch, Technical Information Division,
Naval Research Laboratory

Bulletin 52
(Part 2 of 5 Parts)

THE SHOCK AND VIBRATION BULLETIN

MAY 1982

A Publication of
THE SHOCK AND VIBRATION
INFORMATION CENTER
Naval Research Laboratory, Washington, D.C.

The 52nd Symposium on Shock and Vibration was held at the Monteleone Hotel, New Orleans, LA on October 26-28, 1981. The Defense Nuclear Agency, Washington, D.C. and the U.S. Army Waterways Experiment Station, Vicksburg, MS were Co-Hosts.

Office of
The Under Secretary of Defense
for Research and Engineering

CONTENTS

PAPERS APPEARING IN PART 2

Invited Papers

Space Shuttle Loads and Dynamics

Space Shuttle Data Systems

Space Shuttle Thermal Protection Systems

Space Shuttle Main Engine Dynamics

PAPERS APPEARING IN PART 1

Welcome

Keynote Address

Invited Papers

Rotor Dynamics and Machinery Vibration

PAPERS APPEARING IN PART 3

Environmental Testing and Simulation

Flight Environments

PAPERS APPEARING IN PART 4

Fatigue and Random Loading

Control, Isolation and Damping

PAPERS APPEARING IN PART 5

Mathematical Modeling

DAMPED STRUCTURE DESIGN USING FINITE ELEMENT ANALYSIS
M. F. Kluesener and M. L. Drake, University of Dayton Research Institute, Dayton, OH

DETERMINATION OF NORMAL MODES FROM MEASURED COMPLEX MODES
S. R. Ibrahim, Old Dominion University, Norfolk, VA

THE EFFECT OF JOINT PROPERTIES ON THE VIBRATIONS OF TIMOSHENKO FRAMES
I. Ye hmai, Sharif University of Technology, Tehran, Iran and
D. A. Frohrib, University of Minnesota, Minneapolis, MN

SOIL STRUCTURE INTERACTION AND SOIL MODELS
J. M. Ferritto, Naval Civil Engineering Laboratory, Port Hueneme, CA

FINITE ELEMENTS FOR INITIAL VALUE PROBLEMS IN DYNAMICS
T. E. Simkins, U.S. Army Armament Research and Development Command, Watervliet, NY

Structural Dynamics

A PROCEDURE FOR DESIGNING OVERDAMPED LUMPED PARAMETER SYSTEMS
D. J. Inman, State University of New York at Buffalo, Buffalo, NY and
A. N. Andry, Jr., Lockheed California Company, Burbank, CA

ON THE OPTIMAL LOCATION OF VIBRATION SUPPORTS
B. P. Wang and W. D. Pilkey, University of Virginia, Charlottesville, VA

DYNAMIC BUCKLING OF PINNED COLUMNS
J. M. Ready, David W. Taylor Naval Ship Research and Development Center, Bethesda, MD

LARGE DEFLECTION RANDOM RESPONSE OF SYMMETRIC LAMINATED COMPOSITE PLATES
K. R. Wentz and D. B. Paul, Air Force Wright Aeronautical Laboratories, Wright-Patterson AFB, OH and
C. Mei, Old Dominion University, Norfolk, VA

DYNAMIC CHARACTERISTICS OF A NON-UNIFORM TORPEDO-LIKE HULL STRUCTURE
A. Harari, Naval Underwater Systems Center, Newport, RI

VIBRATION AND ACOUSTIC RADIATION FROM POINT EXCITED SPHERICAL SHELLS
E. H. Wong, Naval Ocean Systems Center, San Diego, CA and
S. I. Hayek, The Pennsylvania State University, University Park, PA

DAMPING OF SHALLOW-BURIED STRUCTURES DUE TO SOIL-STRUCTURE INTERACTION
F. S. Wong and P. Weidlinger, Weidlinger Associates, Menlo Park, CA and New York, NY

TITLES AND AUTHORS OF PAPERS PRESENTED IN THE SHORT DISCUSSION TOPICS SESSION

NOTE: These papers were only presented at the Symposium. They are not published in the Bulletin and are only listed here as a convenience.

TRANSFER FUNCTION ANALYSIS OF LARGE STRUCTURES
H. J. Weaver, Lawrence Livermore National Laboratory, Livermore, CA

SHOCK HARDENED STRUCTURAL ATTACHMENTS FOR HONEYCOMB BULKHEADS
P. W. Buermann, Gibbs & Cox, Inc., New York, NY

DISCOVERING THE THIRD (AND SECOND) DIMENSION
B. Meeker, Pacific Missile Test Center, Point Mugu, CA

A MICROPROCESSOR BASED ADAPTIVE ISOLATION AND DAMPING OF A VIBRATING STRUCTURE
A. S. R. Murty, Indian Institute of Technology, Kharagpur, India

INVITED PAPERS
SPACE SHUTTLE LOADS AND DYNAMICS

SPACE SHUTTLE MAIN ENGINE (SSME) POGO TESTING AND RESULTS

J. R. Fenwick
Rockwell International, Rocketdyne Division
Canoga Park, California

and

J. H. Jones and R. E. Jewell
Marshall Space Flight Center
Huntsville, Alabama

To effectively assess the Pogo stability of the Space Shuttle vehicle, it was necessary to characterize the structural, propellant, and propulsion dynamics subsystems. Extensive analyses and comprehensive testing programs were established early in the project as an implementation of management philosophy of Pogo prevention for Space Shuttle. This paper will discuss the role of the Space Shuttle Main Engine (SSMF) in the Pogo prevention plans, compare the results obtained from engine ground testing with analysis, and present measured data from STS-1 flight.

INTRODUCTION

Pogo has become one of the classical problems of structural dynamics and can be ranked along with flutter and the Tacoma Narrows Bridge as a textbook demonstration of fluid coupled structural instability. The basic Pogo loop involves resonant tuning of the vehicle structure with the propellant feed system with positive feedback through the rocket engine. The block diagram shown in Figure 1 indicates the interconnection of the major subsystems. Variations in thrust, ΔF, at the structural resonance cause large velocity variations, ΔV, which are in phase with the thrust. Tuning the propellant feedline system to the structural frequency results in engine inlet pressure oscillations, ΔP_{OS}, which are in phase with velocity variations. The engine produces two effects, it acts as a blockage to the flow resulting in a downward force at the engine inlet while any fluid entering the engine is burned in the thrust chamber generating an upward thrust. Assuming negligible phase shift through the engine, it is obvious that if the downward force exerted by the pressure, P_{OS}, is greater than the upward force, the net effect of the engine is that of a damper since the net engine force opposes velocity. If the upward force is the greater (the thrust), the engine acts as negative damping and for large values can become greater than the inherent damping of the structure and feed system causing divergent oscillations. In terms of the model given in Figure 1, if the first term is greater than the area, A_S, the net result is positive and this re-enforces oscillation; however if the first term is less than the area, A_S, the net result is negative and this dampens oscillations.

The second partial in Figure 1 is a measure of the engine gain; i.e. combustion chamber pressure, P_c, to engine inlet pressure, P_{OS}. Consequently, with this simple model, a value of allowable engine gain for neutral or inherently stabilizing engine forces can be written as:

$$\partial Pc/\partial Ps \leq As/\frac{\partial F}{\partial Pc}$$

Allowable gain for engines used in several vehicles which displayed Pogo are shown in Figure 2. Because of the high pressure design of the SSME, an engine gain three to four times that of previous engines could be tolerated without instability. Typical engine gains are from 0.2 to 0.5 except when the engine inlet net positive suction head

(NPSH) is so low that additional gain is produced through cyclic cavitation of the turbopumps.

SIGNIFICANCE IN MANNED FLIGHT

In normal trajectories, structural modes increase in frequency while the frequency of propellant modes vary with engine inlet pressure level and tend to decrease with flight time. When tuned conditions and feedback result in an instability, divergent oscillations occur. The oscillations are a maximum when detuning results in neutral stability. Further detuning results in convergence. The envelope of an accelerometer from the second unmanned flight of Saturn V is shown in Figure 3 where closed loop damping is inferred from the envelope

Payloads are often designed to include a tolerance to Pogo when the vehicle has established a consistent amplitude and frequency over many flights. When the payload includes man, however, the only solution is to avoid Pogo. Figure 4 shows the results of vibration tests of the crew which had been chosen for the first manned Saturn V. Based on these tests and previous studies conducted during the Gemini program a limit of $\pm\frac{1}{4}$G was established for manned flights. Since instability amplitudes are not as predictable as instability itself, the Space Shuttle Program included testing and analysis plans to prevent Pogo.

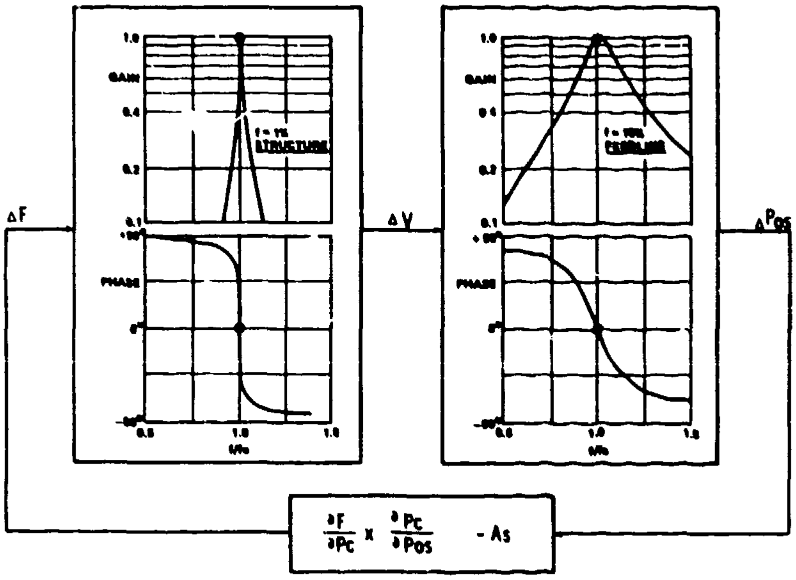

FIG. 1- POGO BLOCK DIAGRAM

VEHICLE	PROPELLANT	$As/\frac{\partial F}{\partial Pc}$
THOR	LIQUID OXYGEN	0.126
	RP-1	0.126
TITAN II	NITROGEN TETROXIDE	0.126
	HYDRAZINE/UDMH	0.087
S-IC	LIQUID OXYGEN	0.312
	RP-1	0.241
S-II	LIQUID OXYGEN	0.245
	LIQUID HYDROGEN	0.245
SPACE SHUTTLE	LIQUID OXYGEN	0.722
	LIQUID HYDROGEN	0.722

FIG. 2- COMPARISON OF $As/\frac{\partial F}{\partial Pc}$ FOR SEVERAL ENGINES INVOLVED WITH POGO

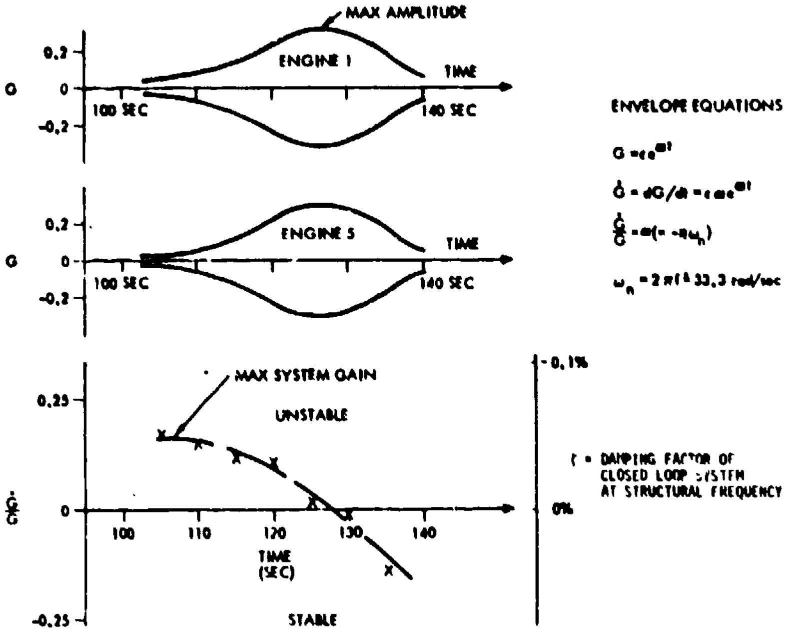

FIG.3- ENGINE GIMBAL BLOCK ACCELEROMETERS FROM APOLLO-SATURN 502 S-IC STAGE, SHOWING ENVELOPE OF OSCILLATION AND METHOD OF DETERMINING DAMPING FACTOR OF CLOSED LOOP SYSTEM AT THE STRUCTURAL MODE FREQUENCY.

ENGINE SUPPORT TO POGO PREVENTION

In the SSME (Space Shuttle Main Engine) proposal phase, dynamic testing of the engine system was included which would produce engine transfer functions of sufficient quality to allow valid vehicle stability studies. Immediately after contract awards the Pogo Integration Panel was formed and a Pogo prevention plan was formulated. It was assumed that an engine mounted Pogo suppressor would be required and, with rough estimates supplied by the vehicle contractor, Rocketdyne began generating suppressor concepts.

The Titan-Gemini vehicle propelled by storeables used a precharged nitrogen standpipe on the oxidizer system and a spring loaded piston on the fuel side. The first and second stages of the Saturn V had cryogenic propellants and the suppressor designs amounted to helium filled accumulators with a small continual gas bleed into the propellant system. Since the SSME vehicle interface is the inlet flange of the LPOTP (Low Pressure Oxygen Turbopump), an engine mounted suppressor must operate downstream of the LPOTP at a pressure level of about 500 psi with severe pressure transients at start and cutoff. Four candidate systems were chosen for further study.

SUPPRESSOR CONCEPT SELECTION

A helium charged accumulator was initially considered due to the success on Saturn V. While initial charging could be satisfied, engine cutoff would result in release of helium to the HPOTP with gross cavitation and pump overspeed. Venting and level control were not feasible. Bellows with low spring rate and structural stability could not be designed in the available volume (Figure 5). A plug valve at the suppressor throat added significant weight and operational complexity. No desirable helium system was found.

An accumulator, mounted remotely where more volume was available, was assessed. The inertia of the fluid column was so large that the frequency range and suppression capability was very limited.

As a spin-off from an LeRC (Lewis Research Center) contract, an active Pogo contract was designed. Essentially the control sensed vehicle velocity and used it to drive a piston mounted in a tee at the pump inlet as in Figure 6 and 7. As the aft end of the vehicle moves forward, the piston moved outward. Since fluid compression at the pump inlet is prevented, no significant pressure oscillations are generated due to structural

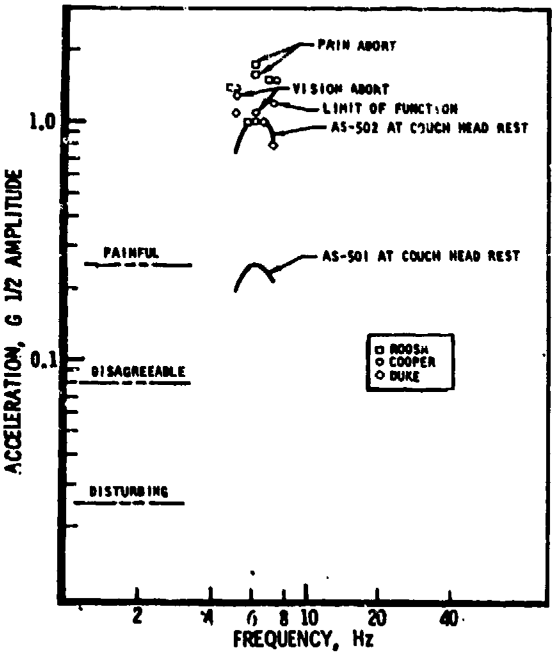

FIG. 4- COUCH VIBRATION AND AS-503 CREW ACCELERATION TOLERANCE

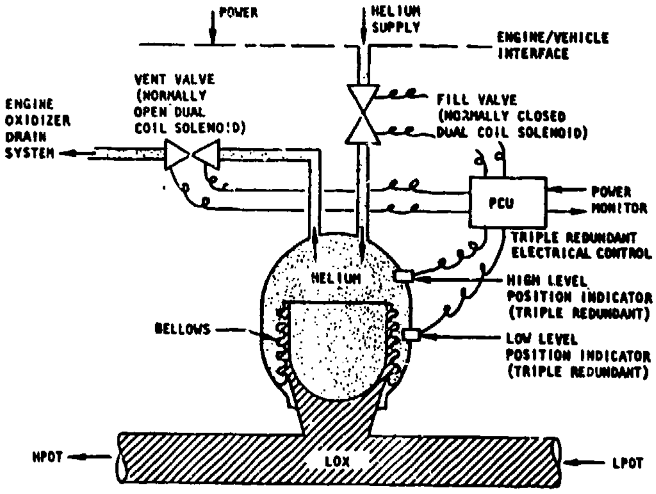

FIG. 5-BELLOWS SYSTEM SCHEMATIC

motion and the engine feedback gain is reduced. Tests and MSFC analysis indicated significant pressure attenuation in the low frequency range. The most significant problem was design of a filter to attenuate pulser motion at higher frequencies while providing less than 90° phase error through the control loop. This problem is identical to that of active dampers in large structures. While the problems of a wider bandwidth hydraulic servovalve and an adequate filter were being worked, meetings with the vehicle contractor indicated that any additional hydraulic requirement would be assessed a 1000 lb weight penalty since the hydraulics capability of the vehicle was already at its limit. The active suppressor actively was curtailed.

The fourth concept was an accumulator for the liquid oxygen system using hot gaseous oxygen. This supply was available from an engine heat exchanger which supplies pressurant for the external tank. The major potential problem was ullage stability due to heat

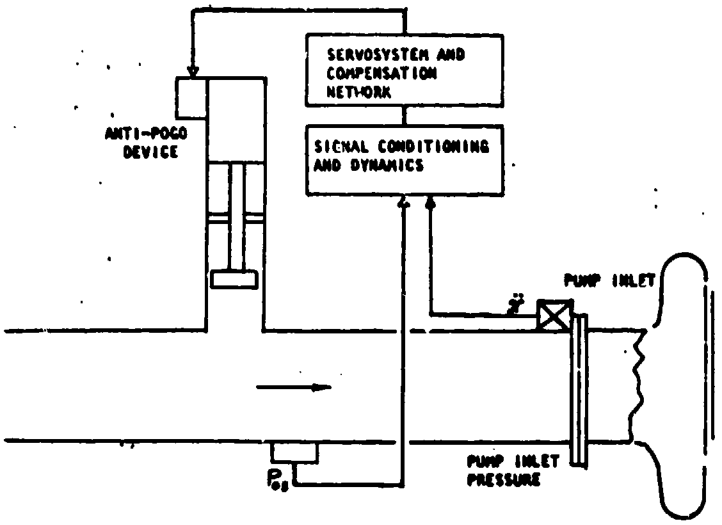

ACTIVE POGO SUPPRESSOR SCHEMATIC
FIG. 6

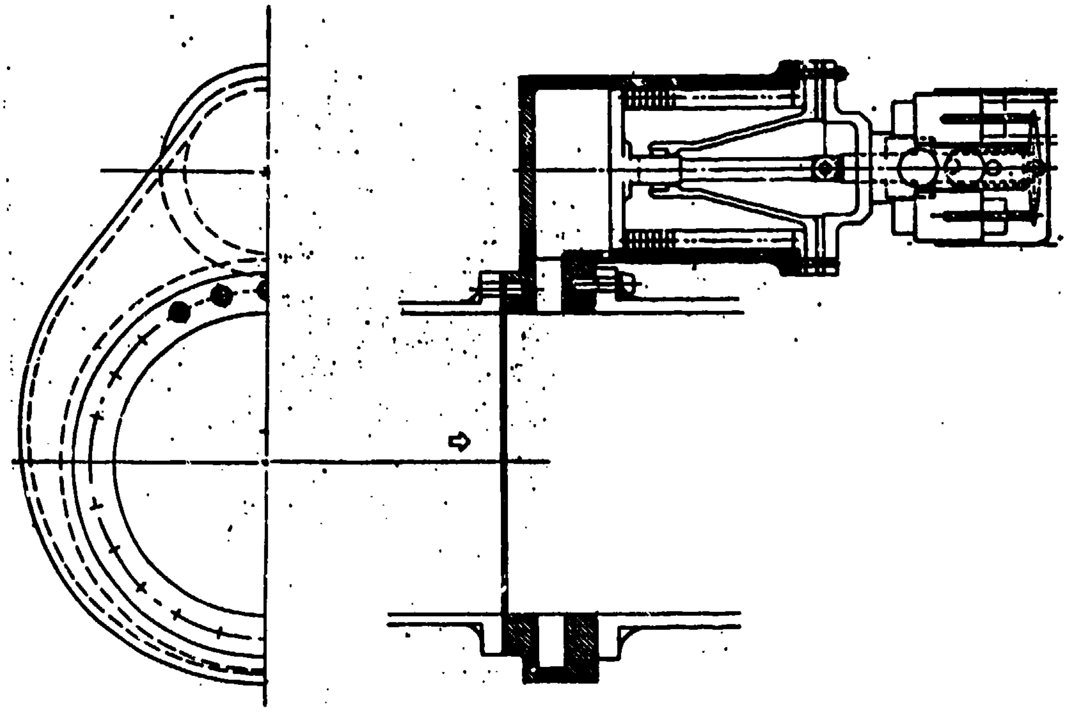

FIG. 7
CONCEPTUAL DESIGN OF FLIGHT WEIGHT POGO CONTROL

and mass transfer across the free gas-liquid interface. This problem involved the effects of sloshing, circulation of the liquid below the interface and the design of a good diffuser. The original concept is shown in Figure 8.

The suppressor systems design is shown in Figure 9. The accumulator is helium charged during engine start to about 2/3 its ullage capability. The charging valve is then shuttled to allow flow of hot oxygen gas (GOX), cutting off the helium flow. Ullage level is controlled by a tube with bleed holes at the desired interface level. The mixed gas-liquid bleed flow recirculates into the propellant system about 15 ft. upstream of the LPOTP. At cutoff most of the gas vents through the level control. A small amount may enter the main duct but is collapsed by the flow in the main duct. Later during

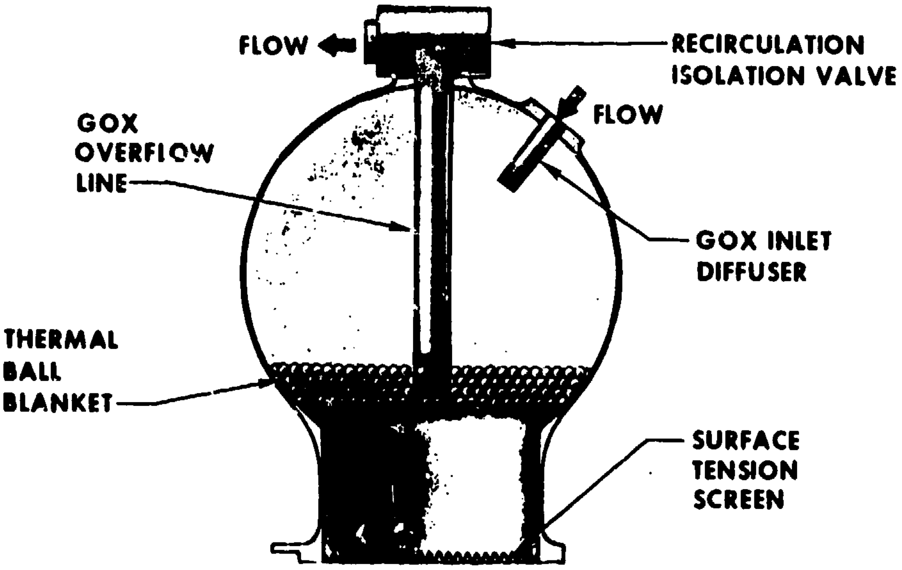

FIG. 8
POGO SUPPRESSION ACCUMULATOR

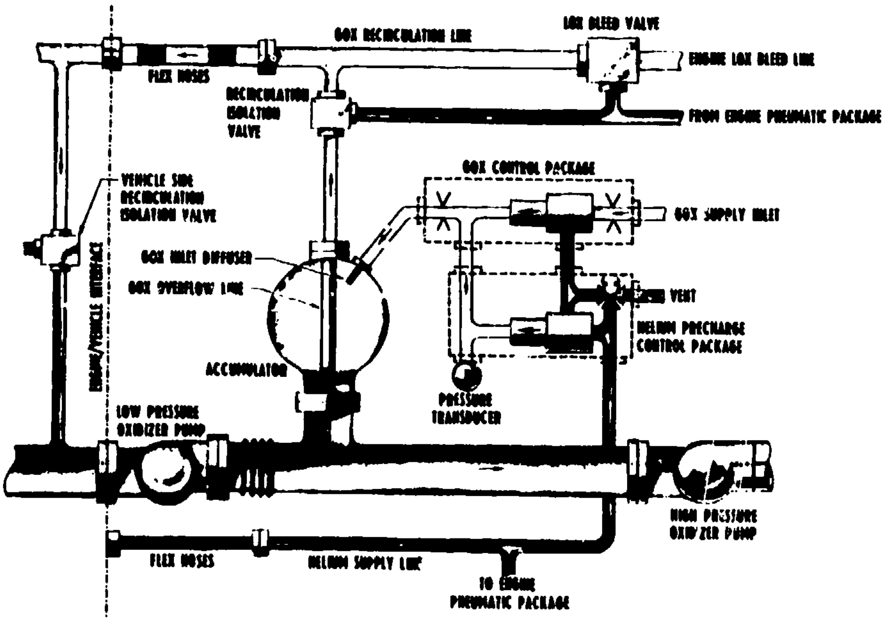

FIG. 9
POGO SUPPRESSION SYSTEM SCHEMATIC

engine testing it was found that a surge at engine cutoff could collapse the cavity sending a sharp water-hammer wave into the propellant system. A small amount of helium is now added during the cutoff sequence to eliminate the surge. This suppressor was chosen for the engine baseline primarily for its light weight (60 lb/engine) and simplicity of operation. The actual Pogo suppression system installation is shown in Figure 10.

Initial tests using low liquid flow rates and gaseous nitrogen were run to verify the level control concept and the stability of a liquid-gas interface. A plastic accumulator was also run with gaseous nitrogen and water to evaluate baffle requirements to minimize sloshing.

APPROACH TO MODEL CONSTRUCTION AND VERIFICATION

A schematic of the SSME is shown in Figure 11. The interface is at the inlet to the low pressure pumps. Frequency dependent equations representing the engines are required for the large vehicle stability models. At a minimum, transfer functions are required for the engine inlet impedance ($\Delta P_O / \Delta \dot{M}$) and the thrust transfer function ($\Delta F/\Delta P_O$). A detailed linear model of the engine was formulated for frequency domain solution with input interfaces at both the fuel and oxidizer low pressure pump inlet flanges. A schematic of this model is contained in Figure 12

While only transfer functions connecting the interfaces are required, simpler transfer functions breaking the SSME into three subsystems were more desirable. Interfaces were chosen at the low pressure fuel and oxidizer pump inlet, the inlet to high pressure oxidizer pump and the suppressor tap-off point. The subsystems then were the LPOTP - oxidizer interpump duct, the suppressor and the powerhead. The powerhead includes the closed loop control system, preburners and thrust chamber and the complete fuel system to the vehicle-engine interface. Splitting the engine into subsystems followed the plan of subsystem testing and verification. Further, vehicle stability models are quite complicated and subsystems which can be described with low order frequency dependent polynomials are preferred to a few high order polynomials.

The initial analysis of fuel system interaction indicated that due to the low density of liquid hydrogen, the vehicle geometry and the engine mixture ratio, the contribution of the fuel system to Pogo was very small. The effect of the fuel system feedback was actually less than the predicted error band of the oxidizer system and was not required in initial analysis. These effects however were available for final vehicle verification studies.

While the engine model was quite detailed, coefficients associated with pump cavitation and suppressor dynamics could only be estimated.

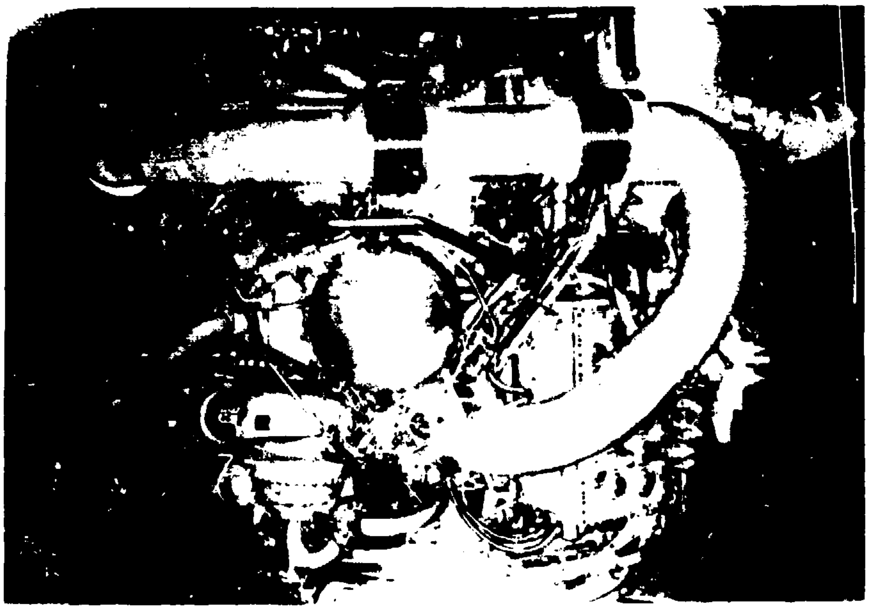

FIG. 10 - POGO SUPPRESSION SYSTEM INSTALLATION

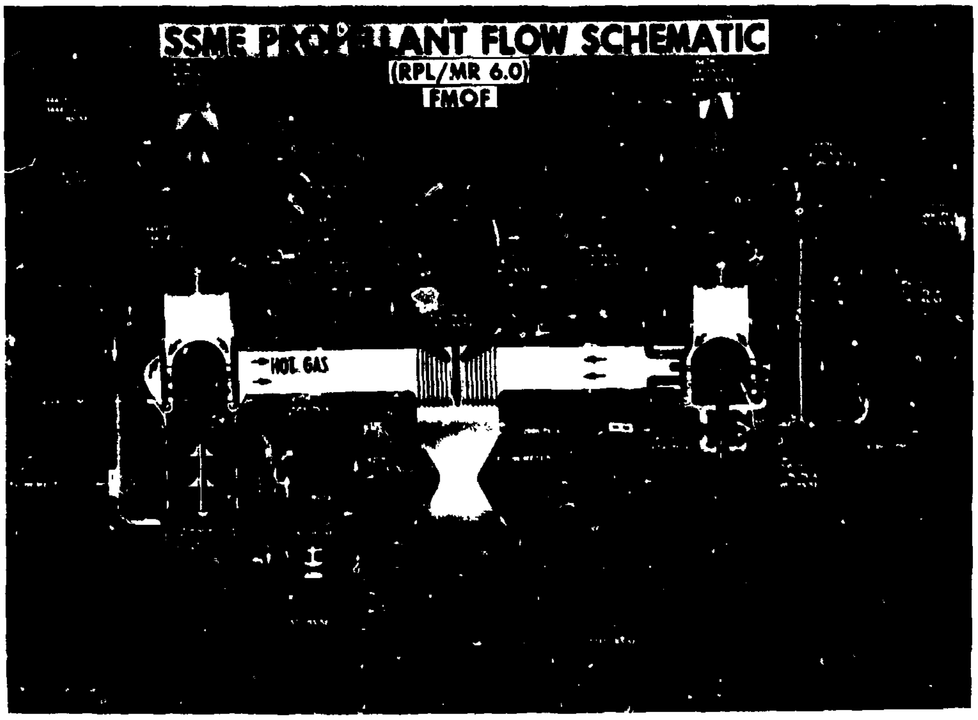

FIG. 11

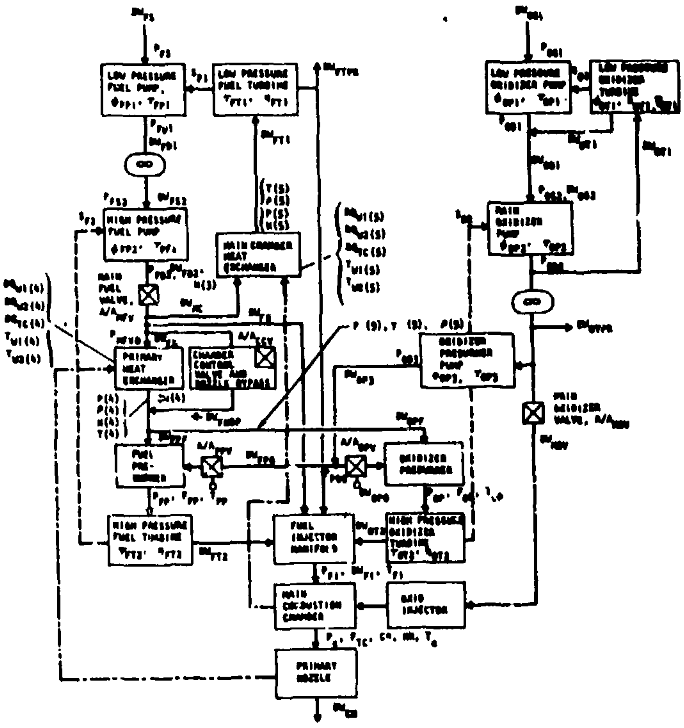

FIG. 12- SSMF Flow Schematic

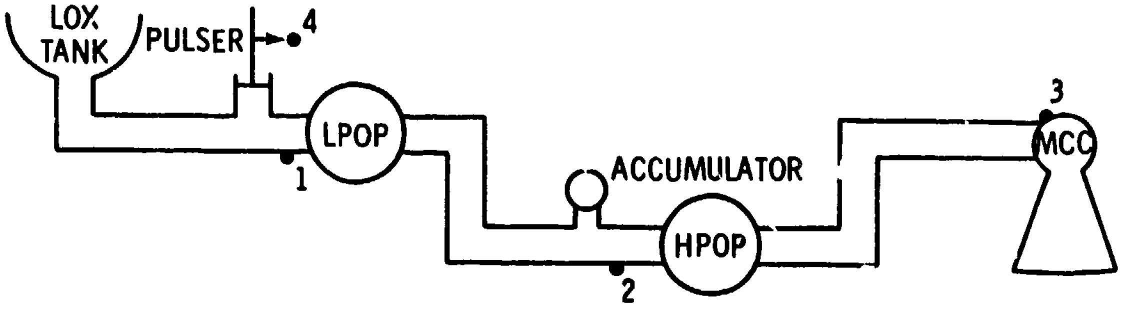

MEASUREMENT	DESCRIPTION
1	LOW PRESSURE OXIDIZER PUMP INLET PRESSURE (LPOP)
2	HIGH PRESSURE OXIDIZER TURBOPUMP INLET PRESSURE (HPOP)
3	MAIN ENGINE CHAMBER PRESSURE (MCC)
4	PULSER DISPLACEMENT

FIG. 13- GENERAL SCHEMATIC OF SSME POGO PULSING SYSTEM

The models did allow vehicle stability studies to proceed by the use of liberal tolerances on the estimated coefficients. The engine models also allowed early pretest simulation of engine testing on the various test stands so that testing methods and hardware could be designed.

TEST METHOD DEVELOPMENT

The plan was to sinusoidally excite the oxidizer feed system over the 1½ to 50 Hz range. The transmission of the disturbance would then be measured at the LPOTP inlet and outlet, HPOTP inlet and in main chamber pressure, Fig. 13. It was also planned to develop 4-terminal transfer functions for the LPOTP which could be compared with work being performed at CIT (Calif. Institute of Technology). The engine and test stand model was used to define the capability of an inlet system pulser, to provide excitation through the engine system so that instrumentation requirements could be defined and to test out data reduction methods.

Accuracy requirements for engine transfer functions were tentatively set at 10 percent on amplitude and 10 degrees on phase. To achieve this accuracy requires an even greater accuracy for the measurements used to obtain the transfer functions. A goal of 5% amplitude error and 5° phase error on any measurement relative to the excitation input was defined. This error includes the transducer, recording system, spectral analyzer and inherent signal/noise effects at the measurement point. Assuming excitation producing 10 psi P-P at the engine inlet (10% of steady state), the pressure fluctuations should be about 10 psi P-P (2% of SS) at the HPOTP inlet and about 3 psi P-P (1/10% of SS) in chamber pressure. Flow fluctuations should be about 1/10% of SS. AC coupled pressure transducers (PCB) with integral first stage amplifiers allowed a high signal level which minimized instrumentation and recording system noise. Spectral cross-correlation using the Time/Data 1932 at Rocketdyne and Hewlett Packard 5451C Fourier Analyzer at MSFC provided a very low noise method for data processing. Remaining noise inherent in the engine system became the limit for pressure measurement accuracy. That level was approximately 0.2 psi squared per Hertz.

Flow measurements to support evaluation of 4-terminal pump transfer function definition were not accomplished.

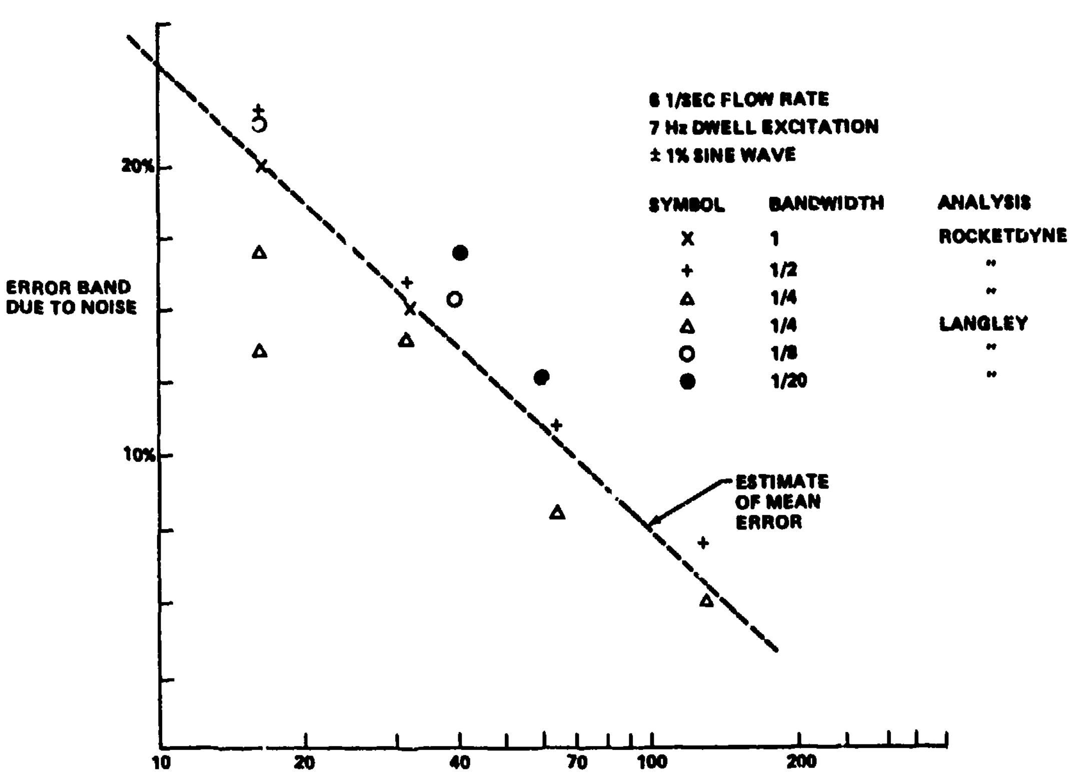

FIG. 14- LANGLEY USFM TEST
Analysis Time-Sec.

Several approaches were attempted, however, the best being a meter developed by ONERA (Office National D'Etudes Et De Researches Aerospatiales). The meter had excellent accuracy and response as shown in tests at the NASA Langley Research Center and at Rockwell's Space Systems Division. Signal/noise ratio in the actual application to Rocketdyne testing, however, showed that it was not applicable to SSME testing. A 1% flow variation at 7 Hz requires nearly 70 seconds for 10% accuracy; see Figure 14. With expected flow variations in the range of 1/10%, the engine test time required for meaningful accuracy was prohibitive. It was quite obvious that the 4-terminal pump dynamics could not be directly evaluated.

The system excitation device chosen for all transfer function testing was the hydraulic servo driven piston, pulser, shown in Figure 15. Initially the electronics were designed so that pulser position followed input voltage but studies showed that it was preferable to use a nearly constant flow rate excitation over the frequency range. The electronics were then changed so that for frequencies from 2 to 50 Hz the flow rate produced by the device was proportional to the input voltage. Later, when the device was chosen for use on the MPTA (Main Propulsion Test Article) stroke and velocity limiting circuits were added for safety. With the servo driven pulser, any excitation profile could be used. The most desirable mode of testing involved prerecording the profile on FM tape and playing it into the pulser electronics during the test. Gain of the input signal could be adjusted during a test.

Approximately 300 seconds is available for a single engine test. This is limited by the size of the propellant tanks. If one test is available to obtain transfer functions for each combination of inlet pressure and engine power level, the problem is to cover the required 2 to 40 Hz range in an efficient and safe manner.

Simulations indicated that, with constant bandwidth spectral processing, a linear frequency sweep produces uniform power across the frequency band except for transient lobes at both ends of the frequency band. Using spectral averaging techniques and starting each

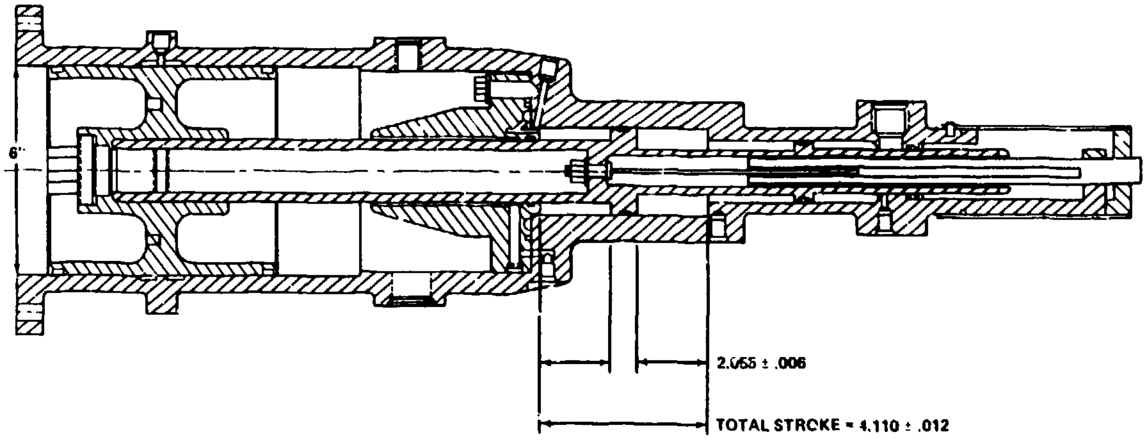

FIG. 15 - SSME PULSER

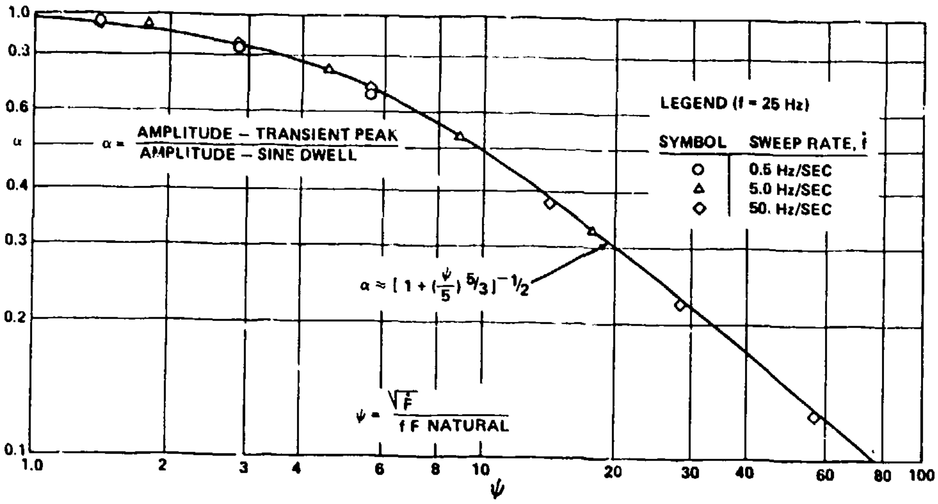

FIG. 16- TRANSIENT MAXIMUM RESPONSE FOR SWEPT SINE EXCITATION OF A SECOND ORDER SYSTEM

sweep with a unique initial condition results in a very uniform power spectrum. While a sweep does not give the accuracy of dwell excitation at any particular frequency, it does a good job over the entire range. The effect of sweep rate was then investigated by applying the excitation to a second order system and determining the velocity response function with the Time/Data 1932. Except for systems with extremely small damping the transfer function accuracy was only a function of accumulated test time regardless of the sweep rate. It became obvious that much of the prejudice against the use of fast sweep techniques was associated with its use in very lightly damped systems and by those using tracking filter techniques rather than spectral analyzers. Figure 13 is a non-dimensional plot of the attenuation of peak velocity obtained by fast sweeping compared with the peak velocity obtained from a dwell or slow sweep test. The conclusion was that sweeps as fast as 5 to 10 sec., from 2 to 5 Hz could be used in SSME testing.

SUBSYSTEM TESTING

Component interactions in real systems obey Murphy's first law, so, to avoid program impacts, a major subsystem test facility was activated. The subsystem was composed of an LPOTP modified for electric motor drive, an interpump duct and a bread-board suppressor. The existing facility was modified as shown in Figure 17 to anchor the inlet directly into the ground. An oil fired heat exchanger was installed to provide hot oxygen and a large decoupling accumulator was installed downstream of the test system orifice in the propellant return line (Figure 18).

The first phase of testing established the static cavitation performance of the LPOTP verifying its design goals. System testing under flow without the suppressor was next. A fast sweep profile was used and the noise problem associated with flow measurement was recognized. Initially the problem was thought to be the result of bubbles in the liquid oxygen flow stream affecting the ultrasonic beam. Even dwell pulsing did not improve the data significantly.

After the matrix of inlet pressure and simulated power level was complete the suppressor was installed. Initial checkout tests resulted in a surging condition in the system. At low helium and liquid oxygen flows the system was stable. Alternate diffuser designs and use of gaseous oxygen increased the stability range somewhat but surging still continued at flows corresponding to 50% of full power level. Tests of the plastic accumulator in a system using water and gaseous nitrogen showed the problem to be associated with high circulation in the suppressor, leading to cyclic flushing of the ullage. Several designs were tried to suppress the circulation without adding appreciable neck inertance or resistance. The Z-baffle shown in Figure 19 was chosen on the basis of best stability and performance. Tests were then run over the operational range to verify ullage stability, gaseous oxygen flow requirements and to obtain dynamic data to verify suppressor inertance and compliance.

The subsystem tests, while not providing all the information desired, were sufficient to verify the suppressor characteristics, to evaluate compliance and inertance values and to ensure compatibility with the LPOTP-interpump duct system. The strengths and weaknesses of fast sweep testing were also defined. The next step was verification of suppressor operation in single engine testing.

SINGLE ENGINE TESTING

The engine test program was being conducted on test stands A-1 and A-2 at NSTL (National Space Technology Laboratories) in Mississippi. Modifications to include a pulser tee and hydraulics as well as a level control recirculation line were made to the facilities. Initial dynamic tests showed rather lower pressure response to pulsing than had been anticipated. Ultrasonic flow meter

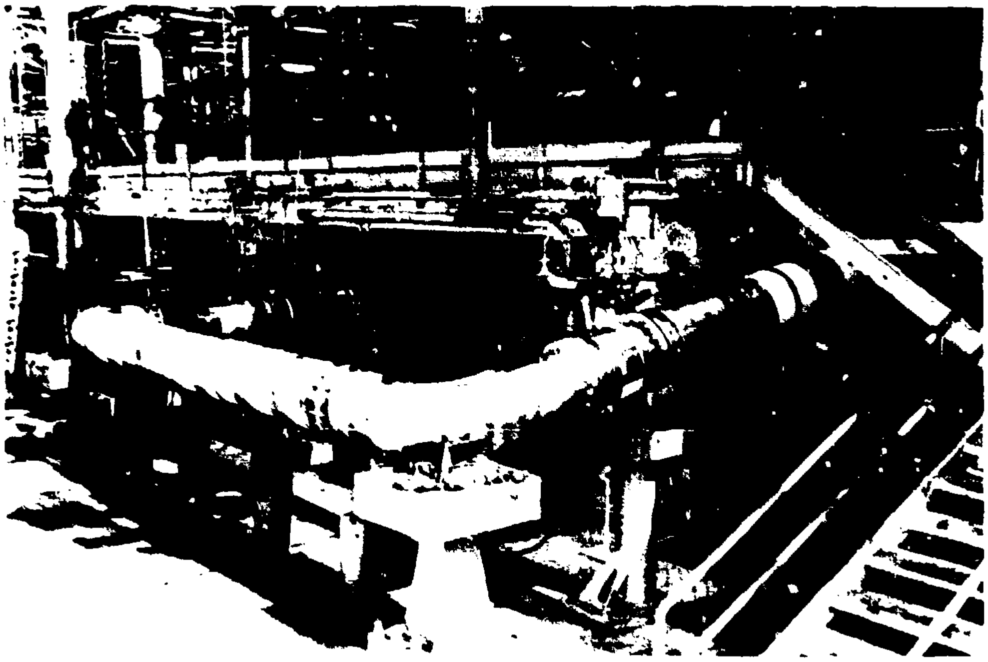

FIG. 17

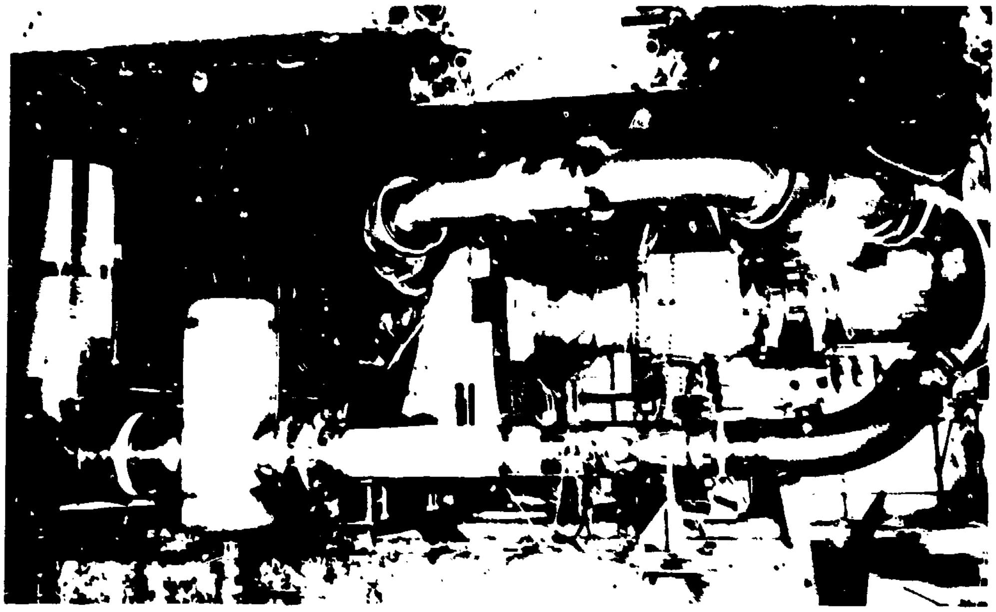

FIG. 18

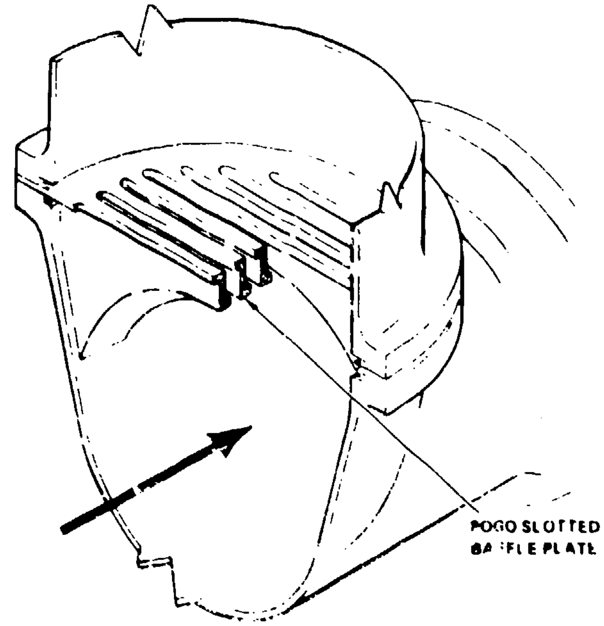

POGO SLOTTED BAFFLE PLATE
FIG. 19

ports which had been added earlier were utilized and again confirmed the flow noise level previously found in subsystem testing.

During static engine firings, an occasional tendency for bubble collapse at high power levels and with engine throttling transients was noted. Although the ullage re-established, an additional stage of baffling was added. These are shown in Figure 20.

Before a significant amount of dynamic testing could be accomplished, an additional test stand (A-3) was activated in Rocketdyne's Santa Susana Test Facility. At that time a program decision was made to dedicate all testing at NSTL to verification firings for the flight engines. All Pogo testing was switched to A-3.

From the minimal dynamic tests run at NSTL it was obvious that a combination of fast sweep and dwell excitation was necessary to obtain the best data over the frequency range required. The excitation profile used in this testing is shown in Figure 21. The initial 100 sec was composed of a fast sweep from 1¼ to 50 to 1¼ etc. with a cycle time of 15 seconds. This resulted in about six complete sweep cycles. Following this was 20 seconds at 4 Hz and 10 seconds each at 5 Hz increments to 50 Hz for a total of 110 sec of dwell. Since tests were normally about 300 seconds, the first 80 seconds were used for other test objectives i.e.; for adjusting inlet pressure and power level and for all AC coupled instruments to settle out.

The gain between the FM tape recorded reference voltage and the pulser was adjusted to ensure a safe but adequate pressure oscillation at the engine inlet. Normally this took about 2 full sweeps. Data was then obtained at a constant gain setting for the remainder of the fast sweeps and through the dwell portion.

Accelerometers installed at critical locations on the facility were initially monitored to prevent test stand damage. Note that a 12" diameter feedline pressurized to 20 psi develops a separating force of over a ton. With 1% structural damping, a ±10 psi pressure oscillation can develop equivalent static loads of over 50 tons peak to peak. Since structural resonances in the test stand did not correspond to feed system resonant frequencies where large oscillatory pressures were generated, no serious test stand loads were generated.

The most critical dynamic data collected in a test included piston input signal and pressures at the piston, the engine inlet (LPOP), the HPOTP inlet, the suppressor ullage and in the main combustion chamber pressure (see Figure 13). These data were recorded on FM magnetic tape for spectral analysis.

The test matrix was composed of engine operation at 70% and 100% power level with inlet pressures of 100 and 45 psia with and without the suppressor installed. Repeat tests were run to provide a measure of test to test differences and whenever a primary measurement was of questionable quality.

DATA ANALYSIS

Although strip charts provided a quick look for data quality, all data reduction was done using Rocketdyne's Time/Data 1932 real-time time-series analyzer and MSFC's 5451C Fourier Analyzer. Transfer functions for each pressure relative to the input pulser signal were computed using a 50 Hz low pass anti-aliasing filter and ¼ Hz analysis bandwidth with a spectral band of 0 to 100 Hz.

A typical set of reduced data is shown in Figures 22 through 26 although a listing of the data was actually used to develop transfer functions for the substructured engine. Data were analyzed with spectral averaging in two independant sections, the fast sweep and dwell segments. Some of the single frequency dwell segments were analyzed separately but the minor change in data quality did not warrant this effort.

After spectral data were reduced relative to the pulser they were algebraically manipulated to obtain the substructured engine transfer functions. A special software package has been developed for use on the HP5451C (Ref. 1). This approach is shown as follows:

Let:

F_X (f) → Fourier Spectrum of Input

F_Y (f) → Fourier Spectrum of Output

The Transfer Function is then Defined As:

$$H_{XY}(f) = \frac{F_{XY}(f)}{F_{XX}(f)}$$

Where:

F_{XY} (f) → Cross Spectrum

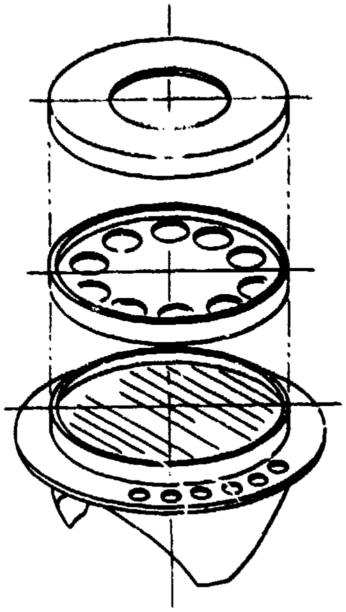

FIG. 20- POGO SPLASH PLATE

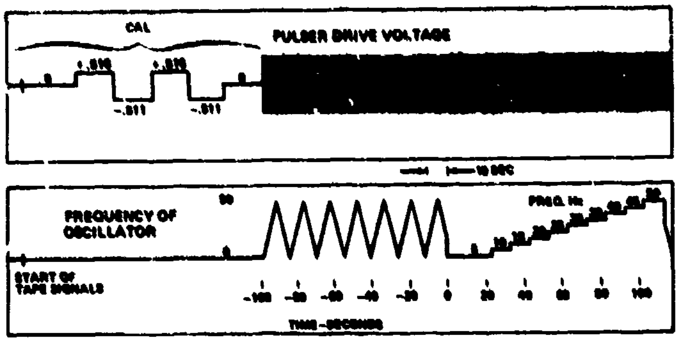

FIG. 21
POGO PULSER DRIVE TAPE FOR
SINGLE ENGINE TESTS ON A-3

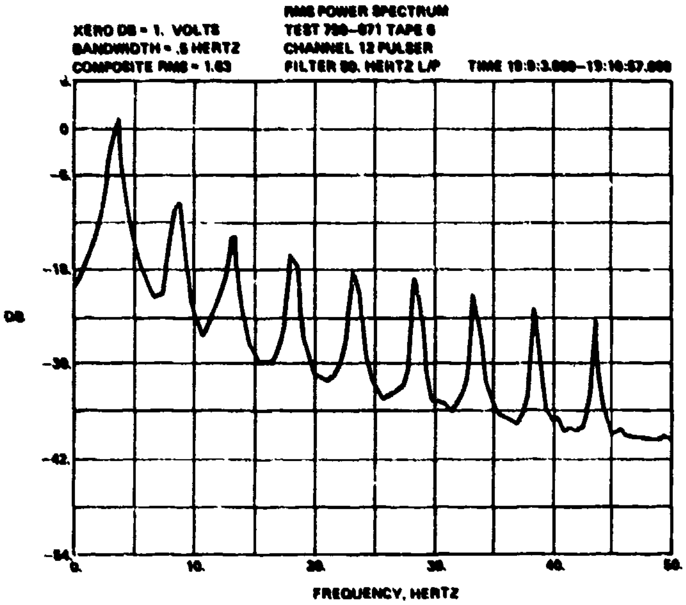

FIG. 22

F_{XX} (f) Auto Spectrum

Using the concept of referencing to a common signal (the Pulser) the transfer function and coherence becomes:

$$H_{21}(f) = \frac{H_{24}(f)}{H_{14}(f)} = \frac{F_{24}(f)/F_{44}(f)}{F_{14}(f)/F_{44}(f)}$$

$HPOP_{IN}/LPOP_{IN}$

$$H_{32}(f) = \frac{H_{34}(f)}{H_{24}(f)} = \frac{F_{34}(f)/F_{44}(f)}{F_{24}(f)/F_{44}(f)}$$

$MCC/HPOP_{IN}$

$$H_{31}(f) = \frac{H_{34}(f)}{H_{14}(f)} = \frac{F_{34}(f)/F_{44}(f)}{F_{14}(f)/F_{44}(f)}$$

$MCC/LPOP_{IN}$

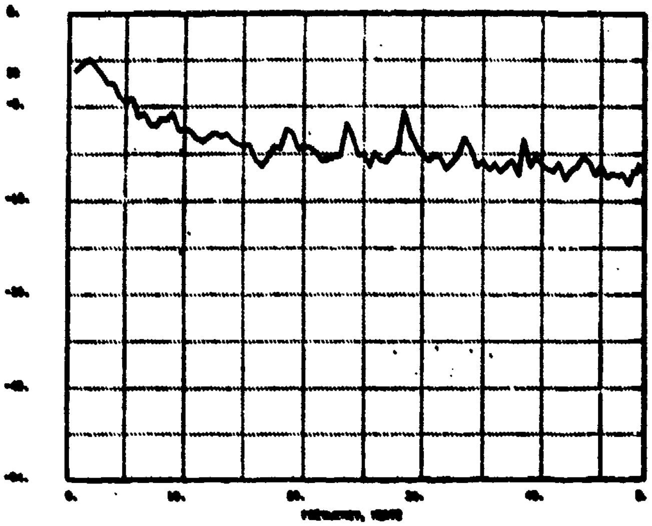

(left)
ZERO DB=1. PSI
BANDWIDTH= .5 HERTZ
COMPOSITE RMS= 3.70 PSI

RMS POWER SPECTRUM
TEST 750-071 TAPE 6
CHANNEL 11 MCC PR
FILTER 50. HERTZ L/P

FIG. 23

(right)
TRANSFER FUNCTION GAIN
TEST 750-071 TAPE 6
CHANNEL 11 MCC PR/CHANNEL
12 PULSER
FILTER 50. HERTZ L/P

ZERO DB= GAIN OF 1. PSI/VOLTS
BANDWIDTH = .5 HERTZ

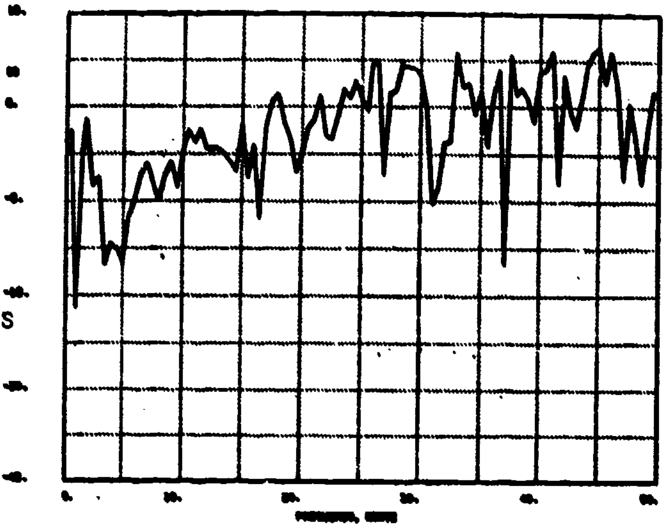

FI. 24

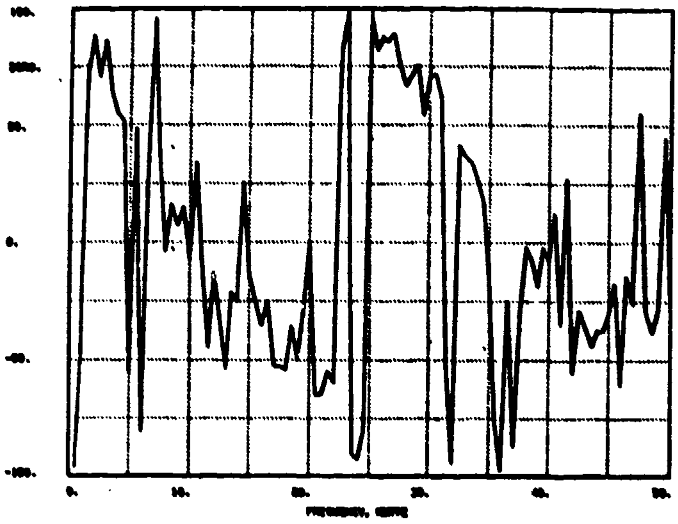

FIG. 25

(left)
TRANSFER FUNCTION PHASE
TEST 750-071 TAPE 6
CHANNEL 11 MCC PR /CHANNEL 12 PULSER
FILTER 50. HERTZ L/P

BANDWIDTH = .5 HERTZ

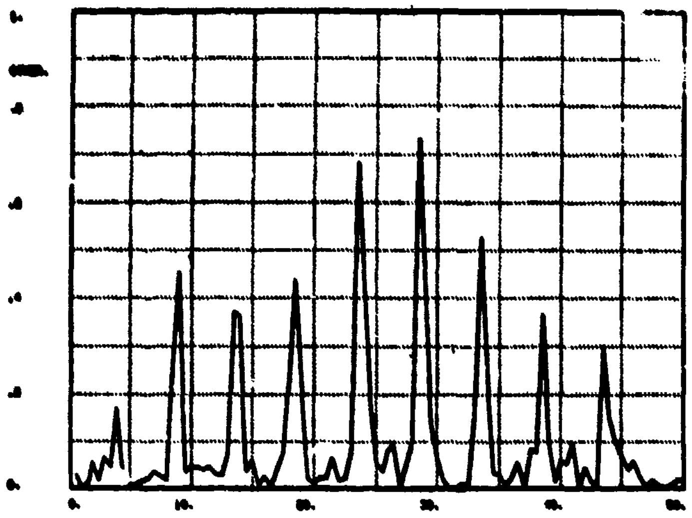

FIG. 26

(left)
COHERENCE
TEST 750-071 TAPE 6
CHANNEL 11 MCC PR/CHANNEL 12
PULSER
FILTER 50. HERTZ L/P

BANDWIDTH = .5 HERTZ

The coherence (squared) for $HPOP_{IN}/LPOP_{IN}$ is:

$$\gamma^2_{21}(f) = \left[\frac{1}{\gamma^2_{24}(f)} + \frac{1}{\gamma^2_{14}(f)} - 1 \right]^{-1}$$

The subscripts in these equations refer to the measurement numbers in Figure 13.

This approach minimized correlation of signals in the parameters which are coherent but generated in the engine itself. This engine generated noise is not associated with Pogo signals which are generated upstream of the engine and yet this engine noise shows high coherence (and erroneously high engine gain) if the pressures are correlated directly. Using the known disturbance as an intermediate reference minimizes engine generated noise effects.

INTERPRETATION OF SINGLE ENGINE TEST DATA

The two major transfer functions are the LPOTP - Interpump Duct-Suppressor $HPOP_{IN}/LPOP_{IN}$; i.e. $(\Delta P_{OS2}/\Delta P_{OS1})$ and the Power Head $MCC/HPOP_{IN}$; i.e. $(\Delta P_c/\Delta P_{OS2})$. The low pressure system transfer function changes dramatically dependent on whether the suppressor is or is not active. Figures 27 and 28 compare the test results and the original predictions.

Comparison of test data with predictions for the system with no suppressor indicated that only a very small HPOTP cavitation compliance was required to justify the model with the test data. The gain of the LPOTP-Duct is slightly less than predicted while the Power Head gain is slightly higher than predicted. Resonant dipoles were found in the LPOTP-Interpump Duct response (Figure 27) which were most readily justified with structural motion of the flexible duct.

Correlation of the model with data from tests with a suppressor installed resulted in well defined values of R, L and C for the suppressor which were within the design goals. Best of all, the suppressor is an excellent filter in the 5 to 40 Hz range with no unexpected adverse response. Gain below 4 Hz is almost unaffected by the suppressor although there is a phase effect. The suppressor effectively operates as a notch filter.

The Power Head should be defined accurately only without the suppressor since both the HPOTP inlet and main combustion chamber pressure oscillations developed by the pulser were severely attenuated by the suppressor. Thrust chamber pressure noise generated in the engine was not affected by the suppressor and the noise at the HPOTP was only slightly reduced. The net effect was a decrease in signal to noise ratio in both measurements but to a very great extent in thrust chamber pressure. A comparison of the predicted and demonstrated full engine transfer function $(MCC/LPOP_{IN})$ without suppressor is shown in Figure 29.

Extensive transfer function analysis has been performed on the SSME Pogo data obtained to date. A representative reporting of these results is given in

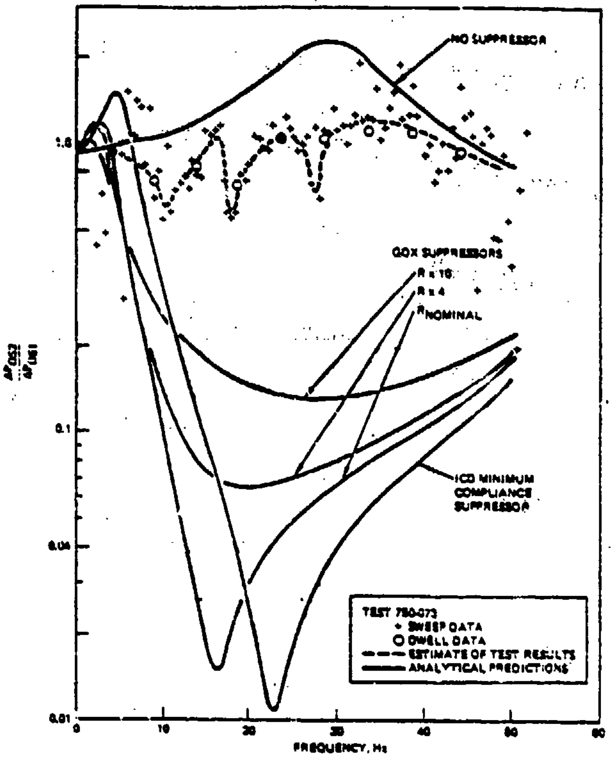

FIG. 27
Low-Pressure Oxidizer Turbopump Duct Response

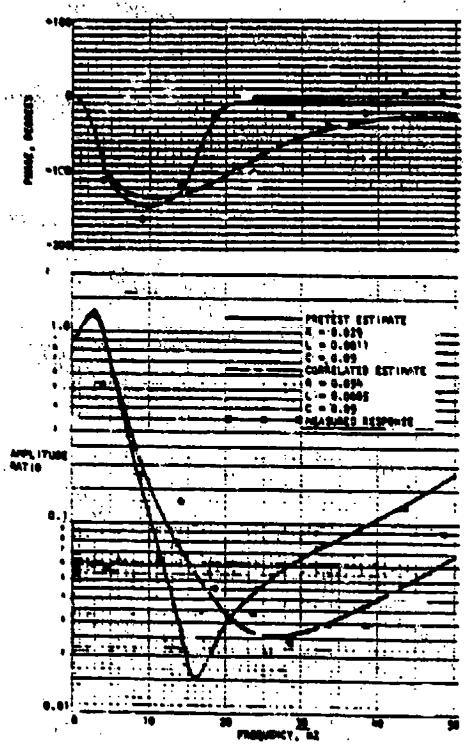

FIG. 28
HPOTP Inlet Pressure Response to Engine Oxidizer Inlet Pressure Oscillations, $\Delta P_{osz}/\Delta P_{osi}$

3 thru 6. Some test data was analyzed using a narrower spectral bandwidth (1/5 Hz). Since only 10 seconds were available for each dwell frequency, this allowed only a two sample coverage. With such a small sample the calculation indicated higher gain (due to the noise bias) and higher coherence (a single frame would show 100% coherence).

LPOTP COMPLIANCE

In parallel with the Rocketdyne testing, CIT (California Institute of Technology) conducted 4-terminal transfer function tests of a ¼ scale model of the LPOTP impeller in water. These tests included excitation both upstream and downstream of the pump over a range of inlet conditions including deep cavitation. The results of these studies are partially represented in references 7 through 21.

In actual vehicle use the inlet NPSH (net positive suction head) is higher than the critical value. This allows low risk extrapolation of the CIT results in water to the full size pump in liquid oxygen. A liberal band was placed on the extrapolated compliance values. Fortunately the feed system

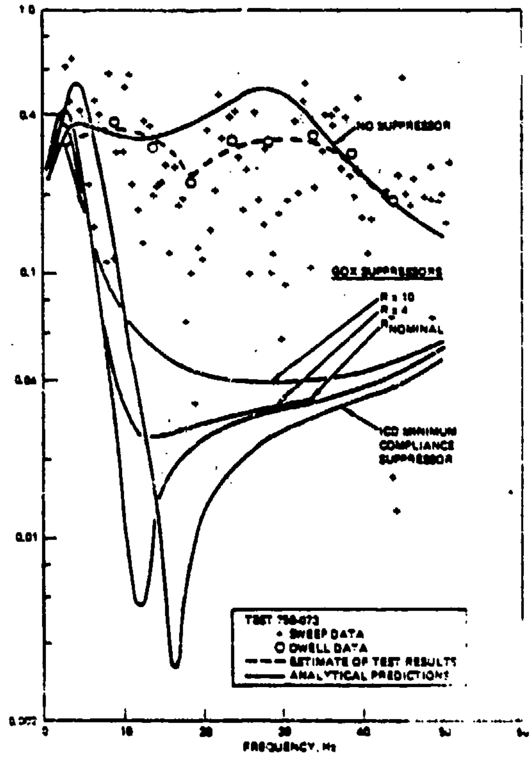

FIG. 29- ENGINE RESPONSE, CAI

dynamics are such that the changes in pump compliance cause only a small feedline frequency shift.

SUMMARY

A simple analogy of engine feedback in the Pogo loop indicates that the high pressure design of the SSME should result in the vehicle having considerably greater stability than vehicles using engines with lower internal pressure levels.

The initial analytical estimates of engine transfer functions were in good agreement with data obtained from engine and subsystem test. Over the expected operating range, cavitation affects are minor.

The suppressor design using liquid and gaseous oxygen is quite stable and an effective notch filter for the system. All the major problems of ullage stability involved circulation in the liquid below the liquid-gas interface. Design estimates of the compliance and inertance of the design were conservative although the effective resistance exceeded the initial estimate.

The use of a fast linear swept sine wave is feasible and desirable in determining transfer functions over a wide frequency band. The additional use of a few dwell excitation frequencies in the spectrum to provide accurate bench marks was also required.

The best excitation for the system involved constant velocity disturbances (flow rate perturbation) over the frequency band. The redesign of the pulser electronics to produce piston velocity proportional to command voltage eliminated input signal/noise problems in the high frequency range and allowed safety circuits to be included in the electronic package.

ACKNOWLEDGEMENTS

The work presented here is the result of the efforts of many people in many places. At Rocketdyne, the solution of difficult problems leading to the development of the two-phase suppressor was primarily due to G. H. Karigan, E. A. De Gaetano and M. C. Kan. J. G. Absalom, G. M. Smith and H. P. Yarnall were responsible for pulser development, while the electrical modifications which ensured its safe operation during testing were due to E. C. Buchanan.

At NASA MSFC, A. L. Worlund and J. E. Harbison furnished much of the early guidance in Shuttle pogo suppression. E. H. Hyde was of great support in development of both the active suppressor concept and later of the baseline suppressor. L. A. Gross contributed his own expertise in turbomachinery and was responsible for obtaining funding for Professors Brennan and Acosta leading to their timely contribution. Dr. L. Schutzenhofer and K. L. Spanyer provided estimates of the subsystem's transfer function based upon the Rocketdyne modeling equations. T. E. Nesman provided much of the transfer function analysis used at MSFC. Tony Gardner of Wyle Laboratories is recognized for his timely completion of the pogo transfer function software package.

Finally, we would like to thank J. J. Dordain and J. C. Demarais of ONERA and T. D. Carpini of NASA LaRC for their valiant effort in ultrasonic flowmeter development.

REFERENCES

1. Gardner, T. G., "Evaluation of SSME Fluid Dynamic Frequency Response Characteristics," Wyle Laboratories, Research Staff Technical Memorandum MT-80-6, Contract NAS8-33508, October 1980.

2. Jewell, R. E., "Trip Report on 24th Space Shuttle Pogo Integration Panel Meeting," NASA, MSFC, Memo ED21-80-15, June 1980.

3. Jones, J. H. and Nesman, T. E., "Single Engine SSME Pogo Data for 25th SSIP Meeting," NASA, MSFC, Memo ED24-80-33, October 1980.

4. Nesman, T. E., "Single Engine SSME Pogo Data, Quick Look," NASA, MSFC, Memorandum ED24-80-22, September 1980.

5. Nesman, T. E., "Space Shuttle Main Engine Pogo Test Results," NASA, MSFC, Memorandum ED24-80-35, November 1980.

6. Nesman, T. E., "STS-1 Pogo Analysis," NASA, MSFC, Memorandum ED24-81-31, June 1981.

7. Spanyer, K. L., "Results of Calculations from Theoretical Equations Pertaining to Pogo Transfer Functions," NASA, MSFC, Memorandum ED24-80-17, August 1980.

8. R-3128, "Final Technical Report, Thor Block 2 Test Program (20 yrs. Oscillation Problem)," Rocketdyne

Division of North American Aviation Inc., Canoga Park, CA, August 1961.

9 Prause, R. H. and Goldman, R. L., "Longitudinal Oscillation Instability Study- POGO," Martin Company, Baltimore MD, December 1964.

10 R-6929, "Engine System Transfer Functions for Support of S-V Vehicle Longitudinal Stability (POGO) Analyses Program," Rocketdyne Division of North American Aviation Inc., Canoga Park, CA, March 1967.

11 R-7970, "Investigation of 17 Hz Closed-Loop Instability on S-II Stage of Saturn V," Rocketdyne Division of North American Rockwell, Canoga Park, CA, August 1969.

12 R-7317-1, "F-1 Engine Operation in the S-IC-2 Stage of the Saturn V AS -502 Flight, Rocketdyne Division of North American Rockwell, Canoga Park, CA, September 1968.

13 Lipput, S., "Vibration Standards Proposal," SAE Journal, May 1947.

14 Saturn V Pogo Working Group, "Unpublished Briefing Charts Presented by Participating Members," NASA, MSFC, Huntsville, AL, 1968-1971.

15 RSS-8506, "Pogo-SSME Phase CD, Volume 30," Rocketdyne Division of North American Rockwell, April 1971.

16 Farrel, E. C. and Fenwick, J. R., "Pogo Instabilities Suppression Evaluation," (NASA CR-134500) Rocketdyne Division of Rockwell International, Canoga Park, CA, November 1973.

17 Fenwick, J. R., "SSME Model, Engine Dynamics Characteristics Related to Pogo," RSS-8549, Rocketdyne Division of Rockwell International, September, 1974.

18 Alais, P. and Demarais, J. C., "Measurement of Rapidly Varying Hydraulic Flow Rates by Ultrasonic Waves," (NASA Technical Translation TT F-14, 392, August 1972) originally in La Recherche Aerospatiale, No. 2, March-April 1972, pp. 61-73.

19 Brennan, C. and Acosta, A. J., "The Dynamic Transfer Functions for a Cavitating Inducer, "ASME, 75-WA/FE-16, 1975.

20 Ng, S. L., 1976, "Dynamic Response of Cavitating Turbomachines, "Ph.D Thesis, California Institute of Technology, Pasadena, CA.

21 Braisted, D. H., 1979, "Cavitation Induced Instabilities Associated With Turbomachines," Ph.D. Thesis, California Institute of Technology, Pasadena, CA.

SPACE SHUTTLE SOLID ROCKET BOOSTER WATER ENTRY CAVITY COLLAPSE LOADS

R. T. Keefe and E. A. Rawls
Chrysler Corporation
Slidell, Louisiana

D. A. Kross
NASA/Marshall Space Flight Center
Huntsville, Alabama

SRB cavity collapse flight measurements included external pressures on the motor case and aft skirt, internal motor case pressures, accelerometers located in the forward skirt, mid-body area, and aft skirt, as well as strain gages located on the skin of the motor case. This flight data yielded applied pressure longitudinal and circumferential distributions which compare well with model test predictions. The internal motor case ullage pressure, which is below atmospheric due to the rapid cooling of the hot internal gas, was more severe (lower) than anticipated due to the ullage gas being hotter than predicted. The structural dynamic response characteristics were as expected. Structural ring and wall damage are detailed and are considered to be attributable to the direct application of cavity collapse pressure combined with the structurally destabilizing, low internal motor case pressure.

INTRODUCTION

The Space Shuttle vehicle concept, illustrated in Fig. 1, was developed to provide a cost effective means for putting men and payloads into earth orbit. The primary cost saving feature of the design is the reuseability of most of the major elements including the two Solid Rocket Boosters (SRB's). The SRB recovery sequence consists of using parachutes for deceleration purposes followed by tail-first water impact at approximately 90 ft/sec and subsequent retrieval at sea. Although tail-first water entry takes advantage of the greater hydrodynamic drag of this mode of entry to minimize penetration depth and associated hydrostatic case pressures, it subjects the nozzle, aft skirt, and aft bulkhead to tremendous impact pressure loads.

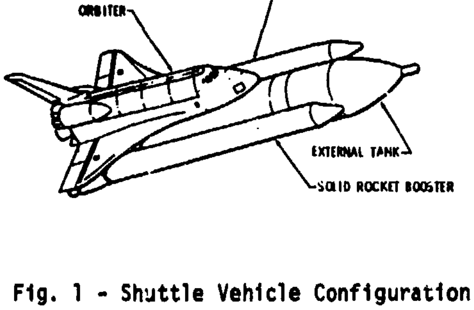

Fig. 1 - Shuttle Vehicle Configuration

The overall structural design of the SRB was greatly influenced by these loads. The water impact analytical and experimental program task sequence to establish design criteria is illustrated in Fig. 2. For the present paper, emphasis is focused on those tasks associated with water impact loads research and loads definition.

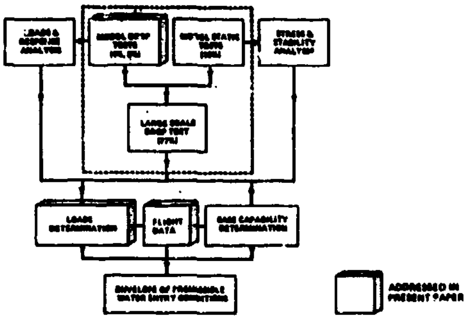

Fig. 2 - Integrated Analytical and Experimental Program

Of particular interest and importance were the 8.56% scale model water impact tests conducted at the Naval Surface Weapons Center in which extensive measurements of pressures, forces and accelerations were made during the various phases of water penetration. The hydrodynamic phenomena studied included the dynamic behavior of water in the annulus between the aft skirt and the rocket nozzle, ingestion of water through the nozzle, cavity formation and collapse, maximum penetration depth, rebound and slapdown.

Froude similarity relationships, which were verified to be applicable for scaling the transient loadings, were used to generate full scale predictions of pressure, acceleration, and loads as functions of initial impact conditions. These results were used as the basis for water impact design loads definition.

One of the most significant loading events from a structural design viewpoint, and the subject of this paper, is the sharply transient pressure exerted on the motor case and aft skirt upon collapse of the external cavity generated during vehicle water penetration. To withstand these pressures, the aft motor case is stiffened by external, circumferential stubs and rings as shown in Fig. 3.

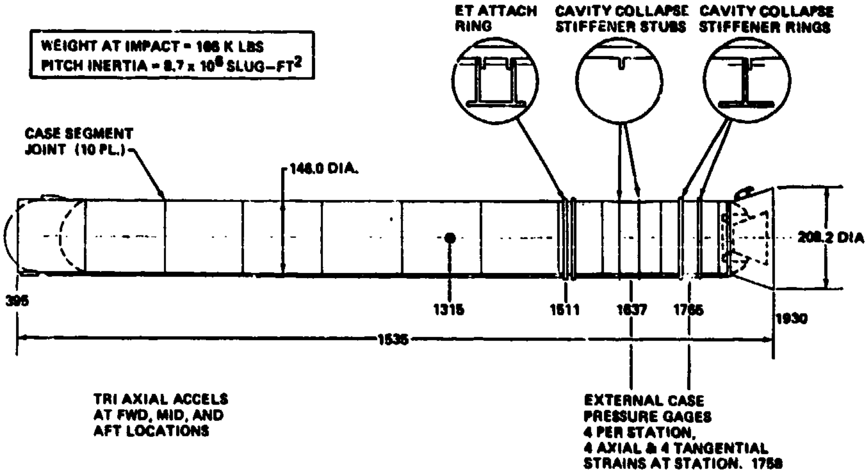

Fig. 3 - SRB Water Impact Configuration

The recent flight test of the Space Shuttle System (STS-1), where both boosters were successfully recovered, has provided the opportunity to analyze the validity of cavity collapse pressure predictions through direct comparison with full scale measurements.

The present paper briefly discusses the significant cavity collapse loading phenomena observed and measured on STS-1 relative to predictions based on the model tests. The discussion includes applied loads comparisons and a structural response summary.

CAVITY COLLAPSE DYNAMICS

The various phases of the water impact phenomena associated with tail-first entry of the SRB configuration have been extensively studied in scale model tests (1) and (2). As shown in Fig. 4, rapid penetration of the SRB creates a large, open cavity surrounding the tail of the vehicle. Prior to reaching maximum penetration depth, this cavity collapses suddenly and generates sharp, large amplitude pressures. Fig. 4 qualitatively illustrates the relationship between the vehicle initial trajectory at impact, the asymmetry of the cavity, and the location of the cavity collapse relative to the centerline of the vehicle. The upper sketch presents an example of impact conditions which cause cavity collapse and peak pressures to occur in the region behind the vehicle. A more critical case is presented in the lower sketch in which the cavity collapses on the vehicle surface thereby inducing extreme, sudden pressures and loads.

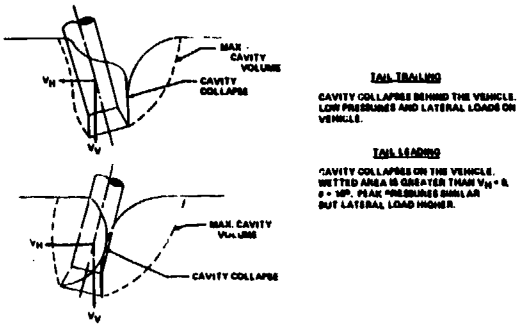

Fig. 4 - Cavity Collapse Dynamics

High speed photographs of the collapse phenomenon in this case show that the initial water contact occurs at a longitudinal station forward of the aft skirt, with subsequent, rapid fore and aft propagation of the wetted surface. Below the point of initial contact, the closing cavity impinges downward on the flared aft skirt generating an initial downward axial acceleration followed by a net forward or upward acceleration. Also, centerline asymmetry of cavity collapse induces lateral accelerations in the vehicle.

STS-1 SRB INSTRUMENTATION AND MEASUREMENTS

On the STS-1 flight, the cavity collapse event was recorded by means of 8 pressure transducers placed on the external motor case walls at longitudinal stations 1637-inches and 1765-inches, as illustrated in Fig. 3. Three other pressure transducers located to measure external pressure on the aft skirt of the right SRB were found to be non-functioning at the moment of impact. Additional instrumentation included 4 axial and 4 tangential strain gages located at station 1758-inches, lateral and axial accelerometers, and tri-axial rate gyros.

At the moment of water impact, sea conditions were very calm with a wind speed of approximately five knots. Vertical velocity at impact was estimated from photographic data at 92 FPS. The angle of impact was approximately zero degrees. Acceleration traces for the STS-1 SRB impact are presented in Fig. 5. These graphs show axial and lateral acceleration time histories relative to launch time, T_o. Each trace shows the high "g" level of initial impact, followed by the cavity collapse event, occurring about one second later. Significant vehicle elastic response is evident in each trace. The lateral acceleration levels measured are consistent with predictions based on model data for the observed initial conditions at impact. The axial accelerations are approximately 20% lower than predicted.

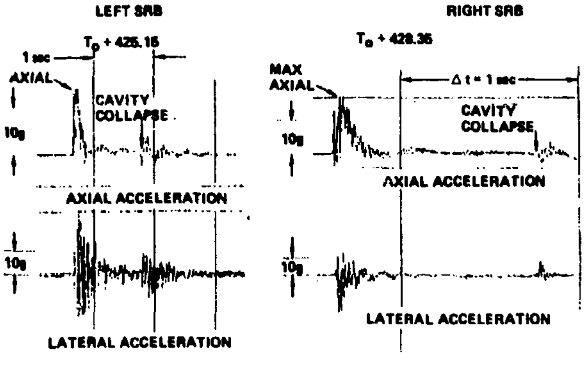

Fig. 5 - SRB STS-1 Water Impact Accelerations

Fig. 6 shows the time history of pressure measured on the aft motor case of the right SRB. A sharp pressure pulse of approximately 165 psig is observed at a circumferential location of $\phi = 45^{\circ}$ at station 1765-inches. Shortly afterward a smaller peak pressure is observed at the same circumferential location at station 1637. Correlation of these data with the initial conditions at impact, and acceleration and rate data suggest that cavity collapse occurred on the surface of the vehicle in the approximate circumferential range between $\phi = -45^{\circ}$ to $+135^{\circ}$.

All other pressure data at other circumferential locations shows gradual increases prior to the instant of cavity collapse, indicative of a wetted keel-side surface with increasing depth of immersion or penetration. The instant of cavity collapse on these traces is indicated by a slight increase in pressure coupled with an unexplained oscillation. The pressure fluctuation approximately 0.5 seconds ahead of cavity collapse at $\phi = 225^{\circ}$ for both measurement stations is thought to be wave slap from initial impact.

Circumferential plots of the pressure measurements at the instant of cavity contact at station 1765 are presented in Fig. 7. At this instant, the cavity has not yet contacted the surface at station 1637, which explains the zero pressure reading at $\phi = 45^{\circ}$. The solid lines represent the predictions based on model tests. Also included on Fig. 7 is the cavity collapse longitudinal pressure distribution as measured and predicted. The STS-1 data shows a perceptible shift forward resulting from greater depth of penetration at the onset of cavity collapse than predicted from model tests. The greater penetration of each booster occurred because of unexpected and significant reductions of internal case ullage pressure at impact, as shown in Fig. 8. These pressure reductions and the subsequent reduction in bouyancy were caused by quenching of the hot ullage gases as water sprayed through the rocket nozzle on impact.

Figure 9 is a pictorial assessment of the water impact damage on each aft motor case and skirt. This diagram includes both initial impact internal and cavity collapse external damage. As a result of cavity collapse loads and the structural destabilization caused by lower ullage pressure, extensive ring damage occurred on both SRB's in the form of sheared bolts which fastened the rings to the motor case. In addition, motor case permanent deflection or dimpling was observed on the left SRB.

Fig. 10 presents the strain data which indicates a partial shell buckling at cavity collapse.

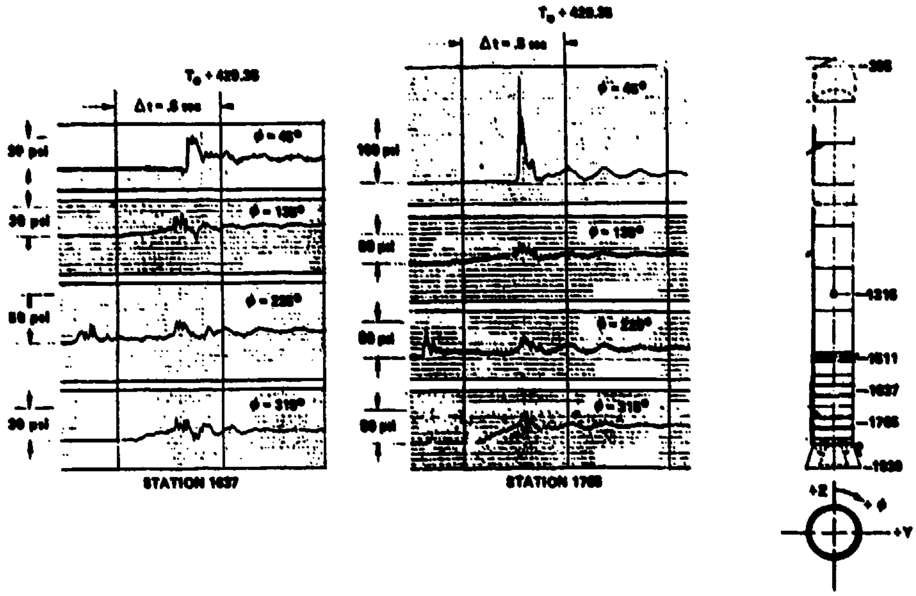

Fig. 6 - SRB STS-1 Cavity Collapse Case Pressures

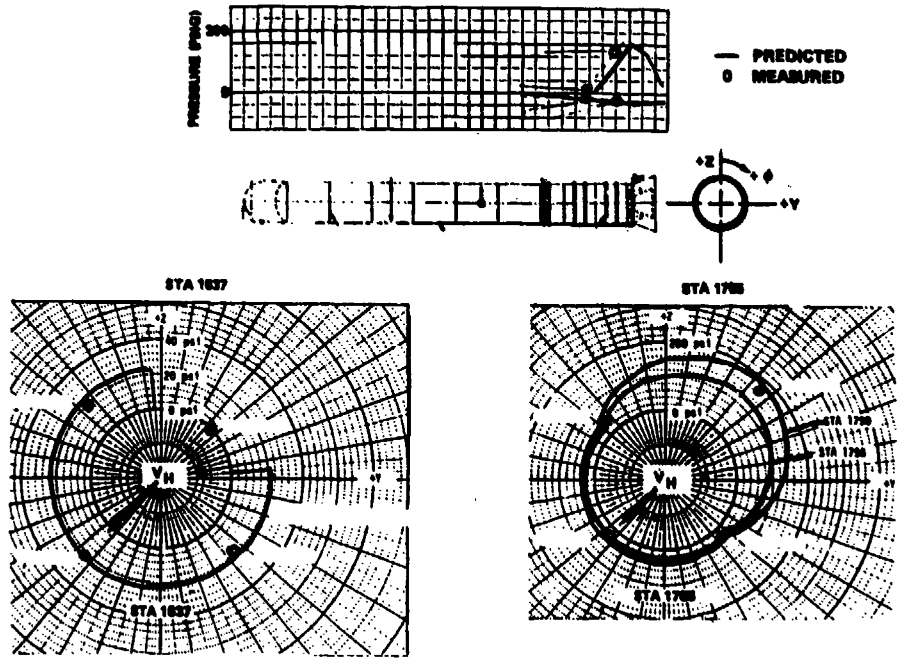

Fig. 7 - SRB STS-1 Cavity Collapse Pressure Distribution

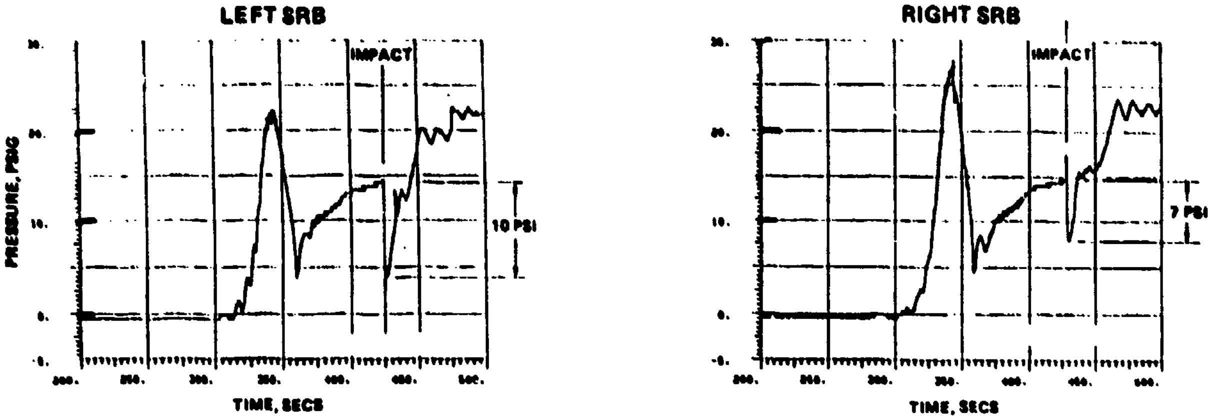

Fig. 8 - SRB STS-1 Internal Case Ullage Gas Pressure

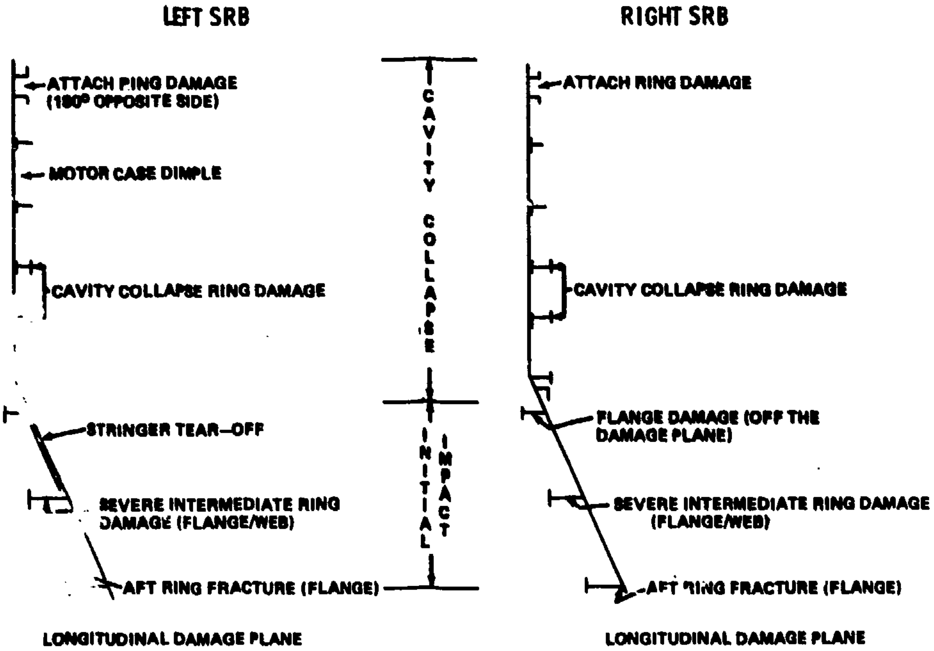

Fig. 9 - SRB STS-1 Water Impact Damage Summary

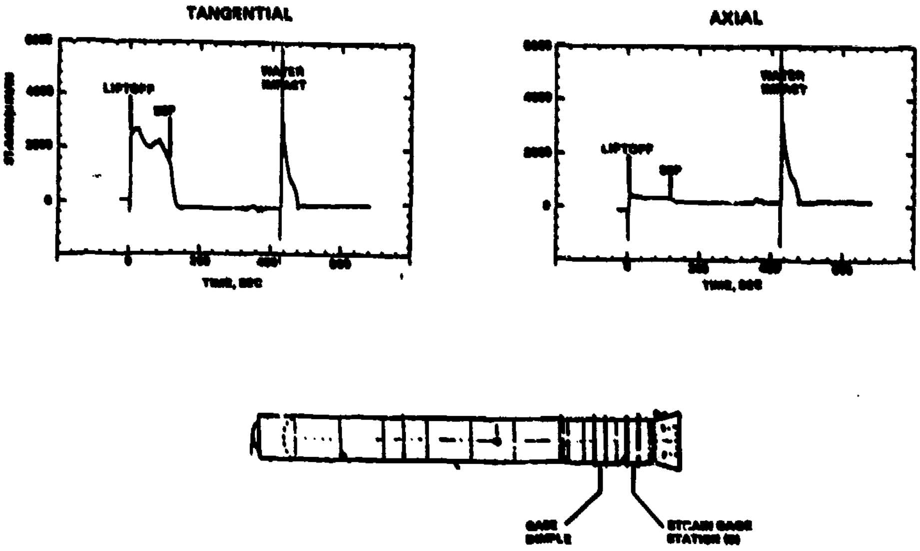

Fig. 10 - Left SRB STS-1 Aft Case Segment Strains

SUMMARY

Measurements obtained from the first Space Shuttle Solid Rocket Booster indicate high water impact cavity collapse pressures consistent with the preflight predictions which are based on scale model test results. Cavity collapse, however, occurred at a deeper penetration depth than predicted. This was due to the high internal case ullage gas temperature which caused a significant pressure drop at impact of -10 psig on the left SRB. Although some damage was sustained due to cavity collapse loads, the motor case has been deemed reuseable.

REFERENCES

1. E. A. Rawls and D. A. Kross, "A study of the Space Shuttle Solid Rocket Booster Nozzle Water Impact Recovery Loads," The Shock and Vibration Bulletin 46, August 1976.

2. R. Madden and D. A. Kross, "Scaling of Water Impact Data for Space Shuttle Solid Rocket Booster," The Shock and Vibration Bulletin 44, October 1973.

SPACE SHUTTLE SOLID ROCKET BOOSTER REENTRY AND DECELERATOR SYSTEM LOADS AND DYNAMICS

RICHARD MOOG
MARTIN MARIETTA/DENVER DIVISION
DENVER, COLORADO

DENNIS KROSS
NASA/MARSHALL SPACE FLIGHT CENTER
HUNTSVILLE, ALABAMA

Recovery of the Space Shuttle Solid Rocket Boosters required development of a heavy duty large decelerator subsystem. Successful recovery of the first launch pair of boosters demonstrated the adequacy of the design. Flight data consisting of accelerometers and parachute attach point loads provide a basis for evaluation of the decelerator subsystem performance. These results are summarized and compared to preflight predictions.

INTRODUCTION

The Space Shuttle system employs two reusable Solid Rocket Boosters (SRB). After burnout, these SRB's separate from the External Tank and coast to apogee at over 250,000 ft. altitude. The SRB's, shown in Fig. 1, approximately 145 ft. long and 12 ft. in diameter, reenter in a tumbling mode. As the aerodynamic pressure increases, the SRB trims in a coning motion to a high angle of attack broadside attitude. At between 16,000 to 15,000 ft. altitude, deployment of the SRB decelerator subsystem is initiated by separation of the nosecap. The decelerator subsystem (DSS) is used for stabilization and deceleration to a terminal velocity of approximately 90 ft/sec of the spent 175,000 lb. SRB.

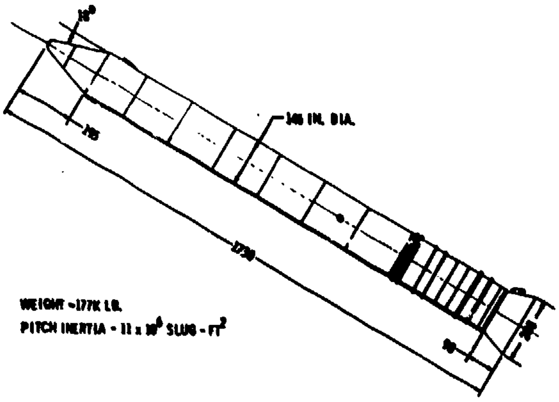

Fig. 1 - SRB Reentry Configuration

The deployment of the DSS induces high structurally critical loading conditions to the SRB frustum and forward skirt. The design of the subsystem and deployment sequencing had to accommodate several constraints imposed due to shell buckling, tension loadings, and dynamic acceleration conditions. The first Space Shuttle flight, which included the successful stabilization, deceleration, and recovery of both SRB's, verified that the DSS design was adequate.

SYSTEM DESCRIPTION

The DSS, prior to deployment, is stowed in the nose cone compartment of the SRB as shown in Fig. 2. Deployment is initiated by separation of the nose cap followed by pilot chute inflation as shown in Fig. 3. The pilot chute is used to deploy the drogue chute, which, in turn, stabilizes the SRB by rotation to a tail-first attitude and decelerates the vehicle in preparation for main chute deployment. At an altitude of approximately 6,500 ft., the drogue chute pulls the frustum from the SRB while deploying the main chutes contained within the frustum. The configurations of the 11.5 ft-D_o

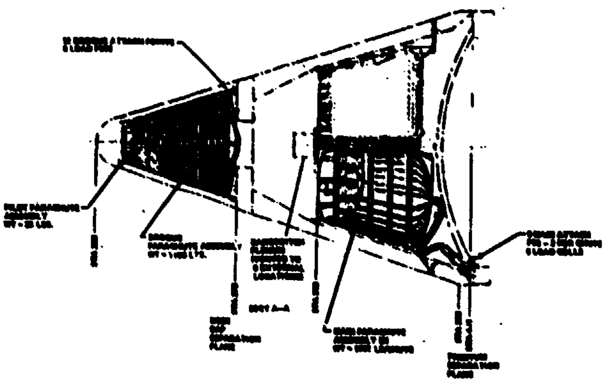

Fig. 2 - Decelerator Subsystem Installation

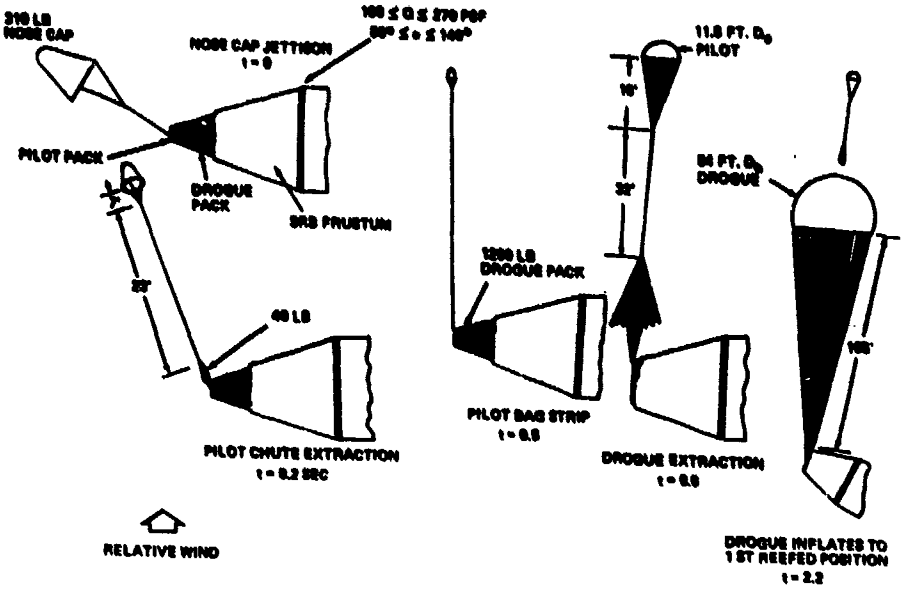

Fig. 3 - Deployment Sequence

pilot chute, the 54 ft-D_o drogue chute, and the 115 ft-D_o main chutes are shown in Fig. 4. To alleviate high loads, the drogue and main chute systems have two stages of reefing.

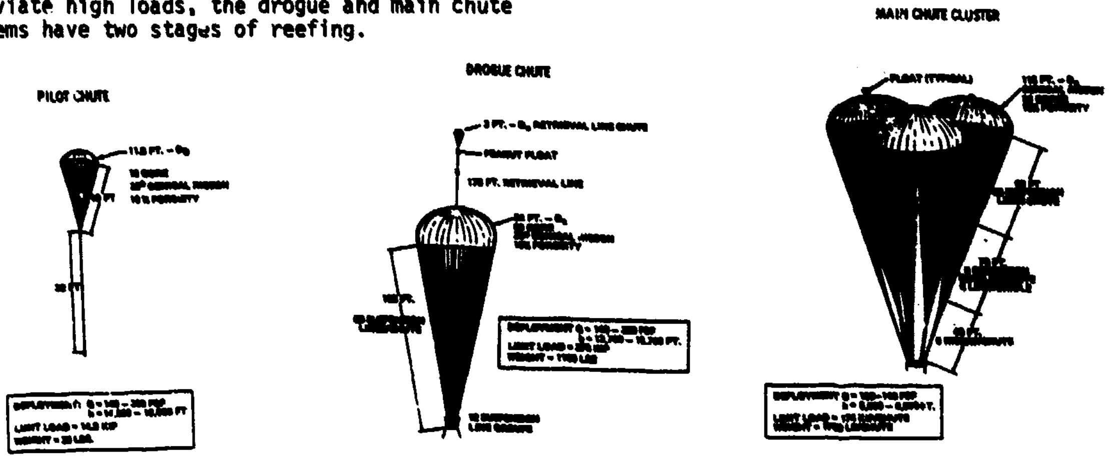

Fig. 4 - Plot, Drogue, and Main Chute Geometry

REENTRY DYNAMICS

The first Space Shuttle launch (STS-1) occurred on April 12, 1981, from the Kennedy Space Center. The reentry profile for the right SRB shown in Fig. 5 was obtained from shipboard radar and photographic coverage. The SRB separated at an altitude of 173,000 ft. coasted to an apogee of 270,000 ft, then reentered to a maximum dynamic pressure of 2,000 psf at an altitude of 40,000 ft. Plots of preflight predicted vs. actual flight altitude, Mach number, dynamic pressure, and angle of attack are presented in Fig. 6.

The peak SRB axial deceleration of 5 g's occurred during the maximum dynamic pressure region of reentry as illustrated in Fig. 7.

DECELERATOR SUBSYSTEM PERFORMANCE

Tables 1 and 2 summarize the DSS performance and chute loads experienced during the STS-1 flight test. Trajectory data was available only for the right SRB. The significant events of nose cap separation, frustum separation, and water impact took place within the preflight predicted ranges.

Time histories containing the total measured parachute load traces, shown in Fig. 8, indicated that the peak drogue chute load of

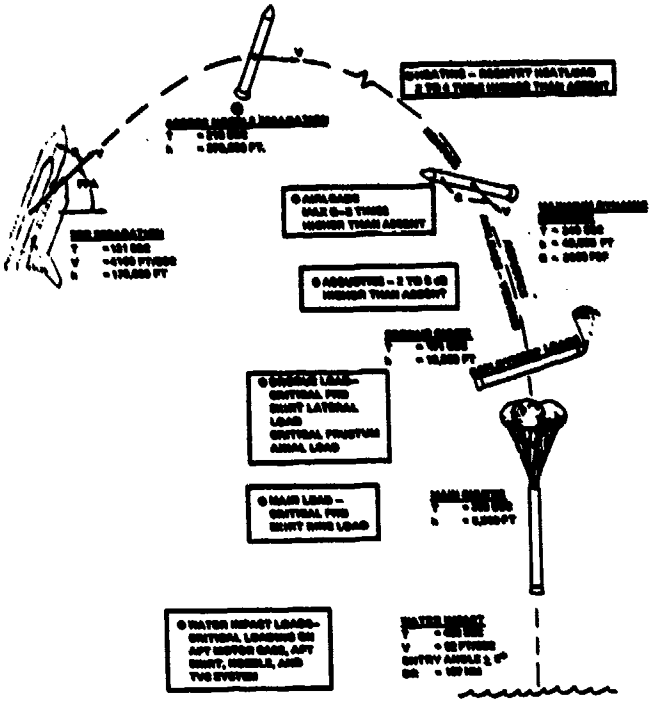

Fig. 5 - SRB STS-1 Reentry Profile (Right SRB)

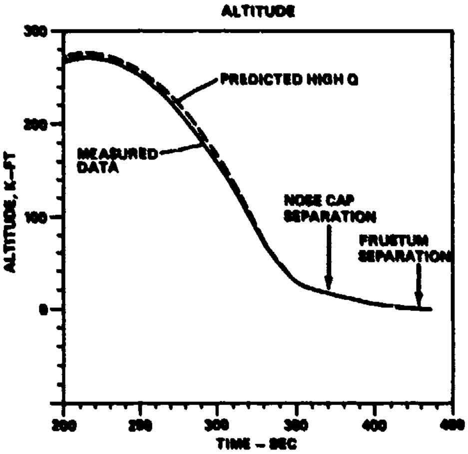

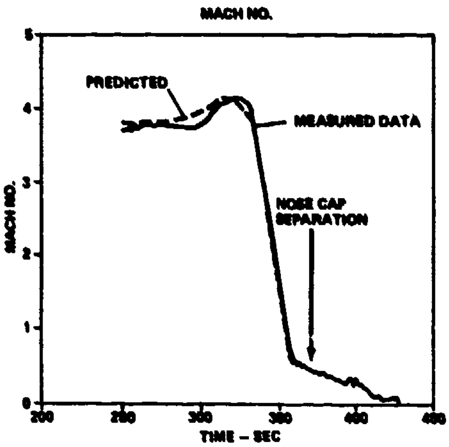

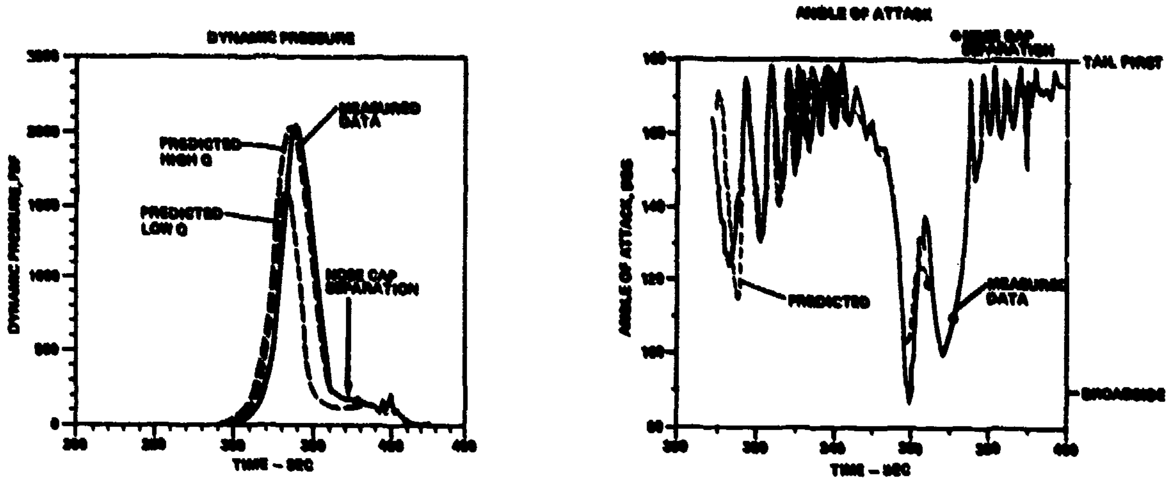

Fig. 6 - Right SRB STS-1 vs. Predicted Reentry Characteristics

of 275,000 lb. experienced on STS-1 was slightly higher than the parachute design limit load value of 270,000 lb. and occurred during second disreef while going to the full open condition. This load is reacted at the nose cone frustum by twelve attach fittings. The SRB structural load capability is a function of the relative angle between the SRB and the drogue chute load vector. High lateral load components are critical for the forward skirt buckling condition whereas high axial load components are critical for the frustum tension condition. The drogue chute loading conditions experienced during STS-1 fell within these SRB load constraints.

The main chute cluster total peak load of 446,000 lbs. fell well within the SRB forward skirt tension load constraint of 522,000 lb. This peak loading occurred during the first disreef. In addition, the peak single main chute load of 158,000 lb. experienced in STS-1 was well under the parachute design limit load value of 174,000 lb. Some revision to the main chute first stage reefing area, however, is warranted in order to achieve a better balance of the three main chute load peaks.

SUMMARY

In summary, the STS-1 SRB reentry characteristics were as predicted. The maximum vehicle deceleration occurred during the maximum dynamic pressure regime of reentry. The pilot, drogue, and main chutes deployed and inflated successfully. The deceleration subsystem loads were within the preflight predicted ranges. Terminal SRB impact velocities of 92-93 ft/sec were experienced. In conclusion, the STS-1 flight demonstrated the adequacy of the SRB decelerator subsystem.

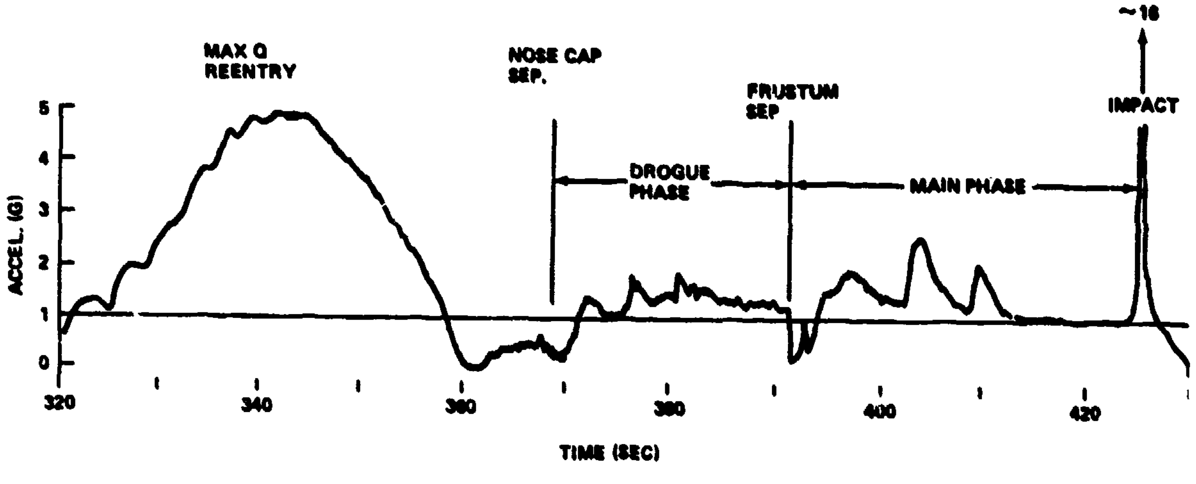

Fig. 7 - Right SRB STS-1 Axial Acceleration

TABLE 1
SRB STS-1 Decelerator Subsystem Performance

	PREFLIGHT PREDICTED MIN.	PREFLIGHT PREDICTED NOMINAL	PREFLIGHT PREDICTED MAX.	STS-1 FLIGHT LEFT	STS-1 FLIGHT RIGHT
NOSE CAP EJECTION					
ALTITUDE – FT.	14,868	15,524	16,180	N/R	15,861
DYNAMIC PRESSURE – PSF	184	210	234	N/R	177
TIME FROM REFERENCE – SEC.*	347	362	377	369.00	371.34
FRUSTUM SEPARATION					
ALTITUDE – FT.	5,653	6,240	6,827	N/R	6,520
DYNAMIC PRESSURE – PSF	116	123.5	131	N/R	120
TIME FROM REFERENCE – SEC.*	386	394	402	391.40	393.70
SPLASHDOWN					
TIME FROM REFERENCE – SEC.*	401	419	437	424.82	428.02
IMPACT VELOCITY – FT./SEC.	83	88	93	92.7**	91.6

N/R – RADAR TRACKING OF LEFT SRB NOT ACHIEVED

*REFERENCE TIME: 12:00:03 GMT

**TORN CANOPY

TABLE 2
SRB STS-1 Parachute Loads Summary

CONDITION	PREDICTED			MEASURED	
	MIN	NOM	MAX	LEFT	RIGHT
DROGUE - 1ST STAGE	140	176	259	188	145
2ND STAGE	203	237	276	251	219
3RD STAGE	210	241	280	275	256
MAIN - 1ST STAGE	91	114	135	107-113-81	83-68-106
2ND STAGE	102	142	180	113-153-140	154-137-155
3RD STAGE	78	124	160	122-118-116	142-125-104

SRB STS-1 DROGUE CHUTE LOADS

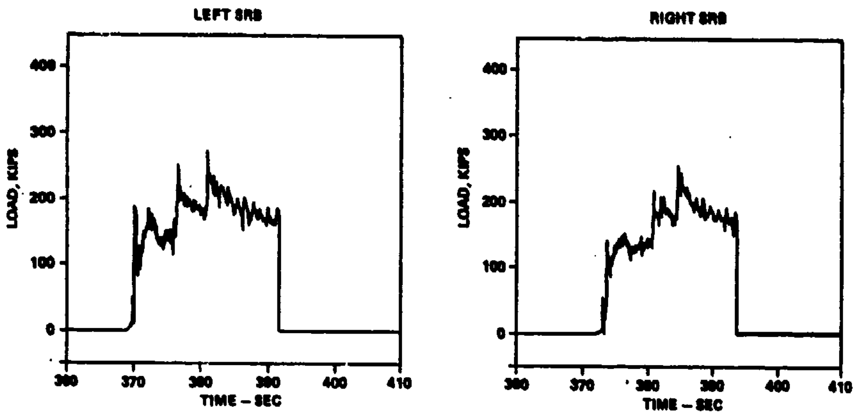

SRB STS-1 MAIN CHUTE TOTAL LOADS

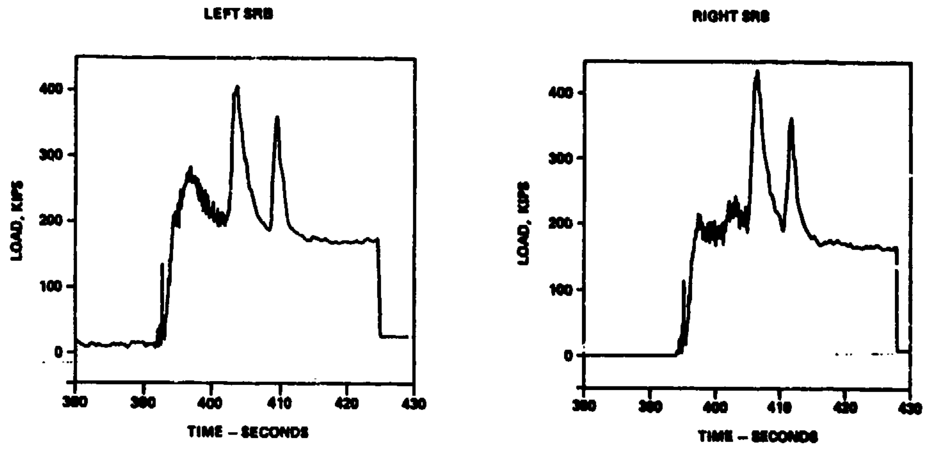

Fig. 8 - SRB STS-1 Measured Chute Loads

DISCUSSION

Voice: How was the impact velocity of the solid rocket booster measured?

Mr. Kross: The impact velocity was measured from the Vandenberg radar tracking data, the Vandenberg tracking ship and by photographs.

Voice: Was that accurate within a millisecond?

Mr. Kross: The radar track is very accurate.

Voice: Did you have anything to measure the water entry impact? What frequency range could you measure on impact?

Mr. Kross: The rise time for that spike you saw on the acceleration for water impact is about 150 - 200 milliseconds. It is not a shock; it is a lower frequency than that. Again, we are good for 200 Hz on that system; it is a flight system.

Voice: Is a 200 Hz system accurate?

Mr. Kross: Yes. It is adequate for our needs.

INVESTIGATION OF SIDE FORCE OSCILLATIONS DURING STATIC FIRING OF THE SPACE SHUTTLE SOLID ROCKET MOTOR

M. A. Behring
Thiokol Corporation/Wasatch Division
Brigham City, Utah

Low frequency oscillations in measured side forces have occurred during static testing of the Space Shuttle Solid Rocket Motor. An investigation was undertaken to define a forcing function to simulate the effect of these oscillations in vehicle loads studies. This paper summarizes data analyses and analytical studies conducted during this investigation.

INTRODUCTION

During development and qualification of the Space Shuttle Solid Rocket Motor (SRM), seven motors were static fired. Each of these motors exhibited oscillations in lateral forces measured by load cells located at the forward and aft ends of the motor in the static test facility. These oscillations were present throughout the motor burn, including periods during which the nozzle was not being vectored. The frequencies and magnitudes of these oscillations were of interest with respect to vehicle loads. A study was undertaken to determine, if possible, the mechanism causing the oscillations and also to define a forcing function to simulate the effect in vehicle loads analysis. The intent of this paper is to summarize the study into the lateral force oscillation question conducted at Thiokol. Full documentation of this study may be found in Ref. [1].

DISCUSSION

The SRM was developed by the Wasatch Division of Thiokol Corporation in conjunction with the National Aeronautics and Space Administration (NASA) under contract NAS8-30490 and was sponsored by NASA/Marshall Space Flight Center. The lateral force oscillation study was conducted under Technical Directive No. 131 issued by Marshall Space Flight Center.

The SRM is approximately 125 ft long and 146 in. in diameter. Weighing approximately 1,250,000 lb at ignition, it consumes about 1,110,000 lb of propellant and develops a maximum thrust of nearly 3,000,000 lb during its 120 sec burn. The motor is fabricated in four segments, with the motor case made from 0.5 in. thick D6AC steel. The propellant grain has a center port design with a star configuration in the forward end of the forward segment.

Fig. 1 - DM-1 prior to static test

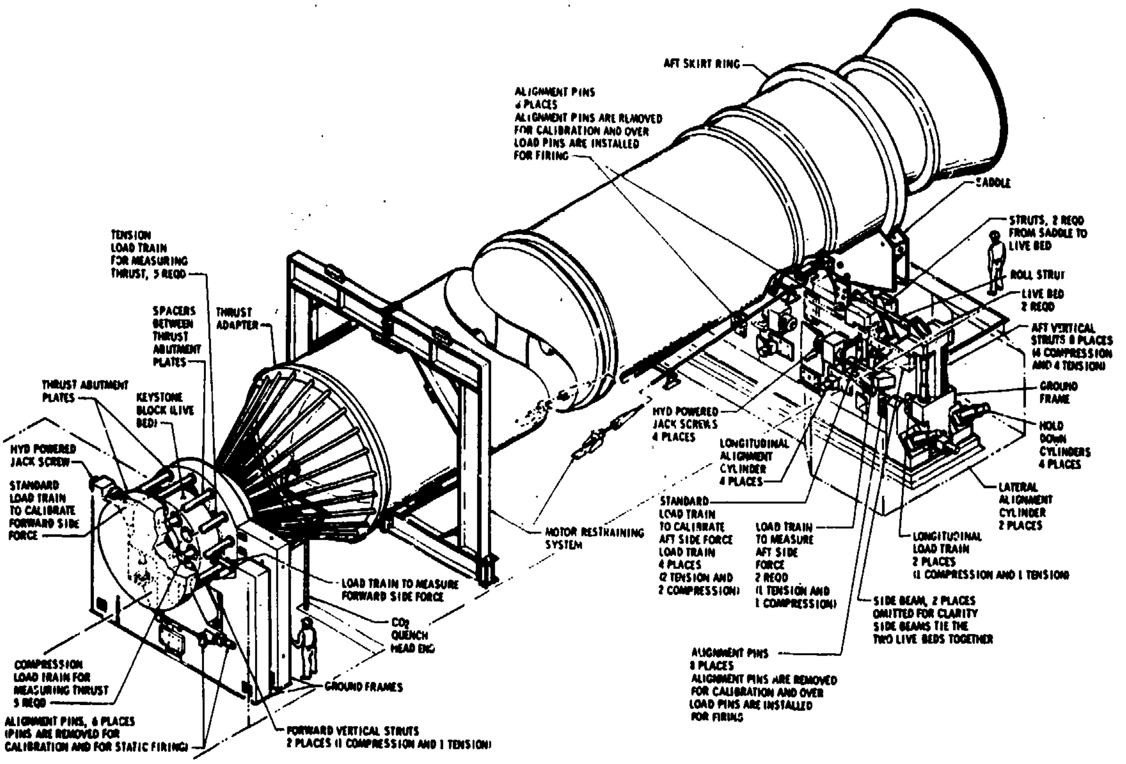

Fig. 2 - SRM test stand

The motor is static fired in the horizontal position as depicted in Fig. 1, where the first Development Motor (DM-1) is shown prior to static test. When assembled in the static test facility, the motor is held by the forward and aft skirt attach rings, with all axial loads carried by the forward support. Fig. 2 shows the arrangement of the test stand components and load measurement devices. The subject of this paper is oscillations in the forces measured by the forward and aft side force load trains. This study consisted of an intensive data analysis effort coupled with analytical studies.

TEST DATA ANALYSIS

Data from several test parameters were analyzed to characterize the lateral force oscillations and to provide a basis for validation of the mathematical model. Among the test parameters analyzed were forward and aft side forces, actuator pressure, and nozzle position extensometers.

Initial data analysis was conducted with a spectral analysis program wherein the Fourier amplitude spectra for successive time slices of data are plotted one above another (waterfall plot), showing amplitude vs frequency vs time. With this technique, discrete frequency trends are easily identifiable, as are variations of magnitude with time. Figs. 3 and 4 show, respectively, the waterfall plots of forward and aft side forces from DM-2. Four distinct frequency bands are apparent on the plots. Waterfall plots of forward and aft side forces from DM-4 are shown in Figs. 5 and 6. These are very similar in nature to those of DM-2 with the exception of the rapidly increasing frequency band during the latter portion of the motor burn. However, a comparison of this plot with the Thrust Vector Control (TVC) duty cycle, Ref. [2] reveals that the increasing frequency trend was due to a nozzle frequency response test during which the nozzle was vectored sinusoidally at increasing frequencies. Fig. 7 shows the 45 deg actuator pressure on DM-1. No discrete frequency trends are apparent in this data. This is typical of all actuator pressure data analyzed. A waterfall plot of a nozzle position extensometer is shown in Fig. 8. As with actuator pressure data, no discrete frequency trends are evident in these data.

Several points became apparent during the data analysis process: (1) very large amplitude oscillations in side force (equivalent to approximately 0.6 deg thrust vector oscillations) only occur during TVC oscillation commands and during motor tail-off; (2) there is no evidence of thrust vector oscillations at discrete frequencies at any times other than when such oscil-

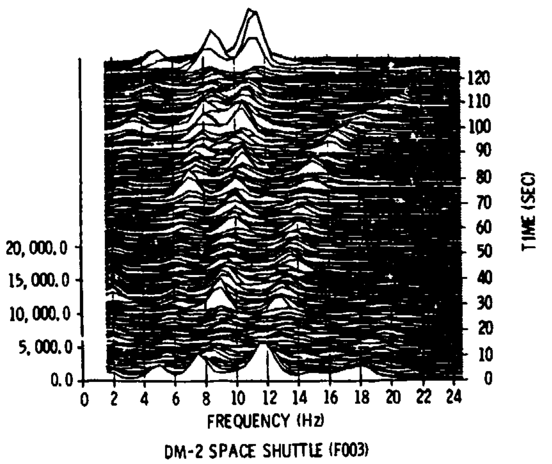

Fig. 3 - Waterfall plot of forward side force on DM-2

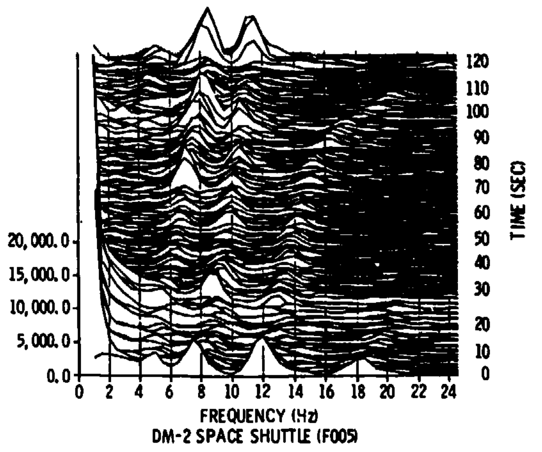

Fig. 4 - Waterfall plot of aft side force on DM-2

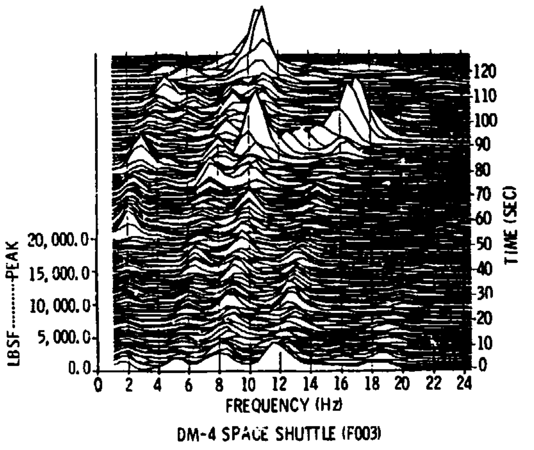

Fig. 5 - Waterfall plot of forward side force on DM-4

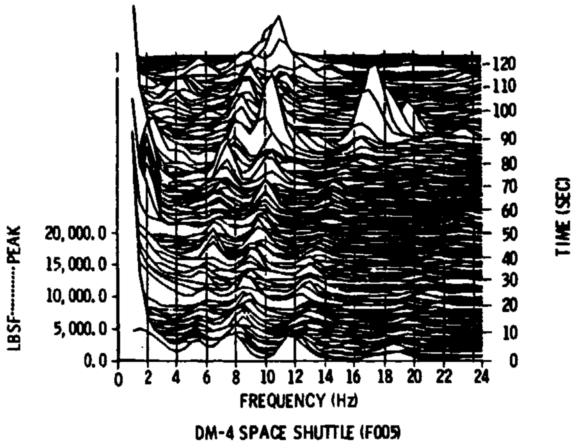

Fig. 6 - Waterfall plot of aft side force on DM-4

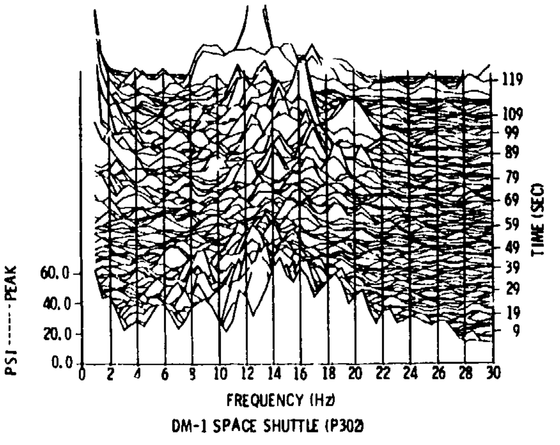

Fig. 7 - Waterfall plot of 45 deg actuator pressure on DM-1

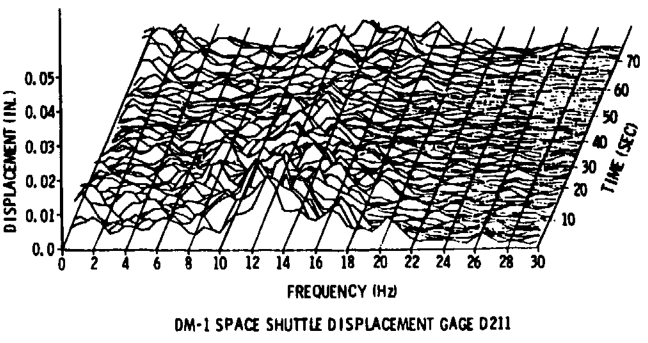

Fig. 8 - Waterfall plot of extensometer D211 on DM-1

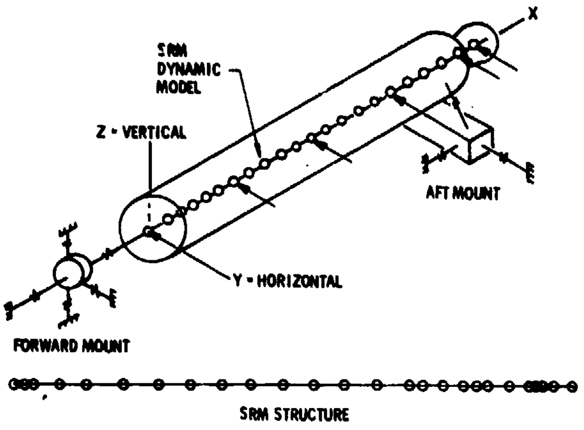

Fig. 9 - SRM in test stand (simplified for clarity)

lations are commanded; and (3) a comparison of the frequency trends in the side force data with predicted lateral vibration modes of the motor in the test stand showed very good frequency correlation throughout the motor burn.

These observations led to the conclusion that the oscillations present in the side force measurement data were attributable to the response of structural vibration modes of the motor in the test stand to small amplitude, random perturbations in the pressure field inside the motor and in the flow field through the nozzle.

Additional data analysis was then performed in order to characterize the side force oscillations in the form of Power Spectral Density (PSD) functions. PSDs were generated from forward lateral force (F003) and aft lateral force (F005) measurements from DM-1 and DM-2 for each 5 sec time slice from 40 to 120 sec. The PSD response level for each of the first four lateral modes was determined for F003 and F005 for each 5 sec time slice. The data were grouped in the following time periods to correspond to the model times:

TIME PERIOD (sec)	MODEL TIME (sec)
40 to 60	50
60 to 90	75
90 to 110	100
110 to 120	End of Burn

For each time period, a nominal response was calculated by averaging the responses from each 5 sec time slice contained in the period. This calculation was carried out for each of the first four lateral modes for both F003 and F005. After calculation of a nominal response, the standard deviation, for each time period, was calculated for each of the first four lateral modes for both F003 and F005.

An analytical effort was then undertaken to determine a random spectrum which, when applied as a multi-point excitation, would produce oscillations in lateral forces in the model of the same magnitudes as observed in the static tests.

MATHEMATICAL MODEL

A mathematical model of the motor in the static test facility was developed to study the low frequency dynamics of the static test configuration. The model was developed using finite element modeling techniques and the NASTRAN computer code. A simplified representation of the motor in the static test facility is shown in Fig. 9.

As only fundamental transverse and axial modes were of interest, a shell model of the motor case was not considered necessary. Consequently, the motor case was modeled with a series of bar elements having stiffness characteristics equivalent to the motor case. It was assumed that, for the fundamental modes, the propellant could be considered to be rigidly attached to the motor case; thus, only the mass contribution of the propellant was considered. The mass distribution of the motor case and propellant was simulated by concentrated masses at the grid points representing the motor case.

Twenty-four bar elements, located along the motor centerline, connect the 25 grid points representing the motor case. Mass distributions for five motor burn times were modeled. These were: ignition, 50 sec, 75 sec, 100 sec and end of burn.

The nozzle assembly was modeled as a concentrated mass with scalar springs providing 5 deg of freedom with respect to the motor case. The nozzle actuators were modeled with rod elements.

The thrust adapter, connecting the motor to the forward test stand, was modeled with concentrated masses, bar elements, and rigid connections.

The test stand was considered to be a major influencing factor on the fundamental axial and lateral modes of the motor in the test facility. The test stand, consisting of forward and aft components, was a complex structure consisting primarily of large rigid masses supported by a complex arrangement of load cells, flexures, and struts, as shown in Fig. 10. Both the forward and aft test stand were modeled with a series of grid points representing the load string attachment locations. Each of these grid points was rigidly connected to a grid point representing the mass center of the test stand component.

Following the static test firing of DM-3, a modal survey test was conducted on the burned out motor while it was still in the test stand, Ref. [3]. This test was conducted by Structural Dynamics Research Corporation of San Diego, California, and coordinated by Rockwell International/Space Division. In this test, natural frequencies, mode shapes, and damping factors for modes up to 50 Hz were experimentally measured.

The end of burn mathematical model was modified to represent the configuration that existed during the modal survey test. Major changes to the basic model consisted of the addition of the external tank attachment ring and the new nozzle mass properties representative of the nozzle assembly after severance of the aft exit cone. Natural frequencies and mode shapes were calculated using the modified model and compared to the experimental frequencies and mode shapes. Adjustments were then made to the model until a reasonable correlation was achieved. Not surprisingly, several modes of vibration were noted during the modal survey test that were not predicted by the model. Most of these, however, were dominated by shell activity which is not reproducible by a lumped parameter beam model. In the modal survey test, many of the beam modes were modified by shell activity and local deformations, but the basic beam mode shapes were obtained by the simplified model.

Although reasonable correlation was achieved between the modal survey configuration model and the modal survey test results, when lateral mode frequencies at various burn times from the models were compared to the frequencies contained in the lateral force measurements obtained during static testing, some anomalies were noted. As the lateral modes were of primary interest in this study, an adjustment was made to the model to improve the correlation in this area. The comparison of the first four lateral mode frequencies from the model to the static test data is shown in Fig. 11. The natural frequencies and modal identifications for modes up to 16 Hz are summarized in Table 1.

Additional correlation of the lateral modes in the model with those present during static testing of the motor was shown by comparing the phase relationship and relative magnitudes of the forward and aft lateral force responses from the model and the test data. This comparison is shown in Table 2.

Within the limits of the modeling approach taken, correlation of the model with available experimental data is very good.

FORCING FUNCTION DEVELOPMENT

The development of a random forcing function to represent the excitation sources acting on the motor due to the combustion process was a relatively straightforward process, but was based

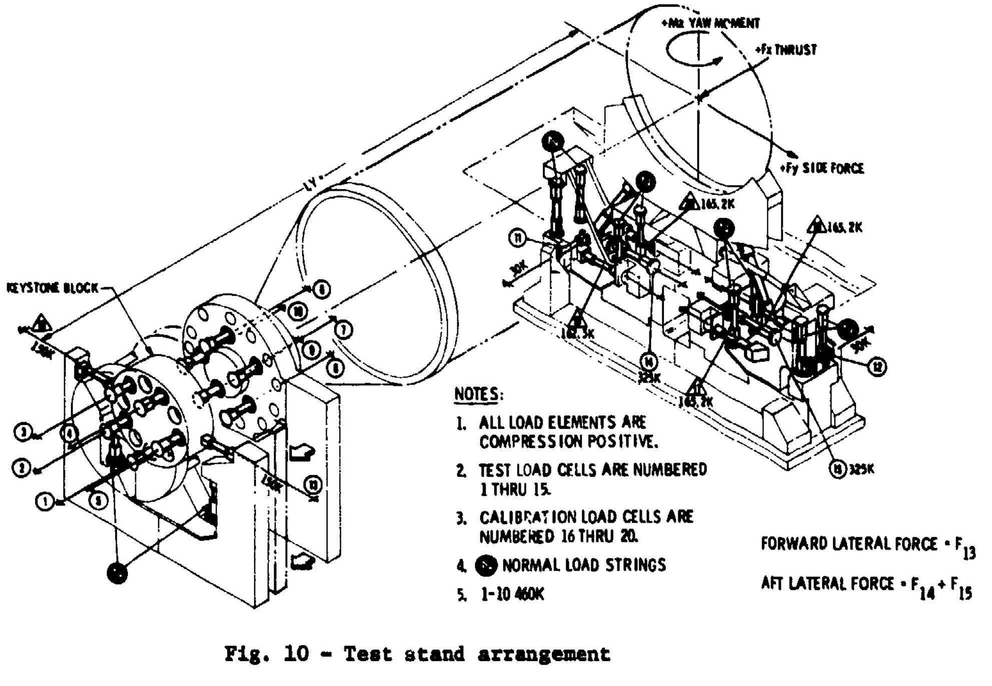

NOTES:

1. ALL LOAD ELEMENTS ARE COMPRESSION POSITIVE.
2. TEST LOAD CELLS ARE NUMBERED 1 THRU 15.
3. CALIBRATION LOAD CELLS ARE NUMBERED 16 THRU 20.
4. ● NORMAL LOAD STRINGS
5. 1-10 460K

FORWARD LATERAL FORCE = F_{13}

AFT LATERAL FORCE = $F_{14} + F_{15}$

Fig. 10 - Test stand arrangement

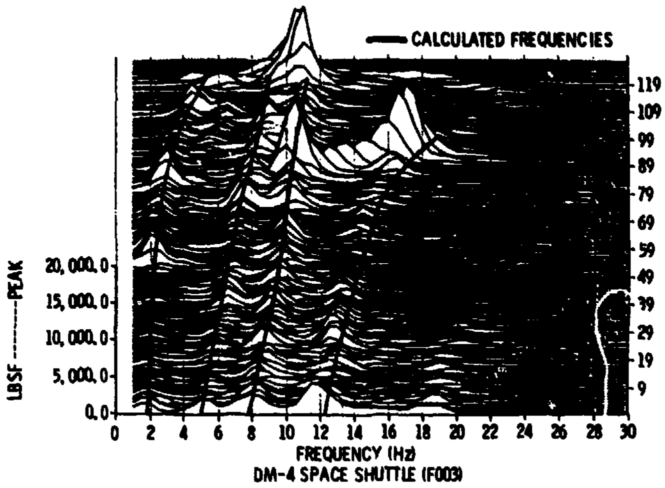

Fig. 11 - Comparison of lateral mode frequencies from revised model to static test data

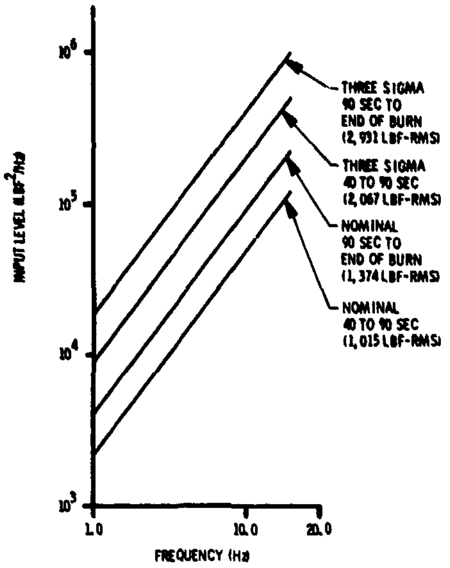

Fig. 12 - Recommended input spectra

upon several assumptions. The fundamental assumption made was that the actual excitation in the motor during operation was random in nature. This assumption is supported by the fact that the structure responds in several of its normal modes, which suggests excitation across a broad band. It was further assumed that the excitation of the structure occurred throughout the motor bore and over the nozzle flow area. While this assumption in itself is probably valid, no data were available regarding the spatial variation of the forcing function spectrum. It was therefore necessary to also assume that the excitation spectrum was the same at all locations. It was also assumed that, except for having the same spectrum, the forcing functions acting on the structure were statistically uncorrelated. In actual fact, there probably is some degree of correlation between forcing functions at different locations, however, no data were available concerning the correlation from one location to another.

For multi-point random excitation, given that the forcing functions are uncorrelated, the PSD of the response at a point j is given by

$$S_j\ (\omega) = \sum_a \left| H_{ja}\ (\omega) \right|^2 S_a$$

Where:

$S_j\ (\omega)$ = PSD of the response at point j

$S_a\ (\omega)$ = PSD of the excitation at point a

$H_{ja}\ (\omega)$ = Frequency response function at point j due to an excitation at point a

For our problem we have assumed that $S_a\ (\omega)$ is the same for all a.

Therefore, $S_j\ (\omega) = S_a\ (\omega) \sum_a \left| H_{ja}\ (\omega) \right|^2$

From this we can say that

$$S_a\ (\omega) = \frac{S_j\ (\omega)}{\sum_a \left| H_{ja}\ (\omega) \right|^2}$$

The solution of this equation required the development of a set of frequency response functions and the PSDs of the measured responses.

For simplicity, both in this study and in future vehicle loads analysis, it was assumed that reasonable results could be achieved by applying excitation at six locations along the motor length. Grid points were chosen as excitation points in our model whose locations corresponded as closely as possible to grid point locations in the vehicle loads model. The grid points chosen and their correlations with loads model grid points are shown in Table 3.

Frequency response functions were calculated for the lateral force response at the forward and aft lateral force measurement locations due to a sinusoidal force in the lateral direction at each of the six input points. These frequency response functions were calculated for burn times of 50, 75, 100 sec, and end of burn.

Damping used in the model for calculation of the frequency response functions closely envelopes the modal damping measured during the modal survey test. This damping is conservative at end of burn but may introduce some nonconservatism for early burn times. The damping values used, input as structural damping coefficients, varied linearly from g = 0.06 at 0 Hz to g = 0.02 at 20 Hz and then remained constant at g = 0.02.

For each of the first four lateral modes, the input PSD level required to obtain a response from the model equal to the nominal value obtained from the test data was calculated. This calculation was carried out for each of the four model times (only the first three modes were used for end of burn) for both head end and aft end responses. The required input levels were enveloped by a 4 dB/oct line from 1.0 to 20.0 Hz to obtain the nominal input spectra for use in the vehicle loads analysis. This process was repeated using 3 sigma response values to establish 3 sigma input spectra. The nominal and 3 sigma input spectra for both early and late burn times are shown in Fig. 12. These random functions should be applied at each of the six input locations in both transverse axes. These input spectra were supplied to Marshall Space Flight Center for inclusion in flight vehicle loads analyses.

CONCLUSIONS

The low frequency dynamics of the Space Shuttle SRM in the static test facility are adequately represented by a beam model. Good correlation was achieved between mathematical model results and modal survey test results for low order bending modes of the motor in the test stand. Good correlation was also shown between the frequencies evident in the lateral force data from the static tests and the predicted natural frequencies of the lateral vibration modes of the motor in the test stand. This correlation held for all five burn times modeled.

While it cannot be conclusively shown that random pressure oscillations inside the motor are, in fact, responsible for the observed side force oscillations, the available evidence does support this supposition. The forcing functions defined in this study, when applied to the static test model, produced responses of similar magnitudes to those observed during the static tests.

TABLE 1

Measured and Calculated Natural Frequencies

TEST FREQUENCY (Hz)	ANALYSIS FREQUENCY (Hz)	MODE DESCRIPTION
4.44	5.29	LATERAL MODE
5.57	--	FIRST TORSION, SHELL
6.06	6.16	VERTICAL BENDING
6.86	6.49	FIRST ROLL
8.82	9.11	LATERAL MODE, SHELL, SKIRT FORE AND AFT
9.18	--	LATERAL MODE, SHELL
9.49	9.64	AFT SKIRT AND SADDLE FORE AND AFT, SHELL ACTIVITY
10.25	--	SHELL ACTIVITY
10.30	11.32	LATERAL MODE
11.24	--	SECOND TORSION, SHELL ACTIVITY
12.30	--	SHELL ACTIVITY
12.90	--	SHELL ACTIVITY
13.40	13.11	ISOLATED F&A MOTION OF AFT LIVE BED
13.57	--	AFT SADDLE; SKIRT, NOZZLE, AND KEYSTONE BLOCK MODE
15.30	16.34	FIRST AXIAL

TABLE 2

Comparison of Phase Relationship and Magnitude Ratio of Aft End Response (F005) to Headend Response (F003) From Experimental Data and Mathematical Model

EXPERIMENTAL DATA				ANALYTICAL MODEL			
TIME (SEC)	FREQ* (Hz)	RELATIVE PHASE (DEG)	|MAG RATIO|	MODEL TIME	FREQ (Hz)	RELATIVE PHASE† (DEG)	|MAG RATIO|
22	2.00	36	2.06	IGN	1.74	0	0.99
22	6.25	-195	3.73	IGN	4.96	180	1.41
22	9.50	-30	2.87	IGN	7.72	0	2.18
22	14.75	-185	1.05	IGN	12.35	180	1.52
54	2.25	-1	1.57	50	2.30	0	1.06
54	7.00	-168	2.22	50	6.40	180	1.58
54	10.50	9	1.22	50	9.44	0	1.91
54	14.00	166	0.99	50	14.18	180	1.65

*DATA ANALYSIS PROCEDURE PROVIDES 0.25 Hz FREQUENCY RESOLUTION

†FROM NORMAL MODES. DAMPING NOT INCLUDED

TABLE 3

Excitation Locations

SRB STATION (IN.)	CORRESPONDING LOADS MODEL STATION
484.36	482
851.48	851
1,171.48	1,203
1,511.00	1,511
1,817.00	1,800
1,863.70	1,863

REFERENCES

1. M. A. Behring, "Investigation of Side Force Oscillations During Static Firing of the Space Shuttle Solid Rocket Motor," Thiokol Corporation/Wasatch Division Rpt TWR-12996, 24 Mar 1981.
2. "Test Plan for Space Shuttle Development Motor No. 4 Static Test," Thiokol Corporation/Wasatch Division Rpt TWR-11752 (CD), Revision A, 1 Feb 1979.
3. "Test Results for Solid Rocket Motor DM-3 Modal Survey Ground Test," Structural Dynamics Research Corporation/Western Operations Rpt, SDRC Project No. 1531, 1 Dec 1978.

DISCUSSION

Mr. Neubert (Pennsylvania State University): Did you find that one of the transfer functions dominated? You had six input points. Did you use an averaging technique?

Mr. Behring: No. We treated the input level of each location as though it were the same in this study. We did do some other response analyses using single point excitation. We found that an input at one location gave a much stronger response than at another location for some of the modes.

Mr. Zurnaciyan (Northrop Electronics): Why did you assume an uncorrelated distribution of the forcing function?

Mr. Behring: It was the only option open to us at that time. We had no way of defining the correlation functions from one point to another. There is probably some correlation between the points, but unless somebody were to do some pretty detailed work on the internal gas dynamics in the motor, I don't think we have any way of defining them.

Mr. Zurnaciyan: Was that for simplification?

Mr. Behring: Yes.

SPACE SHUTTLE DATA SYSTEMS

DEVELOPMENT OF AN AUTOMATED PROCESSING AND SCREENING SYSTEM FOR THE SPACE SHUTTLE ORBITER FLIGHT TEST DATA

D. K. McCutchen
National Aeronautics and Space Administration
Lyndon B. Johnson Space Center
Houston, TX

J. F. Brose
Lockheed Engineering and Management Services Company, Inc.
Houston, TX

W. E. Palm
McDonnell Douglas Corp.
Houston, TX

One nemesis of the structural dynamist is the tedious task of reviewing large quantities of data. This data, obtained from various types of instrumentation, may be represented by oscillogram records, root-mean-squared (rms) time histories, power spectral densities, shock spectra, 1/3 octave band analyses, and various statistical distributions. In an attempt to reduce the laborious task of manually reviewing all of the Space Shuttle Orbiter wideband frequency-modulated (FM) analog data, an automated processing system was developed to perform the screening process based upon predefined or predicted threshold criteria.

INTRODUCTION

The Orbital Flight Test program for the Space Shuttle defined requirements for the analysis and evaluation of enormous quantities of flight test data. The data is acquired via the Shuttle Development Flight Instrumentation system and includes up to 525 channels of wideband Frequency Modulated/Frequency Multiplexed analog data for each of the four orbital flight tests. Each channel contains data acquired from accelerometers, microphones, strain gages, or pressure transducers and has a frequency bandwidth that varies from 50 Hz to 8 kHz, with the majority having a 2-kHz bandwidth.

The requirements for such large quantities of flight test data stemmed from the need to:

- Verify or update vibration, acoustic, and shock specifications.
- Provide data to certify the vehicle pogo and flutter free.
- Provide flight load information for large components and their secondary structures.
- Verify the adequacy of the ground test program for sonic fatigue.
- Determine if any anomalies have occurred on the flight which must be resolved prior to the next flight.

The volume of data to be reviewed and analyzed for such a large number of measurements would be more than 25,000 plots or graphs. Unless an abundance of qualified analysts were available to review the data, the workload created would cause a significant impact at any organization. Therefore, in order to accomplish the analysis with existing personnel, the reviewing process was automated.

A team of engineering personnel critically involved in analyzing the Shuttle structural dynamics data developed the Shuttle Wideband Analog Processing System (SWAPS), which provides the structural dynamist with a method of analyzing large quantities of Shuttle flight test data by automating portions of the analysis process, thereby reducing the laborious task of manually reviewing all of the data records. The basic concept is to screen out data that is of no immediate concern by automatically comparing the data to "thresholds of interest" and only continuing the analysis process on the data that exceeds these thresholds.

SYSTEMS REQUIREMENTS

The basic data available to the dynamist for the structural evaluation is oscillogram records, rms time histories, power spectral densities, mean-squared spectral distributions, shock spectra, 1/3 octave band analyses, and various statistical analyses. The SWAPS automated review process is limited to data in digital form; oscillogram records require manual review. Inputs to the system include the following items:

- Recorded wideband FM/FM multiplexed analog tapes.
- Calibration information.
- A file containing flight parameters such as Mach number, dynamic pressure, and angle of attack versus time.
- Specifics regarding each transducer's structural location and expected response characteristics.
- A table of mission events, such as liftoff and maximum dynamic pressure (max Q).

A stand-alone system to both process and analyze the data obviously would have been desirable, but one of the system constraints was to utilize the existing hardware and software capabilities of the Central Computer Facility at the Lyndon B. Johnson Space Center. Included in the Central Computer Facility is the telemetry ground station, which provides analog-to-digital processing and produces a digital tape compatible with existing wave analysis software implemented on the facility's large mainframe computer systems. Remote terminals, currently available on the Central Computer Facility systems, provide the users with the capability of processing data in the "demand" mode for immediate results or submitting runs for scheduled batch output. In utilizing the existing capabilities, minimum software development was required. The resulting system, however, requires some manual interface and coordination between major system functions.

FUNCTIONAL SPECIFICATIONS

The SWAPS (figure 1) is comprised of three functional capabilities:

- Analog-to-digital processing.
- Transient and steady-state wave analysis processing.
- Screening, display, and data base maintenance.

Operationally, the analog-to-digital processing system performs all analog-to-digital conversions, generates oscillograms, performs the process of screening the data for transients, and produces rms time history data. The transient and steady state wave analysis software generates data in the frequency domain; i.e., power spectral densities (PSD's), 1/3 octave band analyses, and shock spectra. The screening, display, and data base maintenance function performs the screening and display of rms time history and frequency domain data, as well as all necessary peripheral data management functions.

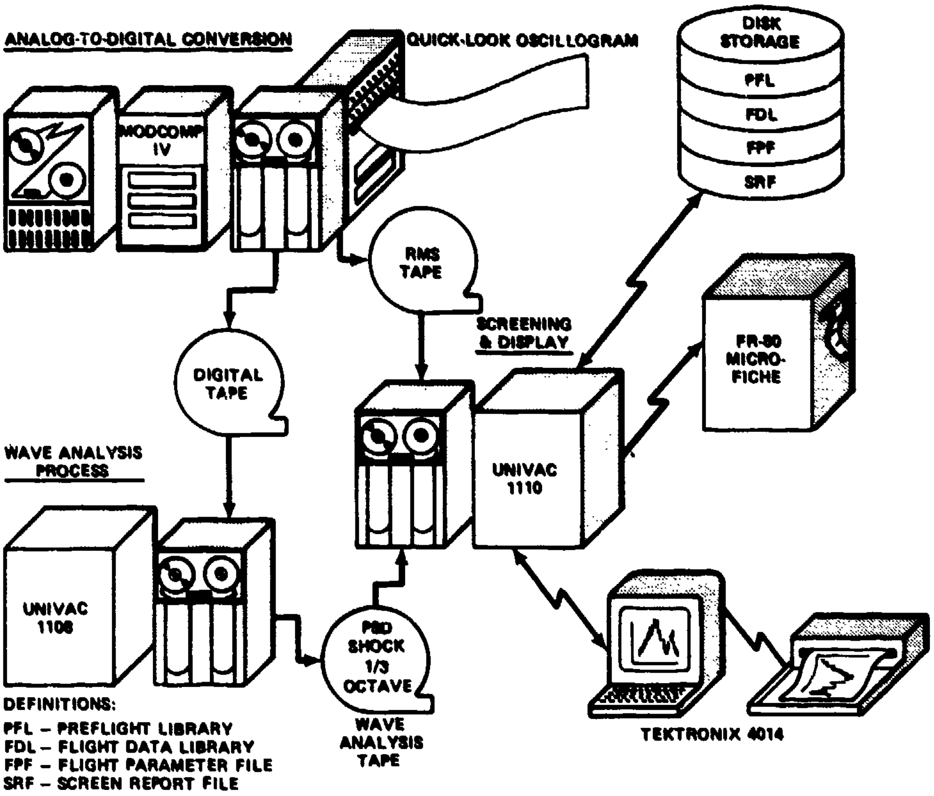

Figure 1 - SWAPS system diagram

Initially, quick-look, low-speed oscillograms (0.2 in. per sec) are used to perform cursory screening of data to eliminate further processing of anomalous instrumentation and identify time periods where individual measurements should not be processed. These measurements are then digitized at preselected rates dictated by the frequency response of each instrument, and rms time history data is computed. Since flight data tends to be nonstationary, rms values are computed over contiguous time increments of 0.4 sec.

The rms time history is then compared to a Shuttle flight screening profile (figure 2), which is constructed from the minimum rms threshold for each mission event identified in the flight profile. The mission events are defined in a data base and are used by the analyst to specify a flight profile for each sensor. Because each sensor may satisfy multiple Flight Test Requirement (FTR) specifications, different threshold levels can be assigned for each mission event so that the screening threshold can be varied. The system then selects the minimum values unless the profile for a specific FTR is requested.

In addition to the rms time histories, the crest factor is computed for each rms interval and is screened for values within the 1.4 to 4.0 range. Values greater than 4.0 reflect transient data or electrical noise; values less than 1.4 indicate data that appears to have a square wave form. The distribution of the crest factor data with respect to these limits is used as an indication of data quality.

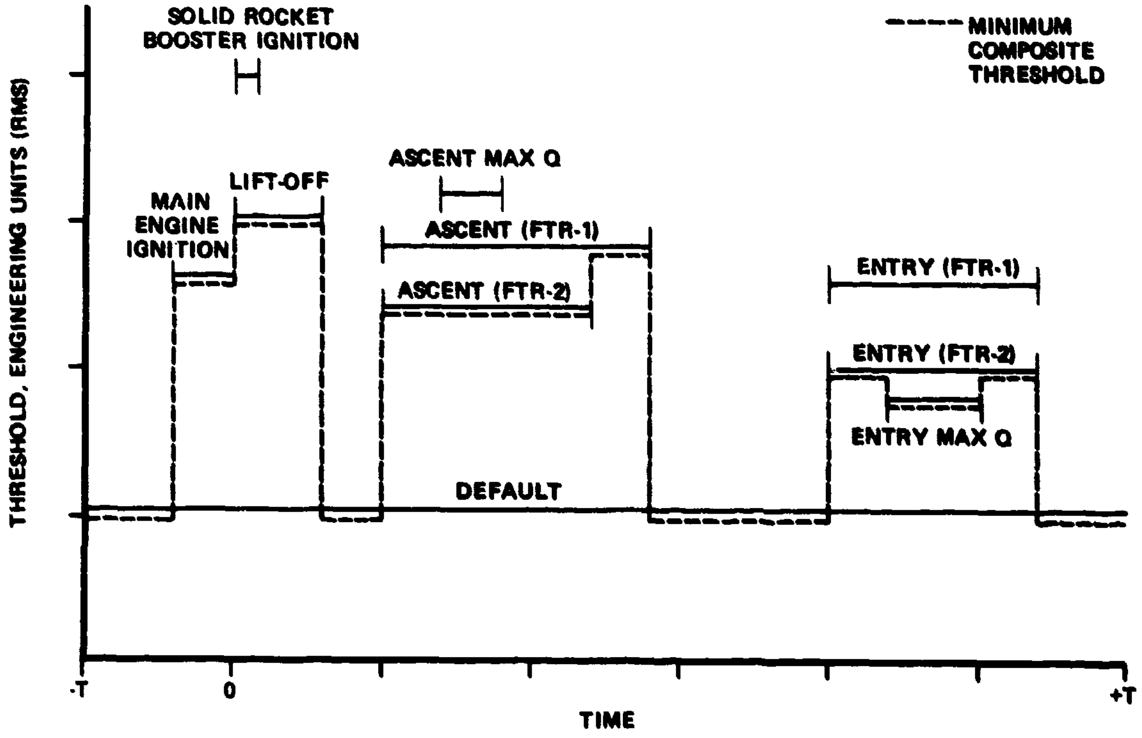

Figure 2 - Flight screening profile

The output of the screening process is the RMS Screen Report (figure 3). It contains the sensor identification (MSID), tape number, mission event, time interval, data base threshold rms level, screening level applied as defined by the FTR source, data source from which the threshold was obtained, statistical distribution of the rms data, maximum instantaneous and maximum rms values with their associated times, and distribution of the peak-to-rms ratio (crest factor). If any rms value exceeds the threshold level, a graphical representation of the rms data for the complete flight profile with an overlay of the threshold levels (figure 4) is produced. The peak-to-rms ratio data (figure 5) is also plotted.

The tabular results of the screening process are stored in a data base and can be recalled and displayed by the user on request. The rms time history data is retained on tape rather than on-line mass storage. It is estimated that five million words of mass storage would have been required to retain the rms data on-line for each flight.

The rms time history is used to select intervals of interest for further processing through the statistical wave analysis processing program, which produces PSD and 1/3 octave band analyses. Spectral screening thresholds, stored in the same data base as the rms threshold levels, provide the same variation for mission event requirements and FTR's. The flight data is screened against an envelope spectrum which represents the minimum threshold defined for any FTR for the mission event in which the data interval is contained. The system automatically selects this envelope unless the user requires that a specific criteria be employed. The threshold spectra specified are derived from analyses or test data and may be modified as flight test data is acquired. They are not limited in shape, but generally reflect one of the several basic forms of envelopes shown in figure 6.

```
                                              RMS SCREEN REPORT
         FLIGHT NO. - 01                                                                      DATE - 11/24/81, 15:38:37

                                                           DISTRIBUTION OF RMS AS A    MAX                    DISTRIBUTION OF PEAK/
                                 TIME        RMS           PERCENT OF SCREEN VALUE     VALUE       TIME       RMS RATIO IN PERCENT
  MSID       TAPE MISSION       START/       PFL/            0    25    50    75   100 PEAK/        OF             0    1.4   4.0
              NO   EVENT         STOP       SCREEN SOURCE   25    50    75   100    +   RMS         MAX           1.4   4.0    +

V08Y9774    X04558 DEFALT 102:11:59:30   170.0 08V03    0.0 100.0   0.0   0.0   0.0  .1901 102:11:59:35    0.0  88.6  11.4
                          102:11:59:57   151.6                                       144.0 102:11:59:44

V08Y9774    X04558 LFTOFF 102:11:59:58   170.0 08V03    0.0   2.5   2.5   0.0  95.0    3.1 102:12:00:00    0.0  75.0  25.0
                          102:12:00:13   155.1                                       167.0 102:12:00:00

V08Y9774    X04558 DEFALT 102:12:00:14   170.0 08V03    0.0   0.0  30.0  26.2  43.8  .8391 102:12:00:20    0.0  73.7  26.2
                          102:12:00:45   151.6                                       157.6 102:12:00:15

V08Y9774    X04558 ASCNXG 102:12:00:46   170.0 08V03    0.0   0.0 100.0   0.0   0.0  .4373 102:12:00:48    0.0  87.5  12.5
                          102:12:00:48   155.1                                       151.1 102:12:00:47

V08Y9774    X04558 TRANS  102:12:00:49   170.0 08V03    0.0  51.4  24.3  18.9   5.4  .7840 102:12:00:54    0.0  67.6  32.4
                          102:12:01:03   155.1                                       156.5 102:12:00:54

V08Y9774    X04558 DEFALT 102:12:01:04   170.0 08V03    0.0  82.5  13.0   3.8   0.6    1.5 102:12:01:32    0.0  86.1  13.9
                          104:18:17:48   151.6                                       153.7 104:18:16:37

V08Y9774    X04558 ENTRXG 104:18:17:49   170.0 08V03    0.0   0.0   0.0   0.0 100.0  .4154 104:18:19:38    0.0  84.2  15.8
                          104:18:20:48   144.0                                       153.8 104:18:20:26

V08Y9774    X04558 DEFALT 104:18:20:49   170.0 08V03    0.0  70.1  29.9   0.0   0.0  .2691 104:18:21:25    0.0  88.7  11.3
                          104:18:21:59   151.6                                       146.4 104:18:21:25
```

Figure 3 - An RMS Screen Report for microphone V08Y9774 located on the vertical stabilizer

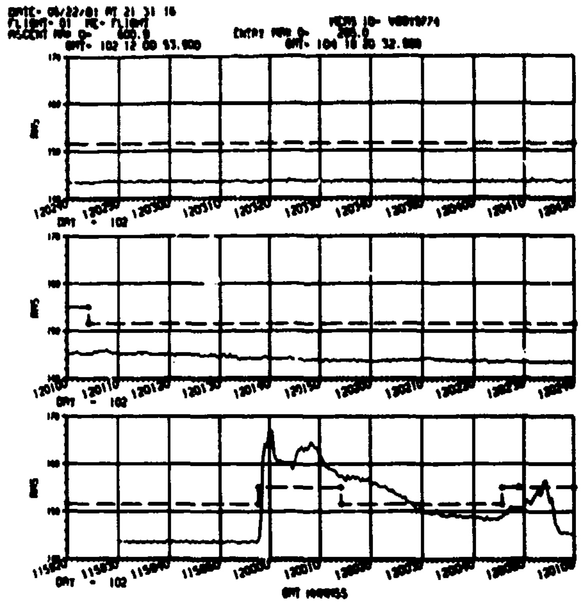

Figure 4 - An rms time history plot of microphone V08Y9774

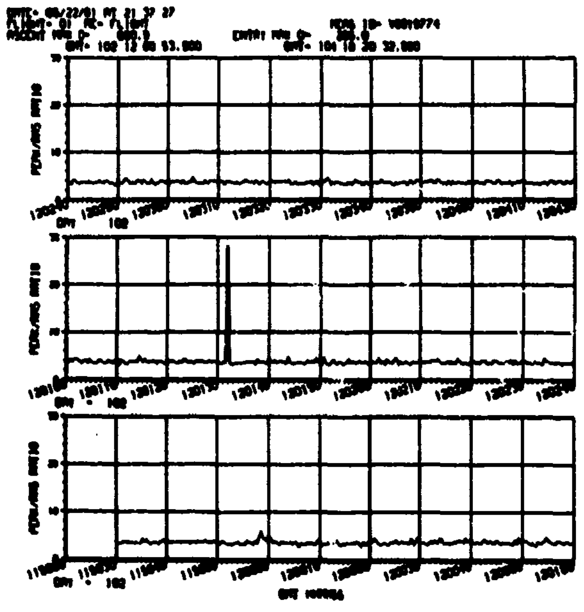

Figure 5 - Crest factor plot of microphone V08Y9774

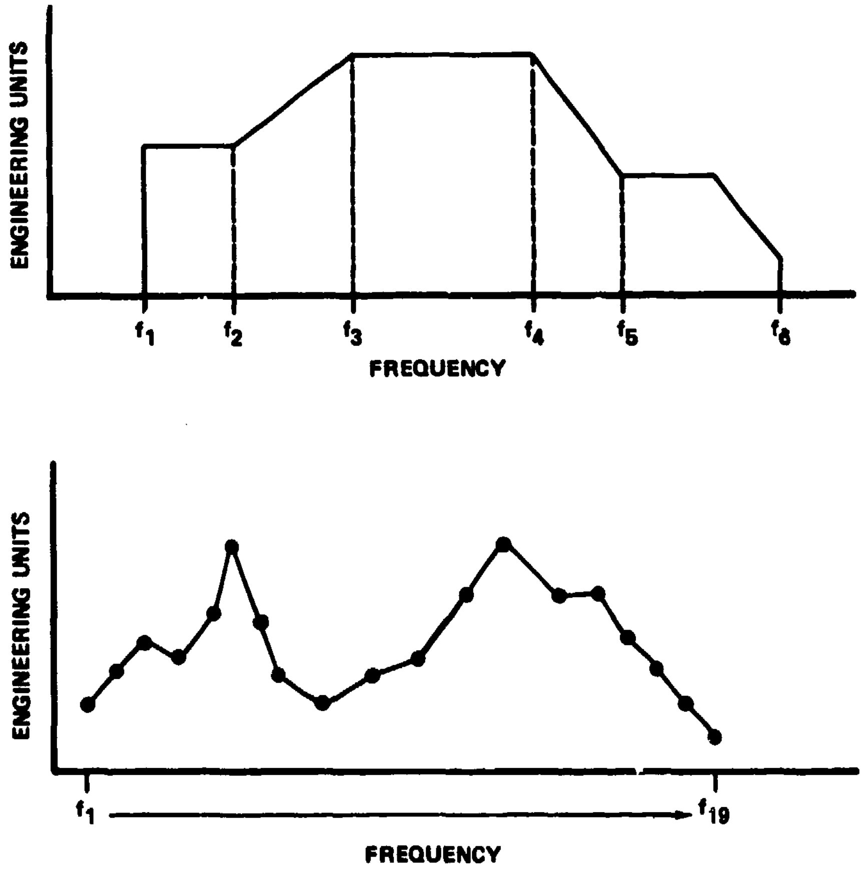

Figure 6 - Test envelope formats

PSD screening results are displayed in the Wave Analysis Screen Report (figure 7). This report is similar in content to the rms report. It contains pertinent information identifying the instrument, time interval processed, rms level of the screening threshold employed, rms level of the flight data, percentage of the envelope applied, data source from which the threshold was obtained, statistical distribution of the PSD amplitude with respect to the threshold used, and maximum amplitude and corresponding frequency.

```
                                       WAVE ANALYSIS SCREEN REPORT

      FLIGHT NO. - 01                                                                  DATE - 11/24/81, 15:35:03

      MSID - V08D9440                       SUBSTRUCTURE - THRUST STR                            ZONE - Z27

                                       PFL      DATA                     DISTRIBUTION OF DATA AS A
                             TIME       DB       DB   PROFILE            PERCENT OF SCREEN PROFILE
MISSION  DATA   TAPE        START/     RMS      RMS   SCREEN              0     25    50    75   100    MAX
EVENT    TYPE    NO          STOP      PEAK     PEAK    %    SOURCE      25     50    75   100    +    VALUE       FREQ

 DEFALT PSD    X02895 102:11:59:50.000    15.1    1.4  20.0 8V005   98.4   1.2   0.3   0.1   0.0  .02398      1110.5
                      102:11:59:51.000

 ASCENT PSD    X02895 102:12:01:50.000    15.1    5.0  50.0 8V005   85.2   8.0   2.1   1.4   3.4  .40036      1768.5
                      102:12:01:51.000

 ASCENT PSD    X02895 102:12:03:50.000    15.1    5.6  50.0 8V005   79.8  10.6   4.3   1.8   3.5  .50461      1761.2
                      102:12:03:51.000

 ASCENT PSD    X00282 102:12:05:50.000    15.1    5.6  50.0 8V005   80.2  10.0   3.4   2.3   4.2  .74077      1841.1
                      102:12:05:51.000

 ASCENT PSD    X00282 102:12:06:50.000    15.1    5.5  50.0 8V005   80.7  10.3   3.4   2.0   3.6  .72893      1289.4
                      102:12:06:51.000

 ASCENT PSD    X00282 102:12:07:50.000    15.1    5.6  50.0 8V005   79.9   9.3   4.2   2.1   4.4  .44203      1348.0
                      102:12:07:51.000

 ASCENT PSD    X00282 102:12:08:00.000    15.1    6.7  50.0 8V005   78.0   7.0   4.3   2.8   8.0     1.4       726.6
                      102:12:08:01.C00

 ASCENT PSD    X00282 102:12:08:10.000    15.1    8.4  50.0 8V005   77.5   8.5   3.6   1.9  10.5     1.6      1427.9
                      102:12:08:11.000

 ASCENT PSD    X00282 102:12:08:20.000    15.1   10.6  50.0 8V005   77.8   6.1   3.4   1.5  11.1     4.1      1347.8
                      102:12:08:21.000

 ASCENT PSD    X00282 102:12:08:30.000    15.1    9.9  50.0 8V005   76.1   8.5   4.0   1.9   9.4     3.3      1286.9
                      102:12:08:31.000

 DEFALT PSD    X17776 102:12:09:50.000    15.1    1.3  20.0 8V005   98.9   0.7   0.2   0.0   0.1  .03141      1042.8
                      102:12:09:51.000
```

Figure 7 - Wave analysis screen report for PSD data for accelerometer V08D9440 located on the thrust structure

If any PSD value exceeds the 100-percent level of the threshold within the frequency range identified, graphical outputs of the PSD (figure 8) and mean-squared spectral distribution (figure 9) are produced. Acoustic data being processed through the system is compared to 1/3 octave band thresholds. The same control and variation of the threshold by mission event and FTR are provided. The wave analysis screen report for acoustic data provides the same content as the PSD report. Again, if any data amplitude exceeds 100 percent of the applied threshold, a graphical representation of the data (figure 10) is produced.

Transient data is processed in the system in much the same manner as the steady state data. The screening for transients utilizes the digitized input data and compares the amplitudes to the peak threshold level for the mission event specified. Again, the threshold level utilized is the minimum for any FTR. The output of the procedure consists of a tabulated list of the time the threshold was first exceeded and the time and amplitude of maximum exceedance. This information is used to select time intervals for high-speed oscillograms (8 in. per sec) and/or periods for shock spectrum analysis processing.

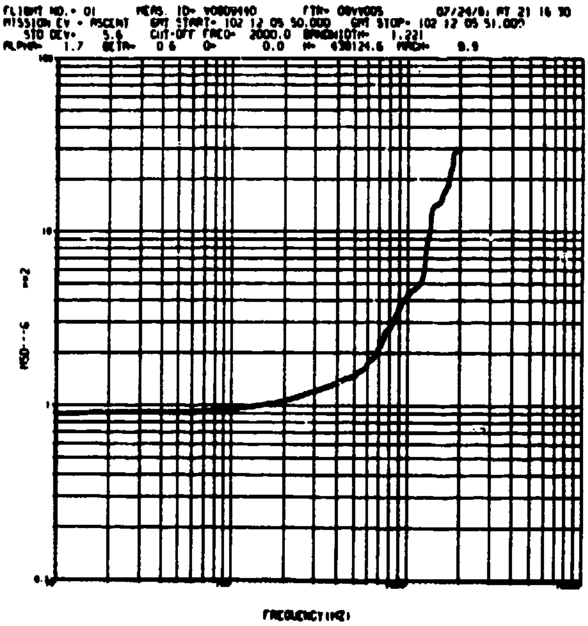

Figure 9 - Mean-squared spectral distribution plot for accelerometer V08D9440

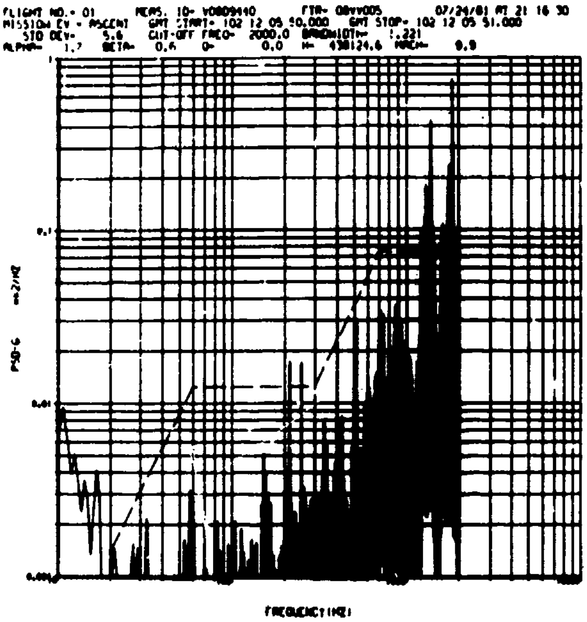

Figure 8 - PSD plot for accelerometer V08D9440 located on the thrust structure

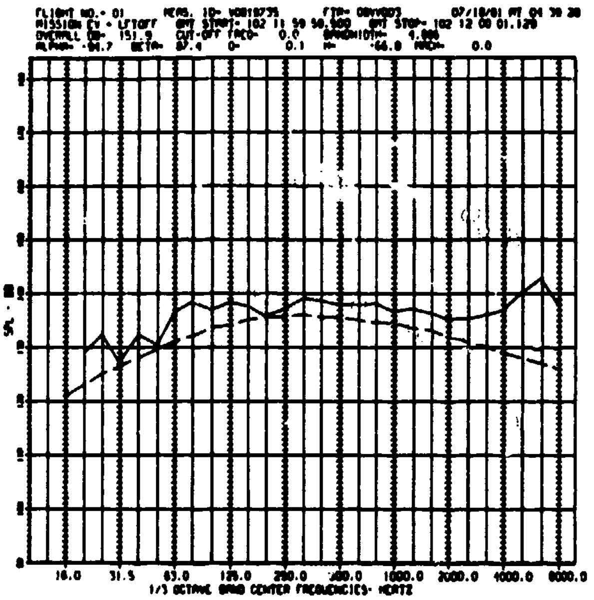

Figure 10 - A 1/3 octave plot of microphone V08Y9735 located on the elevon

The screening procedure employed for shock spectra is basically the same as that previously described for PSD and 1/3 octave screening. Shock spectra are compared to thresholds contained in the data base for each measurement. The results are displayed in the Wave Analysis Screen Report format (figure 11). If the maximum absolute response amplitude exceeds the threshold, the graphical representation of the maximum absolute shock response spectrum (figure 12) is produced; the user also has the option of having the excitation function (figure 13) produced.

```
                                        WAVE ANALYSIS SCREEN REPORT

        FLIGHT NO. - 01                                                                              DATE - 11/24/81, 15:38:36

        MSID - V08D9877                  SUBSTRUCTURE - CREW MODULE                                          ZONE - Z06
                                         PFL     DATA                       DISTRIBUTION OF DATA AS A
                               TIME       DB      DB  PROFILE               PERCENT OF SCREEN PROFILE
MISSION  DATA    TAPE         START/     RMS     RMS  SCREEN                  0     25    50    75   100    MAX
 EVENT   TYPE     NO           STOP      PEAK    PEAK    %     SOURCE        25     50    75   100    +    VALUE         FREQ

 DEFALT SHOCK  X04658 102:12:00:04.100 0.0000    10.0 100.0 8V005        0.0   0.0   0.0   0.0 100.0    11.0          18.7
                      102:12:00:04.500

 DEFALT SHOCK  X12732 102:12:00:04.069 0.0000    10.0 100.0 8V005        0.0   0.0   0.0   0.0 100.0    12.0          18.0
                      102:12:00:04.699
```

Figure 11 - Wave analysis screen report for shock data for accelerometer V08D9877 located in the crew cabin

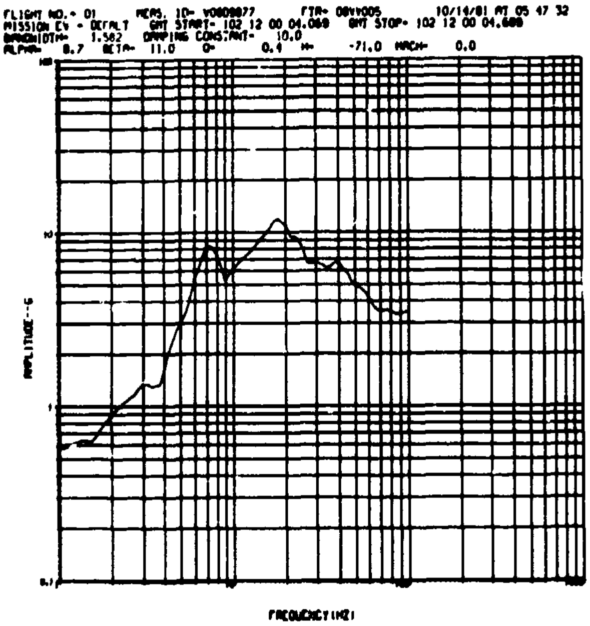

Figure 12 - Shock spectrum plot for accelerometer V08D9877

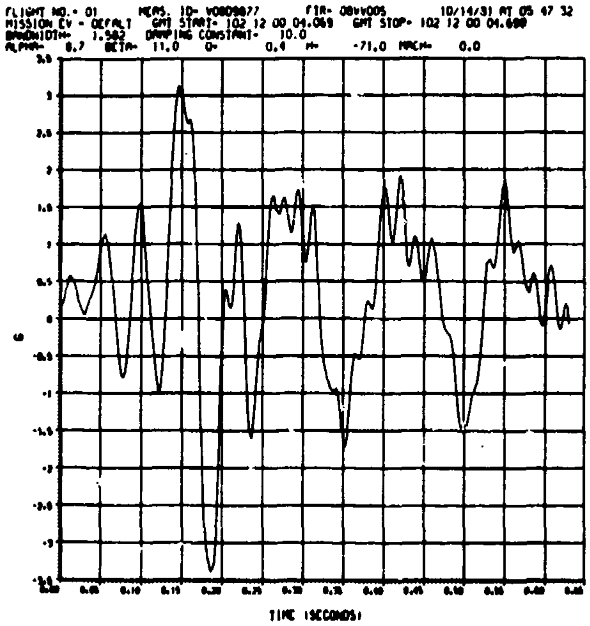

Figure 13 - Shock excitation function plot for accelerometer V08D9877

USER INTERFACE

The screening and display subsystem is implemented on a UNIVAC 1110 computer system and is executed in a demand environment via a TEKTRONIX 4014 graphics display terminal with hard-copy capability. This subsystem is designated as the Wideband Analog Data System (WADS). An FR-80 computer output microfilm processor is available at the Central Computer Facility to process any batch output created. The system diagram (figure 1) depicts the relationship between the three functional processes.

After the data has been digitized and the rms or wave analysis processing has been performed, the data is ready for input to the WADS. The WADS is tutoria in design and prompts the user to initiate a desired process or function for all inputs required. The master menu (figure 14) displays the functions available in the system. The 14 functions provide the user with the means of establishing and maintaining the data bases, producing listings of the screening results of data processed, providing catalogs of data available in the system, and performing the basic screening process in both the demand mode and the demand-initiated batch mode. Initially, rms and wave analysis tapes are processed using functions 1, 2, and 3 to perform the automatic screening procedure and store the results. The user then selects the desired option. Function 10 is used to determine if a specific measurement or group of measurements has been processed by the WADS; if so, it displays the results of the screening process. The screen report log menu (figure 15) provides several options for the retrieval of data from the data base. The output products are similar to those shown in figures 3, 7, and 12, depending on the type of data requested. Graphical display of the data is produced by selecting master menu function 11 (figure 14).

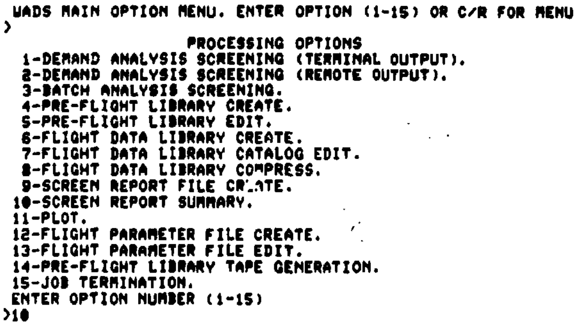

```
 WADS MAIN OPTION MENU. ENTER OPTION (1-15) OR C/R FOR MENU
>
                    PROCESSING OPTIONS
  1-DEMAND ANALYSIS SCREENING (TERMINAL OUTPUT).
  2-DEMAND ANALYSIS SCREENING (REMOTE OUTPUT).
  3-BATCH ANALYSIS SCREENING.
  4-PRE-FLIGHT LIBRARY CREATE.
  5-PRE-FLIGHT LIBRARY EDIT.
  6-FLIGHT DATA LIBRARY CREATE.
  7-FLIGHT DATA LIBRARY CATALOG EDIT.
  8-FLIGHT DATA LIBRARY COMPRESS.
  9-SCREEN REPORT FILE CREATE.
 10-SCREEN REPORT SUMMARY.
 11-PLOT.
 12-FLIGHT PARAMETER FILE CREATE.
 13-FLIGHT PARAMETER FILE EDIT.
 14-PRE-FLIGHT LIBRARY TAPE GENERATION.
 15-JOB TERMINATION.
 ENTER OPTION NUMBER (1-15)
>10
```

Figure 14 - WADS main option menu

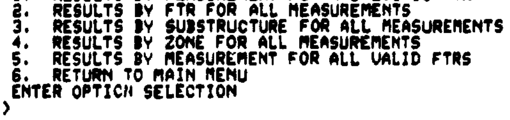

```
 ** REPORT LIST OPTIONS **
 1.   RESULTS BY MEASUREMENT FOR A SPECIFIC FTR
 2.   RESULTS BY FTR FOR ALL MEASUREMENTS
 3.   RESULTS BY SUBSTRUCTURE FOR ALL MEASUREMENTS
 4.   RESULTS BY ZONE FOR ALL MEASUREMENTS
 5.   RESULTS BY MEASUREMENT FOR ALL VALID FTRS
 6.   RETURN TO MAIN MENU
 ENTER OPTION SELECTION
>
```

Figure 15 - WADS subfunction 10 (screen report summary) menu

The plot menu (figure 16) provides the user with options for plotting each type of data. Upon selecting an option, the plot default criteria defining the characteristics of the plot grid to be produced is displayed. The user may alter any default desired. The data retrieval keys are then solicited; these define a specific data set to be extracted from the data base, or a specific plot to be generated from tape in the case of rms processing. If composite overlay plots are desired, additional data set retrieval keys are solicited. Otherwise, graphical results are produced as shown in figures 4, 5, 8, 9, 10, 12, and 13.

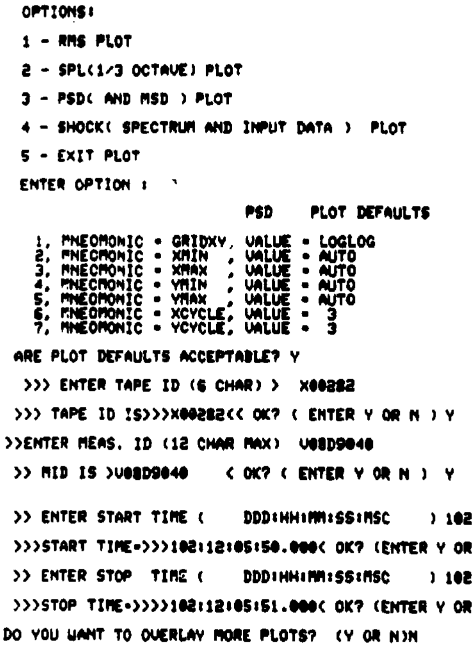

```
  OPTIONS:

  1 - RMS PLOT

  2 - SPL(1/3 OCTAVE) PLOT

  3 - PSD( AND MSD ) PLOT

  4 - SHOCK( SPECTRUM AND INPUT DATA )  PLOT

  5 - EXIT PLOT

  ENTER OPTION :

                          PSD    PLOT DEFAULTS

   1, MNEOMONIC = GRIDXY, VALUE = LOGLOG
   2, MNECMONIC = XMIN  , VALUE = AUTO
   3, MNECMONIC = XMAX  , VALUE = AUTO
   4, MNECMONIC = YMIN  , VALUE = AUTO
   5, MNEOMONIC = YMAX  , VALUE = AUTO
   6, MNEOMONIC = XCYCLE, VALUE =  3
   7, MNEOMONIC = YCYCLE, VALUE =  3

 ARE PLOT DEFAULTS ACCEPTABLE? Y

  >>> ENTER TAPE ID (6 CHAR) >  X00282

 >>> TAPE ID IS>>>X00282<< OK? ( ENTER Y OR N ) Y

>>ENTER MEAS. ID (12 CHAR MAX)  V08D9040

 >> MID IS >V08D9040    < OK? ( ENTER Y OR N )  Y

 >> ENTER START TIME (    DDD:HH:MM:SS:MSC    ) 102:12:05:50.000

 >>>START TIME=>>>102:12:05:50.000< OK? (ENTER Y OR N)  Y

 >> ENTER STOP  TIME (    DDD:HH:MM:SS:MSC    ) 102:12:05:51.000

 >>>STOP TIME=>>>>102:12:05:51.000< OK? (ENTER Y OR N)  Y

DO YOU WANT TO OVERLAY MORE PLOTS?  (Y OR N)N
```

Figure 16 - WADS subfunction 11 (plot) options

SUMMARY

Using the SWAPS to process data from the first Space Transportation System (STS-1) flight has significantly reduced the overall analysis effort. The manual screening of the quick-look oscillograms reduced the number of measurements to be evaluated by 15 percent. The rms time history screening process further reduced the number of measurements requiring additional processing by another 40 percent. The remainder of the measurements were processed through the transient and/or steady state wave analysis programs, resulting in 600 PSD's, 125 1/3 octaves, and 150 shock spectra analyses.

The results provided the analysts with a condensed set of data which exceeded predetermined "thresholds of interest". This minimized the dilution of effort and allowed the analysts to concentrate only on data which was pertinent to satisfying the Flight Test Requirements.

DEVELOPMENT OF A VIBROACOUSTIC DATA BASE MANAGEMENT AND PREDICTION SYSTEM FOR PAYLOADS

Frank J. On
NASA Goddard Space Flight Center
Greenbelt, Maryland

and

William Hendricks
Lockheed Missiles and Space Company
Sunnyvale, California

A data base management and prediction system called "Vibroacoustic Payload Environment Prediction System (VAPEPS)" has been developed to serve as a respository for Shuttle or expendable booster payload component flight and ground test data. This system is to be made available to the aerospace community for multiple uses including that of establishing the vibroacoustic environment for new payload components. VAPEPS data includes that spectral information normally processed from vibration and acoustic measurements (e.g., power spectra, sound pressure level spectra, etc.). Results of development to provide this capability by NASA Goddard Space Flight Center and Lockheed Missiles and Space Company are described.

1.0 INTRODUCTION

Developing design and test requirements for the vibroacoustic environment of a Shuttle payload, or that of an expendable booster, becomes a difficult problem when uncertainties exist concerning the magnitude and spectral characteristics of the environment itself. These uncertainties can exist because of unknowns associated with either the acoustic excitation or the response characteristics of the payloads. Attempts to define this environment analytically have met with limited success and an empirical prediction, using data obtained from previous flight or ground tests, is usually relied on. Present practices for defining a vibroacoustic environment empirically are noted by the lack of a complete and organized data base, and the use of rather simple extrapolation procedures for accounting for structural differences between that of the payload for which an environment is being established and that of the structures represented by the data base being used. Each payload contractor responsible for making a prediction will do so using those data sets with which he is familiar and will account for excitation/structural differences as his experience indicates appropriate. Design and test requirements can thus be based on an environment that was not necessarily obtained using the best data sets and/or extrapolation procedure that could be provided by the aerospace community.

Recognizing this as a problem, a program was initiated by NASA Headquarters Office of Aeronautical/Space Technology (OAST) with the objective to develop a more consistent and reliable methods for predicting the vibroacoustic environment of Shuttle payloads.

A data base management and prediction system called "Vibroacoustic Payload Environment Prediction System (VAPEPS)" has been developed to serve as a repository for Shuttle or expendable booster payload component flight and ground test data. This system is to be made available to the aerospace community for multiple uses including that of establishing the acoustic induced environment for new payload components. VAPEPS data includes that spectral information normally processed from vibration and acoustic measurements (e.g., power spectra, sound-pressure level spectra, etc.). Time history data is presently not a part of the data base. The data base now includes only data obtained from expendable booster payloads. Data from Shuttle payloads will be included in the future.

The VAPEPS data base management system has been configured to serve the unique requirements of a local site or it can be configured to serve many sites (figure 1). When shared by a community of users it provides for a single uniform, consistent and organized data base which can be used in a cost effective manner to establish the vibroacoustic environment of payloads/components for either space Shuttle or expendable booster mission.

The prediction procedure which has been implemented in VAPEPS is specifically designed to establish random vibration and acoustic environments of new payload components using data obtained from similar design that had been previously flown or ground tested. The expanded extrapolation method implemented in the prediction procedure is based on the application of statistical energy analysis (SEA) parameters for high frequencies and nondimensional scaling parameters

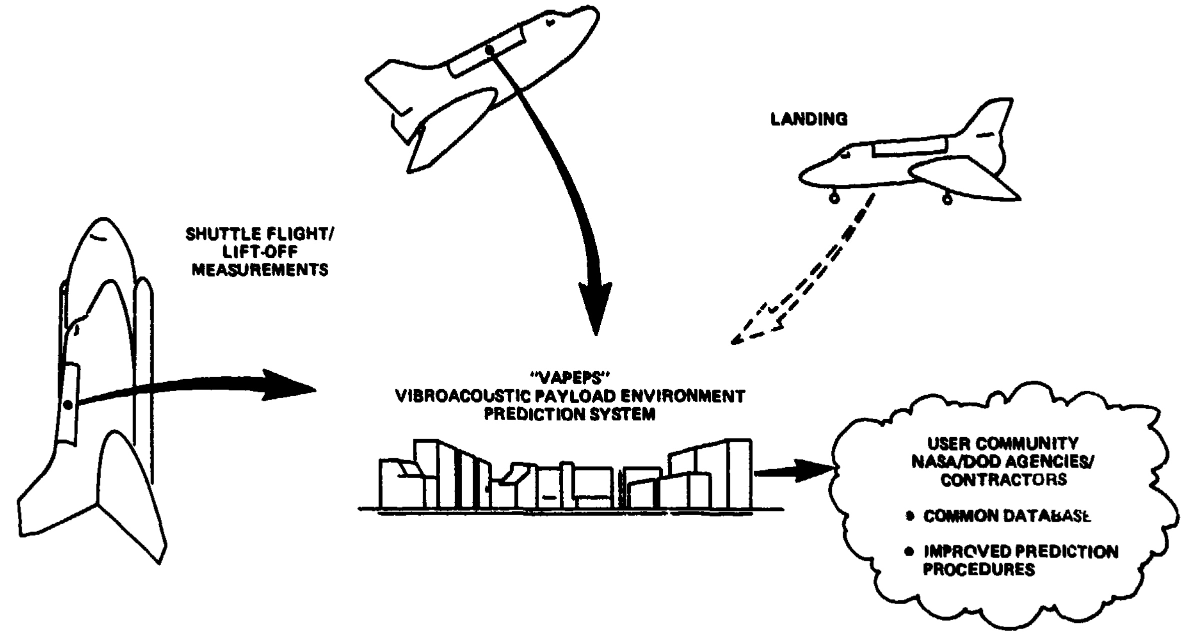

Fig. 1 – VAPEPS – Data Base Management/Prediction System

for low frequencies. This procedure also includes features that permit taking data from any given flight or ground test to perform mathematical and statistical operation on it to obtain such information as averaged or maximum levels, noise reduction and other such analysis normally included in flight/ground test reports. To enhance the interrogation of the data base information, a search processor has also been implemented into VAPEPS.

The development of the VAPEPS Program will meet the current need for a common data base that can be conveniently and rapidly updated as new data becomes available, and for an improved extrapolation procedure wherein the structural parameterization is much larger than that now employed. The VAPEPS software has been written to be compatible with the Univac 1100 series (exec. 8), DEC VAX 11/780 (VAX/VMS) and CDC 6600/7600 operating system computers. The NASA/Goddard Space Flight Center (GSFC) served as contracting center and technical monitor for the Program. The purpose of this paper is to present the results of the development by the Lockheed Missiles and Space Company (LMSC) to provide this capability.

2.0 VAPEPS SYSTEM CONCEPT

Payload structures are subjected to a wide variety of loads during all aspects of flight. The vibroacoustic loads result from the response of the structure to acoustically induced vibration environments during actual flights. A significant amount of data has been acquired of these environments during actual flights and simulated flight ground tests. In the past, only a small percentage of these measurements have been used effectively. Reasons for the lack of efficient use are primarily the result of inadequate measurement definition, and the lack of knowledge of their existence.

The design goals of the VAPEPS system are to provide an approach for compiling these measurement data in a unified data base which can be rapidly, and conveniently updated as new data becomes available, and to provide a rapid, reliable, and efficient means for establishing payload vibroacoustic environment criteria/specifications from this updated common data base. To meet these design goals, the following phases of work were undertaken:

- Develop optimum data base and management system concept.
- Create initial data base summary data bank based on extensive collection of past vibroacoustic flight and ground test data.
- Develop improved data search and prediction procedures.
- Develop computer software requirements.
- Validate VAPEPS Program.

The basic framework upon which the VAPEPS system concept has been developed is illustrated in figures 2 and 3. The VAPEPS system is configured to operate in four principal modes:

- Data Input/Storage
- Data Interrogation/Retrieval
- Data Extrapolation/Prediction
- Data Processing

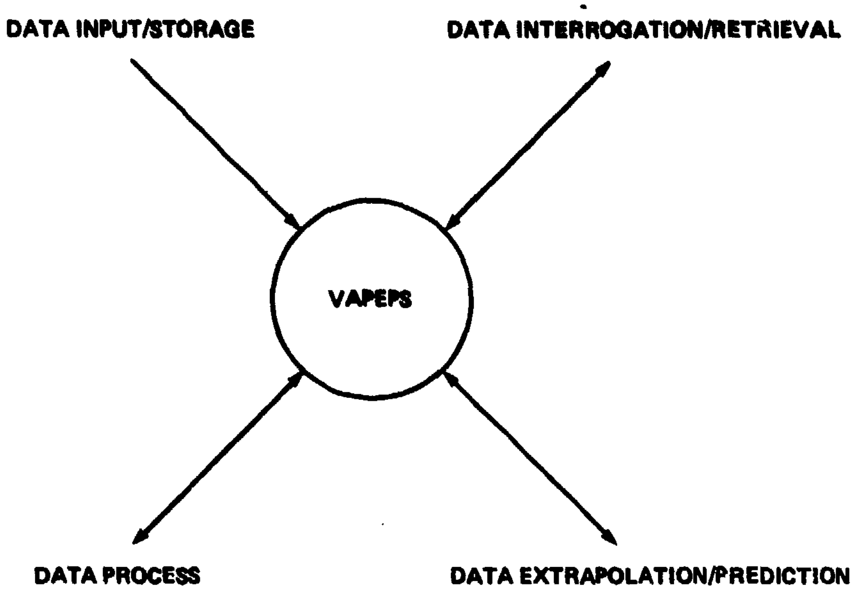

Fig. 2 – VAPEPS System Concept

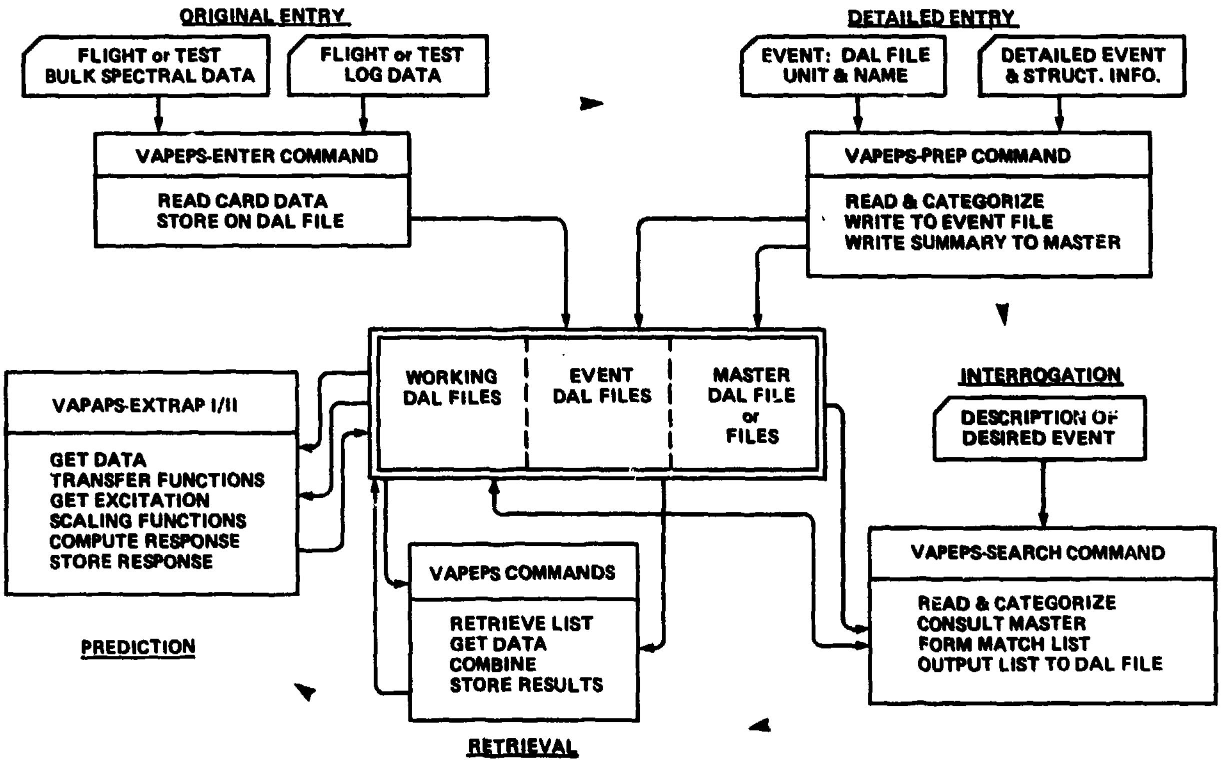

Fig. 3 – VAPEPS System Overview

Data Input/Storage

In this mode, the data from a given ground test or flight is collected and arranged in a manner that can be input to VAPEPS to be stored as a data base. The data is composed of two parts:

- Spectral data from microphone and accelerometer measurements during the event. This data is read by the VAPEPS processor ENTER.

- A description of the event through the specification of keywords and parameters. This includes the classification of the excitation, location and the structure. This data is read by the VAPEPS processor PREP.

Data Interrogation/Retrieval

In this mode, the user is looking for data of a certain type. This may be data from a particular type of excitation, from a general region in a structure, or from a particular type of structure. This data interrogation is performed by the VAPEPS processor SEARCH. The user will get a list of events that satisfy the conditions specified.

Data Extrapolation/Prediction

This mode is designed to operate with SEARCH. After the data base is interrogated for the type of payload component and mounting structure on which the prediction is to be based, the appropriate data modules will then be identified from list of event file names produced by SEARCH. These files will then be called and operated on through VAPEPS to obtain the desired input for the extrapolation or prediction program EXTRAP. EXTRAP consists of a group of VAPEPS commands which allow the user to generate transfer functions or scaling parameters for various vibroacoustic systems and predict the response of these systems to any given input.

Data Processing

VAPEPS includes an extensive data processing capability. Each process is initiated by the user through a VAPEPS command. Each command is essentially a subroutine that operates on one or more input data sets to produce one or more output data sets. In general, operations desired by the user will require the use of several commands. Command packets (called runstreams) may be formed that will perform complex manipulations through minimal user input.

3.0 CREATION OF DATA BASE

3.1 Vibroacoustic Data Base

The vibroacoustic data base consists of two distinct parts:

- Global Data Base–Card Images

- Local Data Base–DAL (Direct Access Library)

Global Data Base

Before data of a given event can be processed by VAPEPS, it must exist in the form suitable for entry into the system. Data input is accomplished through the VAPEPS processors ENTER and PREP. One data deck must be created for each processor for all events to be entered into the system. The data decks are the building blocks of the whole system and form the global data base. When an event is first recorded, the data decks will be created by the processing agency. The decks may then be transmitted to all other sites and entered on each local system.

Local Data Base

The data from the global data base is entered into a local data base at each site. The local data base consists of mass storage files known as DAL libraries.

The VAPEPS data base presently includes over 3000 frequency spectrums in the form of sound pressure level, vibration level or power spectral density from analysis of data from either Space Shuttle or expendable booster payload components obtained during flight or ground test. A summary of the data base, including a breakdown of the number of acoustic and vibration spectrums, is presented in table 1. Narrowband spectrums (10 Hz or less) of the data base cover the frequency range between 20 and 2000 Hz while proportional bandwidth 1/3-octave spectrums include the frequency range between 25 and 10,000 Hz. The number of data sets for each frequency range is also given in table 1.

The data base has been separated into 6 files consisting of over 60 events. Each file represents a significantly different component mounting configuration and each event normally represents a specific test condition. While most any units can be used, the data base presently has the units of G^2/Hz or $(psi)^2$/Hz for the spectral density analysis. Decibels are used for the 1/3-octave band sound pressure and vibration level analyses where in both cases the normalizing factor is 8.4144×10^{-18} $(psi)^2$ or g^2. Additional data that becomes available will be added to the present data base.

3.2 ENTER Processor

The VAPEPS ENTER processor is used to enter and store test data in the VAPEPS system. The user specifies the file that the data will actually be stored in. Prior to reading the test data, ENTER requires that the user supply some basic information about the test in general and the individual channels specifically. When the user supplies complete information, the data set becomes fully self contained. If all records of the test are lost, there is still sufficient description information in the data base to enable the user to determine the purpose of the test, the basic test configuration, the location and type of each measurement channel, the units of the data, the bandwidths and the frequency range. It is important to note that ENTER does not check the validity of the information supplied, it merely requires that the user supply something. It is the responsi-

TABLE 1
Vibroacoustic Data Base (Preliminary)

Filename (VAPEPS*)	No. of Vib. Measurements		No. of Acous. Measurements		Band Width	Start Freq.	Payload Characteristics
	2KHz	10KHz	2KHz	10KHz	Hz	Hz	
STS		118		24	1/3 OCT	25	Space telescope with simulated payload components
ID79		699		78	1/3 OCT	25	Simulated payload components mounted on built-up flat panels
B104		342		84	1/3 OCT	25	Payload components mounted on trusses, built-up panels & conical shells
B152	53		8		10	20	Payload components mounted on truss-mounted built-up panels
		254		178	1/3 OCT	25	
	139		13		1/6 OCT	20	
B156A	360		55		10	20	Payload components mounted on truss-mounted honeycomb panels
		921		120	1/3 OCT		
B156E	685		78		10	20	Panel mounted payload components
		101		46	1/3 OCT	25	
TOTAL	1237	2435	154	530			

bility of the user to insure that the information supplied is complete and accurate.

In addition to this basic descriptive information, ENTER requires that the users supply some information about the data itself. ENTER will accept the data in virtually any format, but the user has to tell ENTER what the format is. Having been provided with all of the information that it requires, ENTER will proceed to read and process the data. ENTER will inform the user of any errors that it detects in reading the data. These errors are only those which affect ENTER's ability to make sense of the data supplied.

ENTER provides the user with the option to enter the data in parts. This makes it possible to separately enter and store related data channels with the same name and still maintain the parts separately. This process is known as sectioning. The most basic form of sectioning, and the one which most often will be used, involves entering microphone and accelerometer data separately.

Output from ENTER consists of DAL elements of the following element names:

SPDT = spectral data matrix

FREQ = frequency matrix

CHAN = channel descriptor matrix

EVNT = event descriptor vector

RMSI = channel root-mean-square value vector

3.3 PREP Processor

This processor reads description from card images that defines an event, vehicle (or test specimen) configuration, data naming or channel details and tye type of modules into which the data has been configured. This information is then entered into the event DAL file. The vehicle or test specimen is described through a configuration tree as illustrated in the example of figure 4 for a Shuttle structure.

The capacity of the configuration tree can be expanded if necessary. The names used in the configuration tree can be any desired, however, standardization is required for VAPEPS to be shared by a community of users. Recommended names for the first subdivision of a Space Shuttle flight vehicle are indicated in figure 4. Further naming can best be performed after the flight measurement program has been finalized. The same is true for ground test programs, a perceptive naming system depends on the payload components from which vibration and acoustic data are to be obtained.

The configuration tree describes the mounting structure for the payload component from which data has been obtained. Structural and acoustic space details of the payload component itself are entered through the data module routine of PREP. This routine takes structural/acoustic/channel information and arranges it into a format consistent with that required by the VAPEPS prediction program—see section 5.0. A data module can be assigned to any subdivision of the configuration tree and any number of data module can be developed from the data obtained for a particular flight or ground test event. This permits for example, measurements made to define the noise reduction characteristics of Spacelab to also be used to define the acoustic environment of the experiments within the lab, or the environment of payload components in the Shuttle cargo bay mounted on pallets outside of Spacelab. Thus, one set of acoustic measurements could show in three different data modules. It should be noted that the data modules can also be used without vibration/acoustic data to define structural/acoustic space parameters of any given branch of the configuration tree. Structural/acoustic parameters that can be assigned are listed in table 2.

One of the features of VAPERS that makes it an extremely powerful tool is the capability to pre-program runstreams which perform generalized tasks. The flexibility of the ENTER processor limits this capability, however. ENTER allows data to be entered for any bandwidth covering any frequency range in any of several units and in several sections. The result is that the form of the data for each event is most probably unique. It is very difficult to write a general runstream to access and manipulate data which are not stored in a consistent manner. The PREP processor solves this problem by creating a single standardized element containing all the data from a particular event. The properties of this standard data set are:

a. UNITS = decibels (dB) for both vibration and acoustic data normalized to 8.4144 $\times 10^{-18}$. $(\text{psi})^2$ or g^2.

b. BANDWIDTH = 1/3 Octave.

c. FREQUENCY RANGE = 10 to 10,000 Hz.

PREP locates all of the sections associated with the event and combines them into a single element having these properties, making conversions as necessary. PREP uses the reference level for bands outside the range of the test data.

TABLE 2
VAPEPS Structural and Acoustic Parameters

	1 EXTA	2 SKIN	3 INTA	4 MONT	5 INST	6 FRAME	DESCRIPTION
1	TYPE	TYPE	TYPE	TYPE	TYPE	TYPE	*
2	ROW	ROW	ROW	ROW	ROW	ROW	Mass density (all structural smeared in)
3				XTYP		XTYP	Cross section type*
4	CO	CL	CO	CL	CL	CL	Wave speed
5	V		V				Volume
6		H		H	H	H	Thickness (equivalent, based on flexural stiffness)
7	AP	AP	AP	AP	AP		Total surface area
8		BL		BL	BL	BL	Length
9	AAC		AAC				Acoustic absorption coefficient
10		ALX		DI	ALX	DI	DI, DO: Inner, outer diameter
11		ALY		DO	ALY	DO	ALX, ALY: Sub-panel dimensions
12				B		B	Width
13		D			D		Diameter
14				CNT			No. of beams
15		DLF		DLF	DLF	DLF	Structural damping loss factor
16		E		E	E	E	Young's modulus
17				G		G	Shear modulus
18				T		T	Torsional stiffness per unit length
19				PJ		PJ	Polar moment of inertia
20				A		A	Cross section area
21				RGF		RGF	Flexural radius of gyration
22		PATA			PATA		Total length of discontinuity*
23				ALPHA			Orientation angle*
24				BETA			Orientation angle*
25				RATE			RATE: Attenuation factor (dB/octave)
26		ROWS		CFRQ	ROWS		ROWS: Surface mass density of bare skin CFRQ: Frequency at which to begin attenuation
27	VEL						Velocity of flying body
28	VISC						Kinematic viscosity of fluid
29	FBL						Length of flying body
30		NSMS		NSMS			Non-structural mass

* Items explained in ref. 2

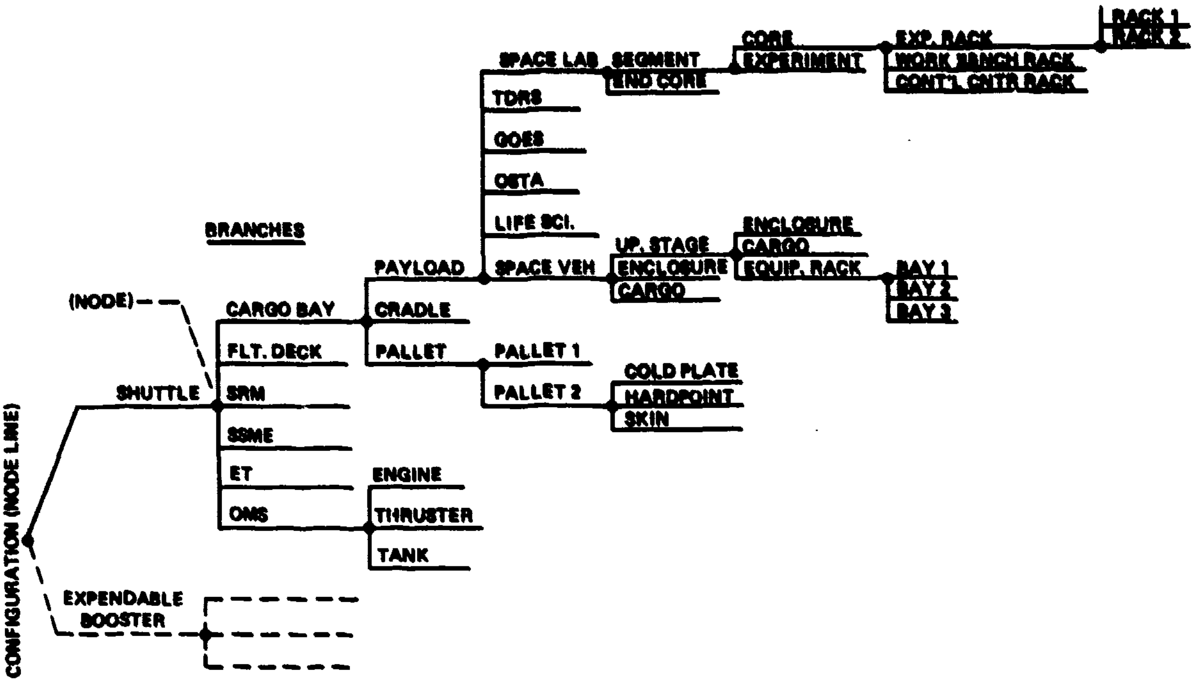

Fig. 4 – Structural Configuration Tree (Shuttle Structure Example)

The advantage of having all data converted to a standard form is that the user can write general runstreams to access and manipulate. The user knows ahead of time that the data represent 1/3-octave bands from 10 to 10,000 Hz and that they are always expressed in terms of dB.

The five major sections to PREP can be summarized as follows:

a. Data collection and conversion (CHECK command)

The first step in PREP is to collect all of the spectral data that was input through ENTER and convert it to standard units. This process is performed automatically the first time an event is PREP'ed as long as there are more than one section. If the ENTER data is changed, the conversions may be redone by issuing the CHECK command while in PREP.

b. Basic bookkeeping information (BOOK command)

In this section, the user supplies descriptive information that is used to categorize the event as a whole. Entries include the time, date and location of the event as well as the various names given the event by participating agencies.

c. Measurement types and locations (CHAN command)

This section is used to edit and/or list the channel table that is created during the CHECK process. This table contains a valid frequency range for each channel as well as the coordinates of the transducer. Initially, all coordinates are set to zero and all frequency ranges are set to the frequency limits used during original data processing. Bad channels may be marked by reducing the valid frequency range or zeroing it out completely.

d. Vehicle configuration tree (CONF command)

This section is used to describe the vehicle that was tested or flown. This description is developed by assigning each component to a branch in a configuration tree and giving the branch a name.

e. Data modules and acoustic/structural parameters (MODULES command)

The purpose of this section is to describe the local environment of each measurement zone. The description takes the form of a SEA (Statistical Energy Analysis) model. Each measurement zone is identified as one of five elements in the SEA model and the parameters required to describe that element are supplied by the user. The section 5.0 on EXTRAP contains a complete description of the SEA model and the parameters required for each element in it.

4.0 INTERROGATION OF DATA BASE

VAPEPS has the capability of extrapolating predicted payload responses from theoretical calculations and measured data. The user supplies models for the system to be predicted and a similar, previously tested system and VAPEPS does the rest. As the models are created and attached to each set of test data for extrapolation purposes, the user need only determine which set of test data is most closely related to the new system to be predicted. As the data base grows, the task of finding that particular set of data will become more and more difficult. A large amount of time would have to be spent inspecting the various parameters associated with each set of test data before arriving at a decision on which set to use.

The VAPEPS SEARCH processor was developed to aid in this task. The user specifies a set of required parameters and SEARCH inspects the information previously entered through the PREP processor to produce a list of test events that meet those requirements, (assuming that all users have been conscientious in supplying the descriptive information in PREP). The importance of PREP to the success of the VAPEPS system becomes obvious.

The SEARCH processor is divided into sections which correspond to the various sections in PREP. The user specifies a list name which SEARCH will associate with the list of events found. Each successive search will modify the list to reflect the results of that search. As an example, the user might enter the BOOK section of the SEARCH processor and request a list of events which were tested at the Eastern Test Range (ETR) during 1979. He might then enter the CONFIGURATIONS section of the SEARCH processor and request a list of events that included a Spacelab. This search could be performed on all events in the data base, or it could be limited to the events in another list, namely the list created in the BOOK section. In this latter case the result would be a list of all events tested during 1979 at ETR which included a Spacelab.

Some basic considerations to be kept in mind when using the SEARCH processor are:

a. The SEARCH processor is divided into sections. Each section searches a different area of information. The sections correspond to the sections in the PREP processor, as follows:

BOOK = Searches all information entered through the BOOK section of the PREP processor.

EVENT = Searches only information entered through the PROC command in the BOOK section of the PREP processor.

CONF = Searches only information entered through the CONF section of the PREP processor.

MODULES = Searches only information entered through the MODULES section of the PREP processor.

A good knowledge of PREP is required for effective use of SEARCH.

b. The user specifies a four-character name for each list created. He can specify that all events are to be searched in creating the list, or he can limit the search to those events contained in some other list.

c. The user specifies a logical operation to be applied to the list of parameters requested. The logical operations are AND, OR and NOT. When the AND operation is specified, each event placed in the output list includes every parameter requested. When the OR operation is specified, each event placed in the output list includes at least one of the parameters requested. When the NOT operation is specified, each event placed in the output list will include none of the parameters requested.

The SEARCH processor includes various list manipulation commands as well as the four basic search sections described above.

5.0 PREDICTION CAPABILITY

The response of new payload component can be predicted by using the combined procedure of data base and theoretical extrapolations. Two extrapolation procedures are available in VAPEPS:

EXTRAP I—Employs statistical energy techniques to make predictions; not recommended for low frequency predictions.

EXTRAP II—Employs a scaling technique to obtain the response of the new component based on measured response of a similar component; recommended for low frequency predictions.

5.1 EXTRAP I

Description

EXTRAP I consists of a group of VAPEPS commands which allow the user to generate transfer functions for various vibroacoustic systems and predict the response of these systems to any given input. It is not actually a processor. Unlike the processors discussed thus far, EXTRAP I does not require that a specific command be issued prior to issuing the EXTRAP I commands. Any of the EXTRAP I commands may be issued at any time directly from VAPEPS.

Prediction Model—The payload component mounting system is modelled using Statistical Energy Analysis (SEA) methods. The complete model consists of five elements which interact with each other in specific ways. An EXTRAP model may consist of any combination of these five elements. The full five element model is shown in figure 5. The names of the elements are EXTA (External Acoustic Space), SKIN, INTA (Internal Acoustic Space), MONT (Mount) and INST (Installation). The name and number associated with each element is fixed, even if some elements are missing in the model of a particular configuration.

SEA elements can be either active or inactive. An inactive element has a negligible amount of energy in comparison with the energy associated with active elements. However, it does establish a path for energy transfer. Shown in figure 6 is the basic and expanded matrix equation of energy balance for the model.

EXTRAP I derives energy balance equations for each SEA element. If a SEA element is missing, the energy balance equation associated with it does not exist. A reduced matrix equation is therefore obtained by eliminating the column and row associated with this missing element in the matrix equation. The elements of this matrix consist of a combination of coupling loss factors which are functions of system configurations and parameters as shown in figure 6. Most coupling loss factors between acoustic spaces and structures can be found in open literature (e.g., reference 1). Mechanical coupling information is relatively limited. Most of them are not readily available in literature.

Transfer Function–The matrix equation shown in figure 6 is a function of 1/3-octave band center frequency. By solving the matrix equation band by band, the transfer functions between any of the SEA elements can be obtained. The transfer function to be obtained is specified by the user.

The calculation of a transfer function involves four steps:

1. The model densities of each SEA element are calculated based on the structural parameters associated with them.
2. The form of the reduced matrix equation is then obtained according to the specified SEA model.
3. Coupling loss factors are calculated.
4. The reduced matrix is solved for each transfer function required.

Any element in the SEA model can be designated as a response element or an excitation element. There may be more than one excitation element for a single response element. As an example, suppose that the external acoustic space (element 1) and the internal acoustic space (element 3) are designated as excitation elements and the installation (element 5) is designated as the response element. The transfer functional relationship would then be:

$$E5 = T1 \times E1 + T3 \times E3 \qquad (1)$$

where T1 and T3 are the transfer functions associated with excitation elements 1 and 3, respectively, and E1, E3 and E5 represent the energy stored in each element. T1 is obtained by solving the governing matrix equation with excitation E3 set to zero.

Extrapolation–The process outlined in the previous section is repeated for both the base-line system and the new system. Because we normally have only one set of independent data for the base-line system, only one transfer function can be established empirically. As in the example of equation (1), more than one transfer function is needed from the base-line configuration. Since only one can be established empirically, it is necessary to determine the rest of the required transfer functions theoretically. The user specifies which transfer function is found empirically and which transfer functions are calculated theoretically. The element of the model for which theoretical transfer function calculations are considered most unreliable should be that which is determined empirically. Suppose that, in equation (1), transfer function T1 is to be determined empirically. The other transfer function, T3 in this case, is theoretically calculated in EXTRAP I. With the measured data E1, E3 and E5 and the calculated transfer function T3, the transfer function T1 can be found through equation (1).

The transfer function T1' of the new system is determined from T1 of the base-line system as:

$$T1' = T1 \times dT1 \qquad (2)$$

where T1 is the empirically determined transfer function of the base-line system and dT1 is the ratio of theoretically calculated transfer functions of the new and base-line systems. The response (in terms of energy E5') of the new system under excitations E1' and E3' is:

$$E5' = T1' \times E1' + T3' \times E3' \qquad (3)$$

where T1' is obtained from equation (2) and T3' is calculated theoretically.

In the procedure outlined above, the energy in 1/3-octave bands is the pertinent quantity. However, excitation and response data are usually expressed in terms of the mean-square value of pressure or acceleration. A conversion process has been incorporated into EXTRAP to handle the transformation.

Parameter Input–The parameters for each SEA element are summarized in table 2. The meanings of most of the parameters are self-explanatory; some are explained in reference 2. The first five columns of this 30 X 6 array contain parameters for the corresponding SEA element (i.e., column 1 goes with element 1, etc.). The sixth column contains the parameters for the mounting frame which is not an element in the SEA model. However, it is used when the mount (element 4) is a truss. The mounting frame is a structure to which the truss is attached. If the truss is directly attached to the skin, the mounting frame should be modelled with the properties of the skin.

5.2 EXTRAP II

Description

EXTRAP II is an alternate prediction technique. EXTRAP II is recommended over EXTRAP I when accurate predictions in the low frequency regime are required. EXTRAP II requires a high degree of dynamic similarity between the previously tested configuration and the new configuration.

Prediction Model–EXTRAP II accesses the same parameter table as EXTRAP I. Thus, it is possible to use the same model for both prediction techniques. However, whereas EXTRAP I allows any of the five SEA elements to be designated as response elements, EXTRAP II will allow elements 2 or 5 as response elements.

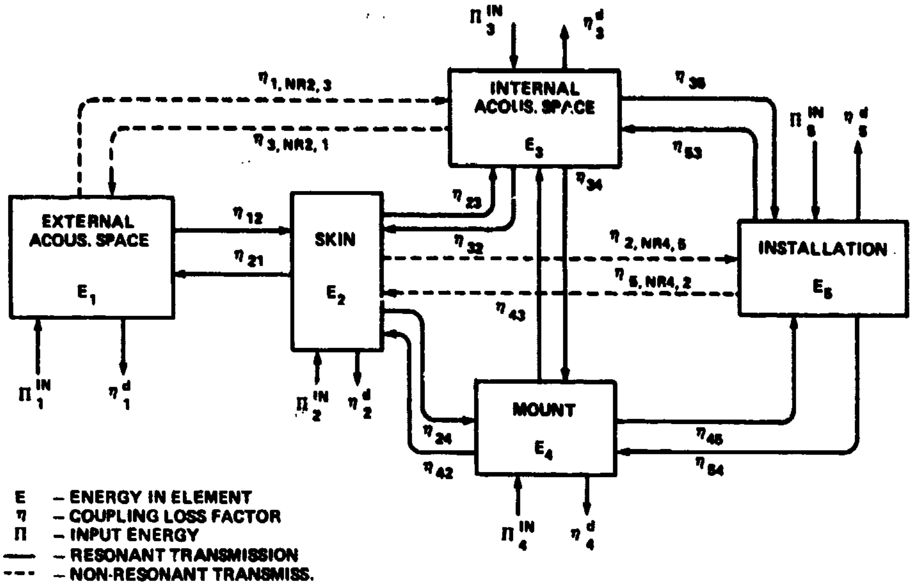

Fig. 5 – Mathematical (SEA) Model of Prediction Procedure

BASIC MATRIX EQUATION

$$\{E\} = [C]^{-1}\{\Pi^{IN}/\omega\}$$

where

C = $C(\eta_{ij})$

η_{ij} = Coupling loss factor from element i to element j

E_i = Energy of element i

Π_i^{IN} = Input power to element i

ω = Radian frequency

EXPANDED MATRIX EQUATION

$$\begin{bmatrix} \eta_{1t} & -\eta_{21} & -\eta_{3,NR2,1} & 0 & 0 \\ -\eta_{12} & \eta_{2t} & -\eta_{32} & -\eta_{42} & -\eta_{5,NR4,2} \\ -\eta_{1,NR2,3} & -\eta_{23} & \eta_{3t} & -\eta_{43} & -\eta_{53} \\ 0 & -\eta_{24} & -\eta_{34} & \eta_{4t} & -\eta_{54} \\ 0 & -\eta_{2,NR4,5} & -\eta_{35} & -\eta_{45} & \eta_{5t} \end{bmatrix} \begin{Bmatrix} E_1 \\ E_2 \\ E_3 \\ E_4 \\ E_5 \end{Bmatrix} = \begin{Bmatrix} \Pi_1^{IN}/\omega \\ \Pi_2^{IN}/\omega \\ \Pi_3^{IN}/\omega \\ \Pi_4^{IN}/\omega \\ \Pi_5^{IN}/\omega \end{Bmatrix}$$

where

$$\eta_{1t} = \eta_{12} + \eta_{1,NR2,3} + \eta_1^d$$

$$\eta_{2t} = \eta_{21} + \eta_{23} + \eta_{24} + \eta_{2,NR4,5} + \eta_2^d$$

$$\eta_{3t} = \eta_{32} + \eta_{34} + \eta_{35} + \eta_{3,NR2,1} + \eta_3^d$$

$$\eta_{4t} = \eta_{42} + \eta_{43} + \eta_{45} + \eta_4^d$$

$$\eta_{5t} = \eta_{53} + \eta_{54} + \eta_{5,NR4,2} + \eta_5^d$$

Fig. 6 – Matrix Evaluation – SEA

Response Scaling Function–The technique employed consists of scaling the response of the old system to obtain the response of the new systems. The scaling is accomplished as follows:

$$Rn(f) = Ro(f) \times Cm \times Cm1 \times Cd \times Ce(f) \qquad (4)$$

where

Rn(f) = Response spectrum of the new system.

Ro(f) = Response spectrum of the old system.

Cm = Mass density correction, defined as

$$\left(\frac{\text{ROWSold}}{\text{ROWSnew}}\right)^2 \qquad (5)$$

Cm1 = Mass loading correction, defined as

$$\left(\frac{\text{ROW} \times \text{H} \times \text{AP}}{\text{ROW} \times \text{H} \times \text{AP} + \text{NSMS}}\right)_{\text{new}} \times \left(\frac{\text{ROW} \times \text{H} \times \text{AP} + \text{NSMS}}{\text{ROW} \times \text{H} \times \text{AP}}\right)_{\text{old}} \qquad (6)$$

Cd = Damping correction defined as

$$\left(\frac{\text{DLF}}{\text{DLF}}\right)\begin{matrix}\text{old}\\\text{new}\end{matrix} \qquad (7)$$

Ce(f) = Excitation correction, defined as

$$\left(\frac{\text{EXCITATION (f)}}{\text{EXCITATION (f)}}\right)\begin{matrix}\text{new}\\\text{old}\end{matrix} \qquad (8)$$

The frequencies are also corrected as follows:

$$\text{fnew} = \left(\frac{\text{AP old}}{\text{AP new}}\right)^{1/2} \times \text{fold} \qquad (9)$$

The corrected data are reorganized into standard 1/3-octave bands based on the corrected frequency values.

Extrapolation–The response scaling function equation (4) and the correction factors equations (5)–(9) are processed by the execution of a single VAPEPS command called SCALE. Detailed description of this command and the required input parameters are presented in reference 2.

5.3 Probabilistic Consideration

The results produced by the VAPEPS prediction procedure (EXTRAP I/II) in some cases should not be used in a deterministic way. For example, one cannot interrogate the data base, obtain data from one payload component location, make a prediction using this data and expect to find very good agreement with data obtained from a measurement made during another acoustic test of a payload component with the same classification as the payload component being used from the data base. Structural parameters can vary significantly among payloads components classified as being the same or in fact are the same with respect to having been constructed against the same requirements. Predictions should be treated in a probabilistic manner and the usefulness of these predictions will depend on the size of the data base used. The implementation of probabilistic prediction methods in VAPEPS can be accomplished by forming command packets via the use of the extensive data processing capability of VAPEPS.

In general probabilistic prediction methods should be developed to be compatible with prediction models implemented in EXTRAP I/II. Probabilistic models based on the five element SEA model approach of EXTRAP I and on the response scaling approach of EXTRAP II need to be investigated. The extent to which these probabilistic models can be implemented in VAPEPS will require additional studies.

6.0 VAPEPS VALIDATION

The requirements for validating VAPEPS are characterized as two major types:

- Software Validation
- Prediction Capability

Software Validation

Software validation is defined as tasks specifically performed to evaluate the individual performance of each VAPEPS processor ENTER, PREP, SEARCH and EXTRAP procedure, and to evaluate the performance of the VAPEPS processors operating in an end-to-end system configuration. Each VAPEPS processor, or procedure, is being evaluated and demonstrated via the extensive use of sample problems which will also be included in the VAPEPS documentation. The interfacing aspects of the processors for an end-to-end VAPEPS system application are also being evaluated and demonstrated on sample problems to show relationship and significance of execution.

Prediction Capability

The capability of VAPEPS EXTRAP procedures to predict vibroacoustic results for new configurations is being evaluated by means of demonstration problems. This is accomplished by using one of the event in the data base as a referenced event, walking the user through ENTER, PREP and SEARCH, and with a configuration on which flight or ground test data is available, predict the results via EXTRAP and correlate the results with the measured data.

The above two types of validation based on demonstration problems will be sufficient for validating the VAPEPS system and provide the level of confidence needed by potential users.

7.0 CONCLUDING REMARKS

The discussion presented in the preceding sections has outlined the development of a data base management and prediction system for payload vibroacoustic environments. The development has included the creation of an initial data base summary data bank based on past vibroacoustic flight and ground test data and the development of computer softwares required for efficient data entry, identification, interrogation and retrieval. Included is a prediction procedure specifically designed to establish the vibroacoustic environment of new payloads using data obtained from similar design that had been previously flown or ground tested. Although the overall data base management and prediction system is not yet in its final and complete version, and its validation has not been fully completed, it is apparent that the herein discussed approach used in the development effort has resulted in a prediction procedure which can be expected to give reliable estimates of payload vibroacoustic environmental levels. Furthermore, the VAPEPS data base management and prediction system can be used to serve the unique requirements of a local site or it can be configured to serve many sites. When shared by a community of users, it provides for a single uniform, consistent and organized data base which can be used in a cost effective manner to establish the vibroacoustic environment of payload components for either Space Shuttle or expendable booster missions.

ACKNOWLEDGMENTS

The majority of the work described in this paper was performed by Lockheed Missiles and Space Company (LMSC) under NASA Goddard Space Flight Center Contract NAS5-25156. As might be expected, the technical success of the program resulted from contributions made by numerous people. The authors wish to acknowledge, in particular, the significant contributions made by Mr. Joseph P. Young and Ms. Marjorie Johns at the GSFC, and Dr. Albert Lee, Dr. Dave Crowe, Mr. J. Schafer and Mr. B. Davis at LMSC. Finally, acknowledgment is made of the support provided by NASA Headquarters Office of Aeronautical/ Space Technology (OAST).

REFERENCES

1. Statistical Energy Analysis of Dynamical System: Theory and Applications, R. H. Lyon, MIT Press.

2. Vibroacoustic Data Management System and Prediction Procedure for Shuttle Payload Components, LMSC Report (to be published), Lockheed Missiles and Space Co., W. Henricks et al.

AUTOMATION OF VIBROACOUSTIC DATA BANK
FOR RANDOM VIBRATION CRITERIA DEVELOPMENT

Robin C. Ferebee
Marshall Space Flight Center
Huntsville, Alabama

A computerized data bank system has been developed for utilization of large amounts of vibration and acoustic data to formulate component random vibration design and test criteria. This system consists of a computer, graphics tablet, and a dry-silver hard copier which are all desk-top type hardware and occupy minimal space. Currently, the data bank contains data from the Saturn V and Titan III flight and static test programs. The vibration and acoustic data are stored in the form of power spectral density and one-third octave band plots over the frequency range from 20 to 2000 Hz. The data was stored by digitizing each spectral plot by tracing with the graphics tablet. The digitized data was statistically analyzed and the resulting 97.5% probability levels were stored on tape along with the appropriate structural parameters. Standard extrapolation procedures were programmed for prediction of component random vibration test criteria for new launch vehicle and payload configurations. This automated vibroacoustic data bank system greatly enhances the speed and accuracy of formulating vibration test criteria. In the future, the data bank will be expanded to include all data acquired from the Space Shuttle flight test program.

INTRODUCTION

The engine generated acoustic and aerodynamic fluctuating pressure environments produced by space launch vehicles create substantial vibratory motion of the vehicle structure. The prediction of these vibration environments is critical for the success of the missions. The broadband response characteristics of the complex vehicle structures preclude established analytical methods of prediction, so an extrapolation method based on past space vehicle test programs was developed (1). This method relies on an established scaling technique to predict the new structure's response. Because of the large and rapidly growing data base and the voluminous amount of criteria required to support Space Shuttle launches, an automated method was needed to speed up the prediction process. A computer system was developed that stores the data base and scales the data to predict and formulate new component design and test criteria.

SCALING TECHNIQUE

Vibration response prediction using data banks is based on the principle of dynamic similarity. An acoustic or fluctuating pressure field impinging on a vehicle's skin will produce a vibration response that can be extrapolated from past vehicles that had similar structures. The scaling is based on the following equation:

$$G_N(f) = G_R(f) \left[\frac{P_N(f)}{P_R(f)}\right]^2 \left[\frac{W_R}{W_N}\right]^2 \qquad (1)$$

where: $G_N(f)$ = the predicted response of the new vehicle structure as a function of frequency, in g^2/Hz

$G_R(f)$ = the data bank (reference) vibration response, in g^2/Hz

$P_N(f)$ = the new acoustic forcing function

$P_R(f)$ = the reference acoustic forcing function

W_R = the surface weight of the reference structure

W_N = the surface weight of the new structure

For the convenience of storing only one acoustic spectrum per file, all acoustic data was normalized to an arbitrary acoustic spectrum, Fig. 1, according to the following equation:

$$G_R(f) = G_M(f) \left[\frac{P_R(f)}{P_M(f)}\right]^2 \qquad (2)$$

where the subscript M refers to measured data.

To account for the alteration in response caused by mounting a component to the primary structure, the following correction factor can be applied to the equation (2):

$$\frac{W_N}{W_N + W_C}$$

where: W_N = weight of new structure

W_C = weight of component

Equation 1 now becomes:

$$G_N(f) = G_R(f) \left[\frac{P_N(f)}{P_R(f)}\right]^2 \left[\frac{W_R}{W_N}\right]^2 \frac{W_N}{W_N + W_C} \qquad (1A)$$

Currently, the data bank contains vibration and acoustic spectra from several Saturn V flight and static tests and from the Titan III flight program. These spectra are in the form of 97.5% confidence level frequency plots from 20 to 2000 Hz in 5 Hz increments. The 97.5% confidence level was chosen since it provides a reasonable degree of certainty without being overconservative. The vibration data is in power spectral density form while the acoustic data is in one-third octave band spectra. Several identifying parameters are stored along with each spectrum. In the future, the data bank will contain data from the Space Shuttle program.

The data was categorized according to the type of structure, i.e., ring frame, skin, skin-stringer, and honeycomb. Graphite-epoxy composite structure will be available from the Space Shuttle. The data was further subgrouped according to specific structural parameters such as the size of the ring frame or the thickness of the skin

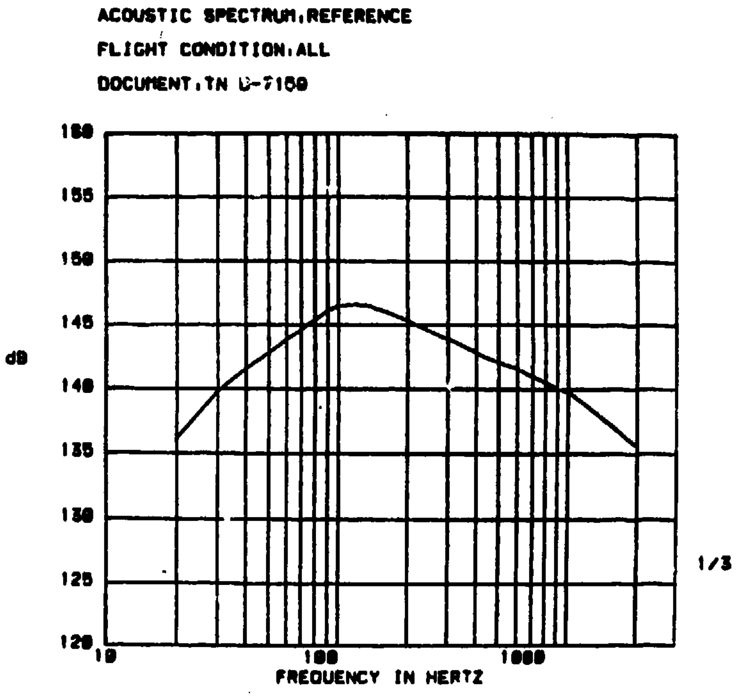

Fig. 1 - Reference Acoustic Function

or the weight of the stringers. Generally, measurements in three directions were available: longitudinal (along the vehicle's axis), radial (perpendicular to the skin), and tangential (along the vehicle's roll axis).

THE COMPUTER SYSTEM

The computer system is based on a Tektronix 4052 computer with 64K bytes of memory and peripheral equipment as shown in Fig. 2. Data is entered into the system using a Tektronix 4956 graphics tablet and cursor. The data is stored on the computer's internal tape cassette or on an optional Tektronix 4907 floppy disk. A Tektronix 4631 dry-silver copier provides a permanent hard copy of all criteria. Total system cost is about $25,000 and all items are easily available.

Data is entered into the system by placing a spectrum on the 4956 tablet and tracing the curve. The tablet digitizes the spectrum and the computer interpolates at 5 Hz increments. Each spectrum is held in memory until the measurements from all flights are stored. From three to eight spectra can be held in memory at one time. The computer then calculates the 97.5% confidence level of the data and stores this spectrum on the tape. Next, the acoustic spectra that correspond to the vibration measurements are digitized and their confidence level is computed. This spectrum is also stored on tape. These two confidence level spectra are then normalized to the reference acoustic spectrum in Fig. 1 and the result is stored on a permanent tape file. Several identifying parameters are stored with the spectrum and some of these parameters are stored on a directory file at the beginning of the tape to provide a quick reference. Up to 63 spectra can be stored on one tape, and approximately twice that number can be stored on a floppy disk. The data bank presently contains 98 skin, skin-stringer, and ring frame vibration spectra. Figs. 3 and 4 show typical vibration and acoustic spectra. The numbers on the right side of the plot are a tape identification number and the file number on the tape.

Once the data has been stored on the tape, the user can access any spectrum for use in deriving vibration criteria. The first step in this process is to review the tape file directories and choose a data bank structure that matches the new structure as closely as possible. Next, a backup area must be chosen and

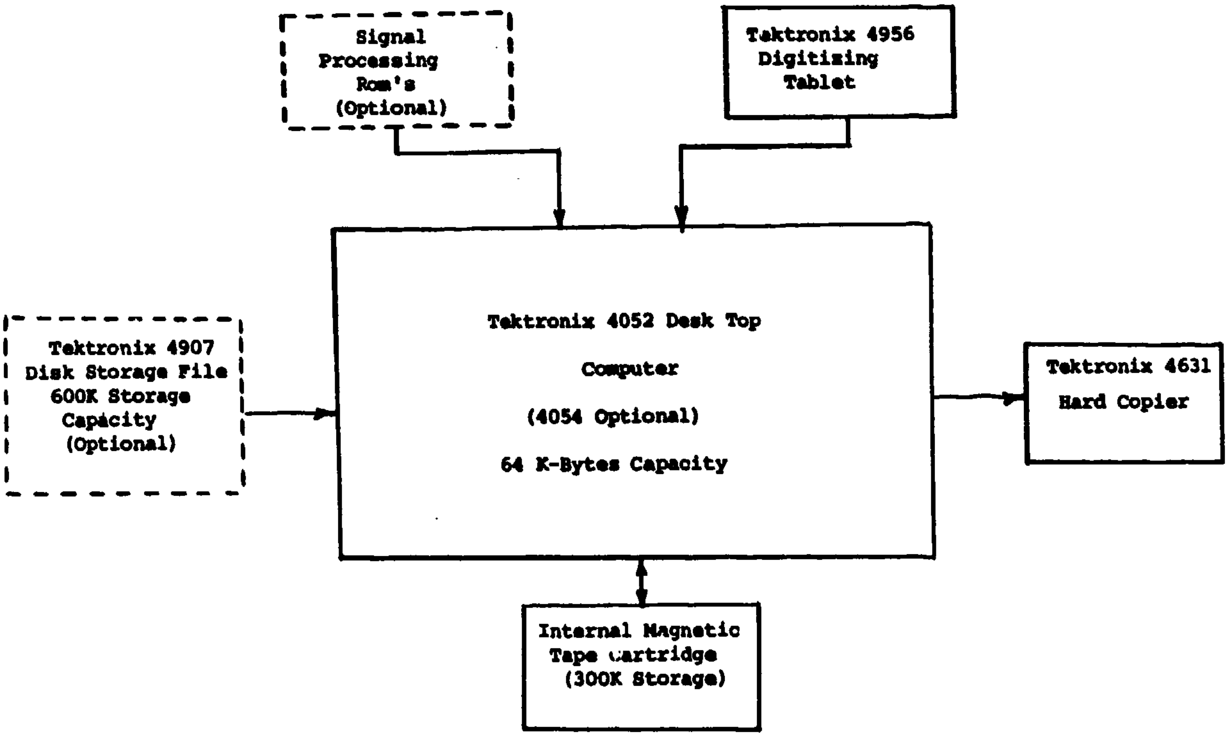

Fig. 2 - Vibroacoustic Data Bank Schematic

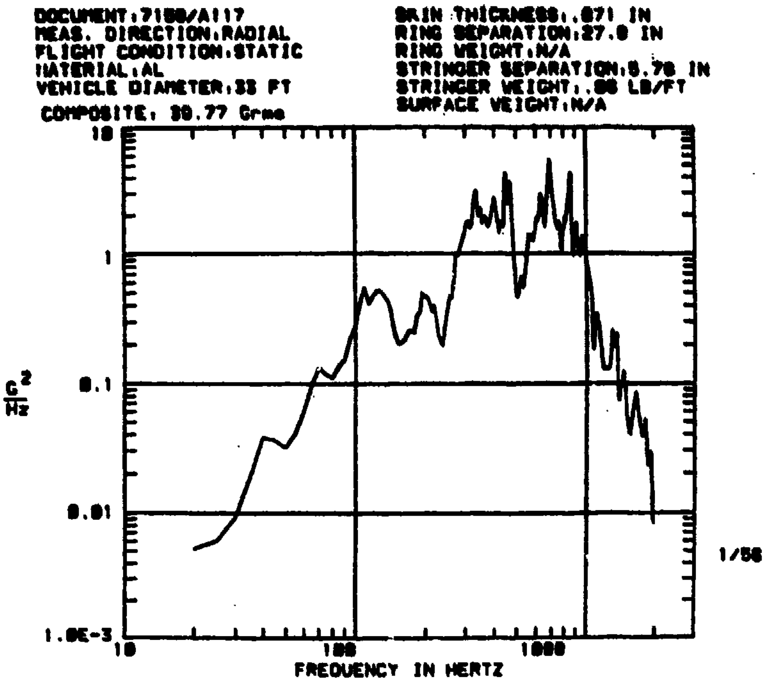

Fig. 3 - Vibration Spectrum

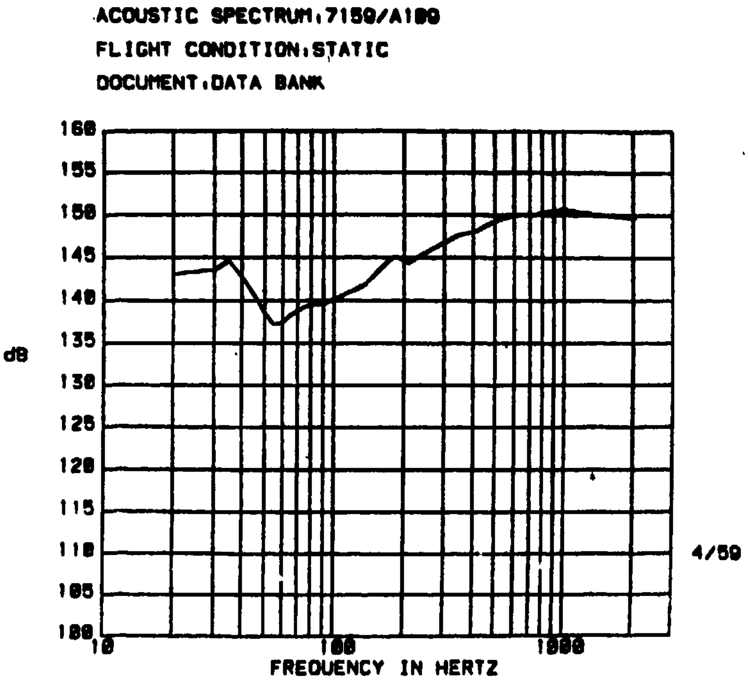

Fig. 4 - Acoustic Spectrum

the structural weight calculated. This is done by adding the weights of the skin, stringers, and rings over the backup area. The backup area should be large enough to encompass any components that may be mounted to the structure. The component weight must also be known.

There are two ways of storing the new acoustic spectrum on a tape file: using the graphic tablet or by hand. If the spectrum is given in the form of a semi-log plot, the tablet can be used to digitize the information and store it on tape. Often, the spectrum is in the form of a specification and just the values at the one-third octave frequencies are given. In this case, the numbers can be entered on the computer keyboard and stored on the tape. All acoustic spectra should be in one-third octave band values.

The program is accessed by reading the program into memory from a tape. Once it is running, the program prompts for the needed information: the file numbers of the reference vibration spectrum, reference acoustic spectrum, new acoustic spectrum, and the component weight, if any. The scaled vibration spectrum is then plotted, allowing for structural parameters to be typed at the top of the page.

The criteria can then be drawn over the spectrum by manipulating the cursor using five user definable keys. When the criteria lines are drawn, another key is pressed and a table of criteria values and slopes are printed. Figs. 5 and 6 show the predicted vibration spectrum with the criteria and the criteria table. Figure 5 contains enough information to reproduce the spectrum if the need arises. The flow chart in Fig. 7 shows the criteria derivation process.

This system takes the burden of repetitive calculation off of the engineer and allows him to concentrate on choosing an appropriate reference structure and refining the final criteria. It takes approximately two to three minutes to derive a criteria once the parameters are chosen. This represents a tremendous productivity increase with increased accuracy and reliability. It is estimated that this system speeds up the criteria derivation process by two to five times at a very modest hardware cost. With the cost of manpower increasing and the cost of computer systems decreasing, this computerized data bank represents a substantial savings to the government and industry.

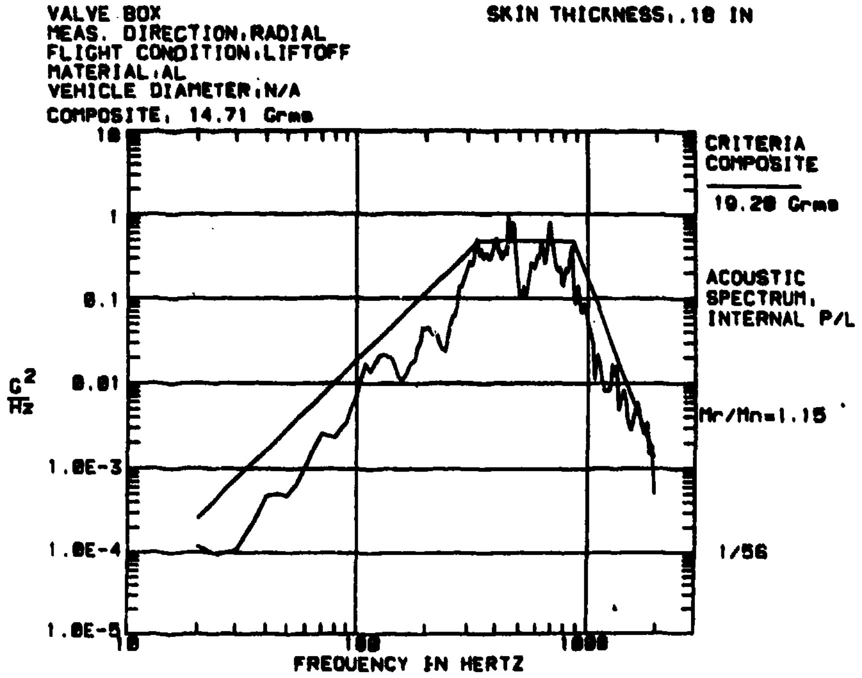

Fig. 5 - Scaled Vibration Spectrum with Criteria

```
IR TELESCOPE VALVE BOX VIBRATION CRITERIA

RADIAL AXIS

        20 Hz @   0.00026 g2/Hz
    20- 340 Hz @  +8.0 dB/oct
   340- 880 Hz @   0.47500 g2/Hz
   880-2000 Hz @ -21.5 dB/oct
      2000 Hz @   0.00136 g2/Hz
 ______________________________
 COMPOSITE = 19.20 Grms
```

Fig. 6 - Criteria Table

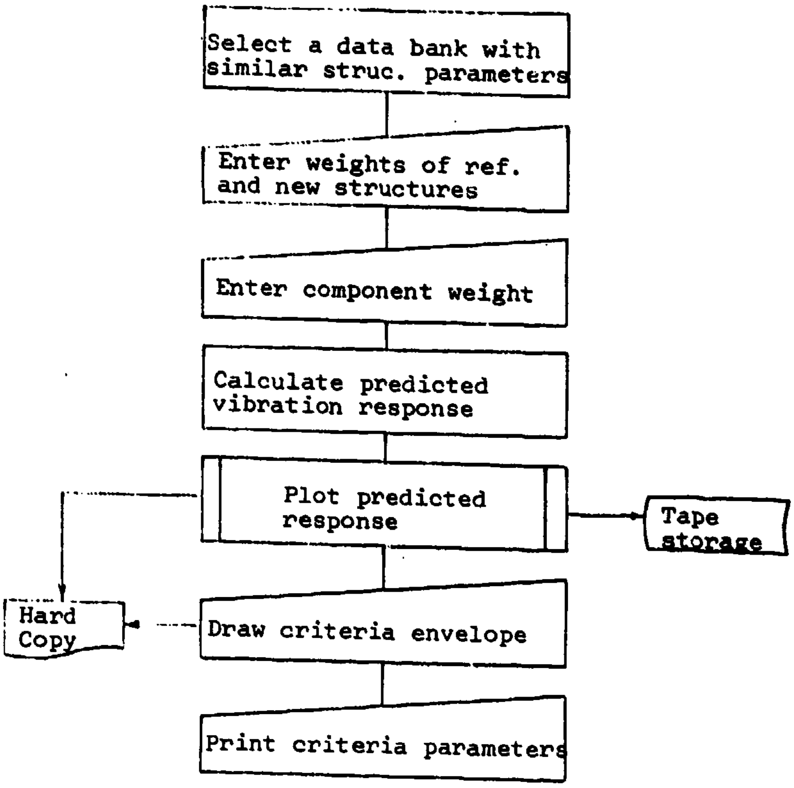

Fig. 7 - Criteria Derivation Process

REFERENCES

1. Bandgren, Harry J. and Smith, William C., "Development and Application of Vibroacoustic Structural Data Banks in Predicting Vibration Design and Test Criteria for Rocket Vehicle Structures," NASA Rept. TN D-7159, February 1973

2. Barrett, Robert E., "Techniques for Predicting Localized Vibratory Environments of Rocket Vehicles," NASA Rept. TN D-1836

THE DEVELOPMENT AND VERIFICATION OF SHUTTLE ORBITER RANDOM VIBRATION TEST REQUIREMENTS

M. C. Coody
NASA Johnson Space Center
Houston, Texas

H. K. Pratt
Rockwell International Corporation
Downey, California

and

D. E. Newbrough
Management and Technical Services Corporation
Houston, Texas

The unique Space Shuttle vehicle size, weight, and configuration have given rise to problems in determining vibration requirements and in verifying structural integrity for anticipated mission environments. The application of large-scale vibration testing has played a prominent part in qualifying the Shuttle for its intended missions.

Severe vibration excitation from rocket engines, aerodynamic noise, and onboard equipment are expected on each Shuttle flight. Scale-model wind tunnel and rocket firing tests, as well as full-size rocket engine tests were relied on to define the random forcing functions. The determination of structural response to these environments is described herein, as well as evaluations of measured flight data and comparison with predicted design and test criteria.

INTRODUCTION

The Space Shuttle, shown in Figure 1, presented new difficulties in predicting aeroacoustic environments and vibration responses. These difficulties became accentuated due to the severity of the environments when, at the beginning of the program, it was recognized that severe acoustic levels would be applied to the Orbiter at lift-off, due to the close proximity to rocket engines, and that severe aerodynamic noise would be applied to several Orbiter locations during the ascent phase of flight, figures 2 and 3.

The difficulty in predicting the acoustic environment at lift-off was due to the proximity and separation of the rocket engines, the complexity of the two launch pads used at the NASA Kennedy Space Center and at the USAF Vandenberg AFB, and the changes of the rocket exhaust flows with vehicle distance above the launch pad. These difficulties were eventually overcome by evaluation of data from a 6.4% scale-model engine/launch pad test program performed at the NASA Marshall Space Flight Center.

The difficulty in predicting the aerodynamic noise environment during ascent was due to the many changes in vehicle cross-section as a function of vehicle length, the

Fig. 1 - Space Shuttle configuration

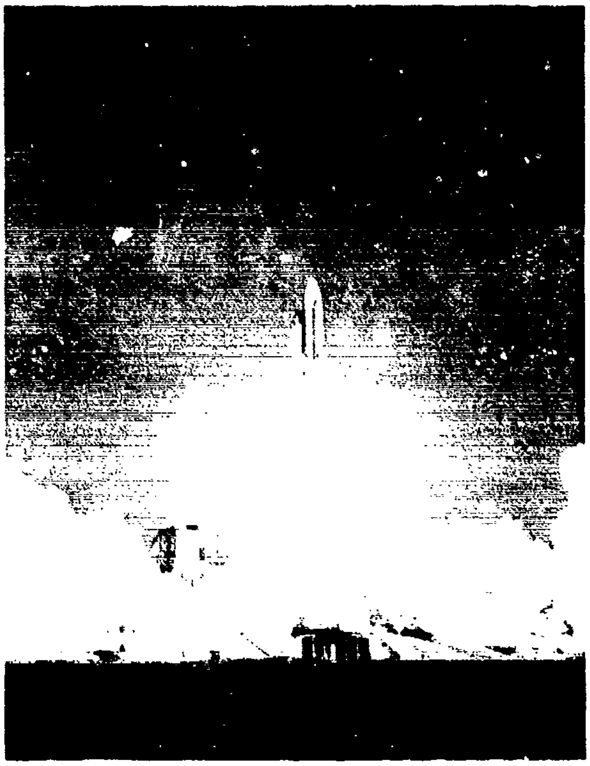

Fig. 2 - Space Shuttle STS-1 liftoff

Fig. 3 - Space Shuttle STS-1 launch

three dimensional nature of the many flow disturbances, the complexity of the large flow interference region between the Orbiter, External Tank (ET), and Solid Rocket Boosters (SRB's), and in some cases the dependence on vehicle attitude. These difficulties were overcome with analysis of data from a 3.5% scale-model Shuttle vehicle wind tunnel test program performed at the NASA Ames Research Center. Once the noise fields were defined, then other procedures as outlined in references 1, 2, and 10 could be used to predict the noise-induced vibration response of the structure and to develop design and test criteria for the many items of equipment.

Shuttle Vehicle and Launch Complex Configuration

Three Shuttle orbiter main engines (SSME) and two solid rocket boosters (SRB's) fire in parallel during lift-off, figure 2. The Orbiter's main engines produce approximately 1.5 million pounds thrust and the two SRB's approximately 5.5 million pounds thrust. This new thrust configuration required extensive redesign of previous Saturn and Titan launch pad configurations.

The Eastern Test Range launch complex, figure 4, is the modified launch complex 39 Saturn V facilities. The flame trench and deflector have been modified to accommodate the

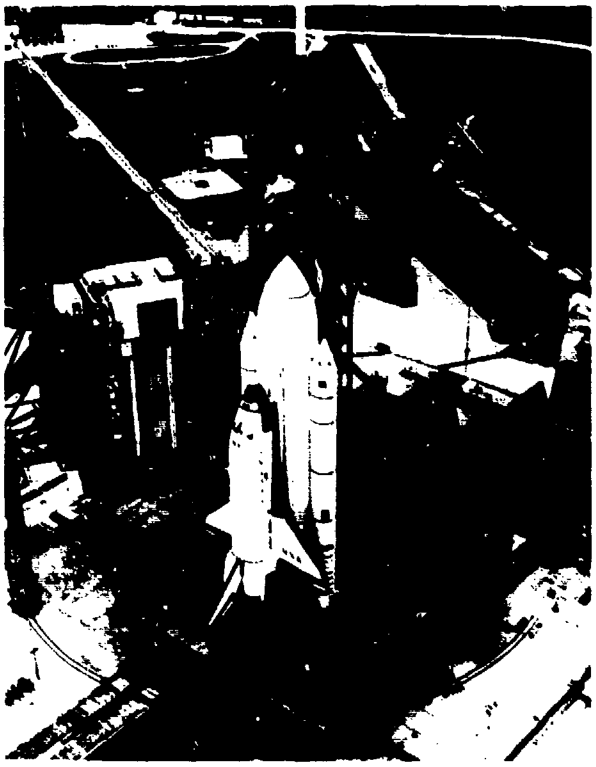

Fig. 4 - Space Shuttle Eastern Test Range launch complex

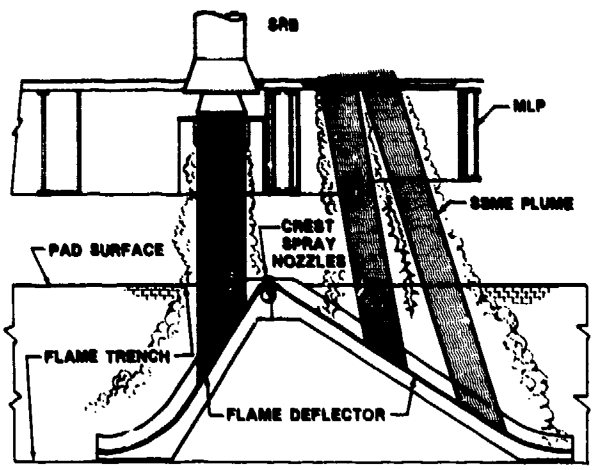

Fig. 5 - Shuttle flame trench, deflector, MLP and engine flame trajectories

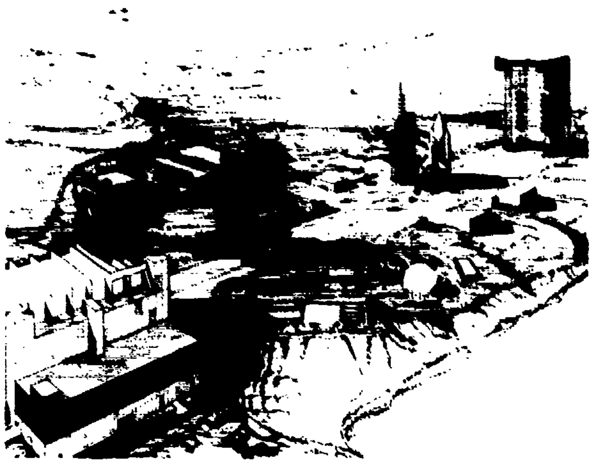

Fig. 6 - Space Shuttle Western Test Range launch complex

Shuttle separated rocket exhaust flow, figure 5. Because of sidewise drift at lift-off due to SSME thrust offset from vertical, the mobile launch platform (MLP) SRB exhaust holes were increased in length to minimize low elevation SRB hot core impingement on the MLP. The Western Test Range launch facilities are the modified Titan III SLC-6 complex, figure 6. Here the flame trenches are covered and separated for each Shuttle element rocket exhaust.

Shuttle Acoustic Environments

The most prominent sources of acoustic excitation occur at Shuttle engines ignition and lift-off and during ascent aerodynamic flight. It is well documented how liquid and solid propelled rocket engine noise is produced in the mixing region between the surrounding atmosphere and the exhaust core high-velocity regions. Deflected or obstructed rocket exhausts cause higher acoustic loadings than exhausts that flow freely from the Shuttle. Noise levels diminish with elevation above the ground reflecting plane and become insignificant above elevations approximately 24 SRB nozzle diameters. Aerodynamic fluctuating pressure levels start becoming prominent at higher altitudes and vehicle speeds. Fluctuating pressures on vehicle surfaces, due to boundary layer turbulence, vary in relation to free stream dynamic pressure q. Various combinations of Mach number, vehicle attitude, and the Shuttle configuration effects on boundary layer flow are the cause of maximum aeronoise. The Mach 1 and maximum q flight regions generally produce the most intense aerodynamic fluctuating pressure levels.

Definition of Acoustic Environments

Lift-off

The techniques listed herein for predicting maximum external lift-off noise involves extrapolations of noise data measured on 6.4 percent models of the Shuttle vehicle and launch pad. Reference 3 states the rationale whereby geometrically similar models with rocket engines exhibiting dynamically similar characteristics can be used to predict rocket noise spectra for larger systems. No adjustments for sound pressure levels are required, and only the frequencies need be adjusted by the non-dimensional parameter known as Strouhal number.

$$S = \frac{f\,De}{V} = \text{Strouhal number,}$$

where: f = frequency
De = system effective nozzle diameter
V = exhaust exit velocity

Reference 4 provides one of the many available references on Strouhal scaling.

More than 250 tests with various combinations of liquid engines, solid rocket motors, elevations above the pad, and several configurations of water injection were conducted. Scale model launch pad configurations for both the Eastern and Western Test Ranges were used.

Early tests of the 6.4% model with model launch pads produced data that indicated excessive noise levels were going to be imposed on Shuttle structure and payloads. Because of design cost impacts to develop the Shuttle to withstand these intense environments, it was decided early in the program to begin state-of-the-art development of rocket noise suppression techniques. The most promising concept was to inject large volumes of water into the flame trenches, figure 7, reference 5.

The optimum noise suppression system was selected from the 6.4% model test data. Acoustic spectra from the selected suppression system were compiled and an envelope defined to equal or exceed all levels. The acoustic data accounted for flight elevations from on pad to 24 solid rocket motor nozzle diameters, or approximately 280 feet above the pad. External Orbiter acoustic spectra, measured during model firings at nine elevations, were adjusted by Strouhal scaling for full-scale Shuttle frequencies and a typical composite as shown in figure 8. It can be seen that noise levels vary 4 to 5 dB at low frequencies and as much as 20 dB at high frequencies. Envelopes were constructed to cover all levels for all model measurements. Therefore, at any instant of time during launch, the envelope levels will be achieved at a few frequencies only. The model data indicate that the envelope levels will never occur at all frequencies simultaneously during launch. Acoustic tests using the envelope spectra as test criteria for the total launch time are conservative, the amount of conservatism varies with each frequency.

To evaluate the internal payload bay noise levels, Orbiter 101 was subjected to jet engine noise acoustic tests at NASA Dryden Flight Research Center. Acoustic measurements were taken inside the payload bay and on the exterior of the sidewalls, bottom and payload bay doors. Reference 6 provides the detail discussions of analyses and test conditions.

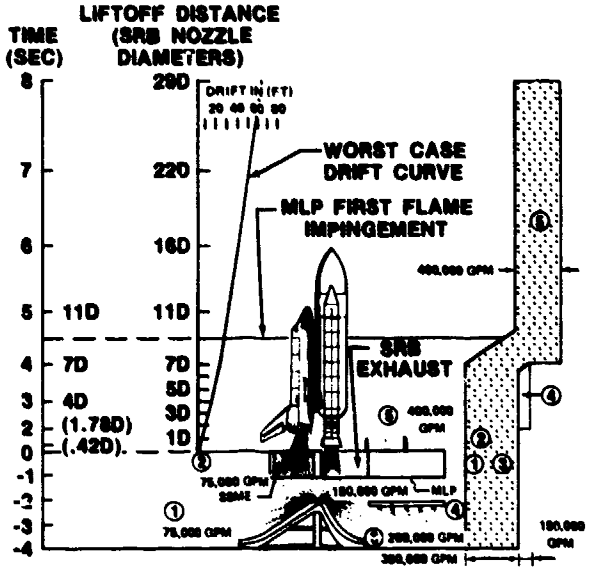

Fig. 7 - Pad sound supression scheme plot of flow/drift versus time

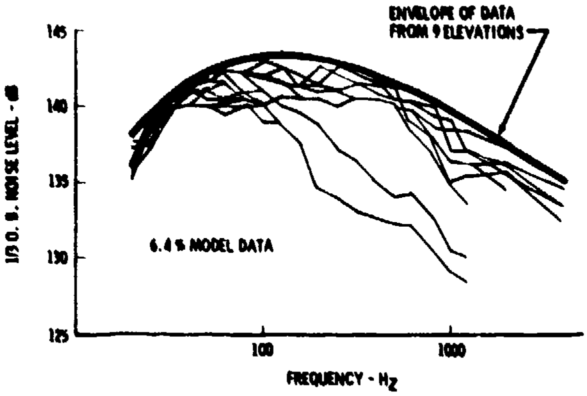

Fig. 8 - Acoustic spectra typical 6.4% composite and envelope

This test phase provided the data to determine transmission loss and noise reduction values for the Orbiter structure.

The present estimates of internal payload bay noise for an empty bay resulted from combining the 6.4% model data with the OV-101 test analysis results. Later in the program, acoustic tests of payload bay door sections were conducted. These test sections provided Orbiter 102 payload door and radiator noise reduction values for use in further refinement of the bay acoustic levels.

A final check of the modeling techniques used herein was accomplished when rocket firing acoustic data were measured on full size SRB's, figure 9, and on the Main Propulsion Test Article SSME, figure 10. These full size tests provided the first check of the 6.4% model as a valid prediction tool. It was observed that the 6.4% model was generally conservative, references 7 and 8.

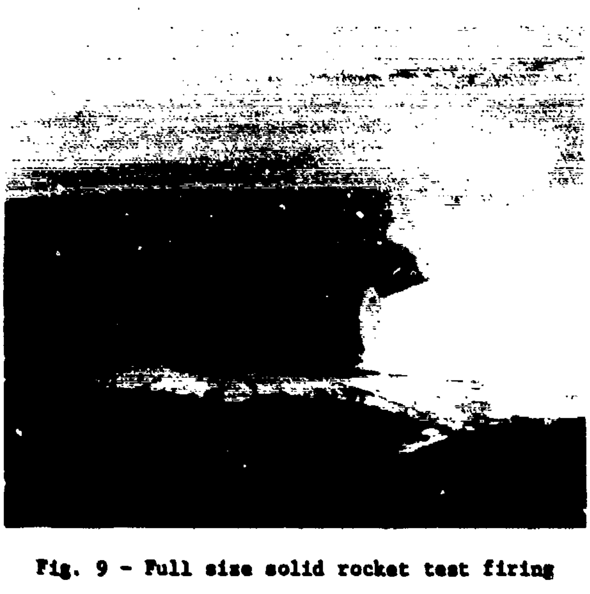

Fig. 9 - Full size solid rocket test firing

Fig. 10 - Space Shuttle full scale main engine firings

Aeronoise

Considering the complex Shuttle aerodynamic configuration, it is generally recognized that analyses of the Shuttle fluctuating pressure environments are difficult. Therefore, several scale model wind tunnel tests were used to assist in flow field analysis and to provide Shuttle aeronoise data. These tests are covered in detail in several other papers, reference 9. The most significant test to provide data for aeronoise prediction was from a detailed 3.5% rigid model, figure 11 - with 237 pressure measurement locations. These tests were performed at NASA-Ames Research Center with Mach numbers ranging from 0.6 to 3.5 and pitch and yaw angles throughout the ranges of -5° to +5°. Adjustments were made to the measured data for differences in wind tunnel q (psf) and actual expected flight q profiles.

Fig. 11 - Space Shuttle 3.5% wind tunnel model

These tests provided several thousand geometrically scaled pressure level spectra. Data were compiled into zones established as areas of the Shuttle with definable structural boundaries or by differences in localized aerodynamic flow, figures 12 and 13. For each zone, the spectra were separated into data associated with Shuttle nominal flight trajectories and data at all attitude combinations from nominal to maximum pitch and yaw. Spectra from all measurements in a particular zone were grouped in a composite and an envelope was constructed to obtain the final zone nominal and dispersed maximum environments. Typical overall time history levels and cor-

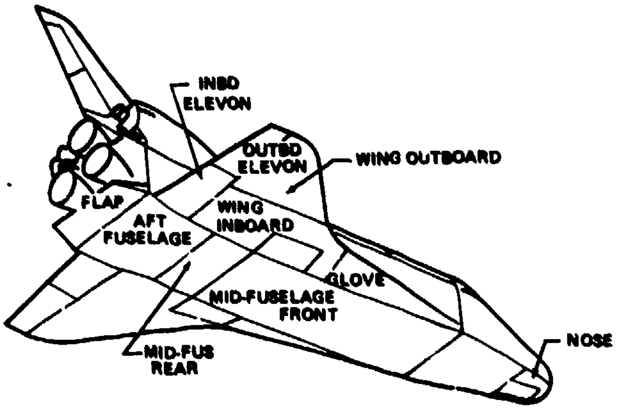

Fig. 12 - Aeroacoustic noise zones of the Shuttle Orbiter - bottom

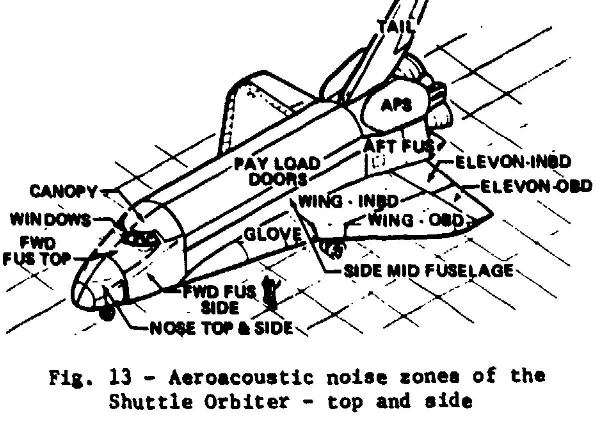

Fig. 13 - Aeroacoustic noise zones of the Shuttle Orbiter - top and side

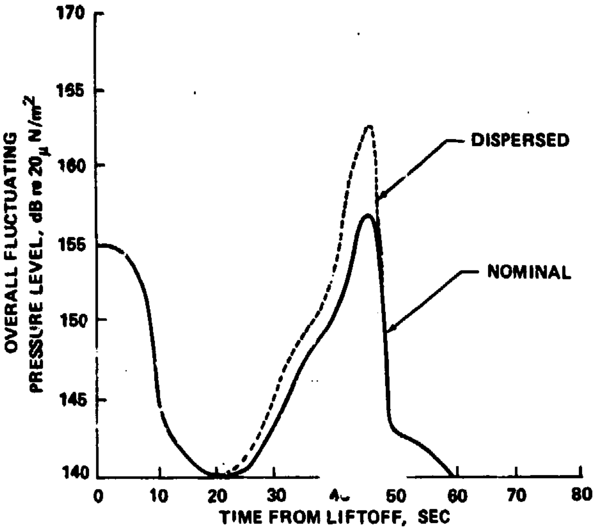

Fig. 14 - Acoustic levels. Typical overall time history

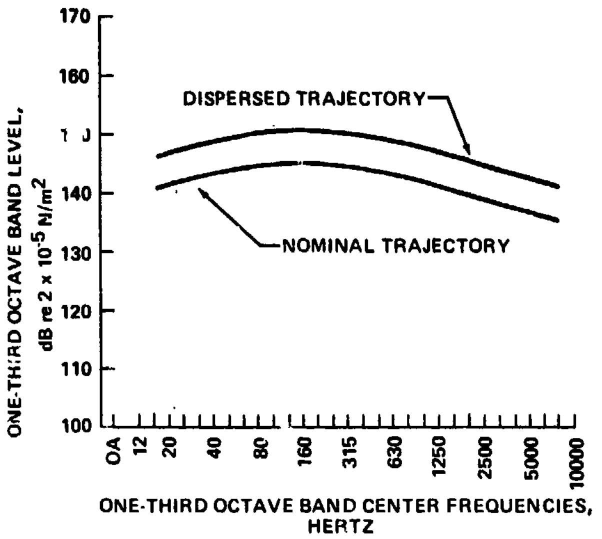

Fig. 15 - Acoustic spectra

responding maximum aeronoise spectra are shown in figures 14 and 15. As was the situation for the lift-off model data, these envelope techniques provide conservatism in design and test criteria development. The maximum levels on various measurements in a zone do not occur at the same Mach numbers and vehicle attitude. Nonetheless, the maximum levels of all measurements in a zone were combined regardless of the naturally excludable ascent flight events.

Orbiter Vibration Environments

Development of vibration design and test criteria was of prime importance to a successful program. The objective in developing the vibration criteria was to provide environments which ensure performance over the intended equipment life, but which will not be excessive and unnecessarily affect equipment cost, weight, or delivery schedule.

In order to maintain consistency in developing the Orbiter vibration environments, the following basic assumptions were established: (1) Orbiter vibration (except SSME engines and thrust structure) results from direct impingement of engine noise and aerodynamic noise during boost; (2) Orbiter structure response to noise will be similar to previous spacecraft structures; (3) Factors affecting vibration response will be noise spectra, vehicle surface density, curvature of surfaces, and type of structure; (4) Similar structures possess similar modal densities; (5) All types of noise sources are equally efficient in coupling with spacecraft structure; and (6) thermal protection system tiles provide only mass participation on the Orbiter exterior structure.

Various methods are available for developing vibration criteria: (a) classical random response analysis, (b) statistical energy analysis and (c) extrapolation techniques. The advantages and limitations of these methods are discussed in reference 10. It is recognized that other aerospace programs have used statistical analysis methods successfully for evaluation of reference vibration data. However, the extrapolation method, also, has been used on other programs and was selected for developing most of the Shuttle Orbiter vibration criteria primarily because it was quick to implement and because a large reference data base was available for extrapolation. Scaling methods were selected utilizing the Condos-Butler equation, which scales the random vibration spectra from a reference vehicle to a new vehicle with respect to the differences between the external acoustic spectra and the surface mass densities of the two vehicles. Here the external acoustic spectrum for the Orbiter was selected from the applicable aeroacoustic noise zone described previously and the surface mass density was calculated to apply to the structural area under consideration. The reference vehicle and its applicable region was selected on the basis of structural similarity between the new and reference vehicle installations. Because of the structural diversity of the Orbiter, five reference vehicles were chosen, Apollo Command Module, Apollo Service Module, Saturn S-IC Stage, Saturn S-II Stage, and the Titan III-C. These vehicles provided vibration response data measured during test that were ground acoustic (reverberant, progressive wave, and uncorrelated multiple duct progressive wave) static rocket firing launch engine noise and boost aerodynamic turbulence. Since basic assumption (5) indicates all acoustic sources are equally efficient, all reference

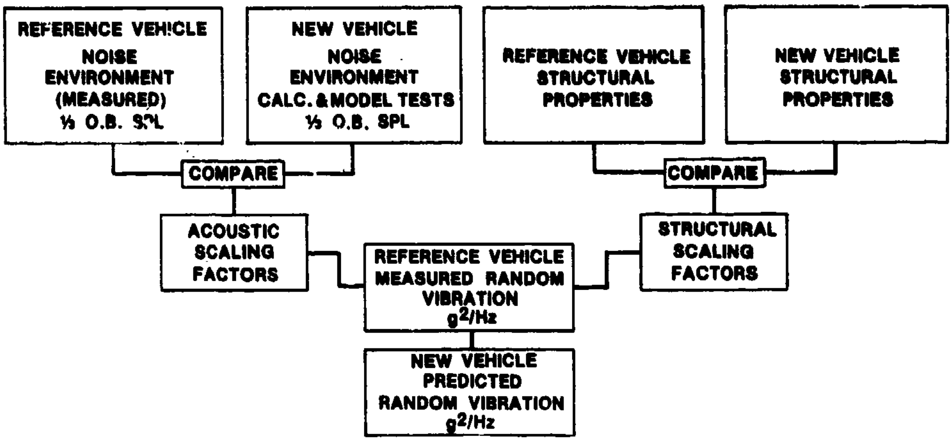

Fig. 16 - Random vibration criteria development

vehicle vibration response data were lumped together.

The procedure involved in vibration criteria development is simplistically illustrated in figure 16. Basically, the amplitude of vibration environment enveloped from the reference vehicle is adjusted based on the differences between the reference vehicle acoustic forcing function and those of the new vehicle and by the square of the ratio of the surface mass densities. In addition, the frequency of the resulting spectrum is adjusted by the ratio of the square root of the diameters of the reference vehicle and the new vehicle, where applicable. The first requirement in developing vibration criteria was to identify a reference configuration sufficiently similar to the new configuration and in some areas, multiple reference structures were used.

The two most complex areas to develop vibration environments were the Orbiter Crew Compartment and the bulkhead which separates the payload bay from aft fuselage, 1307 bulkhead. The Orbiter crew module vibration criteria development will be discussed as an example of the method employed for all extrapolation procedures. Since the orbiter crew compartment is a separate pressurized compartment suspended from the orbiter outer shell, the Apollo Command Module was selected as the reference structure. It was felt that the primary basis for similarity should be the loosely-coupled, double-hull construction with a high equipment density inner compartment and that the differences in shell materials were secondary. Due to vehicle symmetry, the Apollo Command Module was exposed to a relatively uniform aeroacoustic environment which had been duplicated in ground testing. However, the Orbiter external acoustic environments vary significantly over the outer surface, therefore, spatially averaged spectra were developed for the various lift-off and boost conditions. Definition of crew module shell vibration consisted of calculating a surface density scaling factor for the outer shells of the Apollo Command Module and the Orbiter outer shell (+5dB), and then calculating a surface density scaling factor for the pressure hulls of the Apollo Command Module and the Orbiter Crew Module (-7dB). These two factors establish a net surface density scaling factor (-2dB) to be combined with acoustic scaling factors for Shuttle lift-off, nominal boost trajectory and dispersed boost trajectory. A similar procedure was followed in developing the crew module equipment vibration criteria except the envelope of Apollo Command Module was used to obtain the differences in equipment installation density (+3dB). The equipment vibration criteria were sufficiently similar to the pressure hull criteria that a composite, figure 17, was adopted for the whole crew compartment. Although figure 17 shows separate vibration spectra for the lift-off, nominal boost and

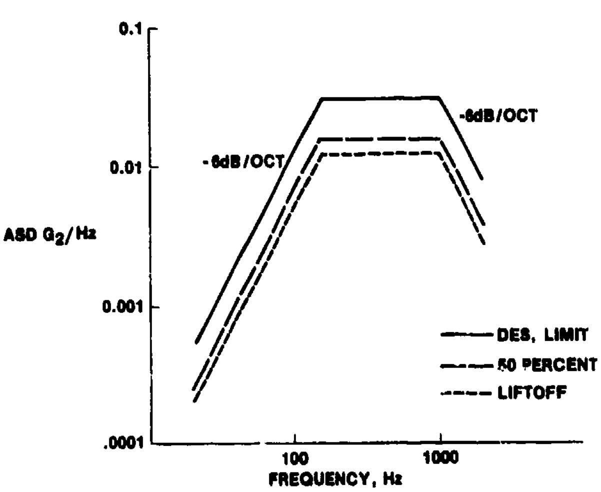

Fig. 17 - Orbiter crew module pressure hull vibration envelopes of scaled responses

dispersed trajectory boost conditions, only that spectrum identified as dispersed trajectory boost was specified for qualification testing. As a general rule, whenever the developed spectra were within 3dB, the higher was specified for all mission conditions.

A specific conservatism factor was not added to the vibration criteria for qualification testing because sufficient conservatism was built into the environment development and qualification test procedures by: (1) vibration environments from reference vehicles were developed by enveloping all applicable ground and flight test data, (2) enveloping Orbiter liftoff noise environments which occur at different elevations, (3) enveloping aeroacoustic environments resulting from mutually exclusive flight conditions, (4) assuming that ground reverberance or progressive wave acoustic testing was representative of service conditions, (5) using composite test spectra for full-duration testing, (6) performing shaker tests sequentially in three mutually perpendicular axes, and (7) defining test criteria as motion input spectra rather than force inputs.

Vibration Test Durations

A typical time history of overall fluctuating pressure levels during lift-off and ascent is shown in figure 18. During the ascent period, the nominal and dispersed trajectory curves shown represent those external noise conditions which will occur on 50% and 1% of the missions respectively. During the remaining 49% of the missions, the acoustic levels will be between those shown. Similar time histories were developed for all Space Shuttle Vehicle noise zones.

Since it is not practical to perform ground vibration tests using continuously varying environments, equivalent fixed amplitide tests durations were established. The equivalent fixed amplitude duration was calculated for each zone such that the test environment would exceed or produce the same fatigue damage as the non-stationary vibration amplitude time history. A fatigue model was used that assures that (a) both stationary and non-stationary loadings cause random stresses between the endurance limit and the ultimate strength, (b) the damage contribution is in accordance with the Palmgren-Langer-Minor hypothesis, (c) the maximum of the random fatigue curve can be used for scaling the relative damage contribution between the highest and lowest non-stationary stresses. Since most of the structure of interest is of 2024 aluminum with a notch concentration of $K_t = 4$, a maximum fatigue curve slope of 4 was selected. In addition, to account for the statistical scatter of the random fatigue curve, a scatter factor of 4 was used to increase calculated fixed amplitude durations for all testing and analyses.

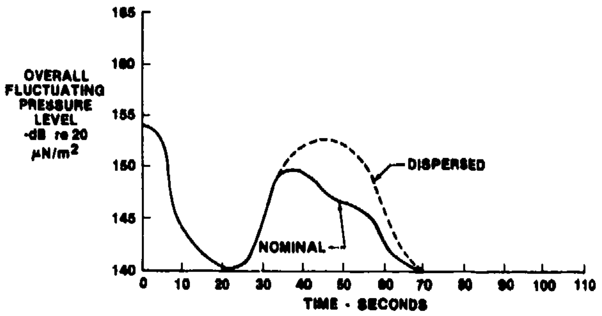

Fig. 18 - Orbiter forward fuselage - side

Flight Data Comparison

Approximately 200 acoustic, vibration and strain measurements applicable to the subject environmental criteria were recorded on the first Space Shuttle flight test. A comprehensive review of these data indicates that nearly all qualification vibration testing has been performed at satisfactory amplitudes and durations. Figures 19, 20, and 21 present typical comparisons of flight test data and component qualification test criteria. Figure 19 is a composite envelope of approximately 40 accelerometers located throughout the crew compartment. The low frequency criteria exceedance illustrated was observed on one accelerometer for less than one second. That particular accelerometer was located at the center of a large shelf and other accelerometers at similar locations on other shelves were within the criteria envelope. In addition, the Avionics components at the location in question had been tested to higher levels than the criteria envelope, so no equipment qualification problems were encountered.

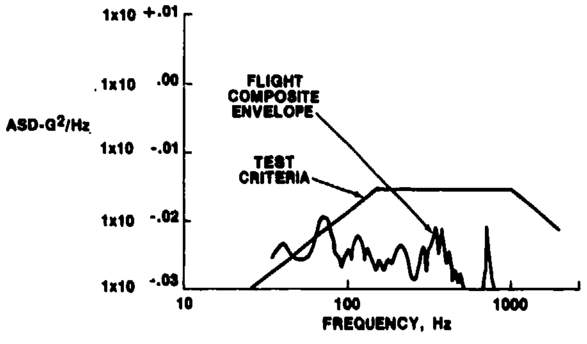

Fig. 19 - STS-1 crew compartment - composite envelope and corresponding test requirement envelope

Figure 20 indicates favorable comparison of the predicted mid-fuselage sidewall vibration environment with that measured during STS-1. Figure 21 indicates that, although

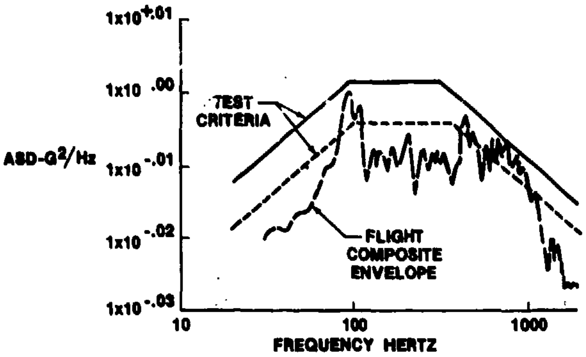

Fig. 20 - STS-1 midfuselage sidewall - composite envelope and corresponding test requirement envelopes

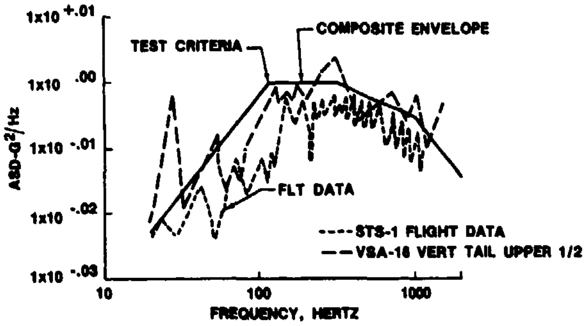

Fig. 21 - STS-1 vertical stabilizer - composite envelope and corresponding test requirement envelope

ground acoustic testing indicated vibration response may exceed predicted values, comparison with the flight data showed no exceedance in flight.

Two significant phenomenon were observed during STS-1 that require further discussion. During the orbiter main engine ignition sequence the engines are momentarily stabilized at 20% thrust prior to proceeding to full-thrust output. During this stabilization period, unburned hydrogen from the fuel-rich startup ignites when it mixes with the atmosphere causing increased transient noise. This condition lasts less than one half second, but produces acoustic levels that exceed all other mission events for some parts of the Orbiter. Even though the ignition transient acoustic environment exceeded that previously predicted for many aft areas, corresponding vibration responses did not exceed those predicted for lower acoustic environments. Nevertheless, the Orbiter vibration responses observed during this main engine ignition transient period were enveloped along with the remainder of the lift-off sequence.

The other significant observation was the pronounced lack of structural response to aeroacoustic excitation, especially in the lower frequency regions. As a result of analyses of ground acoustic test data from large test articles, there were indications that some structural areas could not survive 100 missions due to high amplitude, low frequency responses resulting from simulated aeroacoustic loading. Fortunately, the high amplitude low frequency responses did not materialize during the STS-1 transonic flight period. It is presently assumed that this lack of flight response to aeroacoustic noise can be attributed to poor coupling efficiently of the Orbiter low frequency modes with aeroacoustics.

Conclusion

The techniques used to develop Orbiter random vibration design and test requirements proved to be acceptable for the Shuttle mission schedule and objectives. The reference data base was sufficient to allow use of extrapolation methods. The zonal grouping and scale data envelopes allow reasonable conservatism and timely criteria development. The predicted vibration requirements were validated by flight data.

References

1. Condos, F. M., and W. Butler, "A Critical Analysis of Vibration Prediction Techniques," Preceedings of the Institute of Environmental Sciences, (1963).

2. Barnoski, R. L.; Piersol, A. G.; Van Der Laan, W. F.; White, P. H.; and Winter, E. F.: Summary of Random Vibration Prediction Procedures. NASA CR-1302, 1969.

3. Bies, D. A., and P. A. Franken, "Notes on Scaling Jet and Rocket Noise," Journal of the Acoustical Society of America, Volume 33, Number 9, dated September 1961.

4. Eldred, K. M.: Acoustic Loads Generated by the Propulsion System. NASA SP-8072, June 1971.

5. Donald, E. G. "6.4% Eastern Test Range Acoustic Model Test Report," NASA Internal Note IN-ET17-77-2, dated January 1977.

6. Piersol, A. G., and P. E. Rentz, "Experimental Studies of Space Shuttle Payload Acoustic Environment," SAE Paper 770973, November 1977.

7. Trudell, Richard. "Correlation of Model and Full Scale Acoustic Data Measured on the STS Program," McDonnell Douglas Corporation Report, dated September 1981.

8. Colonna, R. A. "Shuttle Payload Bay Acoustic Environment," NASA letter WA-81-L035, dated September 15, 1981.

9. Kingsland, R. B. "Pretest Information for Test of the 0.035 -- Scale Space Shuttle Vehicle Aerodynamic Noise Model 84-OTS in the AMES Research Center Unitary Plan Wind Tunnels (Test IS2)," Rockwell Report SD75-SH-0155, dated August 1975.

10. Himelblau, H., C. M. Fuller, T. D. Scharton, "Assessment of Space Vehicle Aeroacoustic/Vibration Prediction Design and Testing," NASA CR-1596, dated July 1970.

DISCUSSION

Mr. Mitchell (Naval Air Systems Command): Did you have any requirements for low frequency sinusoidal vibration tests to simulate structure-borne vibration?

Mr. Newbrough: From the beginning we did. We did put in a requirement early in the program for some of the black box developments, but that went away eventually during the program. We decided to divert that over to the loads analysis world and have the low frequency dynamics factored into the steady state loads. Since the subject of this paper was the high frequency random vibration environments, we didn't touch on anything essentially below 20 Hz.

Mr. Mitchell: I think you mentioned you had 200 transducers on this last flight. What was the actual quantity? 200?

Mr. Newbrough: We had approximately 200 vibration, acoustic and strain transducers.

Mr. Mitchell: Will you have similar quantity on future flights? Do you anticipate that the next flight will have a different trajectory and a different environment when you reach max Q? I assume liftoff will probably be the same.

Mr. Newbrough: We have a full complement of measurements on the next three flights. Some are the same as we had before, for repeatability, and we have new locations as well. We also have a new data package that is being put on board to expand our capability in the payload bay. We had only four microphones in the payload bay to define the payload bay environment. We will have 14 more microphones from the Goddard Space Flight Center. They put on the DATE system, which you may have heard about, for those measurements. Yes, there will be slightly different trajectories involved, and we have taken that into account in our data. Our trajectories were scaled to our max Q environment in every case, and we did not achieve the maximum Q environments on this last flight. That is a good point; we adjusted our data to take care of that when you saw the comparisons of the flight data with our test environments.

Mr. Beck (Boeing Company): Would you comment on the effect of the tiles on the response of the structure to acoustic noise or in-flight noise?

Mr. Newbrough: It is in the paper, but it was one of those things I left out of this presentation. We assumed we would not take any kind of a mass effect into account for those tiles. It was another conservatism factor that might be built into the criteria. We basically did not put much in there at all, but we said that the effect is there. The fact that the tiles are there would have to be accounted for, and I guess we had to account for that on some of our acoustic fatigue program panels. I believe we had to account for that on the payload bay doors. We made some corrections to our test environments based on that. So we thought about it, and it was considered. We didn't reduce any of our predicted environments based on that, but we took care of it when we did ground simulation tests.

Mr. Sutherland (Wyle Labs): Did you state the relative amount of water flow relative to the exhaust flow rate in the water cooling suppressor?

Mr. Newbrough: It varies. I don't know the exact breakdown. The total flow rate is in excess of 700,000 gallons per minute.

Mr. Sutherland: What is the mass flow rate ratio?

Mr. Newbrough: It was 3½ to 1 on the main engine side, but I don't believe it was that high on the SRB side.

Mr. Sutherland: Did you say that you didn't feel that the water cooling had any particular benefit?

Mr. Newbrough: Oh, no! It did have significant benefit. Without it we could not have flown the present vehicle. When I said that, I meant that it was for the ignition transient situation only where the SSME starts up; the SSME starts roughly three seconds before the SRB fires. It is during that short time period, half a second to a second before we come to full thrust, that we got this high level, and we felt that perhaps the water did not have too much benefit. That was a postulate; that was a theory on our part. But we know if it was a rough burning condition with the shocks bouncing around inside the nozzles, that the suppression water is down in the flame trench. We had no thrust down in that area at all. So we really believe we could not have launched. In fact we had a launch constraint. If you lose the noise suppression water, do not launch! Hold the flight!

SPACE SHUTTLE ORBITER
ACOUSTIC FATIGUE CERTIFICATION TESTING

R. A. Stevens
Rockwell International
Downey, California

The Space Shuttle orbiter is designed to accommodate a unique combination of loads and environments not previously encountered inasmuch as the reusable vehicle is launched vertically and lands horizontally. The orbiter is subjected to structural vibration caused by engine exhaust-generated acoustic noise during liftoff and aerodynamic noise during atmospheric flight. It was necessary to certify the orbiter structure, thermal protection system (TPS), mechanisms, and equipment, and to gather empirical data to support fatigue analyses and to update vibration and internal noise criteria before the completion of the orbiter flight test (OFT) program.

The requirement has largely been satisfied by the partial completion of a comprehensive acoustic fatigue development and certification test program. This paper addresses the certification portion of the program supporting OFT, including test article selection, objectives, environments, results, and conclusions. Also included are comparisons of ground and flight test data.

INTRODUCTION

The Space Shuttle was developed to satisfy the requirements of NASA and DoD to economically put a variety of payloads (PL's) into low earth orbit, and to serve as a reusable first stage in putting other payloads into higher orbits, geosynchronous orbits, or planetary trajectories at low cost. Orbital servicing and retrieving of payloads are also planned under certain conditions. Payloads are carried in the orbiter cargo bay, which is 60 feet long and 15 feet in diameter. Ref. [1 through 4] provide an overview of the Shuttle configuration and mission and discussions of various technical issues (Figs. 1 and 2).

The fluctuating pressure loads are the principal sources of structural vibration. Structural vibration could cause malfunction and/or fatigue of vehicle components, primary and secondary structure, and/or TPS.

Because of the vibratory loads, requirements were defined to demonstrate the integrity of structure, TPS, mechanisms, and components, and to obtain data to update vibration criteria, noise transmission predictions, and support fatigue analyses prior to flight. The requirements have been satisfied by partially completing a comprehensive acoustic fatigue development and certification test program. The development program was described in Ref. [5 and 6]; this paper addresses the orbiter acoustic fatigue certification test program completed to support the orbiter flight test program. Additional acoustic fatigue testing is planned to support orbiter certification for operational flight; the result of this testing will be reported later.

TEST ARTICLE SELECTION

Test articles for the program were selected based on the diversity of parameters affecting the fatigue life—principally

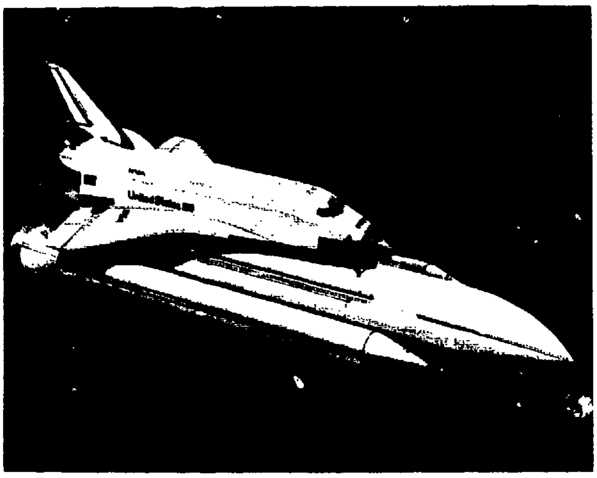

Fig. 1 - Space Shuttle configuration

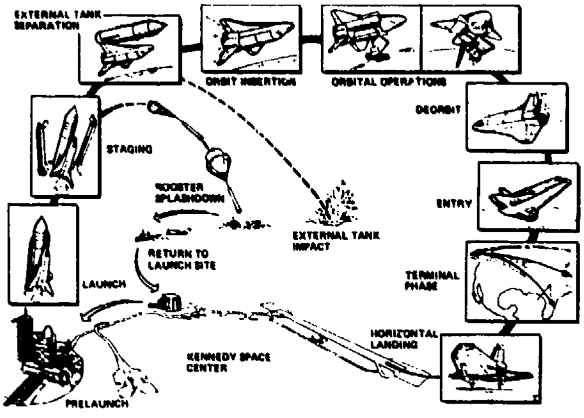

Fig. 2 - Space Shuttle mission profile

the variation in structural and TPS configurations and in aeroacoustic environments. Results of the acoustic fatigue development test program also influenced the selection process.

In most conventional aircraft and spacecraft programs, the contractor performs the design and analysis while the subcontractor does the fabrication. In the Shuttle program, the subcontractor performed all three functions using vehicle loads specified by the contractor. The subcontractor was free to select his preferred structural configuration, so long as certain weight goals were achieved. As a result, the orbiter structure is highly varied: the forward fuselage has mainly hat-stiffeners; the payload bay doors and the skin of the orbital maneuvering subsystem (OMS) are graphite-epoxy honeycomb; the aft fuselage and vertical stabilizer are primarily of integrally machined waffle construction; the mid fuselage is primarily integrally machined I-stiffeners; and the wings have unique hat stiffeners. In addition, most metallic skin-stringer configurations are machined and/or chem-milled. With the exception of the graphite-epoxy sections and the windows, the external structure is made mainly of 2024 aluminum alloy. The orbiter subcontractors are shown in Fig. 3.

The TPS for the orbiter structure generally consists of more than 30,000 coated silica tiles called reusable surface insulation (RSI), each ranging up to 8 by 8 in. in area and from 0.2 in. to 4.75 in. in thickness. The area and thickness of the tiles are determined by local entry heating environments. The lower surface is covered with high-temperature RSI (HRSI); the sides and upper surface are generally covered with low-temperature RSI (LRSI) and felt RSI (FRSI).

The heating on the nose and leading edges of the wings exceeds the capability of the RSI. A graphite composite called reinforced carbon-carbon (RCC) is used for these sections. Thermal and aerodynamic seals are prominently used on many doors and control surfaces of the orbiter. Fig. .4 shows the general layout. Ref. [7 and 8] present a material and mechanical overview of the TPS.

There is a large spatial variation of the aeroacoustic environments, especially during ascent transonic/q_{max} period

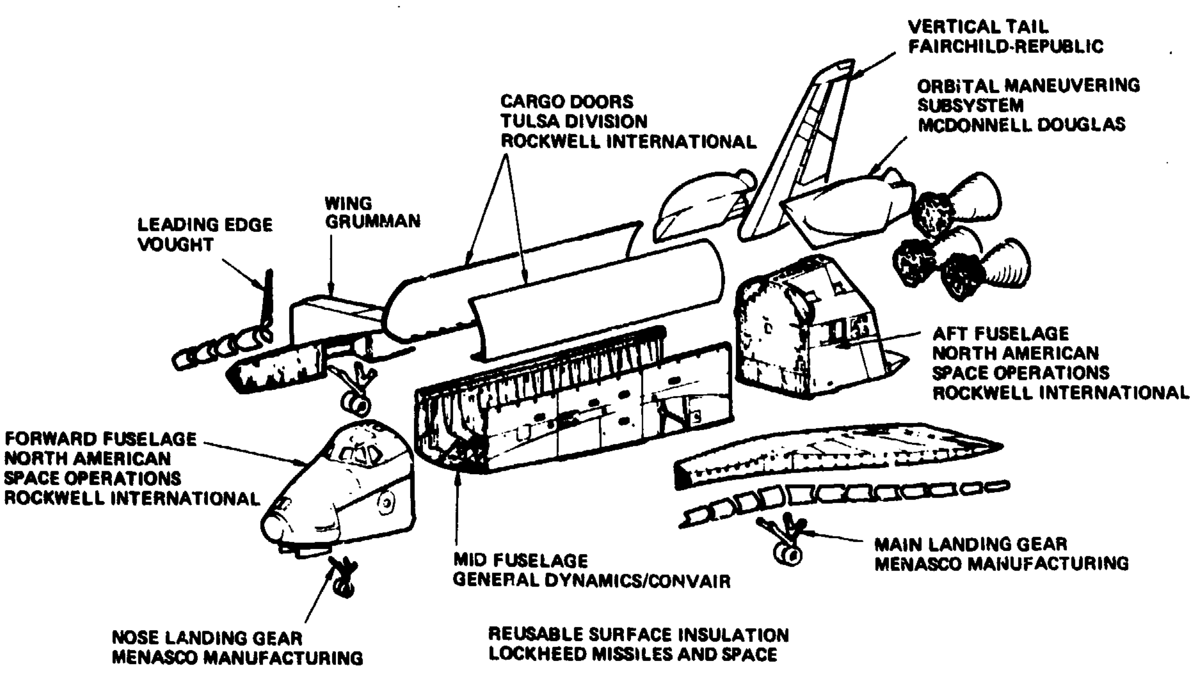

NOTE: THIS ILLUSTRATION DOES NOT INCLUDE ALL
ORBITER SUBCONTRACTORS

Fig. 3 - Structural subcontractors of the Shuttle orbiter

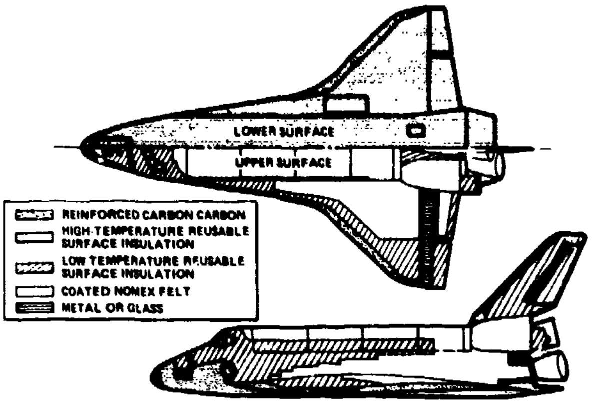

Fig. 4 - Material elements used for the orbiter thermal protection subsystem

of flight, hereafter called aerodynamic noise. For this reason, and the structural variations listed above, the orbiter was divided into many exterior vibroacoustic zones. Figs. 5 and 6 show these zones plus the predicted maximum overall sound pressure level for liftoff (XXX) and the maximum overall fluctuating pressure level for ascent transonic/q_{max} <u>XXX</u>.

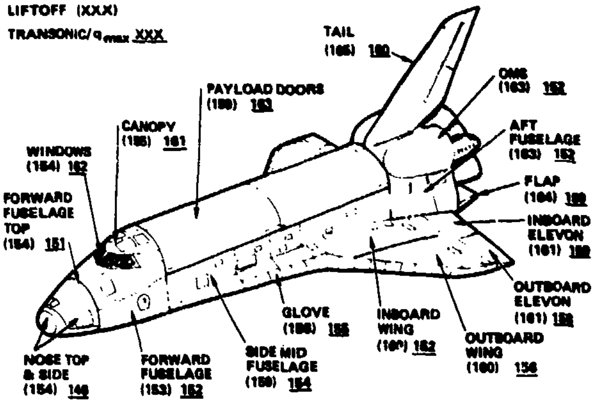

Fig. 5 - Orbiter aeroacoustic zones: top and side with maximum overall sound pressure level for liftoff and transonic

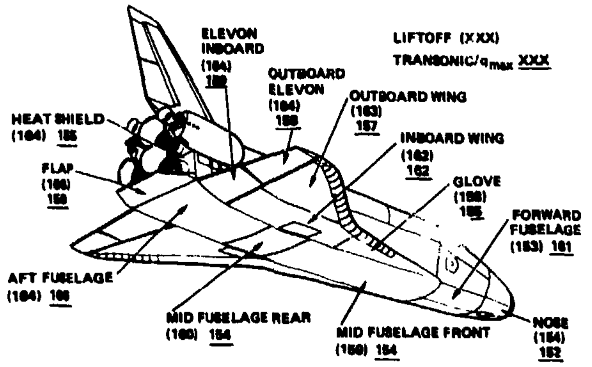

Fig. 6 - Orbiter aeroacoustic zones: bottom with maximum overall sound pressure levels for liftoff and transonic

GENERAL TEST REQUIREMENTS AND RESULTS

Test Objectives

The objectives of each test varied slightly. The general objectives were to demonstrate and/or evaluate the integrity of the structure, TPS, seals, thermal barriers, gap fillers, mechanisms, and components, and to obtain data to (1) support fatigue analysis of structure, (2) expand the vibroacoustic data base, (3) support TPS analysis, (4) correlate with development flight instrumentation (DFI), and (5) compare internal and external noise to determine noise transmission (NT).

Test Article Description

The test articles selected are shown in Fig. 7. The structural configuration of all test articles was according to the production drawings. Because of the availability and cost of production RSI, most of the test articles had some simulated RSI (SRSI). The exceptions were the payload bay doors, which had no acreage RSI; the environment based on the results of development testing was adjusted accordingly. The dynamic characteristics of the SRSI were proven adequate for use in the certification program during the development program. Most of the acoustic fatigue certification test articles had at least 25 percent production RSI.

Test Environment

Prior to acoustic testing, the dynamics of each test article with its test fixture were characterized in a modal survey and analysis. The results of the modal survey and analysis were used to locate critical strain gauges and accelerometers for acoustic testing, to evaluate the test fixture, to ensure that all dynamic inputs to the test article were realistic, and to develop a model to support fatigue life analysis of the primary structure. Because some of the test articles were completely covered with RSI and/or SRSI, visual inspection of the structure was virtually impossible. In these cases, modal testing was used as a supplementary

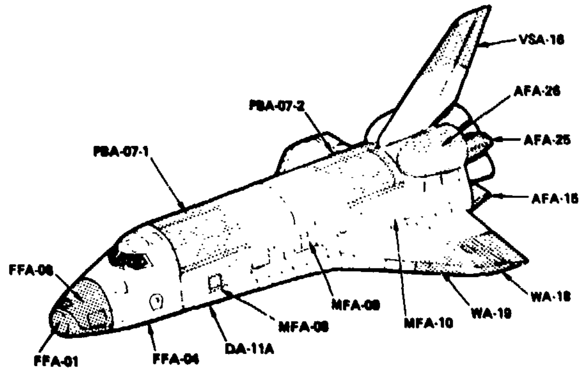

Fig. 7 - General locations of the test articles

inspection tool. Comparisons of mode shapes, frequencies, and damping were conducted periodically between exposures during the acoustic testing. If changes were detected, it was concluded that load path changes had occurred that implied potential structural failure.

Table 1 shows the acoustic environments used for each test article. The environments and durations were developed using the methods described in Ref. [6 and 9]. For some test articles, the acoustic environments (aerodynamic and liftoff) were combined to form a composite. The cumulative damage theory was used to develop the composite environments Ref. [9 and 10]. The primary reason for using composites was to simplify testing. Enveloping of zonal environments (i.e., upper and lower wing, elevon) was also used to develop acoustic test environments. If enveloping procedures were not used, special fixtures would have had to be designed and fabricated; the cost and schedules involved were prohibitive.

Because of the extreme difference in spectrum shape between the aerodynamic shock (hereafter called aeroshock) and aerodynamic environments, composite techniques were not used for these cases. In most cases, the entire test article was exposed to the aeroshock test condition, even though the aeroshock environment (usually caused by a large pressure gradient) was predicted and subsequently found relatively local in flight. The reasons for not confining the aeroshock to a local region during the applicable tests were the cost and schedule needed to fabricate special test fixtures. Aeroshock testing of entire test articles proved to be conservative, of course. On some test articles, however, the aeroshock environment was applied locally. This was called hot spotting. Hot spotting was usually done by positioning low-frequency horns adjacent to the local area of interest. An important observation was made from the hot spot tests: when the aeroshock environment was applied locally and simultaneously with the aerodynamic environment, no significant increase in vibration response was observed over the presence of aerodynamic excitation alone.

If no structural failures were detected after 100 equivalent missions, further acoustic testing was conducted on most test articles listed in Table 1 until failure occured or until a very large number of equivalent missions were applied to preclude the possibility of failure. The most common method of intentionally inducing fatigue failure is called accelerated testing, which is accomplished by increasing the acoustic levels. The determination of the time-to-failure and location of the failure is desirable to support acoustic fatigue analysis. It was determined that 500 equivalent missions was an adequate duration to achieve failure, if failure was possible. When the levels were increased, the durations were reduced using linear fatigue damage hypotheses as described in Ref. [9 and 10].

Test Results

A general overview of the test results is presented in Table 1. Each test article was the subject of a separate report, Ref. [11 through 24]. A thorough description of test results for all of the orbiter test articles is considered beyond the scope of this paper. However, two test articles have been addressed in more detail: the AFA-15 body flap (Fig. 8), and the WA-19 wing (with leading edge) (Fig. 9). These articles were tested at the NASA Johnson Space Center (JSC) Sonic Fatigue Laboratory (SFL). Other facilities are referred to in Table 1.

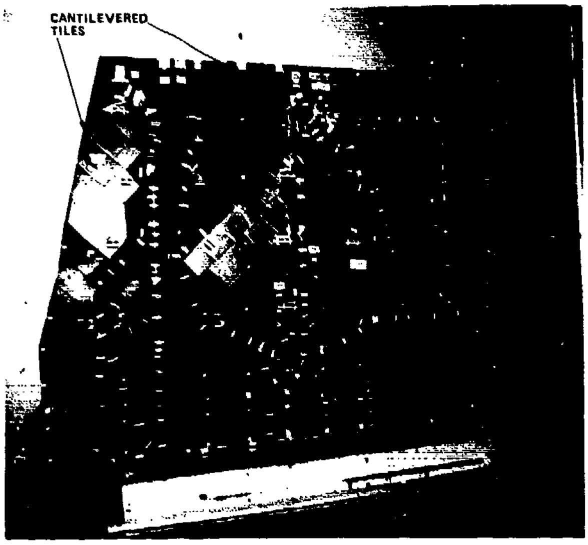

Fig. 8 - Body flap test article AFA-15

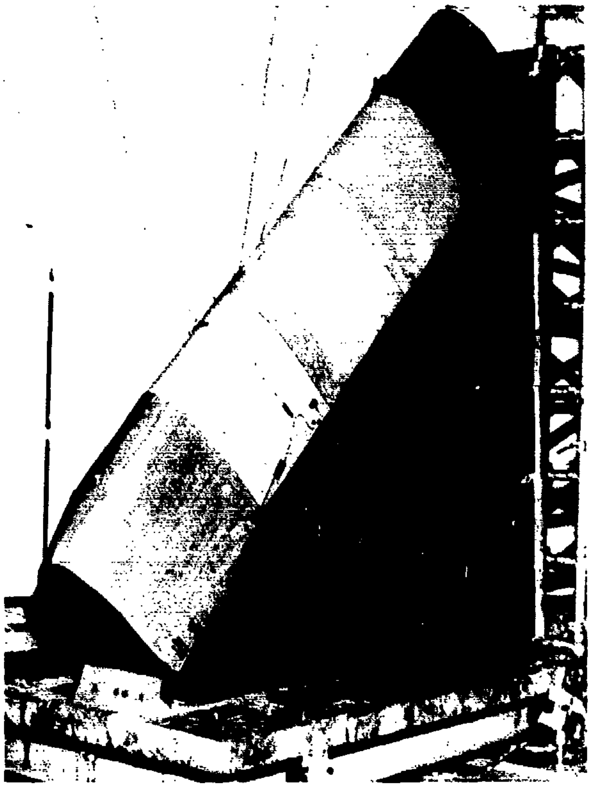

Fig. 9 - Wing (with leading edge) test article WA-19

TABLE 1
Acoustic Fatigue Certification Test Summary

Test Identification and General Description	Structural Configuration (All Production)	TPS Configuration	Environment and Acoustic (OASPL)	Equivalent Missions Accomplished	Comments
FFA-01: Nose cap and forward fuselage	Aluminum hat-stiffened skin with frames and bulkhead	RCC cap and attach points; internal insulation, closeout HRSI, acreage HRSI, and SRSI	Sequenced acoustics airloads, and therms. Liftoff 152 dB, aero 166 dB with sinusoidal hot spot of 151 dB	18	Vibration responses compared favorably with predictions; NT exceeded prediction; strain levels very low; internal TPS blankets required redesign; test conducted in SFL [Ref. 11]
FFA-04: Forward fuselage underbody	Aluminum hat-stiffened skin with frames, representative tubing, antennas, coaxial cabling	Acreage HRSI and SRSI and flight microphone installed in HRSI	Composite liftoff and aero 158 dB, aero hot spot of 165 dB	106	Vibration responses and NT exceed prediction; strain levels low; several secondary structural anomalies: none significant; test conducted in wall SFL [Ref. 12]
DA-11A: Mid fuselage underbody	Aluminum, integrally machined, T-stiffened skin with frames representative plumbing	Closed-cell, rubber-simulated TPS mass effect	Composite liftoff and aero 159 dB	40	Vibration responses exceed; NT as predicted; strain levels low; plumbing isolation system required redesign; test conducted in Rockwell/NAAD reverberant chamber [Ref. 13]
FFA-06: Forward reaction control subsystem	Complete operational module with aluminum hat-stiffened skin, frames, and plumbing	Closed-cell, rubber-simulated TPS mass effect	Composite liftoff and aero 152 dB, with sine of 152 dB at 100 Hz	10	Vibration responses exceed prediction; NT as predicted; strain levels low except for tank struts; test conducted in Rockwell/NAAD reverberant chamber [Ref. 14]
PBA07-1 and -2: Forward and aft payload bay doors	Forward 15 ft. and aft 15 ft. sections of doors, including radiators and mechanisms; graphic-epoxy honeycomb skin with frames and intercostals	Interface seals and thermo barriers with expansion joint; environment reduced by 3 dB due to lack of acreage TPS	Forward section composite liftoff and aero 157 dB; aft 15 ft. 15 ft. sect. composite liftoff and aero 151 dB; aero hot spot 158 dB on aft	10	Forward doors vibration responses exceed prediction; NT as predicted; low strain levels; test conducted in SAL [Ref. 15 and 16]
MFA-08: Mid fuselage sidewall	Aluminum integrally machined, T-stiffened skin with frames, access. door, and representative plumbing	Acreage TPS including FRSI, LRSI, and diced LRSI	Liftoff 154 dB, aero 161 dB, accelerated test 168 dB	450	Vibration responses and NT compared favorably with predicted; strain levels low; test article failed at 9 dB higher than flight condition; test conducted in PWT [Ref. 17]
MFA-09 and -10: Internal panels in wing carry-through area	Aluminum, integrally machined, T-stiffened panels	No TPS required	148 dB	500	Low strain levels; panels exposed at higher levels than flight for longer duration with no anomalies; test conducted at General Dynamics reverberang chamber [Ref. 18]
AFA-15: Body flap	Aluminum honeycomb skin with ribs, front spar, and aft fuselage portion	Acreage, trailing edge, and cove HRSI, SRSI, microphone install, gap fillers, thermal barriers, and aft fuselage/body flap interface seal	Liftoff 165 dB, aero 161 dB	100	Fig. 8 shows test setup; text has further comments; test conducted in SFL [Ref. 19]
VSA-16: Vertical stabilizer	Aluminum fin integrally machined, waffle skin with frames and speed brakes with honeycomb skin	Acreage, trailing edge, leading edge HRSI and SRSI gap fillers and conical seal	Composite liftoff 164 dB	100	Vibration response and NT compared favorably with predicted; strain levels low; test conducted in SFL [Ref. 20]
WA-18: Wing/elevon	Aluminum outboard elevon honeycomb skin with ribs front spar and wing portion skin stiffened with pinched hats	Acreage, trailing edge HRSI and SRSI, gap fillers and thermal seal at interface of wing and elevon	Liftoff 162 dB and aero 156 dB	6	Vibration responses and NT compared favorably with predicted; strain levels low; test conducted in reverberent chamber at Rockwell/NAAD [Ref. 21]
WA-19: Wing, including leading edge	Aluminum wing skin stiffened with pinched hats, frames and front spar	RCC and fiber glass (simulated) leading edges acreage SRSI and production closeout tiles with front spar insulation and gap fillers	Composite liftoff and aero 161 dB, accelerated testing 164 dB	500	Fig. 9 shows test setup. Text has further comments. Test conducted in SFL [Ref. 22]
AFA-26: OMS	Complete operational module with graphite-epoxy honeycomb skin and aluminum secondary structure	Acreage LRSI, FRSI, and SRSI	Liftoff 163 dB, aero 161 dB hot spot gradient	30	Vibration responses prediction; NT and strain as predicted; subsystem met functional reqmts; test conducted in SFL [Ref. 23]
AFA-25: Aft reaction control subsystem	Complete operational module with graphite epoxy honeycomb skin and aluminum secondary structure	Acreage LRSI, FRSI, and SRSI	Liftoff 163 dB, aero 155 dB, accelerated test 166 dB	500	Vibration responses exceed predictions; NT compared favorably with predictions; strain levels low; subsystem met functional reqmts; test conducted in SFL [Ref. 24]

BODY FLAP ACOUSTIC AND FLIGHT TEST DATA

Acoustic Test

The acoustic environments for the body flap test are shown in Fig. 10. The facility was able to achieve the test environment within the specified tolerance in each 1/3-octave band. Vibration responses measured on the skin between frames and at a frame-skin interface are compared with the predicted body flap vibration in Fig. 11. The predicted and measured skin vibration compared favorably except below 100 Hz. The acoustic and vibration criteria were developed using the methods described in Ref. [6]. Fig. 12 compares external and internal noise measured at the liftoff condition. Noise reduction greater than the 10-dB predicted is observed. The predicted noise transmission was developed using data obtained early in the Shuttle program, Ref. [5].

Fig. 13 compares vibration data for the structure and one of the tiles. It can be concluded that the tile and structure responded together in the normal direction up to about 250 Hz, but above this frequency the tile decouples from the structure. Results of this type were typical for several test articles. Using coherence analysis and vibration data from another acoustic test of structure-TPS, Ref. [25] concluded that the structural vibration was the main exciter of tile response below 250 Hz whereas the acoustic pressure was the main exciter between 250 and 800 Hz.

As seen in Fig. 8 and the top of Fig. 14, several edge tiles are cantilevered over the trailing edge and sides of the body flap, leaving only a small area (called a footprint) for attaching an edge tile to the structure. Fig. 14 shows the normal response of one of these tiles, one in the center of the footprint and the other in center of the cantilevered area. Tile rocking is observed, making it susceptible to early failure. Fig. 14 also shows the lateral response, which is significantly lower than the normal.

Flight Data

Fig. 15 shows time histories of acoustic and vibration measurements for the body flap during the liftoff period of the first Shuttle flight (STS-1). Two transitory periods are prominent. The first occurs during Space Shuttle main engine (SSME) ignition (MEI). The design of the engines require a fuel lead and then, because of the extremely high operational pressures, a pause is required in the thrust build-up to permit stabilization of the high-pressure fuel and oxidizer pumps. During this pause, the partially full exhaust flow in the nozzle is extremely rough and small explosive detonations are occurring downstream of the nozzle exit as unburned fuel in the exhaust explosively mixes with the atmospheric oxygen. As shown in the time histories, this transitory noise and subsequent vibration equals or exceeds the levels experienced from combined SSME and solid rocket booster (SRB) operation as the vehicle clears the launch pad.

The second transitory peak, shown only in the acoustic time history, occurs during SRB ignition. This peak is really a low-frequency pressure wave caused by the dynamic interaction between the stationary air mass in and around the nozzle and the sudden onset of high-velocity exhaust gases through the nozzle as engine chamber pressure rapidly

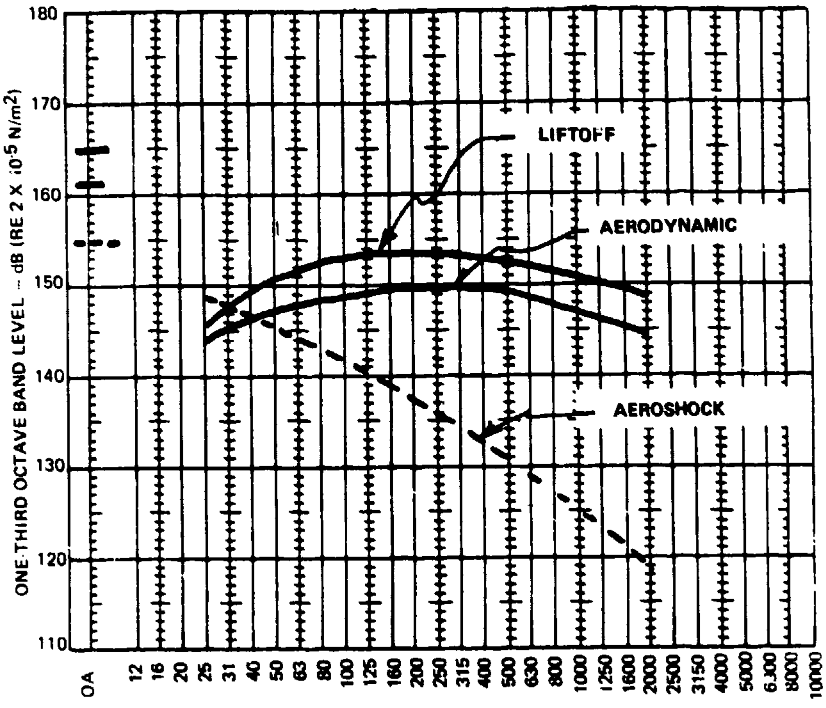

Fig. 10 - Acoustic criteria for body flap acoustic test AFA-15

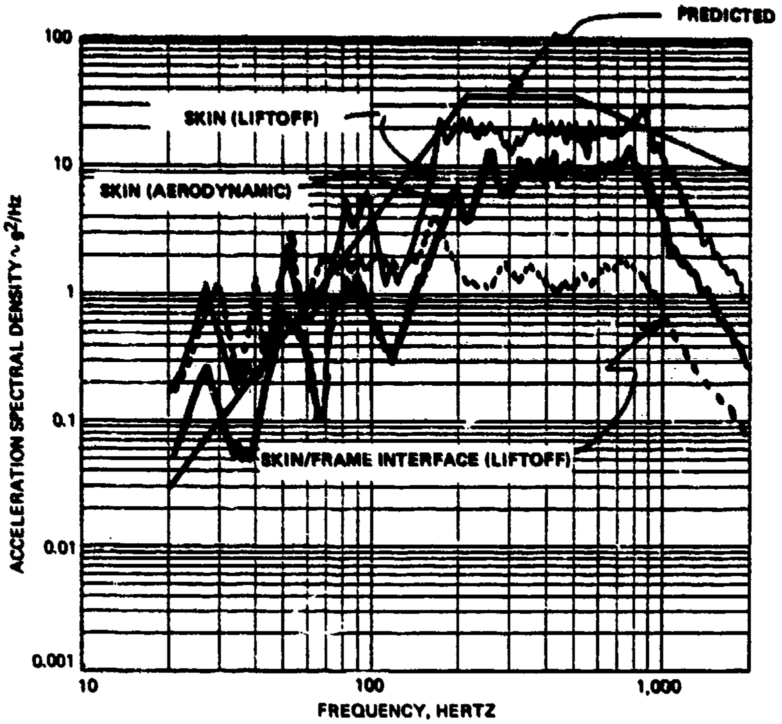

Fig. 11 - Comparison of predicted and measured random vibration response of body flap skin and skin-frame interface (normal direction) obtained from acoustic test AFA-15

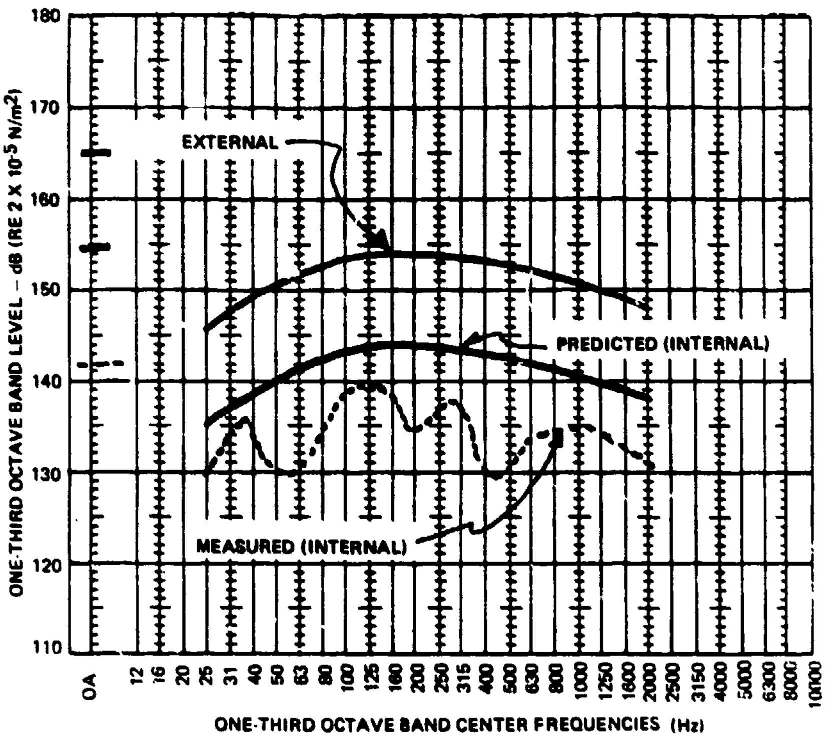

Fig. 12 - Comparison of measured external noise with predicted and measured internal noise obtained from body flap; acoustic test AFA-15

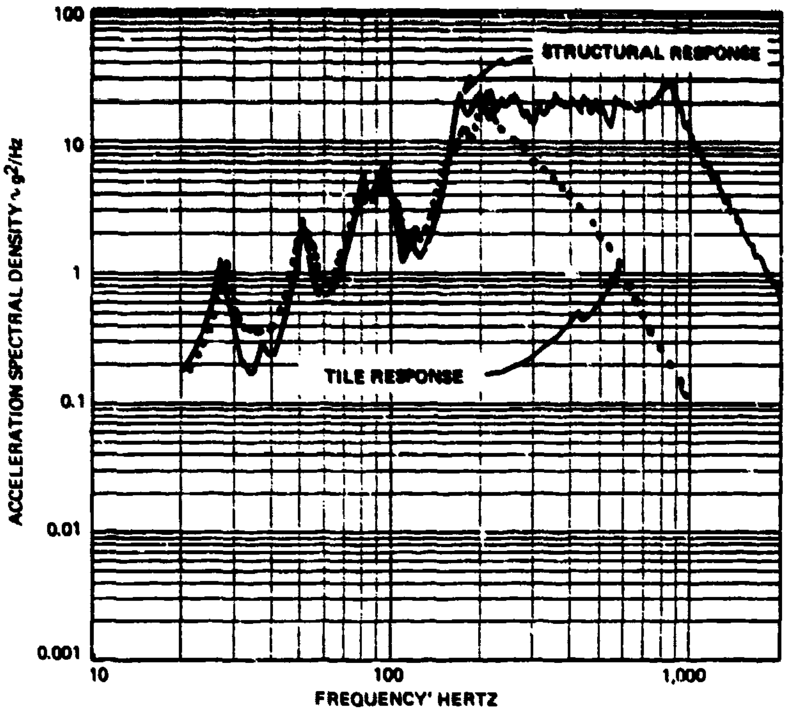

Fig. 13 - Comparison of measured body flap structure and tile random vibration responses (normal direction) obtained from acoustic test AFA-15

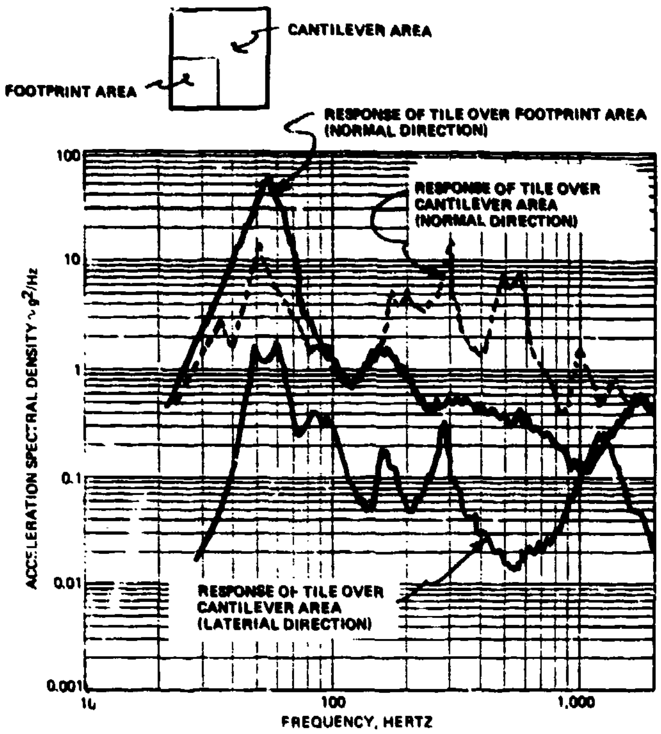

Fig. 14 - Comparison of measured edge tile random vibration response obtained from body flap; acoustic test AFA-15

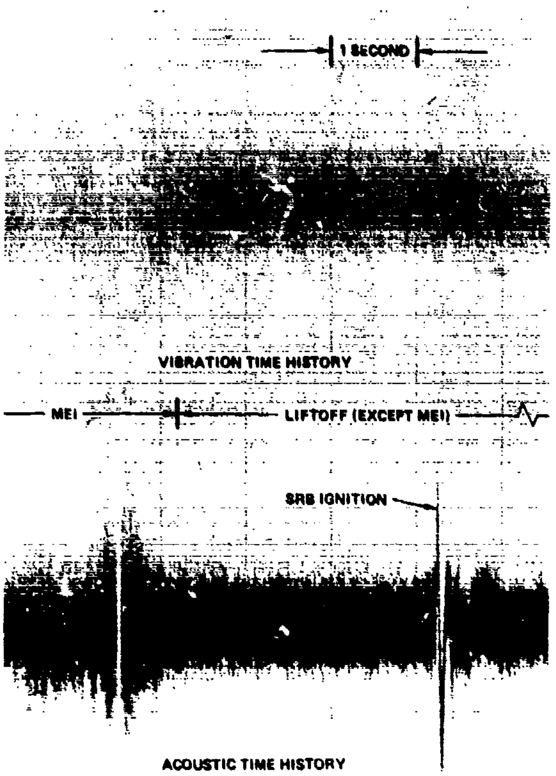

Fig. 15 - Body flap vibration and acoustic time histories obtained from STS-1

increases during the ignition phase. The result is the formation of a weak blast-wave in the air. However, as seen in Fig. 15, the body flap vibration time history shows no significant peak at this time, although other orbiter locations show appreciable responses.

Figs. 16 and 17 compare flight acoustic and vibration spectra for MEI, the remaining portion of liftoff (relatively steady burn of the main engines) and for the aerodynamic period of flight. Fig. 18 shows that the difference between external and internal noise is in excess of 10 dB at liftoff (excluding MEI).

BODY FLAP COMPARISON AND OBSERVATIONS

Figs. 10 and 16 show the predicted acoustic and measured flight acoustic spectra for the liftoff and aerodynamic conditions. At MEI, the flight acoustic environment exceeds the predicted by as much as 6 dB between 50 and 100 Hz and up to 3 dB above 250 Hz. The liftoff predicted criteria exceeds the measured liftoff environment (except MEI) by 4 to 12 dB depending on the 1/3-octave frequency band compared. When the aerodynamic condition is compared, the predicted exceeds the measured in the frequencies of interest by at least 10 dB.

Figs. 11 and 17 present the vibration response of the skin from the acoustic and flight test. The acoustic test vibration response compares favorably with the vibration response measured during MEI, except below 100 Hz. The flight vibration response measured during the remaining portion of

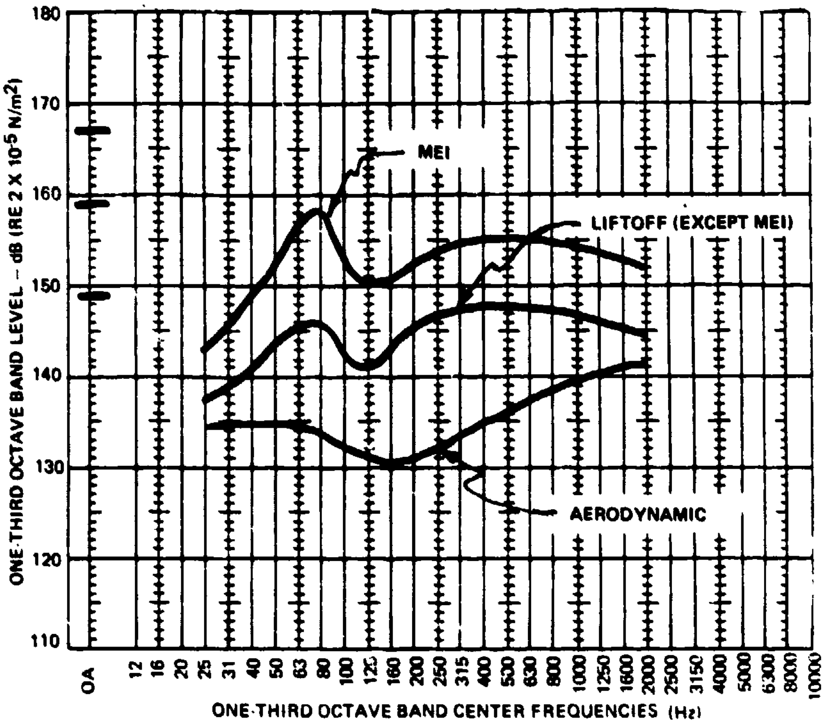

Fig. 16 - Body flap acoustic spectra obtained from STS-1

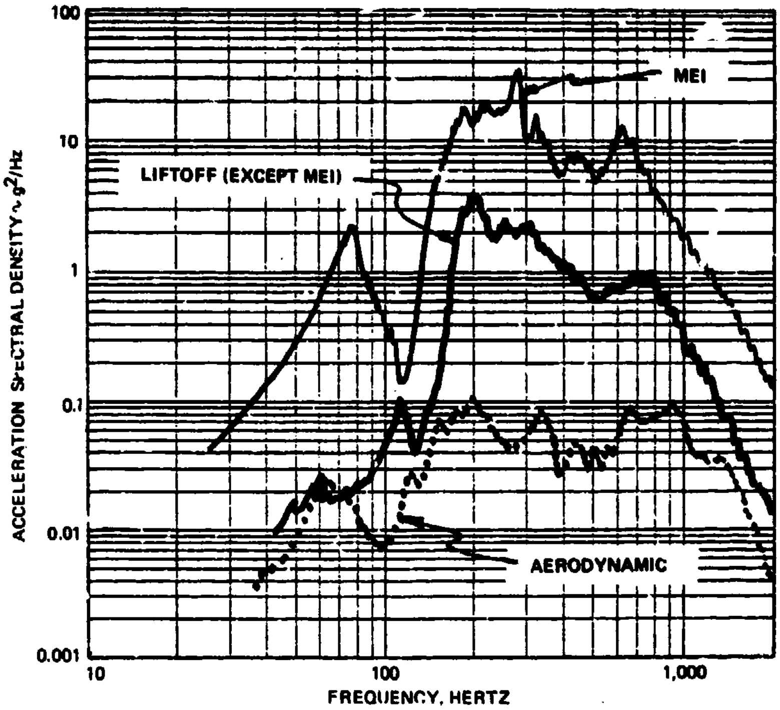

Fig. 17 - Random vibration response data obtained from body flap measurement on STS-1

liftoff is about 10 dB lower than the acoustic test vibration response. If the aerodynamic condition is compared, the acoustic test vibration response exceeds the flight response by about 20 dB.

Figs. 12 and 18 show that the acoustic and flight test external to internal noise differences compare favorably at liftoff (except MEI). In this case, the initially predicted value of 10 dB reduction proved to be conservative.

The exposure time for the liftoff condition for the acoustic test [Ref. 9 and 19] and the flight test (Fig. 15 partially displayed) are 5 and 8 sec., respectively. The duration at high amplitude for the MEI portion of liftoff can be observed from Fig. 15 to be about 0.5 sec.

One can conclude from these comparisons that

- The MEI flight acoustic environment exceeds the acoustic test environment by 6 dB between 50 and 100 Hz, whereas the vibration response from the acoustic test exceeds that from flight by 6 dB in the same frequency band. If the MEI flight acoustic spectrum had been utilized for the acoustic test, a 12 dB overtest would have resulted.

- The exposure time associated with the flight liftoff condition (except MEI) was longer than predicted but the flight acoustic and vibration environments (except MEI) were much lower than the predicted liftoff levels. As a result, the acoustic test could have produced greater fatigue damage than did flight.

- Because the flight aerodynamic acoustic and vibration environments were so much lower than liftoff, their contribution to fatigue damage was considered negligible. Therefore, there was no need to apply to aerodynamic environment during the acoustic test.

The first comparison indicated that the acoustic test produced an overtest of vibration response below 100 Hz. The probable cause for some of the excessive vibration is the semireverberant chamber used for the acoustic test. A comparison of ground and flight test data associated with most of the test articles noted in Table 1 has been conducted. In almost every case, if the test article had low-frequency modes (below 100 Hz), the semireverberent and reverberent chambers excited some of them. No evidence was found during the STS-1 flight that this occurred. This indicates that an overtest, to some degree, in the low frequency region occurred on all of the test articles.

BODY FLAP ACOUSTIC RETEST

During the 100-mission acoustic test exposure of the body flap test article, several TPS and structural failures occurred. The testing was interrupted a few times because of a loss of HRSI tiles, especially those cantilevered over the trailing edge of the body flap. Differences in strain gauge readings during acoustic exposure as well as differences in modal behavior (as measured from modal surveys conducted between acoustic exposure periods) indicated progression of structural failures throughout the test [Ref. 26]. Several structural failures were observed during inspection at the end

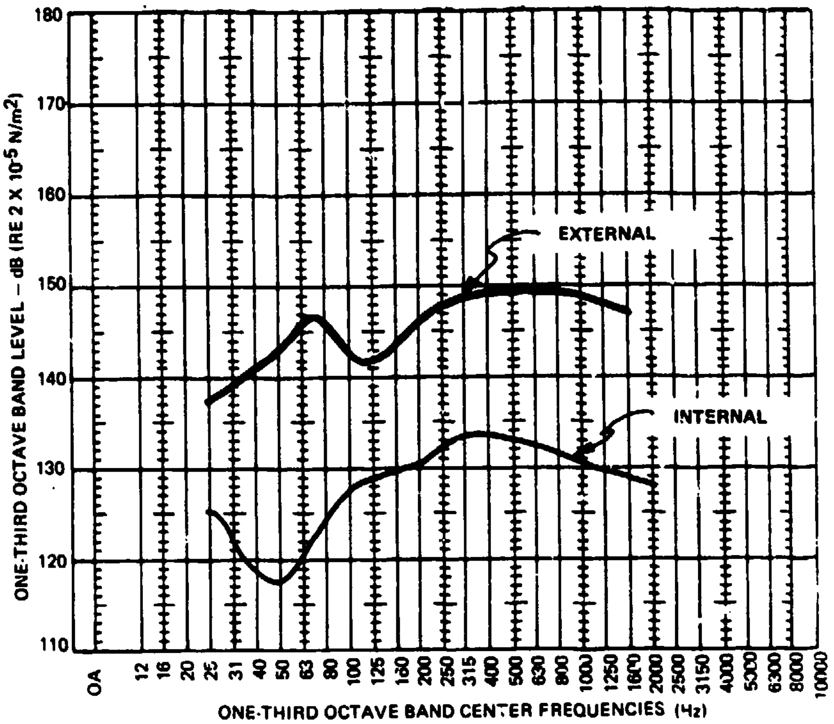

Fig. 18 - Comparison of body flap external and internal noise obtained during liftoff of STS-1

of the test. Because time-to-failures could not be accurately pinpointed, the test article is presently being refurbished and is scheduled to be retested using the revised criteria shown in Fig. 19. The revised acoustic test environment was established using flight data and the vibroacoustic test method concept developed in Ref. [27], i.e., selecting an acoustic environment to produce a given vibration response.

WING (WITH LEADING EDGE) ACOUSTIC AND FLIGHT TEST DATA

Acoustic Test

The acoustic environments shown in Fig. 20 for the wing (with leading edge) WA-19 test were developed by enveloping the predicted upper and lower wing liftoff and aerodynamic flight environments and deriving a composite using Miner's rule [Ref. 24]. The accelerated test environment (used to attempt to fail the structure), also shown in Fig. 20, was also developed using Miner's rule. The acoustic test exposed the test article to the equivalent of 500 missions.

The predicted decrease in noise from outside to inside the wing structure and the RCC cavity was 10 dB [Ref. 5]. Fig. 21 shows external and internal noise spectra obtained from the ground test. The comparison shows a 10 dB or greater reduction in each 1/3-octave band.

Fig. 22 compares predicted and measured wing (including leading edge) vibration response for the skin and the skin-frame interface in the normal direction. The skin vibration responses compare favorably with the predicted; however, as in many other zones of the orbiter, measured skin-frame interface vibration exceeds the predicted. The in-plane skin vibration is also plotted on Fig. 22. Except at 1,500 Hz, it is at least 10 dB less than the normal skin response. Fig. 23 presents measured vibration response in a direction normal to the RCC surface.

At the conclusion of the test, a visual inspection of the test article revealed two points of structural failure in a mini-frame. The locations of the failures are illustrated in Figs. 24, 25, and 26. Complete separation shown in Fig. 25 of the mini-rib occurred at about 350 mission-equivalents of accelerated testing. This was determined from rapid changes in strain gauge readings located near the failure (located as a result of the modal survey). The other point of failure detected after testing was a crack in the same mini-frame (Fig. 26). The strain data at the first point of failure was used to estimate the time the crack occurred to be equivalent to 320 missions.

Flight Data

Fig. 27 shows the time histories of the flight acoustic and vibration measurements for the wing during STS-1 liftoff. A review of the acoustic time history shows a high SRB ignition overpressure pulse; however, as noted earlier with the body flap, no appreciable wing vibration is observed.

Figs. 28 and 29 show the acoustic and vibration spectra that the wing encountered during the liftoff (including MEI and SRB ignition) and aerodynamic portions of Shuttle flight

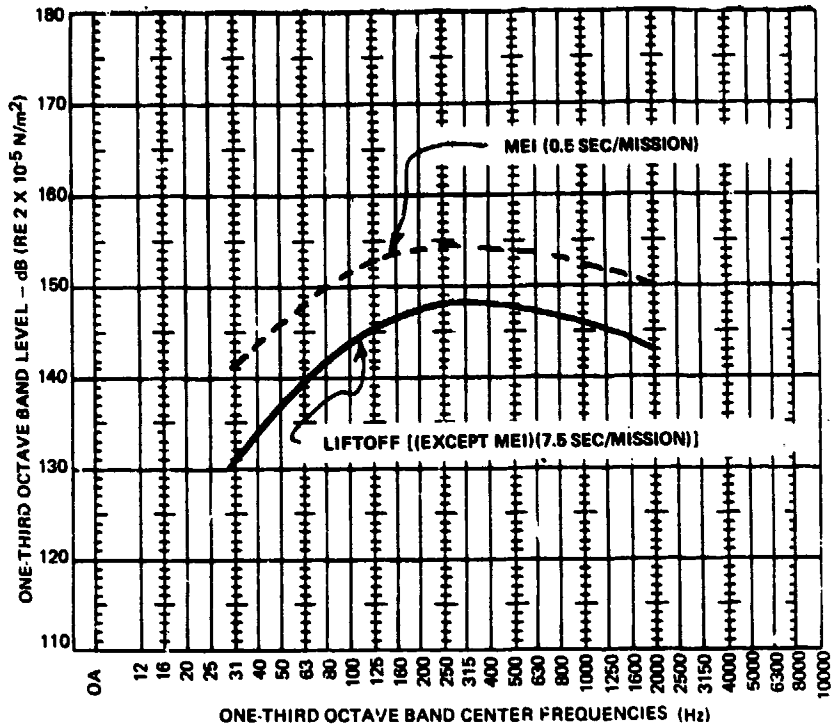

Fig. 19 - Revised acoustic criteria for body flap; acoustic test AFA-15

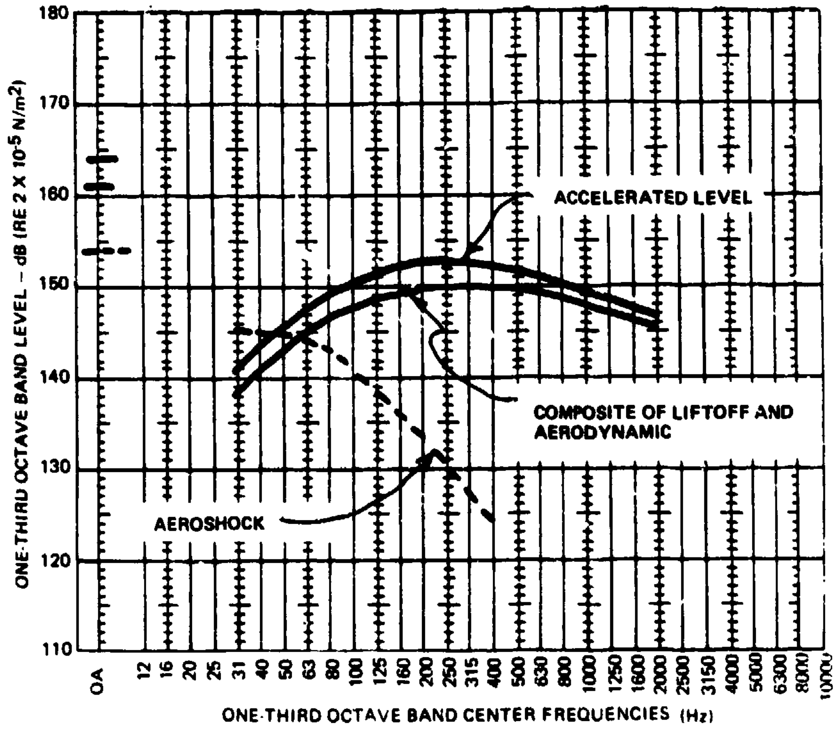

Fig. 20 - Acoustic criteria for wing (including leading edge); acoustic test WA-19

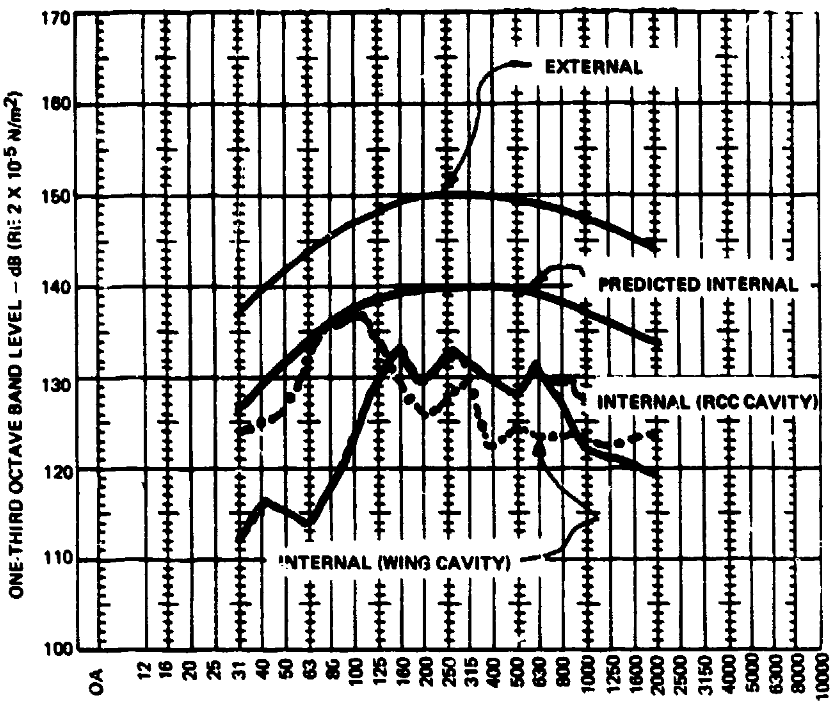

Fig. 21 - Comparison of measured external noise with predicted and measured internal noise obtained from wing (with leading edge); acoustic test WA-19

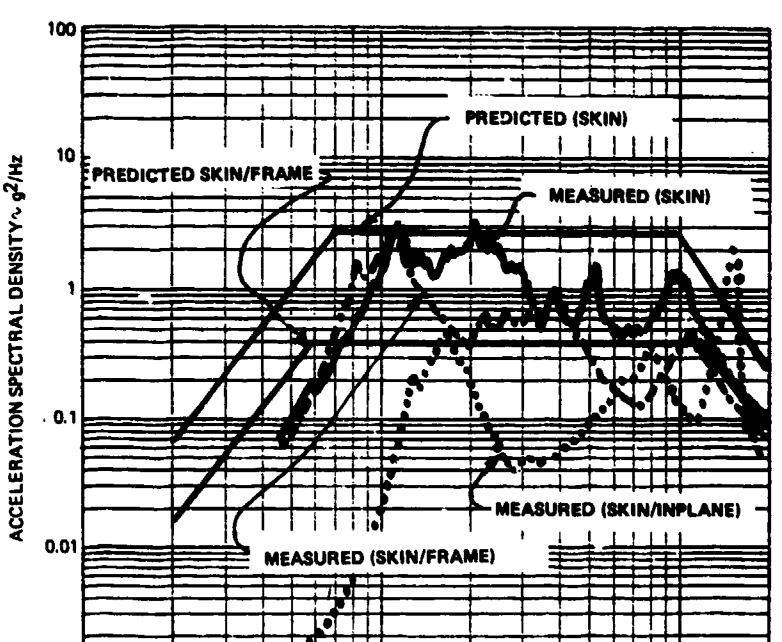

Fig. 22 - Comparison of predicted and measured random vibration from the wing (with leading edge); acoustic test WA-19

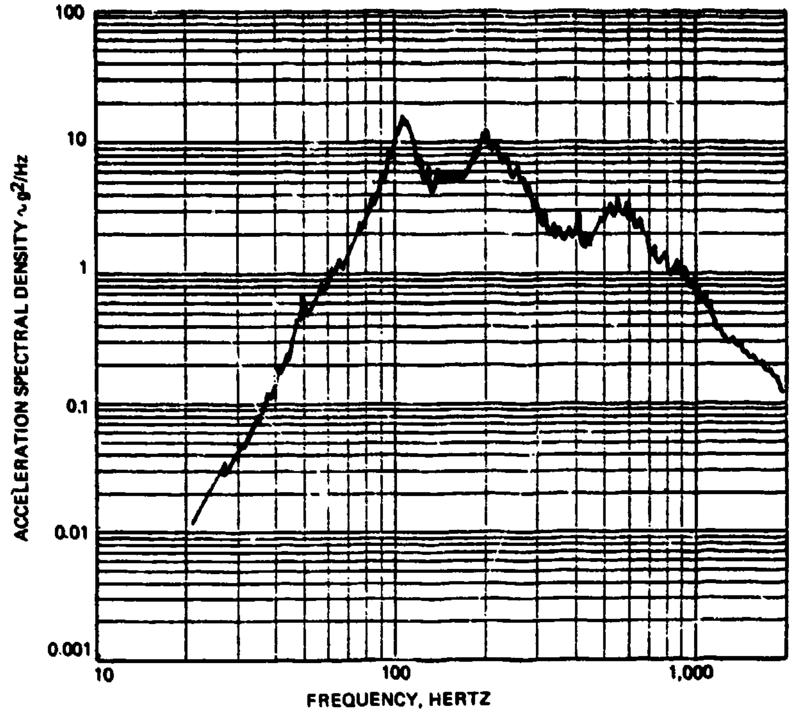

Fig. 23 - Measured random vibration response of the RCC surface (normal direction) from acoustic test WA-19

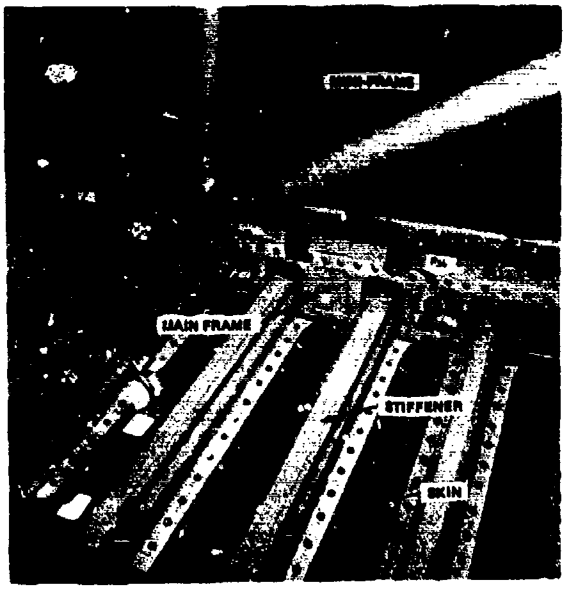

Fig. 24 - General view looking inside wing cavity from wing (including leading edge); acoustic test WA-19

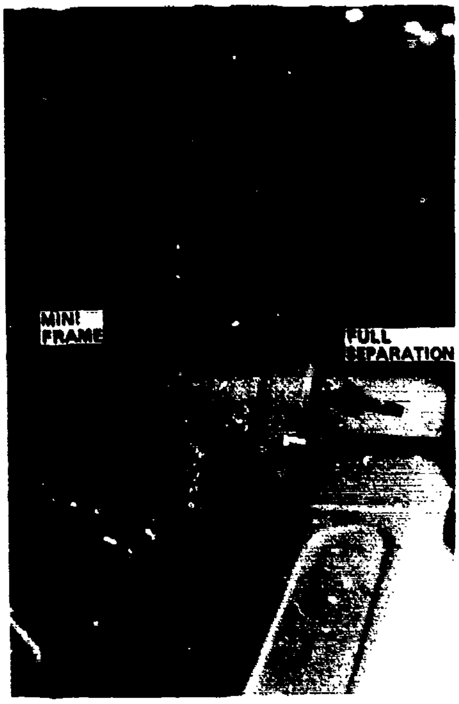

Fig. 25 - Mini-frame complete failure from acoustic test of wing (with leading edge); WA-19

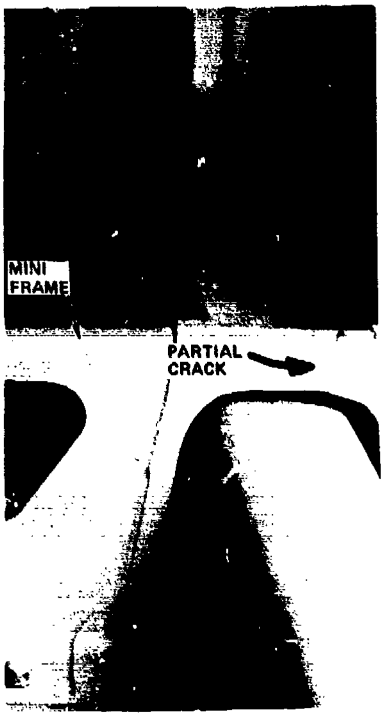

Fig. 26 - Partial crack of mini-frame from acoustic test of wing (with leading edge); WA-19

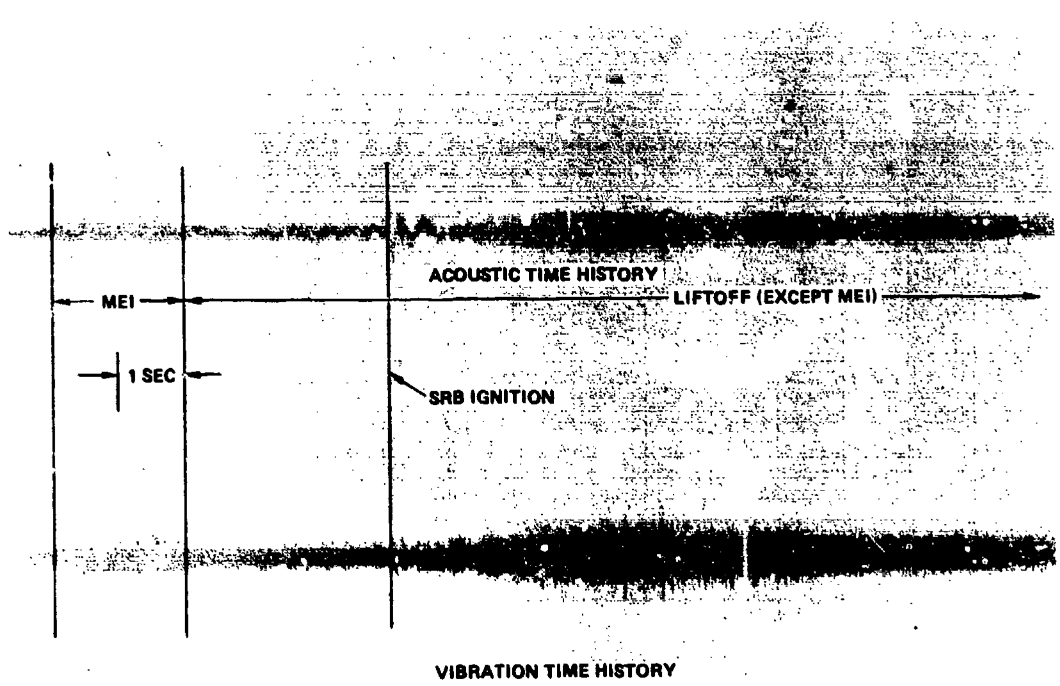

Fig. 27 - Wing vibration and acoustic time histories from STS-1

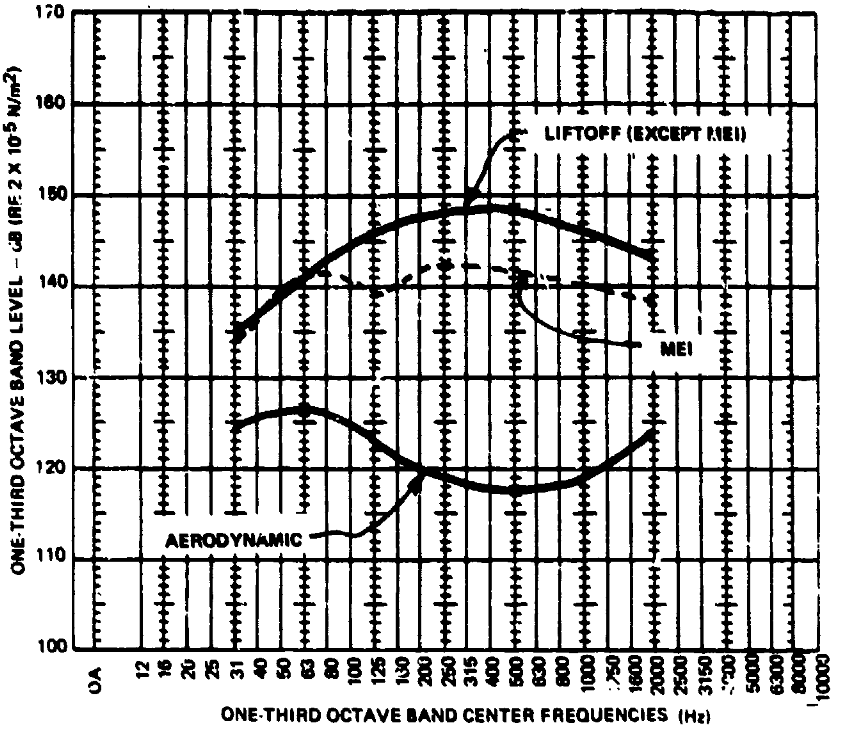

Fig. 28 - Wing acoustic spectra obtained from STS-1

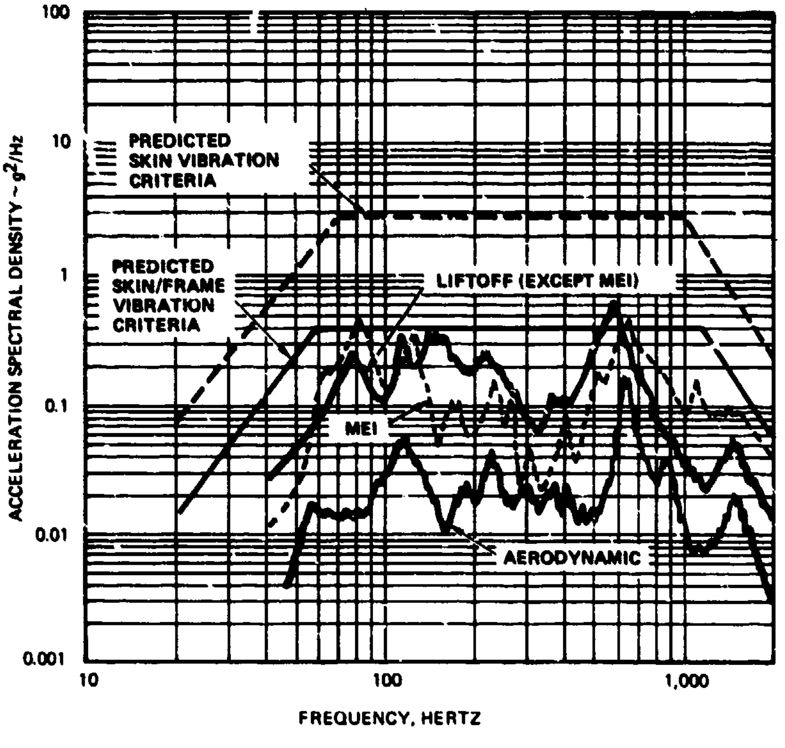

Fig. 29 - Random vibration response data obtained from wing skin measurement on STS-1 and predicted skin and skin-frame interface vibration criteria

STS-1. Fig. 30 displays a comparison of external and internal noise during liftoff of Shuttle flight STS-1.

WING (WITH LEADING EDGE) COMPARISONS AND OBSERVATIONS

Figs. 20 and 28 show the predicted and measured flight acoustic spectra for the liftoff and aerodynamic conditions. The liftoff (except MEI) levels compare favorably. MEI levels above 80 Hz are lower than the liftoff (except MEI) levels by as much as 8 dB. As shown in Fig. 28, the flight aerodynamic spectrum is at least 10 dB lower than the flight liftoff environment and certainly lower than predicted (predicted not shown because of composite).

Figs. 22 and 29 display the vibration of the wing skin from the acoustic and flight test and the predicted vibration critera for the skin and skin-frame interface. The acoustic test vibration response is at least 6 dB higher than the flight liftoff environment except at 600 Hz. The flight aerodynamic vibration shown in Fig. 29 is much lower than the liftoff case. This was expected because of the difference in the acoustic ground and flight test spectra.

Figs. 21 and 30 show that the acoustic and flight test external to internal noise differences compare favorably. The flight test external to internal noise transmission exceeds the 10 dB predicted value.

The exposure time for the liftoff condition for the acoustic test [Ref. 9 and 22] and the flight test at high amplitude (Fig. 27) was 5 sec.

Some conclusions from these comparisons are:

- Even though the acoustic environments compared favorably, the vibration response was lower except at 600 Hz. The result was that the acoustic test conducted was conservative at damaging frequencies.
- Durations at the liftoff condition were the same for the acoustic and flight test; therefore, the acoustic test duration was adequate.
- As in the case of the body flap, the flight aerodynamic acoustic and vibration environments were much lower than liftoff and therefore their contribution to fatigue damage was considered negligible. A composite criteria for the liftoff and aerodynamic conditions for the acoustic test was justified.
- Even though the ground test vibration response at the skin-frame interface exceeded the vibration criteria, the flight data measured on the skin clearly indicates the prediction was conservative (Fig. 29).

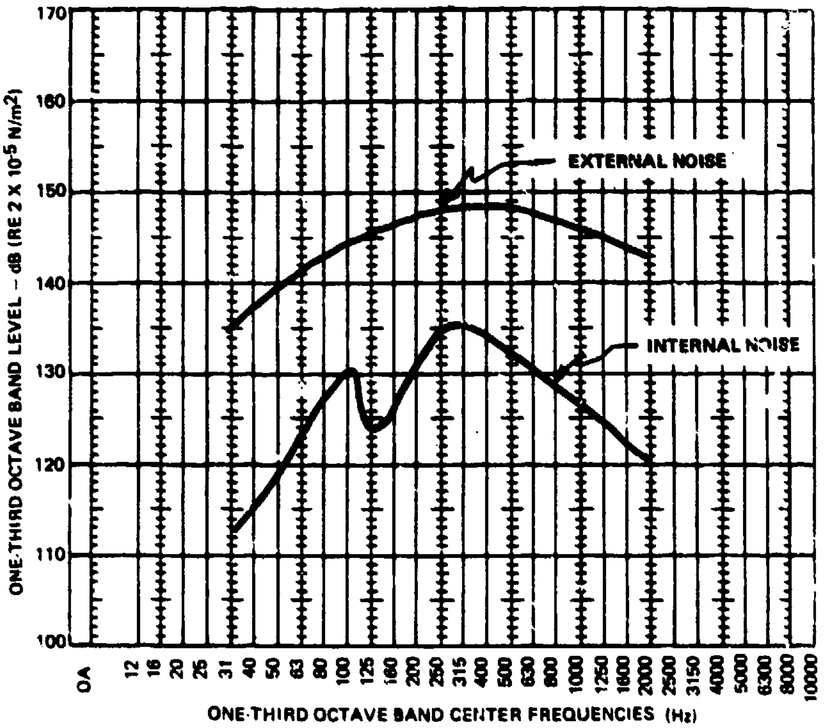

Fig. 30 - Comparison of wing external and internal noise obtained during liftoff of STS-1

WING (INCLUDING LEADING EDGE) RETEST

The acoustic test article has been reconfigured and additional testing of the TPS associated with the wing leading edge (RCC, attach points, and internal thermal insulation) is planned. The test article nomenclature was also revised to T35. The revised acoustic test environment was established using flight data, and, as in the case of the body flap, the vibroacoustic test method concept. Fig. 31 shows the revised acoustic test criteria for the planned test. Duration for the test were developed using data shown in Fig. 27.

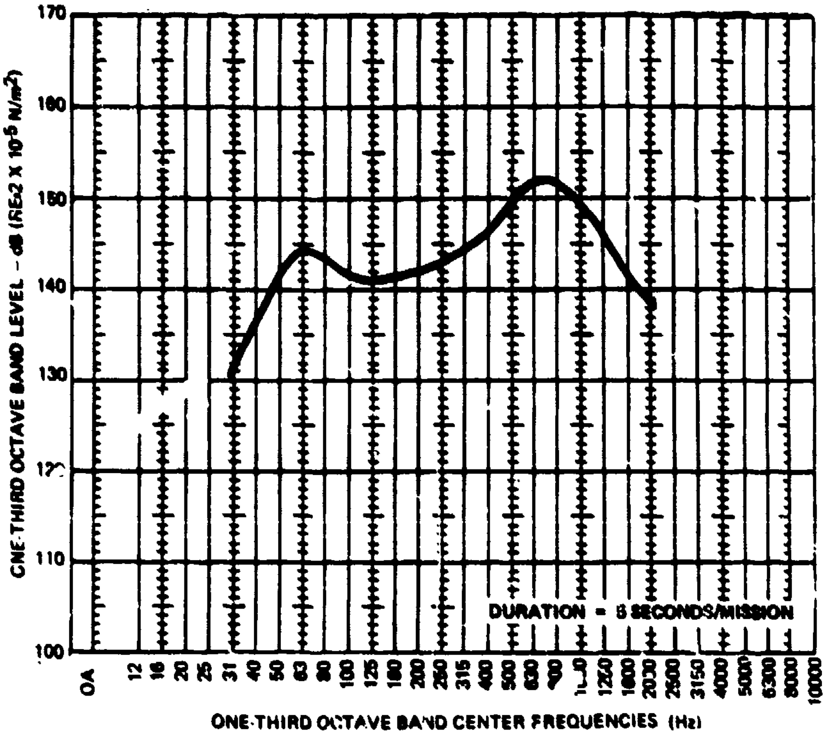

Fig. 31 - Revised acoustic criteria for the wing leading edge; acoustic test T35

ACKNOWLEDGEMENT

The author wishes to thank the many people in the Vibration and Acoustics Group at Rockwell's Space Transportation & Systems Group, particularly Parry Himelblau Jr., and the Structures and Mechanics Division of the National Aeronautics and Space Administration's Johnson Space Center who have contributed their time, knowledge, and effort in the pursuit of this project.

REFERENCES

1. Thompson, R.F., "Space Shuttle Dynamics," *Shock and Vibration Bulletin 44, Pt. 2*, Aug. 1974, pp. 1-17.

2. Malkin, M.S. and Jeffs, G.W., "Space Shuttle 1976: Into Mainstream Development," *Astronautics and Aeronautics*, Vol. 14, No. 1, Jan. 1976, pp. 40-43

3. McIntosh, G.P. and Larkin T..., "The Space Shuttle's Testing Gauntlet," *Astronautics and Aeronautics*, Vol. 14, No. 1, Jan. 1976, pp. 44-56.

4. Strouhal, G. and Tillian, D.J., "Testing the Shuttle Heat Protection Armor," *Astronautics and Aeronautics*, Vol. 14, No. 1, Jan. 1976, pp. 57-65.

5. Stevens, R.A., "Shuttle Orbiter Acoustic Fatigue Testing," *Journal of Environmental Sciences*, Vol. XIX, No. 2, Mar/Apr. 1976, pp. 23-27.

6. Vibration and Acoustic Unit, "An Interim Report on Shuttle Orbiter Vibroacoustics," *Shock and Vibration, Bulletin 47, Pt. 3*, Sept. 1977, pp. 157-201.

7. Korb, L.J. and Clancy, H.M., "Shuttle Thermal Protection System: A Material and Structural Overview," *Material and Process Application to Land, Sea, Air and Space*, Vol. 26, Soc. Adv. Mat. Process Engr., Apr. 1981, pp. 232-249.

8. Cooper, P.A. and Holloway, P.F., "The Shuttle Tile Story," *Astronautics and Aeronautics*, Vol. 19, No. 1, Jan. 1981, pp. 24-36.

9. "Space Shuttle Vibration and Acoustics Unit," *Space Shuttle System Acoustics and Shock Data Book*, Rockwell SD 74-SH-0082A, Dec. 1976.

10. "Shock and Vibration Handbook" edited by C.M. Harris and C.E. Crede, McGraw Hill, 1961.

11. Stevens, R.A., *Engineering Analysis Report: Nose Cap Systems Phase A (FFA-01T5) Acoustic Fatigue Test*, Rockwell SOD 80-0284, Sept. 1980.

12. Stevens, R.A., *Engineering Analysis Report Forward Fuselage Underbody (FFA-04) Acoustic Fatigue Certification Test*, Rockwell SOD 80-0496, Dec. 1980.

13. Stevens, R.A., *Engineering Analysis Report Mid Fuselage Bottom Panel (DA-11A) Acoustic Fatigue Certification Test*, Rockwell STS 81-0289, Jan. 1981.

14. Stevens, R.A., *Engineering Analysis Report: Forward Reaction Control Subsystem (FFA-06) Acoustic Fatigue Certification Test*, Rockwell SOD 80-0434, Nov. 1980.

15. Stevens, R.A., *Engineering Analysis Report: Forward Payload Bay Door/Radiator (PBA07-1) Acoustic Fatigue Certification Test*, Rockwell SOD 80-0476, Dec. 1980.

16. Stevens, R.A. *Engineering Analysis Report: Aft Payload Bay Doors (PBA07-2) Acoustic Fatigue Certification Test*, Rockwell SOD 80-0465, Nov. 1980.

17. Stevens, R.A., *Engineering Analysis Report Mid Fuselage Side Wall Panel (MFA-08) Acoustic Fatigue Certification Test*, Rockwell SOD 80-0400, Sept. 1980.

18. Stevens, R.A., *Engineering Analysis Report: Mid Fuselage Shadow and Carry-Through Panels (MFA-09 and MFA-10) Acoustic Fatigue Certification Test*, Rockwell SOD 80-0475, Nov. 1980.

19. Stevens, R.A., *Engineering Analysis Report: Body Flap (One-Half Span) AFA-15 Acoustic Fatigue Certification Test*, Rockwell SOD 80-0458, Nov. 1980.

20. Stevens, R.A., *Engineering Analysis Report: Vertical Stabilizer (Upper Half) VSA-16 Acoustic Fatigue Certification Test*, Rockwell SOD 80-0466, Nov. 1980.

21. Stevens, R.A., *Engineering Analysis Report: Wing/Elevon (WA-18) Acoustic Fatigue Certification Test*, Rockwell STS 81-0250, Mar. 1981.

22. Stevens, R.A., *Engineering Analysis Report: Wing Leading Edge System (WA-19) Acoustic Fatigue Test*, Rockwell SOD 80-0348, Sept. 1980.

23. Stevens, R.A., *Engineering Analysis Report: OMS Pod AFA-26 Acoustic Fatigue Certification Test*, Rockwell STS 81-0251, Jan. 1981.

24. Stevens, R.A., *Engineering Analysis Report: Aft Reaction Control System Pod (AFA-25) Acoustic Fatigue Test*, Rockwell SOD 80-0427, Jan. 1981.

25. Piersol, A.G. and Pope, L.D., "Analytical and Experimental Evaluations of Space Shuttle TPS Tile Vibration Response," *Journal of Sound and Vibration*, to be published.

26. West, W.M., "Single-Point Random Modal Test Technology Application to Failure Detection," *Journal of Sound and Vibration*, to be published.

27. Stevens, R.A., Allen, H.C. and Pratt, H.K., "Vibration Qualification of Fly-Away Umbilical by Acoustic Test Method," *Institute of Environmental Sciences*, Vol. 2, Apr. 1967, pp. 437-442.

SPACE SHUTTLE THERMAL PROTECTION SYSTEMS

STRUCTURAL CHARACTERISTICS OF THE SHUTTLE ORBITER CERAMIC THERMAL PROTECTION SYSTEM

Paul A. Cooper
NASA Langley Research Center
Hampton, Virginia

The ceramic Thermal Protection System (TPS) consists of ceramic tiles bonded to felt pads which are in turn bonded to the Orbiter substructure to protect the aluminum substructure from the heat of reentry. The successful certification of the TPS for first flight required the joint effort of several NASA centers, the prime contractor, and university consultants led by the TPS system managers from the NASA Johnson Space Center. This paper describes the TPS and addresses the results of some of the experimental work including dynamic response studies performed at the NASA Langley Research Center in support of the efforts to certify the TPS for flight.

INTRODUCTION

Based on both weight and cost considerations, the Shuttle Orbiter was designed in large part as a conventional skin-stringer aluminum aircraft structure. The properties of aluminum dictate that the maximum temperature of the skin be maintained below 350 F. Aerothermal heating during ascent and reentry creates surface equilibrium temperatures well above this level and, in many places, above the melting point of aluminum. This heating necessitates some form of insulation. The Shuttle design goal of 100-mission reusability with minimum turnaround time between flights dictated the use of a lightweight, nonablative Thermal Protection System (TPS) which could withstand the thermal cycles and environmental loads of space flight.

In the early 1970s, NASA and the Space Division of Rockwell International, the prime contractor for the Orbiter, agreed to use a newly developed TPS ceramic material formulated and manufactured by Lockheed Missiles & Space Co. The TPS acts as an excellent insulation for surface equilibrium temperatures up to 2300 F. This ceramic is highly brittle and has strain-to-failure performance of approximately 0.002--considerably below the expected combined mechanical and thermal operating strain of the aluminum skin. In addition, the ceramic has a coefficient of linear thermal expansion well below that of aluminum. Thermal and mechanical expansion and contraction of the aluminum skin would crack ceramic material bonded directly to it.

To protect the reusable surface insulation (RSI) from excessive strain, the ceramic insulation was placed on the aluminum in the form of individual tiles with side dimensions of the order of six inches or less. About 30,000 tiles of various sizes and shapes cover slightly over 70% of the Orbiter's exterior. Gaps between the tiles allow for relative motion as the aluminum skin expands or contracts and the substructure deforms. The allowance for relative motion alone is not sufficient to protect the integrity of the ceramic material. To isolate the strain of the aluminum substructure from the tile, the tile is first bonded to a strain-isolator pad (SIP) using an elastomeric, room-temperature-vulcanizing (RTV) silicone adhesive. Then the tile and SIP combination is bonded to the aluminum skin with the same adhesive. The SIP has very low shear and extensional moduli and protects the brittle ceramic material from deformations of the aluminum structure.

Initially, the loads expected on the TPS came well within the strength of RSI and SIP. As the design of the Orbiter progressed, mission requirements became firmer and load predictions became refined. It became obvious that the TPS would have to withstand loads higher than initially anticipated. Although the refined loads reduced margins of safety, in most cases they caused stresses within the strength of RSI and SIP if considered independently. Because of budgetary constraints on the project, tests of the TPS as a complete system of RSI/RTV/SIP were delayed till the spring of 1979 when most of the tiles had been already installed on the first orbiter. These tests of the RSI/RTV/SIP as a system revealed the system tensile strength to be significantly less than the tensile strength of the individual components. This situation caused negative margins of safety over large areas of the Orbiter TPS.

An intense effort--involving several NASA centers, industrial concerns, and universities--was mounted to understand thoroughly the TPS as a structural system and solve the problems associated with the high-load areas. As a part of this effort, in the fall of 1979 Langley Research Center began investigating static and dynamic structural mechanics of the TPS and its individual components. The results of this investigation will be used to give the reader insight into the material and structural characteristics of the TPS, the problems in its design that contributed to the delay of the first launch, and the techniques used to resolve these problems.

TPS DESCRIPTION

The isotherm plot in Fig. 1 gives typical expected maximum surface temperatures for the Orbiter in a nominal trajectory--a range of maximum surface equilibrium temperatures from a low of 600 F on the upper surface aft of the cockpit to a high of almost 2700 F at the fuselage nosecap. The Orbiter's skin (mainly 2024, 2219, or 2124 aluminum, with graphite/epoxy used for the cargo-bay door) has, as mentioned, a designed maximum use temperature of 350 F, thus all surfaces must be insulated.

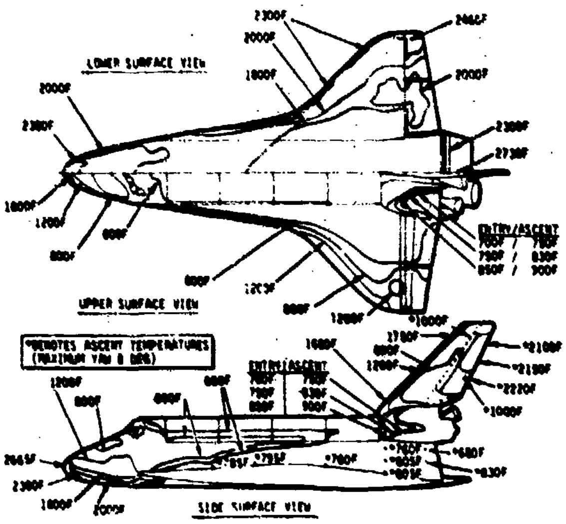

Fig. 1 - Maximum surface temperatures expected

The various insulation procedures used for temperature control of the structural skin (see Fig. 2) include reinforced carbon-carbon (RCC), two types of ceramic reusable surface insulation tiles, and a limited amount of nonreusable ablative material. RCC, a carbon cloth impregnated with additional carbon, heat-treated, and then coated with silicon carbide, has a reuse temperature of 2900 F. The two types of ceramic RSI tiles, one of which is made in two different densities, cover regions experiencing surface temperatures between 700 and 2300 F. A blanket of Felt Reusable Surface Insulation (FRSI) coated with room-temperature curing silicon covers areas where surface temperatures do not exceed 700 F during entry or 750 F during ascent.

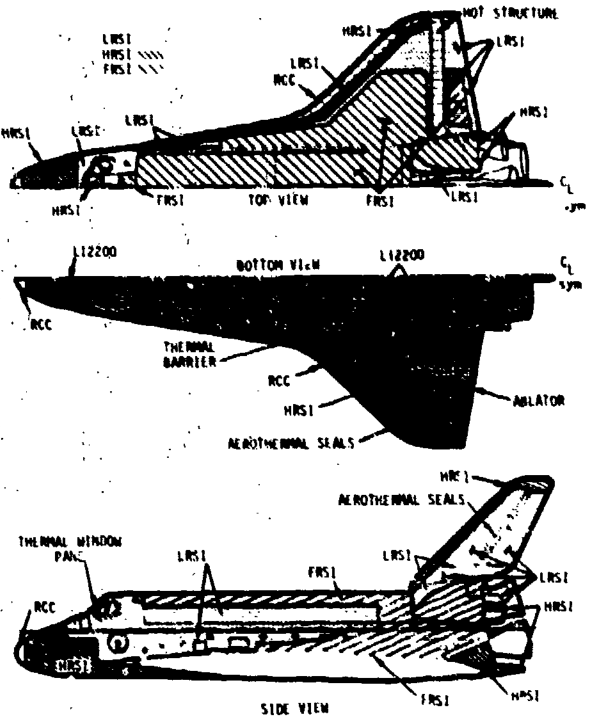

Fig. 2 - Distribution of TPS

Other thermal barriers include thermal windows, aerothermal seals to restrict hot-gas flow into control-surface cavities, and tile filler bars (strips of coated felt bonded to the structural surface between tiles to prevent direct heat-radiation or convection to the skin). Tile-gap fillers--pads made from an alumina mat covered with a ceramic fabric--bonded to filler bars between tiles in high-pressure-gradient areas restrict the flow of hot gas between adjacent tiles. Pads of this type are also used as thermal barriers around structural penetrations such as landing gear doors. Internal blankets are used as insulation to protect the structure from internal surface heat radiation where RCC is used, and are used extensively throughout for thermal management.

There are three types of ceramic RSI: Class I, Class II, and LI-2200 tiles:

Class I tiles cover areas where the maximum surface temperature should run between 700 and 1200 F. They have a white ceramic coating with a low solar absorptance to help maintain low temperature in orbit by reflecting solar radiation. These tiles are designated Low-temperature Reusable Surface Insulation (LRSI).

Class II tiles cover areas where the maximum surface temperatures are between 1200 and 2300 F. They have a black ceramic coating with a high surface emittance to radiate heat efficiently during reentry. These tiles are designated High-temperature Reusable Surface Insulation (HRSI).

Lockheed manufactures both the Class I and Class II tiles from a 9 lb/ft^3 ceramic RSI designated LI-900. The third type of ceramic RSI, designated LI-2200, has the same coating as Class II tiles but a higher density (22 lb/ft^3) and strength. The Orbiter uses only a small number of LI-2200 tiles in areas of high concentrated loads, usually around penetrations such as landing-gear doors or in the forward-fuselage area near RCC interfaces where higher heat resistance is required to handle surface temperatures which can reach 2600 F. Tile thickness varies according to heat load and requirements for maintaining the aerodynamic outer moldline. The tiles range from less than 1/2 in. thick for LRSI at the upper mid-fuselage region to 6 in. thick for HRSI on the body flap's lower surface. Both the LI-900 and LI-2200 tiles are cut and shaped from larger ceramic blocks to fit specific Orbiter areas. The blocks are composed of compacted 1.5-micron-diam. silica fibers bound together by collodial silica fused during a 4-hr. sintering process in which temperatures reach 2400 F. The tiles are then coated on five sides with reaction-cured glass (RCG) consisting of silica, boron oxide, and silicon tetraboride and glazed at 2000 F. A silicon polymer waterproofs the uncoated side. The microstructure of the RSI is shown in Fig. 3; voids comprise over 90% of the resultant tile.

The SIP is formed from nylon fibers (trade name Nomex). A barbed needle is passed repeatedly through the pad in a sewing-like procedure which compacts the fibers oriented transversely to the pad to provide tensile strength through the pad thickness (see Fig. 4).

Fig. 3 - Photomicrograph of LI-900 RSI

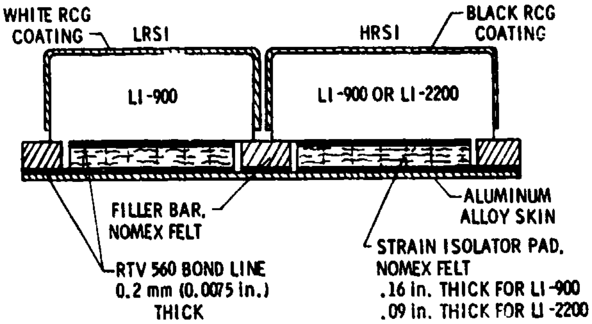

Fig. 5 - TPS assembly

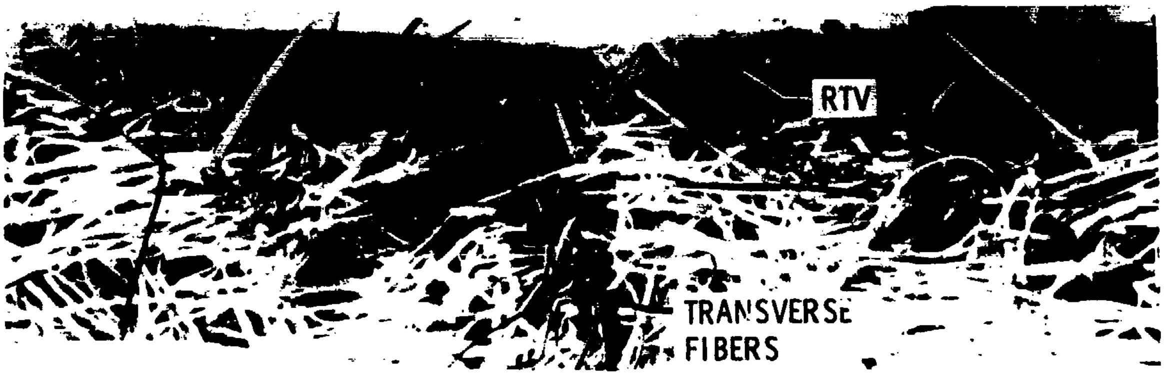

Fig. 4 - Photomicrograph of SIP

Figure 5 depicts the complete TPS assemblage in schematic form, and Fig. 6 shows actual components in various stages of assembly for test specimens. Most filler bars are bonded only to the aluminum substructure, not to the RSI tiles and thus provide a vent path for the SIP during ascent. In selected areas, the tiles also bond to the filler bars to distribute loads over a larger area and reduce the stress on highly loaded tiles. The RCG coating on the sides of the tile does not extend to the filler bar thus allowing the porous tile to vent.

Tensile loads applied normal to the SIP are transmitted across it along the transverse fiber bundles at discrete regions shown in Fig. 4. Stress concentrations from this local load transfer reduce system tensile strength by about

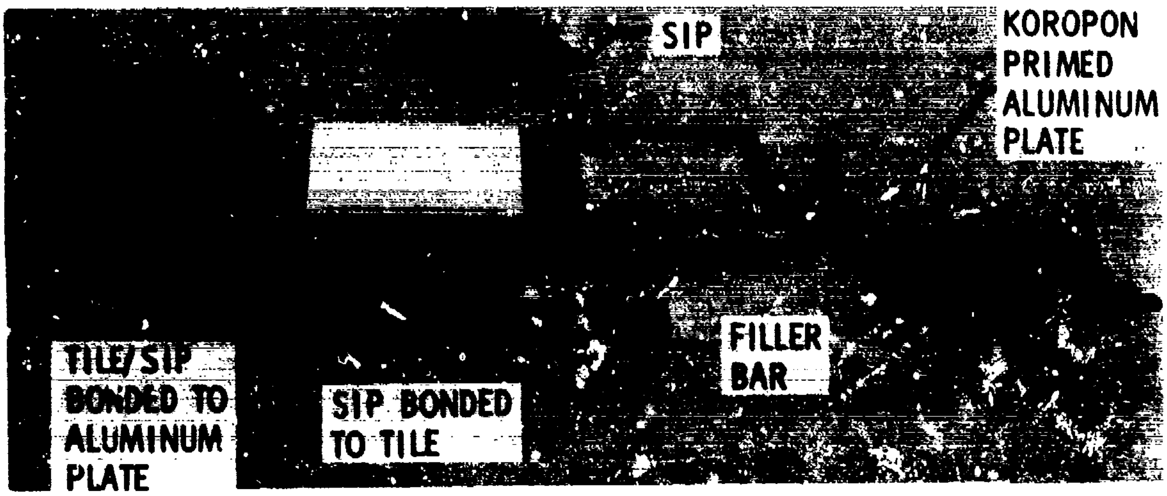

Fig. 6 - TPS assembly sequence

50% for both the LI-900 and the LI-2200 TPS as shown in Table 1. The failure of the system under a transverse tension load occurs at the SIP/RSI interface as shown in Fig. 7.

Table 1

Tensile Strength of TPS Components

	psi
LI-900 Ceramic RSI	24.0*
.160 in. SIP	41.0
RTV 560 Adhesive	480
RTV/LI-900 RSI/RTV/.160 SIP/RTV	11.7
LI-2200 RSI	60.0
.090 in. SIP	68.0
RTV 560 Adhesive	480
RTV/LI-2200 RSI/RTV/.090 SIP/RTV	28.7

* Values obtained from internal Rockwell International Documentation.

Fig. 7 - Tensile failure mode of RSI

A photoelastic study demonstrated that the reduced strength occurred because of the load-transfer mechanisms of the SIP. A highly sensitive photoelastic material was bonded to the SIP using RTV adhesive. The photoelastic material gives optical signals proportional to the internal stress level when viewed under polarized light. Figure 8 shows the photoelastic specimen loaded in tension and the expected resultant stress field for RSI bonded to SIP. The SIP/photoelastic-material interface exhibits discrete stress risers all along the interface. In contrast, the aluminum/photoelastic material interface shows only corner stress concentrations caused by the differential stiffnesses of the materials. The stress concentration factors measured at the SIP/photoelastic-material interface were as high as 1.9 and account for the reduced strength of the SIP/RSI assemblage.

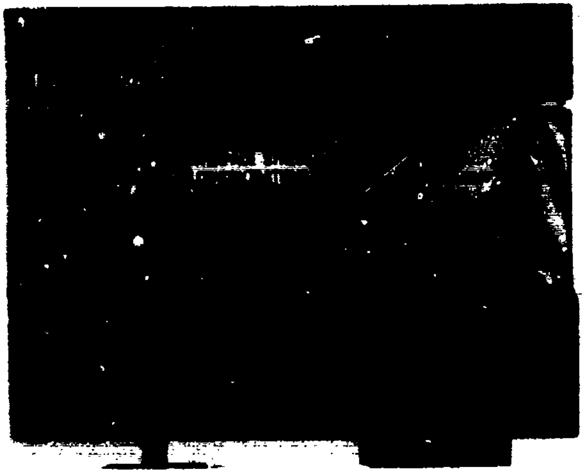

Fig. 8 - Photoelastic study of SIP load transfer to RSI

DENSIFICATION OF BONDING SURFACE

In 1979, Rockwell International, NASA-Johnson and -Ames investigated several procedures to strengthen this RSI/SIP interface. The most effective of these procedures was a densification of the bonding surface of the RSI. In the densification procedure, the voids between fibers at the bonding surface are filled by a ceramic slurry--a mixture of DuPont's Ludox (a colloidal silica) and a silica slip consisting of a mixture of small particles of silica and water. A controlled amount of this mixture, pigmented to give an identifying light-gray color, is brushed on the surface to be densified. The mixture is air-dried for 24 hours and oven-dried at 150 F for 2 hours and then waterproofed by exposing the tile to vapors of methyltrimethoxy silane (Dow-Corning Z-6070) and acetic acid at 350 F. This mixture provides a hard, strong, nearly continuous densified layer. The density decreases gradually toward the interior of the tile. Most of the densification material remains within 0.11 in. of the bonding surface for the LI-900 RSI. The photomicrograph of the bonding surface in Fig. 9 clearly shows the larger particles and the result of densification by comparison with the undensified RSI shown in Fig. 3.

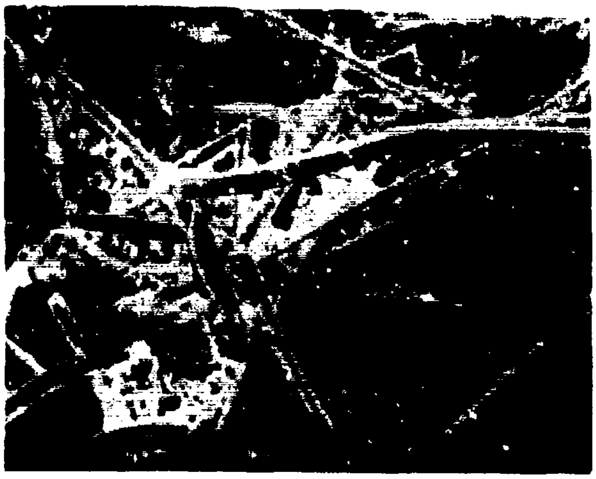

Fig. 9 - Photomicrograph of densified tile

Densification of the tile surface strengthens the SIP/tile interface sufficiently so that the high concentrations of stresses at the interface can be supported and redistributed. Failure under static tensile load occurs in the RSI outside the densified zone for the LI-900 RSI as shown in Fig. 10 and either in the RSI outside the densified zone or in the SIP for the LI-2200 RSI. Densification increases the average static tensile strength almost 100% for the LI-900 RSI and over 60% for the LI-2200 RSI, as shown in Table 2.

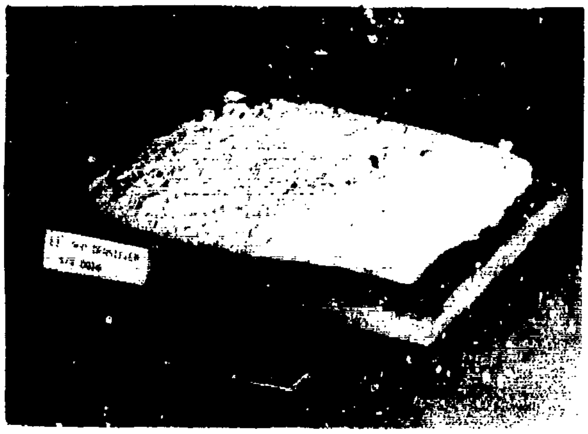

Fig. 10 - Tensile failure mode of densified TPS

Table 2

Comparative Strength of Densified
and Undensified TPS

0.160 SIP/undensified LI-900..............	11.8
0.160 SIP/densified LI-900................	22.6
0.090 SIP/undensified LI-2200..............	30.2
0.090 SIP/densified LI-2200................	46.3

PROOF TEST

To obtain allowable-strength predictions, a large number of tensile tests of individual material components (the RSI, SIP, and RTV) preceded full-scale tile production. When it was discovered that the system had considerably less strength than the weakest of the individual components, these "allowable" values could no longer be used in evaluating the margin of safety of the tile at various places on the Orbiter. Indeed, new statistical interpretations of a small number of complete system tests (RSI/RTV/SIP/RTV) indicated that a large number of tiles already installed on the Orbiter possessed negative margins.

Rather than rely on such predictions, a proof tensile load equal to 1.25 to 1.4 times the maximum equivalent static load expected during flight (limit load) was applied to tiles already installed on the Orbiter. Figure 11 shows the proof-test fixture which incorporated a vacuum chuck to load a tile. If a tile survived the proof load, presumably it had sufficient static strength to give a positive margin of safety. Failure under proof test was determined by either separation from the substructure or exceedance of measured noise counts in an acoustic emission test. If a tile failed under proof test, it was removed and densified

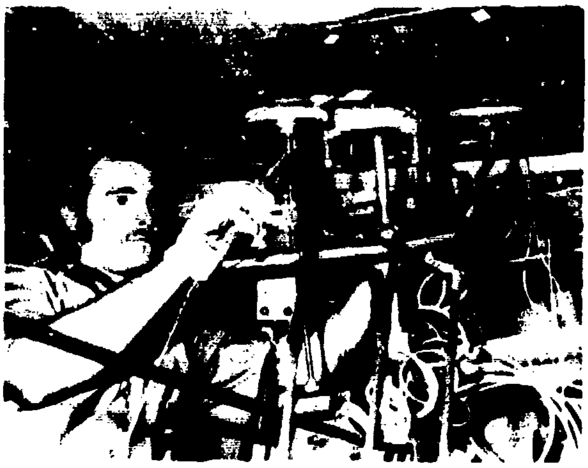

Fig. 11 - Proof test of installed tiles

or replaced with a densified tile. In addition, any tile whose predicted limit stress dictated a proof stress higher than 10 psi was automatically removed, densified, and reinstalled. Every HRSI tile installed after October 31, 1979, has been a densified tile.

Moreover, since the strength of a densified system now depends on the strength of the RSI, a nondestructive test has been introduced that assures using only high-strength RSI tiles. On the basis of several hundred tensile tests, Rockwell has found a strong correlation between the velocity of sound through the tile material and its tensile strength. The combination of tile-material acceptance based on this sonic test and verification of the strength of the bond from the tension tests of tiles in place assures the integrity of the densified tiles under static loading.

SIP STATIC RESPONSE

Problems other than the SIP/RSI interface strength attend the design of the TPS. A tensile load applied normal to the plane of the SIP and slowly increased deforms the SIP a considerable amount at very low loads. As transverse fibers straighten and begin to carry load, the stiffness of the SIP increases. As applied load increases, the SIP shows a decreasing rate of deformation for a given increment in load, i.e., the SIP material exhibits a nonlinear stress-strain behavior. The proof load cycle of Fig. 12 demonstrates this nonlinear behavior.

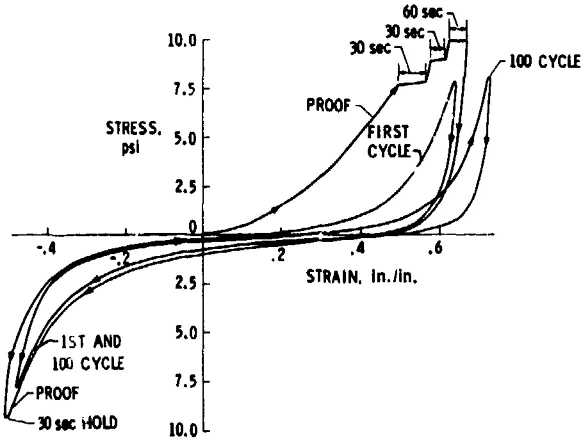

Fig. 12 - Stress-strain behavior of .160 SIP

An added complexity is that during the loading process, transverse fibers realign themselves so that after a complete tension-compression cycle, as would occur during a TPS proof test, the material not only has a permanent set but also has a different and even more nonlinear response to subsequent loads. This behavior is shown in the first cycle loading in Fig. 12 which would be the expected response character of the SIP during the first ascent mission.

Indeed, the form of the static response of the SIP to load continuously changes as more load cycles are applied. The material develops a continuously increasing region of low stiffness. The SIP material behavior thus is highly nonlinear, dependent on its prior load history, and after "load conditioning" has a sizeable low-stiffness region.

Tests also show that under constant load the SIP can exhibit a large amount of nonrecoverable creep and that the ultimate strength is a function of the rate of loading. At higher load-rates the SIP exhibits higher strengths. The shear characteristics of the SIP have similar nonlinear behavior.

Based on the SIP stress-strain response after a proof test has been performed, analysis shows that higher stresses result at the tile/SIP interface under certain load conditions than would be predicted by linear analysis. In general, the nonlinear analysis predicts higher stresses in the SIP than a linear analysis unless the loading is primarily caused by substructure deflection.

TPS DYNAMIC RESPONSE

The SIP's nonlinear displacement under load causes an unusual response of the TPS to sinusoidal dynamic acceleration. The resulting distorted wave form has a sharp peak acceleration as shown in Fig. 13. This behavior causes stress amplification of the maximum input acceleration of up to a factor of 4 at resonance. The Orbiter, however, should experience only random vibration input during a mission and the TPS is not expected to have an amplification of this magnitude.

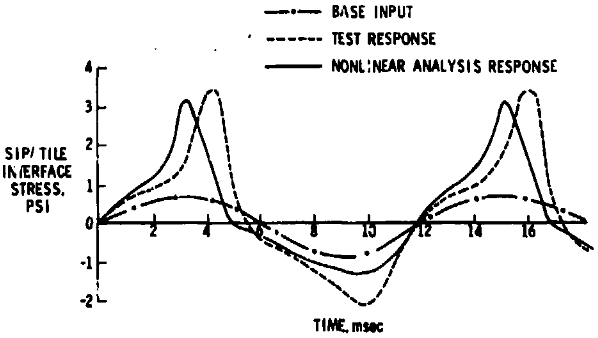

Fig. 13 - Tile response to sinusoidal base shake

Nonlinear characteristics of TPS material and its resultant variable damping create a complex dynamic response. For example, the natural response frequency of the SIP is a function of the applied acceleration, and thus varies with dynamic load. Also, inspection of the transverse fibers (see Fig. 4) in the SIP shows that they do not run completely normal to the plane of the pad, so the in-plane and normal motions of the SIP are coupled. A dynamic analysis accounting for these complexities has been developed that contains both material and viscous damping effects evaluated empirically from vibration tests. A comparison of analytical vs. experimental response to a base drive sinusoidal input is shown in Fig. 13.

An additional dynamic response has been observed in controlled tests and predicted with the nonlinear dynamic analysis. At a driving frequency normal to the tile/SIP interface and different from the natural frequency of the TPS, a large lateral parametric response develops at half the driving frequency. This dynamic instability could become critical under sinusoidal dynamic inputs. It does not develop to any degree under random input, however; and since random inputs only are expected during flight, this instability is not felt to be important.

TPS FATIGUE

Dynamic motion of the TPS poses another concern for structural integrity. Repetitive loadings due to lift-off and high-speed boundary-layer aerodynamic noise plus oscillating shocks repeatedly traversing the tiles could cause fatigue damage.

TPS fatigue curves showing failure stress as a function of number of load cycles are presented in Fig. 14. The greater static strength achieved by densification of the bonding surface of the RSI does not fully translate into an equivalent increase in fatigue strength. The mode of fatigue failure differs between the undensified and densified TPS. Results plotted for the undensified TPS represent failure due to complete separation at the SIP/RSI interface. Results plotted for the densified TPS, on the other hand, represent failure defined as a total out-of-plane SIP deformation of 0.25 in.

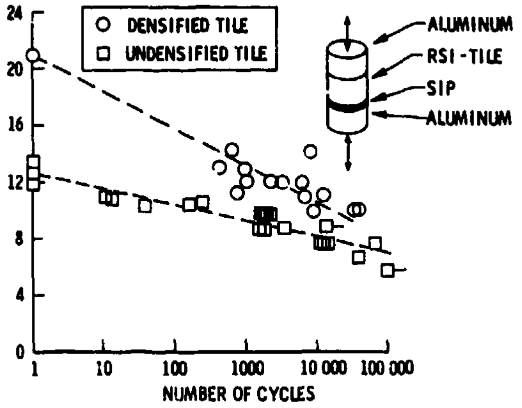

Fig 14 - Fatigue of undensified and densified TPS

Stress-displacement curves of the densified TPS during a typical fatigue test for a constant-amplitude, fully-reversed sinusoidal load applied at 1 Hz are shown in Figure 15. As the number of cycles increases, the SIP continues to unravel with a continual increase in total specimen travel and a continual expansion of the low-stiffness region. Eventually the SIP completely separates, but before this occurs a tile could become loose enough so that a small exciting force during flight might cause it to lift off the filler bar and move into the airstream. The motion of one tile with respect to a neighboring tile during entry could disrupt airflow, trip the boundary layer prematurely, and increase heating downstream. The amount of relative tile motion required to trip the flow depends on the local boundary layer thickness. The measure of acceptable relative motion increases toward the aft end of the Shuttle as the boundary layer thickens. The relative motion between tiles could also allow plasma flow between tiles which could cause unacceptable heating of the filler bar.

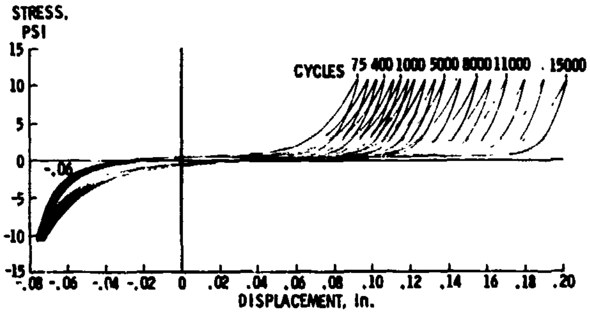

Fig. 15 - Decrease in SIP stiffness during fatigue loading

The fatigue results of Fig. 14 show that cyclic loading causes a relatively large reduction in the stress levels that both the densified and undensified TPS can withstand for a small number of cycles. Since the fatigue failure of densified TPS takes the form of excessive elongation of the SIP, rather than separation in the parent RSI, a further increase in strength of the RSI ceramic by chemical reformulations or changes in manufacturing processes would not improve the TPS lifetime. In fatigue, SIP represents the weak link in the densified TPS.

Since undensified tiles have less life expectancy than the densified tiles, NASA plans to remove and densify the remaining undensified tiles during the normal refurbishment periods between developmental flights.

MISSION RANDOM DYNAMIC LOADS

The sinusoidal dynamic tests which indicated the possibility of large acceleration response due to base drive and the fatigue tests of undensified tile TPS which indicated a possible low cycle fatigue problem dictated an additional series of tests. The tests, which simulated in the laboratory the expected major dynamic random loads the TPS should experience during ascent, were performed to gain confidence that those undensified tiles which passed their static proof test and thus were not replaced would survive the first flight during ascent.

During a typical shuttle flight, the tiles experience a variety of loads including main engine and solid rocket motor ignition overpressures during liftoff, substructure motions due to engine vibrations and aerodynamic loadings, direct acoustic pressure loads caused by boundary-layer noise, and differential pressures due to shock passage, aerodynamic gradients and gust loads, and tile buffeting due to vortex shedding from connecting structure. Many of these loads are dynamic rather than steady, raising the question of the fatigue strength of the undensified TPS when subjected to random dynamic loading at stress levels below the maximum stress level established as acceptable by the static proof test. The number of specimens and the load ranges investigated were limited since the intent of the tests was not to provide an exhaustive fatigue study of the TPS but rather to obtain an evaluation of the expected behavior of the TPS under dynamic loading expected during ascent.

The test fixture is shown in Fig. 16 and consists of a thin aluminum plate riveted to five thickwalled aluminum tubes. The fixture is designed so that after the tile is bonded to the plate, the plate can be deformed to a shape typical of substructure deformations expected in the Orbiter. By bolting the tubes to a rigid base plate with shims under alternate tubes, the aluminum plate deforms to approximately a sine wave with the wave amplitude given by the shim thickness.

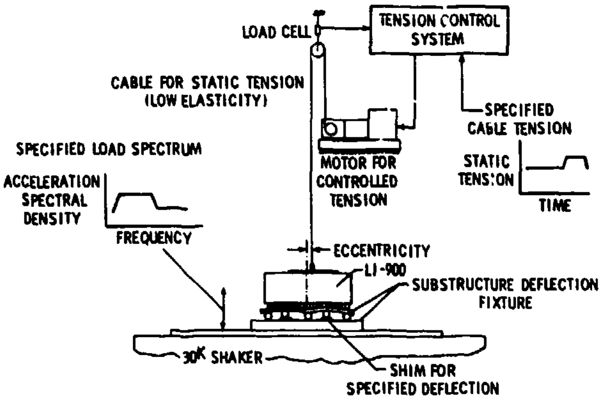

Fig. 16 - TPS mission cycle fatigue tests

Each specimen is given a proof test prior to its acceptance for testing in accordance with techniques approved for proof testing TPS on the orbiter. After proof testing, the fixture is bolted to the rigid plate with shims in place and instrumented with lightweight accelerometers and noncontacting displacement probes. The entire system is mounted to a 30,000 lb shaker. The prescribed broadband random drive acceleration of the tile base plate in the direction normal to the tile/SIP interface was controlled for all specimens and represented a given orbiter region.

To combine the steady state tensile load with the dynamic and local substructure deformation loads, a soft bungee cord was attached to a thin metal plate bonded to the top of the tile at a point offset from the tile center of gravity. The static tension and moment levels were controlled with an automatic control system activated by signals from another channel of the analog drive tape. A schematic of the complete test setup is shown in Fig. 16. During a test, the shape of the input spectrum is fixed (see Fig. 17 for an example of the drive spectrum) but the power level and the static tension levels are changed to simulate different ascent conditions for the wing and mid-fuselage region.

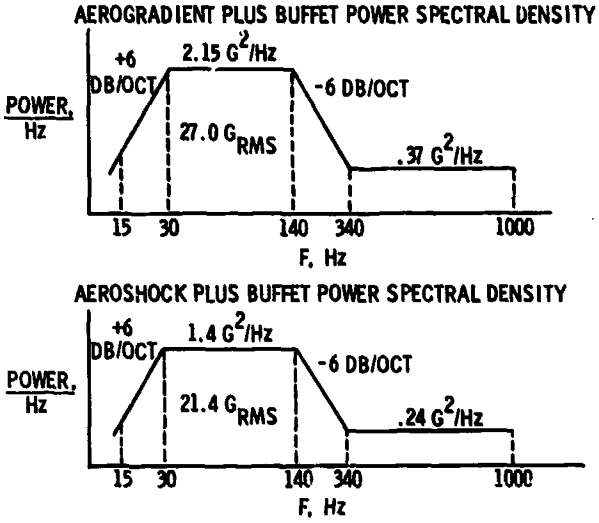
AEROGRADIENT PLUS BUFFET POWER SPECTRAL DENSITY

AEROSHOCK PLUS BUFFET POWER SPECTRAL DENSITY

Fig. 17 - Random vibration spectra wing region

Although the primary intent of the test series was to gain confidence in the reliability of the TPS under simulated load conditions, the tests provided an opportunity for obtaining random dynamic response information on the TPS under controlled conditions. Raw tile acceleration data provided the source data for subsequent detailed analyses of tile response characteristics including power spectral densities, cross spectral densities, coherences, transfer functions, probability density functions and cumulative distribution functions. An example of tile output transfer functions over the active drive frequency range is shown in Fig. 18.

At the conclusion of the ascent mission dynamic simulation tests, each specimen was reproofed and its static response compared with that measured during the initial proof test to determine the extent of tile loosening which might have occurred due to possible degradation of SIP stiffness. Each unit was then given a static tensile test to failure to determine its residual strength with the results summarized in Table 3.

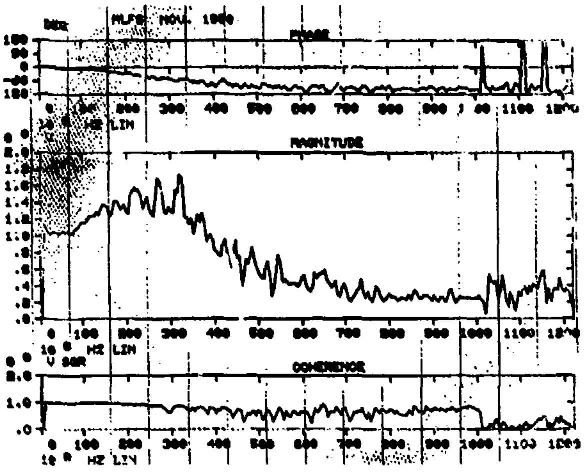

Fig. 18 - Sample response spectrum measured at tile center

Table 3

SPECIMEN RESIDUAL STRENGTH AFTER RANDOM FATIGUE TEST

	NOMINAL MAXIMUM DYNAMIC STRESS TEST LEVEL	STATIC ULTIMATE STRENGTH AFTER DYNAMIC TESTS
W-3 REGION (PROOF LEVEL IS 8 PSI)	6.4 psi	13.6 psi
	6.4	12.6
	6.4	11.7
	6.4	11.0
	7.3	14.3
	7.3	12.0
	7.3	11.7
	7.3	9.0
MF-5 REGION (PROOF LEVEL IS 6 PSI)	4.8	15.4
	4.8	14.0
	4.8	13.3
	4.8	12.1
	5.5	15.4
	5.5	15.0
	5.5	13.6
	5.5	11.8

All specimens survived an equivalent of 72 ascent missions and exhibited residual static strength greater than their original proof loads. These results indicate that the undensified tiles had sufficient strength to withstand ascent loads during the first few flights.

CONCLUDING REMARKS

Recent experiments and stress analyses have shown the original TPS to have marginal strength in many areas of the Orbiter. Modifications of the TPS, such as tile densification, have been made to correct these strength deficiencies. Densification of the tile surface brings the system static strength up to the strength of individual components. The failure level in static tension can thus be predicted accurately using nondestructive sonic testing of the RSI before bonding.

Densified TPS is sufficiently strong in all areas to withstand expected static loads during a mission. In areas where dynamic loads predominate, however, the TPS may have limited life because of excessive SIP extension.

The fragile nature of the brittle ceramic tile and its coating has renewed interest in finding alternative reusable thermal-protection systems. For example, NASA-Ames and Lockheed have developed a stronger but lighter ceramic insulation, called fiber-reinforced ceramic insulation (FRCI).

It will take intense R&D to create and flight-qualify any new TPS with the long-term reliability required for reusable space transportation systems. For the next several years, RSI represents the only reusable TPS ready for flight and even it requires additional effort to insure that it will give the full 100-mission lifetime. All these points notwithstanding, the ceramic RSI is one of the best lightweight thermal insulators ever developed, and in addition to its key role on the Shuttle Orbiter should find wide use in future high technology applications.

BIBLIOGRAPHY

The following publications provide more detail on the material and structural characteristics of the TPS.

— Korb, L. J. and Clancy, H. M., "Shuttle Orbiter Thermal Protection System: A Material and Structural Overview," Presented at the 26th National Symposium Society for the Advancement of Material and Process Engineering, April 28-30, 1981.

— Williams, Jerry G., "Structural Tests on a Tile/Strain Isolation Pad Thermal Protection System," NASA TM 80226, March 1980.

— Housner, Jerrold M., and Garcia, Ramon, "Nonlinear Static TPS Analysis," NASA TM 81785, March 1980.

— Sawyer, James Wayne, and Rummler, Donald R., "Room Temperature Mechanical Properties of Shuttle Thermal Protection System Material," NASA TM 81786, April 1980.

— Ransone, Philip P., and Rummler, Donald R., "Microstructural Characterization of the HRSI Thermal Protection System for Space Shuttle," NASA TM 81821, May 1980.

— Stroud, W. Jefferson, Greene, William H., and Anderson, Melvin S., "Deflections of Beam Columns on Multiple Supports," NASA TM 81829, June 1980.

— Miserentino, Robert, Pinson, Larry D., and Leadbetter, Sumner A., "Some Space Shuttle Tile/Strain-Isolator-Pad Sinusoidal Vibration Tests," NASA TM 81853, July 1980.

— Newman, J. C., Jr. "Notch Sensitivity of Space Shuttle Tile Materials," NASA TM 81854.

— Shore, Charles P., and Garcia, Ramon, "Effect of Substrate Deformation and SIP Thickness on Tile/SIP Interface Stresses for Shuttle Thermal Protection System," NASA TM 81855, July 1980.

— Giles, Gary L., "Substructure Procedure for Including Tile Flexibility in Stress Analysis of Shuttle Thermal Protection System," NASA TM 81864, August 1980.

— Prabhakaran, R., and Cooper, Paul A., "Photoelastic Tests on Models of Thermal Protection System for Space Shuttle Orbiter," NASA TM 81866, August 1980.

— Sawyer, James Wayne, and Cooper, Paul A., "Fatigue Properties of Shuttle Thermal Protection System," NASA TM 81899, November 1980.

— Housner, Jerrold M., Edighoffer, Harold H., and Park, K. C., "Nonlinear Dynamic Response of a Uni-directional Model for the Tile/Pad Space Shuttle Thermal Protection System, NASA TM 81901, November 1980.

— Williams, Jerry G., "Structural Tests on Space Shuttle Thermal Protection System Constructed with Nondensified and Densified LI-900 and LI-2200 Tiles," NASA TM 81903, November 1980.

— Sawyer, James Wayne, and Waters, Allen, "Room Temperature Shear Properties of the Strain Isolator Pad for the Shuttle Thermal Protection System," NASA TM 81900, January 1981.

— Leatherwood, Jack D., and Gowdey, Joe C., "Mission Load Dynamic Tests of Two Undensified Space Shuttle Thermal Protection System Tiles," NASA TM 83148, June 1981.

— Sawyer, James Wayne, "Effect of Load Eccentricity and Substructure Deformations on Ultimate Strength of Shuttle Orbiter Thermal Protection System," NASA TM 83182, September 1981.

— Cooper, Paul A., and Holloway, Paul F., "The Shuttle Tile Story," Astronautics and Aeronautics, Vol. 19, No. 1, January 1981.

SHUTTLE TILE ENVIRONMENTS AND LOADS

Dr. Ralph J. Muraca
NASA Langley Research Center
Hampton, Virginia

INTRODUCTION

This paper will discuss the Shuttle tile ascent environments and outline the procedures used to convert these environments into tile loads. Testing which was performed to quantify or verify the loads will also be discussed, along with the load combination rationale which was used. The discussion of the ascent environment will be limited to the transonic/supersonic portion of the mission since mechanical design loads occur during this time, and to specific regions of the vehicle, in particular those regions in which undensified critical (black) tiles are located.

The induced environments can be broken down into three categories. The first of these are aerodynamic environments. These, in turn, are broken down into two categories-- (1) quasi-steady, which includes spatial surface pressure gradients, pressure differentials due to vent lag, and skin friction, and (2) the unsteady aerodynamics (aerobuffet). The second induced environment is defined as the vibration of the skin-stringer aluminum panels (hereafter referred to as the substrate) due to the acoustic environment. The third environment is defined as a quasi-steady substrate deflection, which results from in-plane and out-of-plane substrate loads (figure 1).

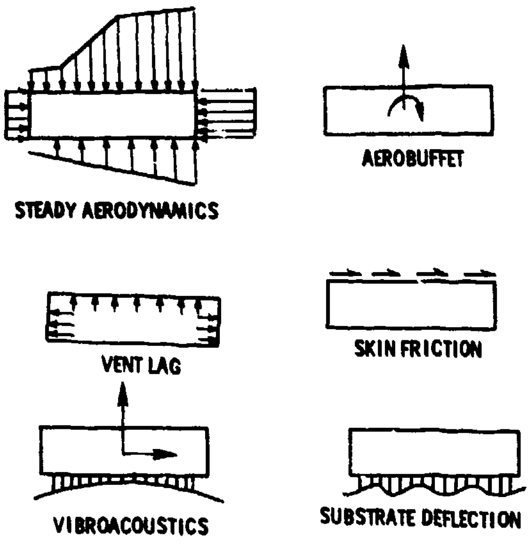

Fig.1 - Tile Loading Sources

STEADY AERODYNAMIC LOADS

During ascent static pressure gradients occur on the Orbiter outer mold line (OML) surface. Due to the porosity of the tiles, SIP, and filler bar, these gradients set up complex flows in the gaps between tiles and through the tiles themselves. These flows are directly related to the OML pressure distributions but their details are dependent on tile and SIP flow characteristics and a number of parameters which characterize the tile installations. The combination of OML pressure gradients and internal flows produce net forces and moments on individual tiles. The major efforts required to quantify these loads were defining the OML pressure distributions with sufficient resolution, and development of a method for computing tile internal flows.

QUANTIFYING TILE OML PRESSURE DISTRIBUTIONS

Typical wind tunnel data from which tile OML pressure distributions were derived are shown on figure 2. Pressure coefficient, C_p, distributions at two spanwise locations are plotted versus chord location. This data was obtained from a 3 percent scale model, consequently, a typical tile would represent an area approximately 0.04

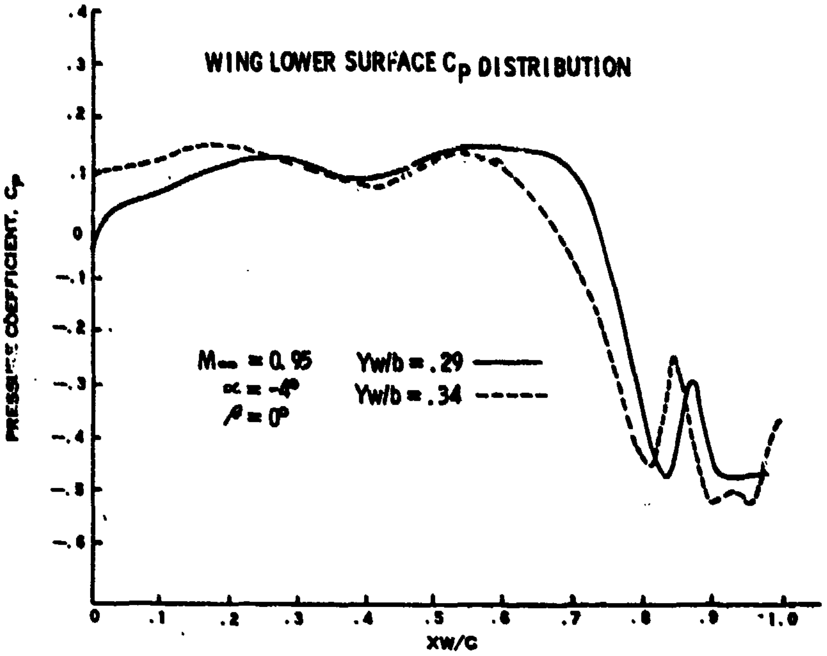

Fig. 2 - Left Hand Wing Lower Surface Pressure Coefficient Distribution

inches square. Since net laods are directly related to local pressure gradients, the primary effort in defining the environment was to determine the maximum pressure gradient which a tile could experience using the relatively sparse model measurements which were available. The approach followed consisted of four distinct steps. Test data were reviewed to determine the existence of shocks. Data from acoustic models, static pressure models, as well as oil flow and Schlieren photographs were used to identify the major shock systems on the Orbiter, and the local Mach number upstream of the shocks. Knowing the local Mach number and the free stream conditions, the shock strengths were calculated. A subjective analysis of static pressure measurements was made to verify the calculated shock strengths. The maximum shock gradient was determined by dividing the shock strength as measured by the pressure jump across the shock by two boundary layer thicknesses. The use of two boundary layer thicknesses to establish the maximum gradients was based on detailed measurements of the static pressure rise through a shock which were available in the literature [1]. Instantaneous pressure measurements indicate the steep portion of the pressure rise is spread over one boundary layer thickness. However, due to shock/boundary layer interaction, shock motion occurs over a distance which can be as little as one boundary layer thickness at frequencies between 10 and 40 hertz. Consequently, the time averaged static pressure measurements would indicate the shock pressure rise occurs over at least two boundary layer thicknesses. Shocks have been observed to move over a distance greater than one boundary layer, however, the highest tile loads result from the steeper gradients. Consequently, it was assumed that all vehicle shocks during transonic/supersonic flight are spread over two boundary layer thicknesses. In addition, the work of Chapman, Kuehn and Larson [2] was used to define the shock pressure ratio at which boundary layer separation could occur.

The results of these analysis were used to define the most severe pressure distribution which individual tiles in the regions under consideration could experience. To eliminate unnecessary conservatism, the vehicle is sub-divided into aerodynamic sub-zones based upon the various configuration induced shocks. The sub-zones defined for the Orbiter wing lower surface are shown in figure 3A, and the major shock systems on figure 3B.

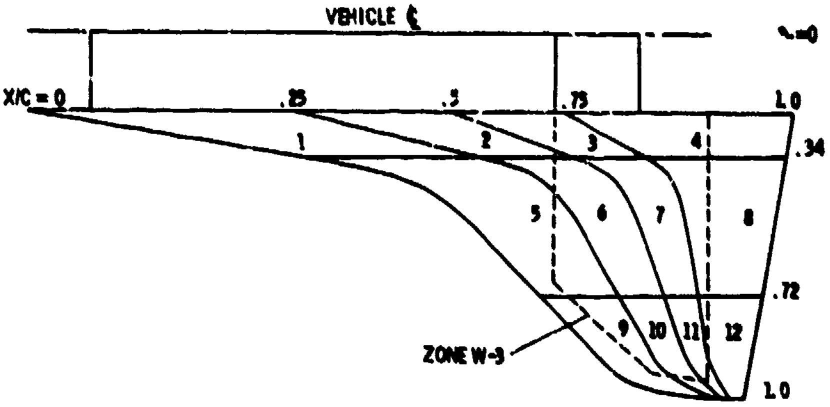

Fig. 3A - Aerodynamic Panels Used in the Definition of Aerodynamic Loading Parameters

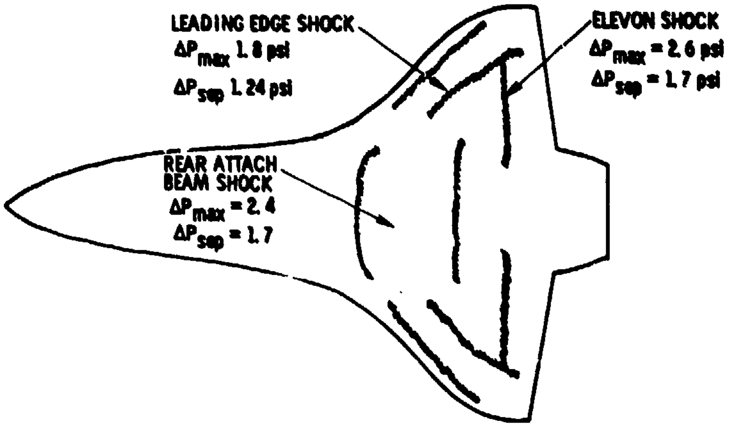

Fig. 3B - Major Lower Surface Shock Systems STS-1 Conditions

CHARACTERIZATION OF ENVIRONMENT

For each sub-zone the induced steady aerodynamic environment is described by the following parameters:

ΔC_{P_S}	The pressure coefficient change through the shock
$\Delta C_{P_{SEP}}$	The pressure coefficient change to the point of boundary layer separation
C_{P_2}	The pressure coefficient at the beginning of the shock pressure rise
ω_1, ω_2	Pressure coefficient gradients upstream and downstream of the shock pressure rise

Table 1 shows typical data for the elevon induced shock, which tiles in sub-zone 4 experience.

IDEALIZED SHOCK MODEL

To determine tile loads an idealized shock shown on figure 4 is used. Most tiles in the regions of interest are oriented such that the surface flow is along a diagonal. The static pressure distribution is defined by: The location of the foot of the shock along a diagonal, X_S; the pressure at the foot of the shock, P_2; the shock strength, ΔP_{shock}; and the gradients upstream and downstream of the steep pressure rise through the shock ω_1, ω_2. The shock pressure gradient is determined by assuming the shock is spread over two boundary layer thicknesses. Thus, given the local boundary layer thickness, δ, the remainder of the OML surface pressure distribution can be completely defined.

TABLE 1
Shock Characteristics in Aero Zone 4

M_∞	$\alpha = -4$				$\alpha = 4$			
	ΔC_{p_S}	$\Delta C_{p_{SEP}}$	$\Delta C_p/\Delta(x/c)$	C_{p_2}	ΔC_{p_S}	$\Delta C_{p_{XEP}}$	$\Delta C_p/\Delta(x/c)$	C_{p_2}
.0000E+00	.0000E+00	.0000E+00	-12.500000	.0000E+00	.0000E+00	.0000E+00	-14.00000	.0000E+00
0.6000000	.0000E+00	.0000E+00	-12.500000	.0000E+00	.0000E+00	.0000E+00	-14.00000	.0000E+00
0.8000000	0.4240000	0.4240000	-13.200000	-0.6600000	0.4270000	0.4270000	-11.50000	-0.6500000
0.9000000	0.5090000	0.5090000	-11.200000	-0.6000000	0.5880000	0.5880000	-10.50000	-0.5500000
0.9500000	0.5940000	0.3900000	-13.000000	-0.6750000	0.5770000	0.5770000	-8.500000	-0.5100000
1.0500000	0.5360000	0.3800000	-12.500000	-0.3400000	0.4250000	0.4250000	-11.50000	-0.1500000
1.1000000	0.5260000	0.3700000	-13.000000	-0.2600000	0.4880000	0.4880000	-12.50000	-0.1250000
1.1500000	0.5070000	0.3500000	-13.000000	-0.2000000	0.4900000	0.4900000	-12.50000	-0.0800000
1.2500000	0.4850000	0.3300000	-11.000000	-0.1250000	0.4610000	0.4610000	-11.00000	-0.0250000
1.4000000	0.4120000	0.2900000	-10.000000	-0.1600000	0.4590000	0.3100000	-12.50000	-0.0400000
1.5500000	0.3820000	0.2700000	-10.400000	-0.1100000	0.3930000	0.2860000	-9.100000	-0.0500000
1.8000000	0.3480000	0.2500000	-6.4000000	-0.0500000	0.3050000	0.2550000	-4.600000	-0.1200000
2.5000000	0.3680000	0.2500000	-5.2000000	-0.0700000	0.2480000	0.1720000	-5.000000	-0.0550000
3.5000000	0.1960000	0.1300000	-2.6000000	-0.3000000	0.1560000	0.1110000	-2.800000	-0.0500000

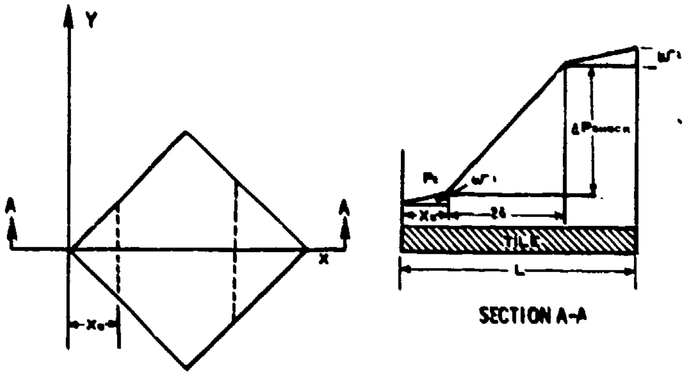

Fig. 4 - Idealized Shock Pressure Distribution

DESCRIPTION OF THE MULTI-TILE FLOW ANALYSIS

The Multi-Tile Flow Analysis computes the pressure field on the outer surface of a tile and at the tile/SIP bondline, which result from a specified OML static pressure distribution such as provided by the idealized shock model shown on figure 4.

The analysis considers a group of nine tiles arranged as shown in figure 5. Although the net loads for the subject tile (tile 9) are of interest, the flow through all nine tiles is computed. Variables such as tile thickness, tile-to-tile gaps, tile-to-filler bar gaps, and tile, SIP and filler bar porosities are considered in the analysis. Given the OML pressure distribution, flow through the tile-to-tile gaps is computed to determine pressures at the bottom of the gaps. Pressure at the bottom of the gap drives the flow through the tiles and the SIP. When a steady-state solution is reached the net forces and moments on each tile are computed and the tiles are allowed to displace until equilibrium is reached between external forces and SIP stress. Both in-plane (SIP shear) and out-of-plane (SIP tension) displacements are allowed. This procedure is repeated accounting for the effect of tile displacement on flow characteristics until convergence is achieved. Net loads are then computed by integration of the pressure field around the tile.

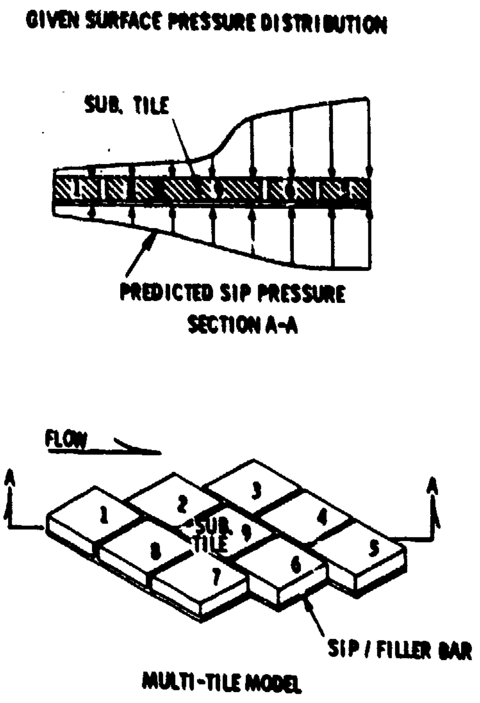

Fig. 5 - Multi-Tile 3-D Flow Model

ANALYSIS VERIFICATION

The analysis was verified by comparison with experimental data from wind-tunnel tests under various conditions and with different tile configurations. In each instance the agreements were excellent. Analysis and test both indicated that for undensified tiles the pressure in the tiles at the bondline was essentially the same as the pressure distribution in the SIP. Typical results are shown in figures 6 through 8 and table 2.

ESTABLISHMENT OF DATA BASE

Since a shock can be located anywhere with respect to a tile, the flow analysis is made with the shock systematically moved along the tile resulting in forces and moments predicted as a function of shock location. The shock location is defined as the point where the steep gradient begins. Shown in figure 9 are representative forces and moments from the flow analysis. The net loads for a given external pressure distribution, although a function of 21 system variables were found to be most sensitive to tile thickness initial tile-to-tile gaps and SIP conductance. To insure that predicted loads enveloped those which could be experienced in flight, the data base was established assuming tiles were installed with minimum tile-to-tile gaps. Loads were then predicted as a function of Mach Number, shock location, tile thickness, and boundary layer thickness for each aerodynamic sub-zone. Typical data are shown in table 3.

VIBROACOUSTIC LOADS

Vibroacoustic loads are defined as the tile inertia load caused by tile response to excitation of the substrate to which the tiles are bonded. Substrate excitation is due to the acoustic environment during lift-off and ascent. The approach taken to quantify vibroacoustic loads was as follows. Subscale vehicle configuration models were used to define the acoustic environments. Initial estimates of panel response were obtained using data from the Apollo Program in combination with the measured Shuttle environments. In some instances the panel response predicted using the Apollo data was superceded when acoustic tests of full scale Shuttle structural panels were completed. Panel and tile dynamic characteristics were measured during these tests. The measured tile response was then used to verify a tile dynamic analysis model which was used to predict tile response for the remainder of the vehicle.

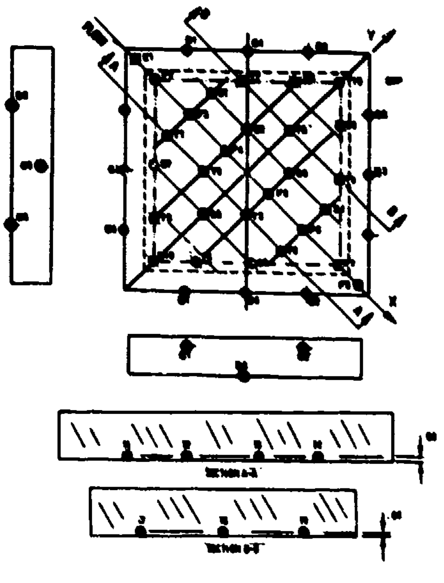

Fig. 6 - Tile Pressure Transducer Configuration

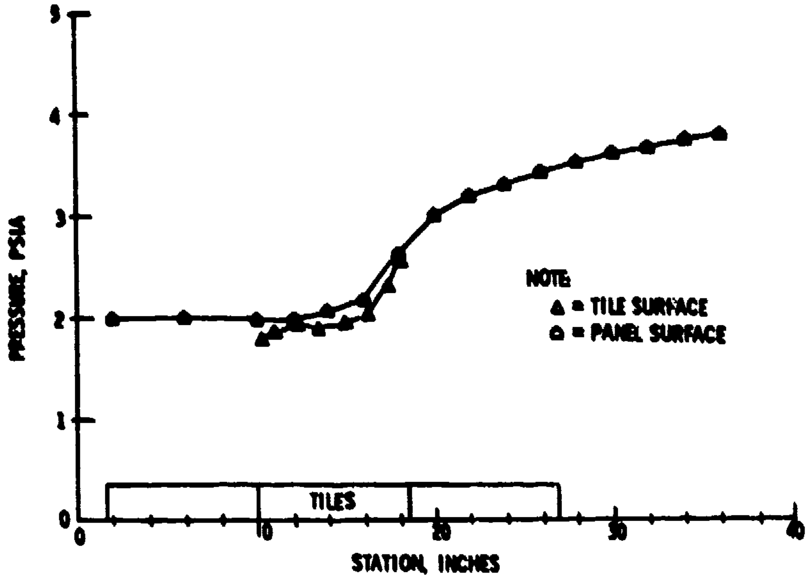

Fig. 7 - External Pressure Distribution

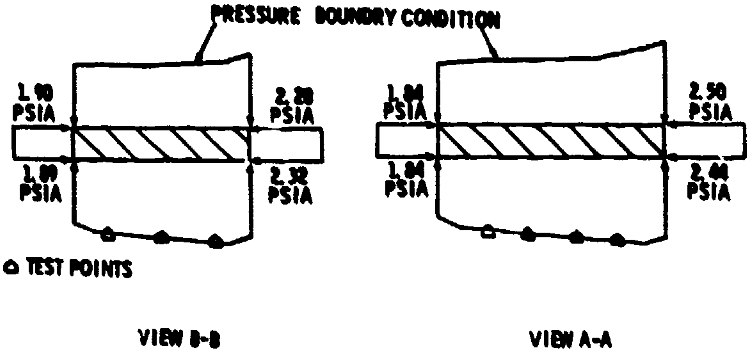

Fig. 8 - Comparison of Measured & Computed Bondline Pressures

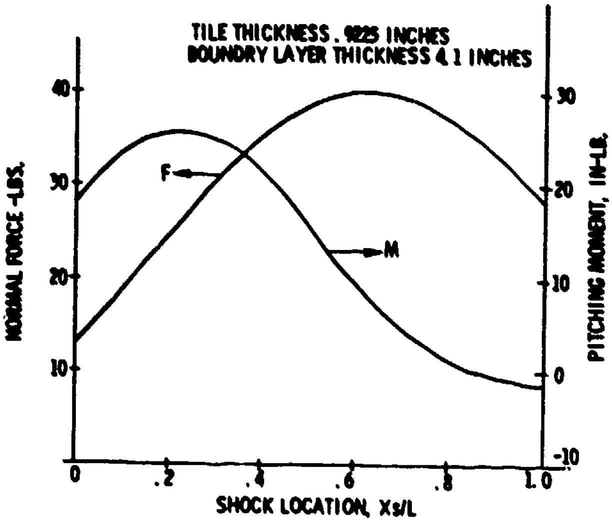

Fig. 9 - Tile Normal Force & Pitching Moment Variation With Shock Location
Wing Sub-Zone 4 M_∞ = 0.95 STS-1 Conditions

TABLE 2
Comparison of Measured With Computed Pressures

Tile Bond Line			Tile Gap		
Sensor	Measured	Computed	Sensor	Measured	Computed
T1	2.26	2.18	B1	2.19	2.06
T2	2.30	2.29	B2	2.21	2.06
T3	2.38	2.41	B3	2.42	2.27
T4	2.47	2.55	B4	2.59	2.22
T5	2.29	2.26	B5	2.11	2.15
T6	2.38	2.38	B6	2.23	2.22
T7	2.28	2.25	G1	2.20	2.02
T8	2.32	2.37	G2	2.47	2.38
			G3	1.98	1.93
			G4	2.07	1.96
			G5	2.31	2.01
			G6	2.48	2.38

TABLE 3
Steady Aerodynamic Loads for Sub-Zone 4, $M_\infty = .95$

	Min. Tile Thickness, t=.927 in.				Max. Tile Thickness, t=1.325 in.			
	δ=6.3		δ=4.0		δ=6.3		δ=4.0	
XS/L	FZ,LBF	MY,IN-LBF	FZ,LBF	MY,IN-LBF	FZ,LBF	MY,IN-LBF	FZ.LBF	MY.IN-LBF
0.0	18.066	17.908	11.898	17.731	17.341	14.457	11.31	14.70
0.25	27.955	17.178	27.528	25.981	25.309	13.709	34.36	12.34
0.50	31.870	8.908	38.861	15.576	29.506	6.653	34.36	12.34
0.75	27.597	1.268	38.597	2.346	25.541	.5431	31.61	.939
1.00	21.158	0.3631	28.331	-1.201	20.092	-.1411	19.71	-1.728

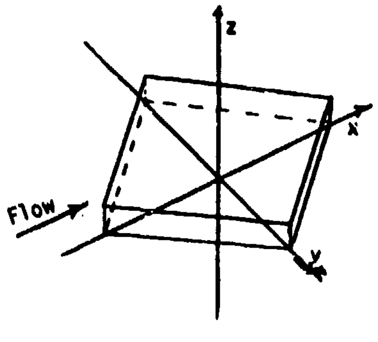

ACOUSTIC ENVIRONMENTS

The ascent acoustic environments were obtained from three separate wind tunnel test programs. The final and most detailed model was a 3.5 percent scale model designated IS2. Data was obtained for $0.6<M_\infty<3.5$ and angles of attack and sideslip between ±5 degrees. These limits are derived from 3σ design limit trajectory analyses. As with the static pressure measurements the fluctuating pressure measurements were sparse and defining the environment for a panel required considerable judgment. Figure 10 shows the instrument location on the bottom surface of the Orbiter. To establish criteria for determining panel response the following procedure was used. Envelopes of 1/3 octave band sound pressure levels were made for each measurement location for all flight conditions. Typical data for the outboard wing area are shown in figure 11. The vehicle was then divided into zones and a composite 1/3 octave band spectrum for each zone was made by enveloping the maximum 1/3 octave band levels previously obtained for all measurement locations within the zone. The composite zonal spectra thus obtained represent the maximum fluctuating pressure levels expected at any locations within the zone. Table 4 shows typical data for the bottom outboard region of the Orbiter wing.

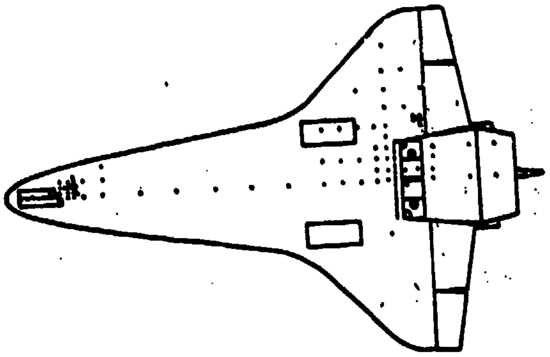

Fig. 10 - Kulite Instrumentation Orbiter Bottom View

PANEL RESPONSE

To determine panel response characteristics the following approach was used. Initially Apollo panel response data was used to estimate Shuttle panel response. These data were scaled to account for differences in acoustic environments, structural characteristics, and panel mass. Using this approach panel response for the entire vehicle was predicted.

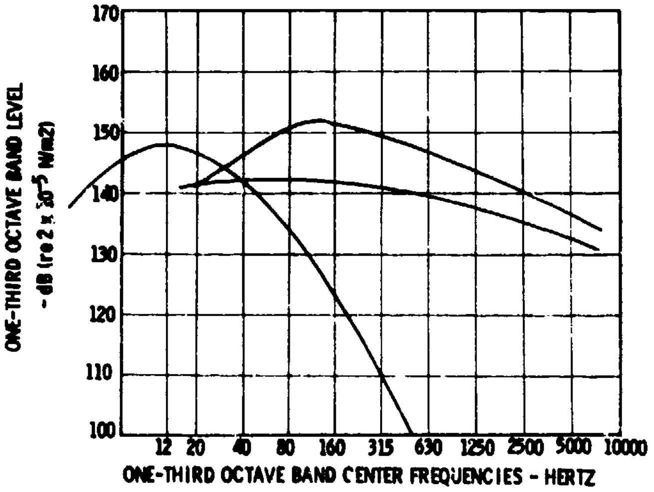

Fig. 11 - Sound Pressure Levels, Orbiter Lower Inboard Wing Surface Xo = 1370, Yo = -150

TABLE 4
Orbiter Wing Bottom SPL Envelope - db (Reference 2 x 10^{-5} N/M^2)

OUTBOARD 250 $\leq Y_o \leq$ TIP

1/3 OCTAVE FREQUENCY	shock		aeronoise
	1120 $\leq X_o \leq$ 1350	1350 $\leq X_o \leq$ 1390	1120 $\leq X_o \leq$ 1390
1.6	136	136.5	-
2.0	138	140	-
2.5	139.5	143	-
3.2	141	146	-
4.0	142.5	148.5	-
5.0	144	150.5	-
6.3	145	152	-
8.0	145.5	153.5	-
10.0	146	154.5	-
12.5	146	154	-
16	146	153.5	150
20	145	152	155
25	144	151	160
31.5	143	149.5	160
40	141	147.5	153
50	139.5	145.5	153
63	137.5	143.5	153
80	135.5	141	149
100	133	138	148.5
125	130	135	148
160	127	131.5	147.5
200	124	128	147
250	-	-	146.5
316	-	-	146
400	-	-	145
500	-	-	144.5
630	-	-	144
800	-	-	143
1000	-	-	142.5
1250	-	-	142
1600	-	-	141
2000	-	-	140.5
2500	-	-	140
3160	-	-	139
4000	-	-	138
5000	-	-	137
6300	-	-	136.5
8000	-	-	135.5
OA	156	163	165

Figure 12 shows overall SPL's and the corresponding panel response for each zone of the vehicle. Subsequently full scale panels representative of specific regions of the vehicle were subjected to the previously determined acoustic environments and the panel response was measured. These measured data were then used to adjust the initial estimates obtained by scaling the Apollo data. Typical results in the form of PSD's for the bottom wing outboard area are shown in figure 13. As can be noted from the figure, the adjusted vibration levels do not envelope all of the measured narrow band peaks. This is justified for the following reason. By definition vibroacoustic loads are due to panel response exciting the tiles. Due to the high damping in the tile/SIP system the tile response occurs over a fairly wide frequency range. It was felt that enveloping all narrow band peaks was not necessary as long as acceleration levels and bandwidth were such that the rms acceleration values were matched.

In defining a vibration environment, differentiation was made between unloaded skin/stringer response and skin-stringer response when attached to major elements of support structure.

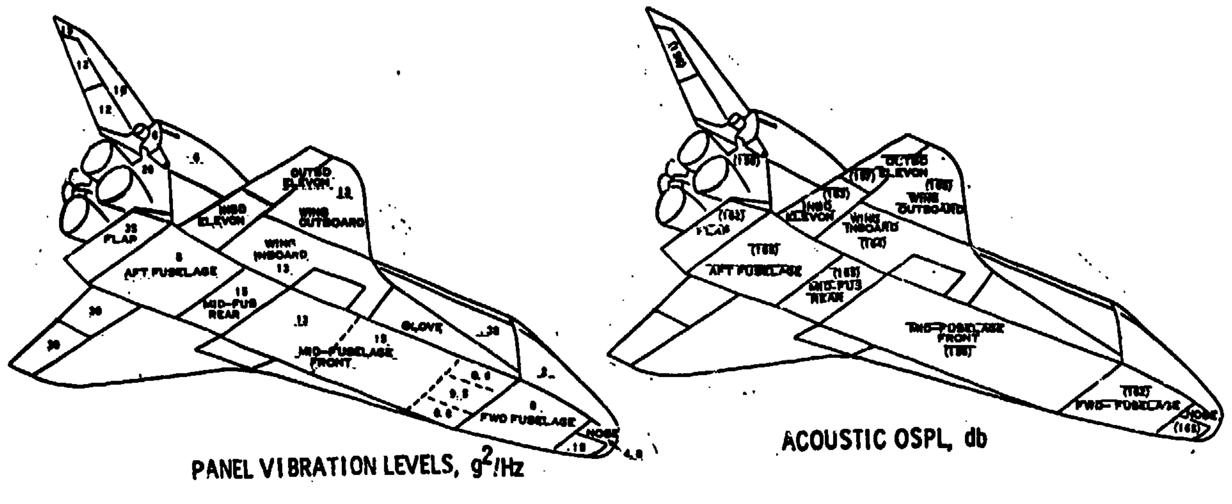

Fig. 12 - Orbiter Acoustic & Vibration Levels - Ascent

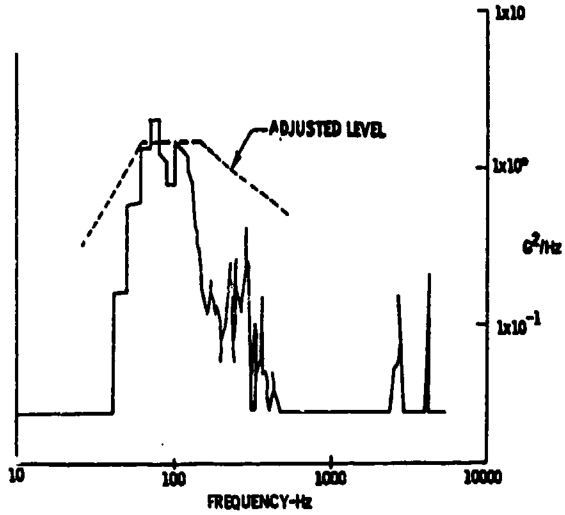

Fig. 13 - Test DA35, Wing Structural Response (Skin/Frame Junction)

TILE INERTIA LOADS

The tile inertia loads were determined by assuming the tile/SIP systems could be represented by a single-degree-of-freedom spring mass damper system. The transfer function for such a system was used to compute tile response spectra for a given panel input spectra. SIP dynamic modulus and damping ratio were obtained from test. The results from this analysis were used to map the entire vehicle . A data base of tile response in terms of peak (3σ) acceleration in g's was generated as a function of tile thickness, tile location with respect to spars, ribs, and frames, and flight Mach Number. Typical data is shown in table 5.

Numerous tests indicated that the SIP caused coupling between out-of-plane and in-plane response to a base excitation. Measurements from a test panel of the forward fuselage region indicated the ratio of out-of-plane to in-plane acceleration response could be as high as 0.3. Consequently an in-plane inertia load of 0.3 of the out-of-plane inertia load was applied to each tile. Test results also indicated that the in-plane and out-of-plane responses were in phase. Figure 14 shows typical test results. These data also verified the use of a factor of three on rms values to obtain tile response with a probability of exceedance of 0.0013.

EFFECT OF SHOCK LOCATION

Figure 15 schematically shows the design load case for tiles, i.e., a shock located essentially over the tile. It was postulated that the location of the shock with respect to the ribs, spars, and frames would effect the panel response. For a shock located at the front of a panel, the total panel area would be subjected to the shock generated fluctuating pressures. If a shock were located at the mid-point of a panel, the area of the panel subjected to intense fluctuating pressures would be reduced, consequently, the panel response could be expected to be lower. Since the tests upon which tile inertia loads were based subjected the full panel to acoustic loads, it was deemed proper to attenuate the tile response as a function of shock location on the substrate panels. The tile inertia loads were assumed to decrease linearly

TABLE 5
Peak (3σ) Tile Response to Panel Vibration

6" x 6" Tiles on Unsupported Skin Panel

Tile Thickness, Inches

Mach Number	1.0	1.25	1.5	1.75	2.0	2.25
0	61	57	55	53	50	49
.9	59.5	59	58	57	56	55
1.25	75	74	73	72	71	69
1.4	75	75	73	72	71	69

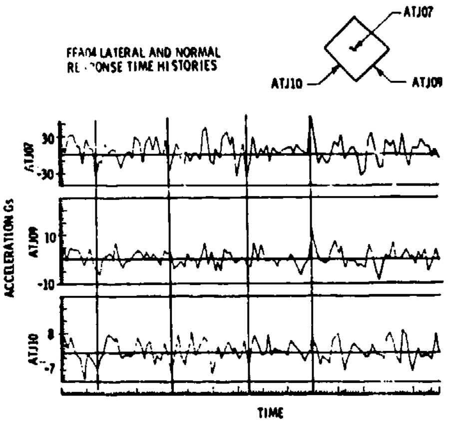

SUMMARY OF FFA04 DATA

PEAK/RMS* RATIO

TRANSDUCER	RATIO
ATJ01 (N)	2.72
ATJ02 (N)	2.74
ATJ04 (N)	2.74
ATJ07 (L)	2.77
ATJ09 (L)	2.81
ATJ10 (L)	2.72
ATJ15 (L)	2.65

*LEVEL EXCEEDED . 13% OF THE TIME

LATERAL RMS / NORMAL RMS

ATJ09/ATJ07	.18
ATJ10/ATJ07	.22
ATJ14/ATJ12	.24
ATJ15/ATJ12	.18

Fig. 14 - Tile Response To Substrate Vibration

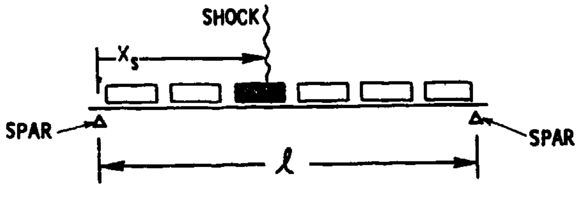

Fig. 15 - Tile Design Case

as the shock location was moved across the panel. The relationship used was

$$g\ (\text{effective}) = g_{3\sigma}\ (1 - 0.5\ X_s/l_p).$$

BUFFET LOADS

Buffet loads consist of net forces and moments resulting from differences in fluctuating pressures at the tile surface and at the tile/SIP bondline. The fluctuating pressures result from separated boundary layers which occur around protuberances and in the vicinity of shocks. The basic environment was defined from wind tunnel model tests in which the fluctuating pressures were measured and from larger full-scale tests which simulated local flow conditions around flaps and other major protuberances which produce shocks. The procedure by which these fluctuating pressure environments were converted to tile loads was based on data from a series of tests in which individual tiles were instrumented to directly measure tile loads due to a known environment. Basically the parameters which were generated were RMS values and peak to RMS ratios of normal force and pitching and rolling moment. The magnitudes of these loads were determined as a function of the shock location on the tile. The results from this empirical model were correlated with a second set of measurements which were obtained from wind tunnel tests performed in the LaRC 8-Foot Transonic Pressure Tunnel. These tests subjected flight configured panels to the STS-1 combined loads environment, and are discussed in detail in the paper by Schuetz, Pinson and Thornton [3].

Buffet environments and loads are discussed in detail in the paper by C. Coe [4] and will not be discussed at length in this paper. Measured values of rms buffet normal force and pitching moment coefficients are shown on figure 16 as a function of shock location. Typical vehicle environments for aero sub-zone 4 are shown in table 6.

TABLE 6
RMS Fluctuating Pressure Coefficient Aero Zone 4

MACH NO.	$\tilde{C}_{P_{RMS}}$	
	Shock	Separation
.6	0	0
.8	.072	.067
.9	.100	.055
.95	.11	.054
1.05	.063	.052
1.1	.073	.052
1.15	.062	.052
1.25	.070	.040
1.4	.062	.047
1.55	.043	.048
1.8	.048	.057
2.5	0	.053
3.5	0	0

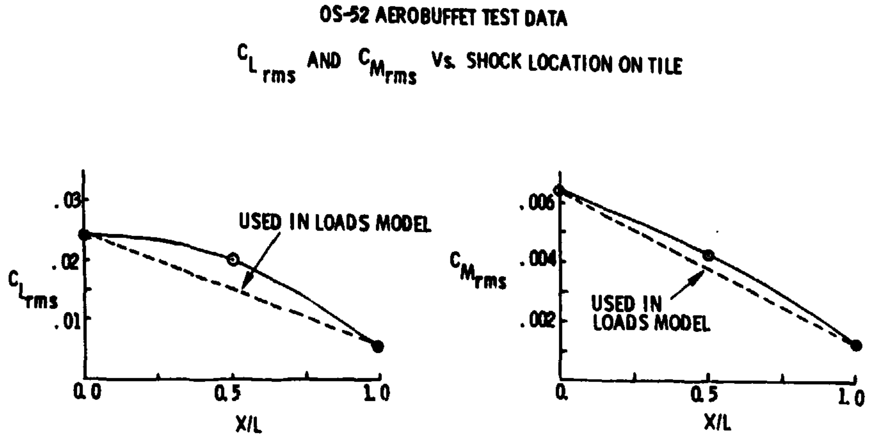
OS-52 AEROBUFFET TEST DATA

$C_{L_{rms}}$ AND $C_{M_{rms}}$ Vs. SHOCK LOCATION ON TILE

Fig. 16 - Aerobuffet Normal Force & Pitching Moment Coefficient Variation With Shock Location

SUBSTRATE DEFORMATION

Deformation of the substrate to which the tiles are bonded produces a stress at the tile/SIP bondline. Substrate deformations result from initial structural imperfections which become amplified as in-plane and out-of-plane pressures differentials are applied to the structure during ascent.

Substrate deformations were quantified through analysis. Detailed finite element models of the vehicle structure were generated. Assuming initial imperfections, loads were applied representative of a wide range of dispersed trajectories. For each load set, the maximum substrate deformation and its characteristic wavelength were computed. The vehicle was then subdivided into a number of zones and the maximum substrate deformation for all load conditions for any location within the zones was determined. This value of substrate deformation and its associated wavelength were then assumed to be applicable for all tiles within that zone, and were considered as the steady state components of substrate deformation. Typical values for the wing lower surface are shown in figure 17. A dynamic component of substrate deformation resulted from vibration of the substrate. Magnitudes and wavelengths for these dynamic components of deformation were also derived from the same analysis which defined the substrate vibration levels discussed under the section on vibroacoustic loads. The wavelengths for dynamic components of substrate deformation were determined on the basis of the spacing of major frames, ribs and spars. They tended to be much longer than those associated with the static deformation, consequently they made relatively small contributions to the tile bondline stresses.

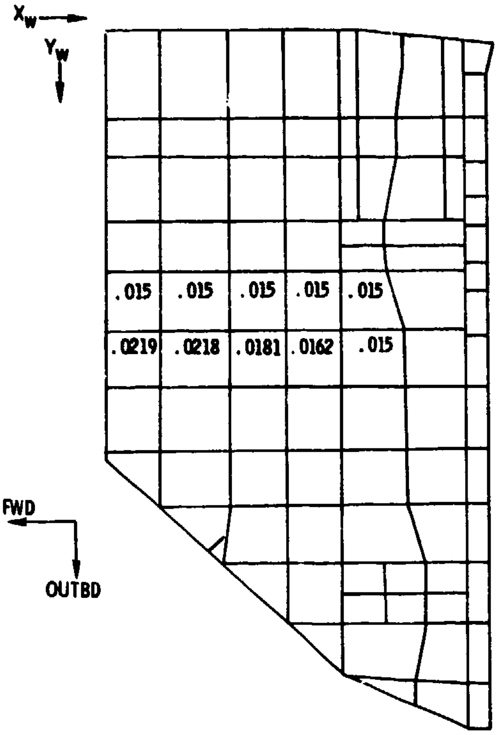

Fig. 17 - Substrate Deformation Map for Wing Lower Surface Envelope of Ascent Conditions

LOADS COMBINATION

Since the tile/SIP system is highly nonlinear, it was necessary to develop an approach for combining the various static and dynamic loads. This required that where enough definition was available, loads had to be referenced to a common parameter. Vehicle free stream Mach Number was selected as the most appropriate parameter. In general, all steady or quasi-steady loads components were added directly. Unsteady or dynamic loads were combined statistically and then added directly to the steady loads. The relationships used to combine loads are:

For Normal Force:

$$F_z = F_{sa} + F_{vl} \pm \sqrt{(K_b F_b)^2 + (K_{va} F_{va})^2}$$

For Pitching Moment About the Y Axis:

$$M_y = M_{sa} + M_{sf} \pm \sqrt{(K_b M_b)^2 + (0.3 \bar{Z} K_{va} F_{va})^2}$$

In these expressions F_{sa} and F_{va} are contributions due to steady aerodynamics and vent lag respectively. F_b and F_{va} are dynamic contributions due to aero-buffet and vibroacoustic. The factors K_b and K_{va} are used in conjunction with rms values of dynamic force and moment to yield total forces and moments with a probability of exceedance of 0.0013. For vibroacoustic terms the factor used was 3.0, for buffet the factor was 4.0. These were derived from test. M_{sa} and M_{sf} are contributions due to steady aerodynamics and skin friction. $\bar{Z}$ is the distance from the center of gravity of a tile to the bondline. A number of issues were identified with regard to treatment of the dynamic load terms. One involved whether the normal force and pitching moment due to buffet were in phase. An analysis of the previously cited wind tunnel test data indicated that buffet forces and moments were highly correlated and that it would be proper to assume they act simultaneously on the tiles. These results are shown on figure 18.

A second issue involved the manner in which vibroacoustic and buffet loads were combined. Since the environment which produces both loads is the same, it was obvious that these loads should be applied to the tiles at the same time. However, an analysis of the spectra for buffet energy indicated that it was concentrated at relatively low frequencies (up to 100 Hz) whereas tile response to substrate vibration extended from about 60 Hz up to about 300 Hz. Consequently it was felt that a direct combination of buffet and vibroacoustic loads would be overly conservative, thus the decision to root-sum-quare dynamic loads.

PHASE ANALYSIS OF AEROBUFFET PEAK NORMAL FORCE AND PITCHING MOMENT

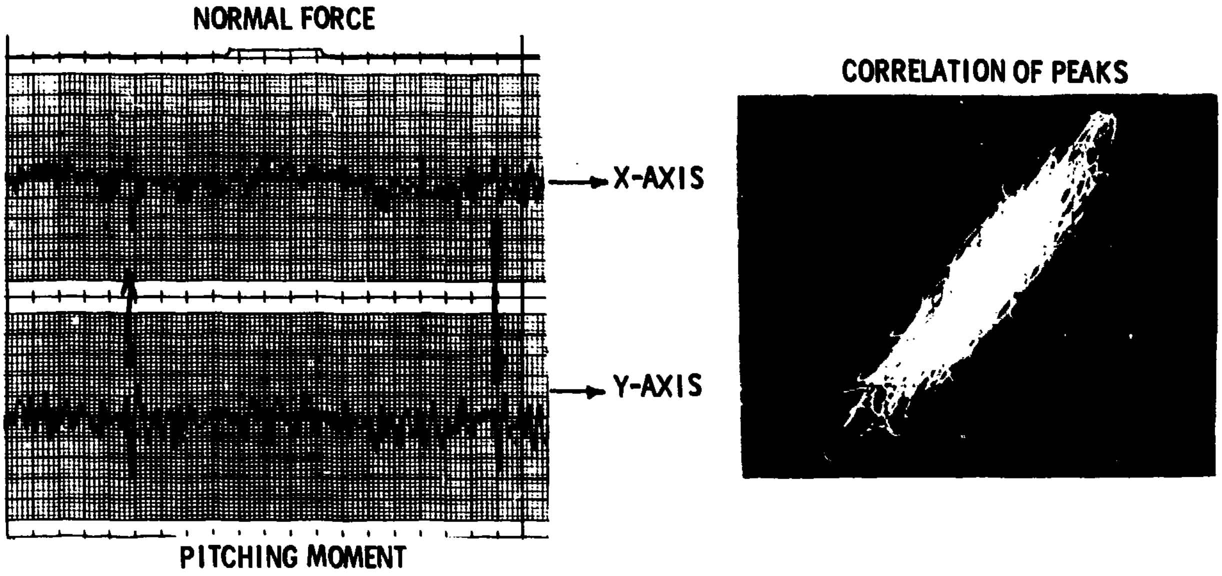

Fig. 18 - Phase Analysis of Aerobuffet Peak Normal Force And Pitching Moment

TOTAL SUBSTRATE DEFORMATION

A total substrate deformation was determined by direct addition of the static and dynamic components. The relationship used for total deflection is:

$$\Delta = \left(A \cos \pi \frac{x}{\ell_1} \cos \pi \frac{y}{\ell_2}\right)_{oop} +$$

$$K_{va} \left(A \cos \pi \frac{x}{\ell_1} \cos \pi \frac{y}{\ell_2}\right)_{va}$$

where both components of deformation were defined as double cosine curves in directions along each diagonal of the tile. In this expression A, ℓ_1 and ℓ_2 are the amplitude of the deflection and its wavelength in the x and y directions for either steady state out-of-plane (oop) deflection or the vibroacoustic deflection.

DETERMINATION OF DESIGN LOADS

The design load set was defined as the combination of force, moment, and substrate deflection which produced the maximum stress at the tile/SIP bondline. To determine this load set the location of the shock relative to the substrate was arbitrarily adjusted until the stresses were maximized. A typical set of design loads for three regions of the vehicle are shown on table 7.

SUMMARY

The STS-1 ascent environments were defined. Induced loads due to these environments were determined and models used to quantify these loads were validated. Issues related to the manner in which these loads combine during the ascent portion of the mission were resolved by test. A data base was created which allowed the loads for over 3000 undensified critical tiles to be determined. These loads were ultimately used to calculate maximum tile stresses during ascent and safety margins for the STS-1 mission.

TABLE 7
Typical Design Loads for Tiles Located On the Orbiter Wing and Fuselage

Tile Part Number	Steady Aero		Vibroacoustic		Buffet	
	Force	Moment	Force	Moment	Force	Moment
W3-191010147	16.0	7.6	8.3	1.8	11.2	15.7
MF6-394020277	20.4	11.6	10.8	3.2	10.2	14.3
MF6-394036082	15.8	6.7	16.4	4.0	10.1	14.2

REFERENCES

1. E. Zukoski, "Turbulent Boundary Layer Separation in Front of a Forward Facing Step," Guggenheim Jet Propulsion Center Report, 66-8-15-1, August 1966.

2. D. Chapman, D. Kuehn, and H. Larson, "Investigations of Separated Flows In Supersonic and Subsonic Streams With Emphasis on the Effects of Transition," NASA TR 1356.

3. P. H. Schuetz, L. D. Pinson, and H. T. Thornton, "Unsteady Environments and Responses of the Shuttle Combined Loads Orbiter Test (CLOT)," 52nd Shock and Vibration Bulletin.

4. C. F. Coe, "Buffet Loads on Shuttle Thermal Protection System Tiles," 52nd Shock and Vibration Bulletin.

DYNAMIC AND STATIC MODELING OF THE SHUTTLE ORBITER'S THERMAL PROTECTION SYSTEM

J. M. Housner, G. L. Giles, and M. Vallas
NASA Langley Research Center
Hampton, Virginia

This paper describes the dynamic and static analysis methods used to model the nonlinear structural behavior of the Shuttle Orbiter's tile/pad thermal protection system. The structural evaluation of the tile/pad system is complicated by the nonlinear stiffening, hysteresis and viscosity exhibited by the pad material. Application of the analysis to square tiles subject to sinusoidal and random excitation is presented along with appropriate test data and correlation is considered good. In order to treat the stress analysis of thousands of individual tiles a nonlinear static analysis was developed which utilizes equivalent static loads derived from the dynamic environment. Using a developed automated data management/analysis system the critical tensile stress at the bondline is examined in thousands of unique tiles in a timely, reliable and efficient manner.

NOMENCLATURE

A_p	tile/pad contact area
c_{zx}, c_{zy}	vertical-lateral coupling terms in pad material property law, see Eq. (7)
C_x, C_y, C_z	damping coefficients, see Eqs. (6)
E_d	energy dissipated by the pad per cycle of steady-state motion
E_k	peak kinetic energy of tile during steady-state motion
E_{zx}, E_{zy}, E_{zz}	components of Green strain tensor
$\{F\}$	applied tile force vector, see Eq. (8)
F_x, F_y	applied tile centroidal forces in x and y directions, respectively
G_{xx}, G_{yy}	transverse shear stiffnesses of pad, in x and y directions, respectively, see Eq. (7)
h_p, h_t	pad and tile thicknesses, respectively
K_x, K_y, K_z	effective stiffness coefficients in nonlinear viscous damping law, see Eq. (6)
m	tile mass
M_x, M_y	applied moments about x and y axes, respectively
[M]	system mass matrix, see Eq. (8)
P	applied tile centroidal normal force in z direction
q_n, q_s	damping law exponents, see Eq. (6)
$\{q\}$	vector of tile displacement components, see Eq. (8)
$\{Q\}$	vector of internal pad stress resultants, see Eq. (8)
r_x, r_y, r_z	tile radii of gyration about x, y, and z axes, respectively
S_{xx}, S_{xy}, S_{yy} S_{zx}, S_{zy}, S_{zz}	Kirchhoff stress components
$\bar{S}_{zx}, \bar{S}_{zy}, \bar{S}_{zz}$	steady-state time averaged Kirchhoff stress components

t	time
T_o	applied tile torque about z axis
u, v, w	displacement components in x, y, and z directions, respectively
u_o, v_o, w_o	values of u, v, and w at tile centroid, respectively
u_s, v_s, w_s	components of substrate displacements in x, y, and z directions, respectively
V_p	undeformed pad volume
α_x, α_y	tile rotation about x, y, and z directions, respectively
z'	$z + h_t/2 + h_p$
β_x, β_y	average linear pad rotations, see Eq. (8)
ε	linear transverse strain component, see Eq. (8)
γ_x, γ_y	linear shear strain components, see Eq. (8)
η	loss factor defined in Eq. (10)
θ	rotation about z axis
σ_a	uniform applied normal stress
$\sigma_{zz}, \sigma_{zx}, \sigma_{zy}$	Euler stress components
τ_a	applied uniform shear stress
ω_n, ω_s	low-amplitude steady-state transverse and lateral resonant frequencies about fixed normal and shear prestress states, respectively
Ω	frequency of sinusoidal substrate motion
Ω_r	reference frequency
ζ	coefficient of nonlinear viscous damper, see Eq. (6)

Subscripts and Superscripts

D	strain-rate dependent stresses
I	strain-rate independent stresses
o	tile centroid
p	pad
s	substrate
$(\dot{\ })$	$\partial(\ )/\partial t$

INTRODUCTION

The Space Shuttle Orbiter thermal protection system consists of over 32,000 ceramic tiles bonded to thin nylon felt pads, known as strain isolator pads, which are composed of thousands of intertwined nylon filaments [1]. The pads, in turn, are bonded to the aluminum skin of the Shuttle Orbiter. During a mission, tile/pad combinations experience dynamic loads arising from acoustics, structural vibrations, and aerodynamic pressure gradients [2]. Thus, the pad experiences motion of varying magnitudes and frequencies. Experiments [3] have shown that as the pad is cyclically loaded and unloaded, hysteresis loops occur in the stress-strain behavior of the material. Furthermore, these loops creep as a function of stress level and number of cycles. The creep of the loops eventually becomes very small with each additional cycle, but its effect is to produce a highly nonlinear hardening pad material which is quite soft at low stress levels and considerably stiffer at higher stress levels. In addition, the hardened material exhibits both coulomb and nonlinear viscous damping.

The integrity of the system has been shown to be dependent upon the tensile stress near the interface between the pad and the tile [1] and when nonlinear effects are included in the analysis, predicted values of this stress may be significantly higher than those predicted by a linear analysis [4-6].

The purpose of this paper is to present a synopsis of the dynamic and static analyses used for the thermal protection system when nonlinear effects are accounted for. Since the system is subjected to time varying loads, a dynamic analysis is most appropriate and such an analysis is reviewed in the paper. However, in order to treat thousands of individual tiles, a static analysis [7-9] which uses equivalent static loads derived from the dynamic environment, as described in Ref. [2], is more feasible. Thus a dynamic analysis is established and used to acquire a general understanding of the system while the static analysis is used for acquiring specific information on individual tiles. The assumptions of the dynamic analysis are first outlined and the governing equations are established from energy principles for large deformations and nonlinear pad behavior while allowing for hysteretic and nonlinear viscous damping in the pad. Only the essentials of the analytical development are given, while details are left to Refs. [4] through [6]. Confidence in the dynamic analysis is gained by comparison with sinusoidal and random excitation tests and results are presented which provide insight into the general dynamic behavior of the system.

The static analysis is central to an automated analysis and data management system which permits efficient and reliable handling of geometry, loads and material property data. These data are unique for each of thousands of tiles. Thus, scope, capabilities, procedure, and typical results of the automated static analysis/data management system are described. The impact of these analyses on the Shuttle project is then summarized.

DYNAMIC ANALYSIS

Dynamic Model Configuration

As shown in Fig. 1, the ceramic tiles of the Space Shuttle Orbiter thermal protection system are bonded to the aluminum skin of the Orbiter (substrate) through a thin nylon strain isolation pad. The pad is bonded to the tile over most of the tile's lower surface. However, around the perimeter of the tile there exists a separate strip of the pad material denoted as the filler bar. To enhance venting of entrapped air in the porous material of the system, the filler bar is bonded only to the substrate and not the tile. Further details as to the system construction may be found in Ref. [1].

Loads

The dynamic analysis treats three or four sided tiles subject to dynamic forces and moments which are assumed to be known as time histories. The histories may be provided directly from tests or if power spectral densities are known, time histories may be derived from random number generators. In addition to the applied tile forces and moments, the system is also subject to static substrate deflections or substrate oscillations wherein the substrate may oscillate flexurally or as a rigid body. The substrate motions are also assumed to be known or derivable as time histories.

Tile Behavior

It is assumed that the tile behaves as a rigid body. This is confirmed by comparing the results of two static analyses, one in which the tile is modeled with flexible finite elements and one in which the tile is assumed rigid [10]. Both rigid and flexible models of different thickness tile rest on the nonlinear pad and are subjected to different combinations of forces and moments. For the case of uniform pressure, Fig. 2 displays the flexible-to-rigid interface stress ratio which is seen to vary with the magnitude of uniform pressure due to the material nonlinearity of the pad. Even for 1.27 cm (half inch) thick tiles, the error due to a rigid tile assumption is less than 4 percent, well within engineering tolerance. Similar findings for other loading states lead to the same conclusion [10].

Pad Material Properties

Conditioning.- Material property tests [3, 11] were conducted in which the pad was slowly loaded in tension, compression, or shear on its surface normal to the z-axis. These tests revealed, as displayed in Figs. 3(a) and 3(b) that under cyclic loading of a prescribed amplitude the pad exhibits hysteretic behavior. Under slow cyclic loading the hysteresis loops creep as a function of load amplitude and number of cycles. As is the case with many materials, the primary creep range in which the creep is rapid, is followed by a secondary range in which the creep is much slower. Hence, the creep of the loop eventually becomes very small with additional load cycles of the same or lower amplitude. This process which produces a quasi-stabilized material is referred to as "conditioning." The hysteresis loop formed by the conditioning load cycles is referred to as the loop "envelope." Provided each point in the pad has not experienced a load amplitude higher than the one conditioned at, it appears that the creep of the hysteresis loops can be safely neglected during a short time analysis. Hence, it is assumed that the pad material has been conditioned at a load amplitude which is not exceeded during the period of time to be analyzed. Analytical responses of the system have indicated that the system is not very sensitive to small additional creeping. As a consequence of this assumption, the analysis may be carried out over a small period of time (e.g., a few hundred cycles) and then restarted using material property data corresponding to additional cycles at the calculated stress amplitudes which meet or exceed the conditioning amplitude.

A typical envelope resulting from slow cyclic loading is shown in Fig. 4(a). Also shown are typical loading and unloading paths from different stress-strain states within and on the envelopes. Similar curves can be established for shear cycles [11]. These loading/unloading curves are valid at each point in the pad. However, since the loading/unloading history at each point in the pad may be different, the path being traced at any time may differ throughout the pad.

Based on the observations of pad behavior, it is further assumed that under slow rate and irrespective of loading or unloading path, the pad strain-rate independent state cannot lie outside of the envelope and that within the envelope loading/unloading paths may be curve fitted by appropriate scaling and translation of portions of the envelope. However, as discussed later, the presence of high loading rate effects allows the total stress-strain state to lie outside the envelope.

Based on measured data, empirical rules are established which allow the load paths traced by the stress-strain history of each point in the pad to be followed. For computer solution, appropriate routines are established which perform the necessary logic decisions and bookkeeping for tracing these paths. Details are provided in Ref. [5].

Stress and Strain Formulation.- In order to account for the large strains associated with the pad, it is convenient to introduce the Kirchhoff stress components S_{ij} and Green strain components E_{ij} [12]. The Green strain components in the pad are calculated from the rigid body motions of the tile as

$$\begin{aligned}
E_{zz} = {} & (w_o + y\alpha_x - x\alpha_y - w_s)/h_p \\
& + (1/2)(u_o - h_t\alpha_y/2 - y\theta - u_s)^2/h_p^2 \\
& + (1/2)(v_o + h_t\alpha_x/2 + x\theta - v_s)^2/h_p^2 \\
& + (1/2)(w_o + y\alpha_x - x\alpha_y - w_s)^2/h_p^2
\end{aligned}$$

$$\begin{aligned}
2E_{zx} = {} & (u_o - h_t\alpha_y/2 - y\theta - u_s)/h_p \\
& + (1/2)\theta(v_o + h_t\alpha_x/2 + x\theta - v_s)/h_p \\
& + (1/2)(\partial w_s/\partial x - \alpha_y)\left[1\right. \\
& \left. + (w_o + y\alpha_x - x\alpha_y - w_s)/h_p\right]
\end{aligned}$$

$$\begin{aligned}
2E_{zy} = {} & (v_o + h_t\alpha_x/2 + x\theta - v_s)/h_p \\
& - (1/2)\theta(u_o - h_t\alpha_y/2 - y\theta - u_s)/h_p \\
& + (1/2)(\partial w_s/\partial y + \alpha_x)\left[1\right. \\
& \left. + (w_o + y\alpha_x - x\alpha_y - w_s)/h_p\right]
\end{aligned} \tag{1}$$

and

$$E_{xx} = E_{yy} = E_{xy} = 0$$

where the displacement components of any point in the pad are assumed to be related to the rigid body tile and substrate motion by

$$\begin{aligned}
u_p &= (u_o - h_t\alpha_y/2 - y\theta - u_s)z'/h_p + u_s \\
v_p &= (v_o + h_t\alpha_x/2 + x\theta - v_s)z'/h_p + v_s \\
w_p &= (w_o + y\alpha_x - x\alpha_y - w_s)z'/h_p + w_s
\end{aligned} \tag{2}$$

The Kirchhoff pad stresses, S_{ij}, are related to the actual (or Euler) pad stress, σ_{ij}, by

$$[\sigma] = \frac{1}{\det(J)}[J][S][J]^T \tag{3}$$

where

$$[J] = \begin{bmatrix} 1 & \dfrac{\partial u_p}{\partial y} & \dfrac{\partial u_p}{\partial z'} \\ \dfrac{\partial v_p}{\partial x} & 1 & \dfrac{\partial v_p}{\partial z'} \\ \dfrac{\partial w_p}{\partial x} & \dfrac{\partial w_p}{\partial y} & 1 + \dfrac{\partial w_p}{\partial z'} \end{bmatrix}$$

For example, in the case of an applied uniform pressure, σ_a, one has

$$S_{zz} = \sigma_a/(1 + w_o/h_p) \tag{4}$$

with all other Kirchhoff stress components vanishing, and for an applied uniform shear, τ_a, parallel to the x axis

$$S_{zx} = \tau_a \tag{5}$$

and all other Kirchhoff stress components vanishing.

Energy Dissipation.- The hysteresis loops associated with pad cyclic loading involve energy dissipation which may be due to static coulomb frictional damping which is strain-rate independent. This is physically reasonable since pad filaments are sliding over one another during loading or unloading. However, it is known that for a driven linear spring/mass/damper system, the energy dissipation due to coulomb damping is not sufficient to produce bounded oscillations at resonant frequencies [13]. Inasmuch as physical oscillations are always bounded, it would appear reasonable to postulate an additional energy dissipation mechanism which is strain-rate dependent. Thus, it is assumed that the pad stress components are the algebraic sum of strain-rate independent and strain-rate dependent components as schematically depicted in Figs. 4(a) and 4(b) for the normal pad stress, σ. The relative amount of energy dissipated by each mechanism is addressed in a subsequent section. The strain-rate dependent component is modeled using a nonlinear viscous damper where the strain-rate dependent stress components are given by

$$\begin{aligned}
S_{zx}^{(D)} &= C_x h_p \dot{E}_{zx} \left|2\pi E_{zx}/\Omega_r\right|^{q_s-1}/A_p \\
S_{zy}^{(D)} &= C_y h_p \dot{E}_{zy} \left|2\pi E_{zy}/\Omega_r\right|^{q_s-1}/A_p \\
S_{zz}^{(D)} &= C_z h_p \dot{E}_{zz} \left|2\pi E_{zz}/\Omega_r\right|^{q_n-1}/A_p
\end{aligned} \tag{6}$$

where Ω_r is a fixed reference frequency; q_n and q_s are damping parameter exponents determined from test; and C_x, C_y, and C_z are assumed to be proportional to an effective dynamic stiffness such that

$$\begin{aligned}
C_x &= 2K_x\zeta_s/\Omega_r \\
C_y &= 2K_y\zeta_x/\Omega_r \\
C_z &= 2K_z\zeta_n/\Omega_r
\end{aligned}$$

in which ζ_n and ζ_s are dimensionless damping parameters determined from tests. Due to the coulomb frictional forces present in the pad, the pad stiffness properties are discontinuous at the strain-rate reversals that occur during cyclic motion. Hence, it is reasonable to define K_x, K_y, and K_z as effective dynamic stiffnesses which are stress dependent; that is,

$$\begin{aligned}
K_x &= m\omega_s^2 \left[\bar{S}_{zx}^{(I)}\right] \\
K_y &= m\omega_s^2 \left[\bar{S}_{zy}^{(I)}\right] \\
K_z &= m\omega_n^2 \left[\bar{S}_{zz}^{(I)}\right]
\end{aligned}$$

where ω_n and ω_s are low amplitude resonant frequencies about mean stress levels, $\bar{S}_{zz}$, $\bar{S}_{zx}$, $\bar{S}_{zy}$, of the fluctuating components of pad stress. The frequencies ω_n and ω_s may be determined on the basis of low amplitude sinusoidal normal and shear tests, respectively, about prestress conditions in the pad. Furthermore, it is convenient to select the reference frequency, Ω_r, equal to the vertical low amplitude resonant frequency about a zero mean stress level in an actual tile/pad system*

$$\Omega_r = \omega_n[0]$$

Vertical-Lateral Coupling.- Pad property tests have revealed a coupling between vertical and lateral motions of the tile on the pad [11]. The coupling occurs as a consequence of two mechanisms as depicted schematically in Fig. 5. One of these mechanisms is geometric while the other is due to the anisotropic nature of the pad's manufacture. The geometric coupling is due to the pad filaments shearing laterally and giving rise to a negative vertical tile motion. Since the pad is quite soft in shear, its lateral motion and consequent vertical motion is not negligible. The geometric coupling is described by employing the large deformation definition of strain in Eqs. (1).

The anisotropic nature of the pad may be expressed as

---

*The tile/pad system considered herein consists of a 152.4 × 152.4 × 95.25 mm LI900 tile on a 127 × 127 × 4.06 mm pad, (6 × 6 × 3.75 in. tile on a 5 × 5 × 0.160 in. pad). An LI900 tile has a mass density of 144.2 kg/m^3 (9 lbs/ft^3).

$$\begin{Bmatrix} E_{zz} \\ 2E_{zx} \\ 2E_{zy} \end{Bmatrix} = \begin{bmatrix} 1/E & c_{zx}/G_{xx} & c_{zy}/G_{yy} \\ c_{zx}/G_{xx} & 1/G_{xx} & 0 \\ c_{zy}/G_{yy} & 0 & 1/G_{yy} \end{bmatrix} \begin{Bmatrix} S_{zz} \\ S_{zx} \\ S_{zy} \end{Bmatrix} \tag{7}$$

where it is understood that E, G_{xx}, and G_{yy} depend on S_{zz}, S_{zx} and S_{zy}, respectively. The relative magnitude of the off-diagonal terms may be ascertained by considering a pure shear case in which

$$S_{zz} = S_{zy} = 0$$

and

$$S_{zx} = \tau_a$$

For different values of τ_a, experimentally determined values of the tile rigid body motions are then substituted into Eq. (1) and the resulting strains are substituted into Eqs. (7) to determine the coupling term, c_{zx}/G_{xy}. This effectively removes the effect of the geometric coupling. The results are plotted in Fig. 6 which reveals that for τ_a less than 5 psi, the anistropic coupling term is less than 4 percent of the diagonal term. Thus, the anisotropic coupling mechanism may be safely neglected and the geometric coupling mechanism constitutes the great majority of the vertical-lateral coupling. This simplification is fortunate since the tracing of the loading/unloading paths in the presence of anisotropy would have added considerable complications to the analysis.

Equations of Motion

The equations of motion which are derived from the principle of virtual work in Ref. [5] may be expressed as,

$$\{Q\} + [M]\{\ddot{q}\} = \{F\} \tag{8}$$

where $\{Q\}$ is the internal resultant force vector whose components are

$$Q_1 = \int_{A_p} \left[S_{zz}(1 + \varepsilon) + S_{zx}\beta_y + S_{zy}\beta_x \right] dA_p$$

$$Q_2 = \int_{A_p} \left[S_{zx} + \gamma_x S_{zz} - (1/2)\theta S_{zy} \right] dA_p$$

$$Q_3 = \int_{A_p} \left[S_{zy} + \gamma_y S_{zz} + (1/2)\theta S_{zx} \right] dA_p$$

$$\begin{aligned} Q_4 = \int_{A_p} \Big\{ & y/h_p \left[(1 + \varepsilon)S_{zz} + \beta_y S_{zx} + \beta_x S_{zy} \right] \\ & + (1/2)S_{zy}(1 + \varepsilon) \Big\} \, dA_p \\ & + (1/2)(h_T/h_p)Q_3 \end{aligned}$$

$$\begin{aligned} Q_5 = \int_{A_p} \Big\{ & -x/h_p \left[(1 + \varepsilon)S_{zz} + \beta_x S_{zy} + \beta_y S_{zx} \right] \\ & - (1/2)S_{zx}(1 + \varepsilon) \Big\} \, dA_p \\ & - (1/2)(h_T/h_p)Q_2 \end{aligned}$$

$$\begin{aligned} Q_6 = \int_{A_p} \Big[& S_{zz}(x\gamma_y - y\gamma_x)/h_p \\ & + (1/2)S_{zx}(\gamma_y + x\theta/h_p - 2y/h_p) \\ & + (1/2)S_{zy}(2x/h_p + \theta y/h_p - \gamma_x) \Big] \, dA_p \end{aligned}$$

and, β_x and β_y are average rotational components,

$$\beta_x = (1/2)(\partial w_s/\partial y + \alpha_x)$$

$$\beta_y = (1/2)(\partial w_s/\partial x - \alpha_y)$$

$[M]$ is the diagonal mass matrix.

$$[M] = m \begin{bmatrix} 1 & & & & & 0 \\ & 1 & & & & \\ & & 1 & & & \\ & & & r_x^2/h_p^2 & & \\ & & & & r_y^2/h_p^2 & \\ 0 & & & & & r_z^2/h_p^2 \end{bmatrix}$$

$\{q\}$ is the vector of displacement components,

$$\{q\} = \begin{Bmatrix} w_o \\ u_o \\ v_o \\ \alpha_x h_p \\ \alpha_y h_p \\ \theta h_p \end{Bmatrix}$$

and $\{F\}$ is the applied tile force vector,

$$\{F\} = \begin{Bmatrix} P \\ F_x \\ F_y \\ M_x/h_p \\ M_y/h_p \\ T_o/h_p \end{Bmatrix}$$

Equations (8) are integrated explicitly using the following recursive relations

$$\{\dot{q}\}_{i+1} = \{\dot{q}\}_i + \Delta t [M]^{-1}\Big(\{F\}_i - \{Q\}_i\Big)$$

$$\{q\}_{i+1} = \{q\}_i + \Delta t \{\dot{q}\}_{i+1} \qquad (9)$$

where Δt is an appropriate time step. The initial conditions are specified on the strain-rate independent Kirchhoff stress components, on $\{q\}$, and on $\{\dot{q}\}$. The initial strains and strain-rates may then be calculated from Eqs. (1) and the strain-rate dependent stresses from Eqs. (4). If the initial state of stress-strain lies outside of the normal or shear envelope, then the strain-rate must initially be nonzero.

At the ith step, the known vector $\{q\}_i$ and $\{\dot{q}\}_i$ are used to compute the Green strains and strain rates from Eqs. (1). In turn, these strains and strain rates, in conjunction with the tracing of the stress-strain curves (see Ref. [4] for details on how the tracking of the stress-strain curves is accomplished on the computer) provides the Kirchhoff strain-rate independent stress components. The strain-rate when substituted into Eqs. (7) yields the Kirchhoff strain-rate dependent stress and the sum of independent and dependent components yields the total Kirchhoff stress. Integration of the total stresses in Eq. (8) yields the total stress resultants in the pad, $\{Q\}$. The integrations of Eq. (8) are performed numerically using standard quadrature subroutines. The velocity and displacement vectors are updated for the i + 1th time step using Eqs. (9).

DISCUSSION OF RESULTS

In this paper application of the analysis presented herein is limited to a typical LI900 thick tile on the Space Shuttle subject to sinusoidal or random substrate motion. Experimental results are taken from Refs. [14] and [15]. As determined in Ref. [4], nonlinear viscous damping coefficients of $q_n = 2$ and $\zeta_n = 0.15$ were used.

Wave Shape

Figure 7 shows the analytically predicted and experimentally observed steady-state tile/pad interface stress, σ_{zz}, as a function of time due to a sinusoidal substrate motion having an acceleration of 30 g's and oscillating frequency of 80 Hz. Both the analytical and experimental wave shapes are highly nonlinear with high stress peaks. (A linear system would give a purely sinusoidal response.) These peaks seem to be due to the tile acquiring a high velocity over the soft material range which causes it to overshoot into the stiff material range, thus producing high stress peaks on each cycle of motion.

Resonant Frequency

Figure 8 displays the variation of resonant frequency with substrate acceleration amplitude measured in g's. The resonant frequency is taken as that frequency which yields the peak amplitude steady-state pad stress. The experimental data were derived from tests on two tile/pad specimens. Variation in pad properties between the two specimens probably accounts for much of the data scatter. The analysis uses average pad data and thus lies within the data scatter. With increasing amplitude of substrate acceleration, analysis and experiment both show a rapid decrease in resonant frequency (nonlinear softening) followed by a slow increase in resonant frequency (nonlinear hardening).

The trend can be understood by considering the material behavior of Fig. 4(a). For small amplitudes of substrate acceleration the material follows a stiff loading/unloading loop (loop A), with little or no portion of the cycle on the lower modulus envelope. This indicates that for small amplitudes the friction forces between pad filaments accounts for the entire load carrying mechanism of the pad. As the amplitude is increased, a larger portion of the cycle lies on the soft portion of the envelope (loop B), and so the resonant frequency decreases. With further increase the resonant frequency starts increasing as more and more of the cycle begins to include the higher modulus region of the envelope at raised stress levels (loop C).

Pad Damping

Damping mechanisms in the pad may be examined by using the analysis to evaluate the loss factor, η, at the resonant steady-state frequency. The loss factor is defined herein as

$$\eta = (1/2\pi)(E_d/E_k) \qquad (10)$$

where E_k is the peak kinetic energy attained by the tile during a steady-state cycle of motion, namely,

$$E_k = (1/2)\ m|\dot{w}_{peak}|^2$$

and E_d is the energy dissipated by the pad per cycle of steady-state motion which may be calculated by evaluating the integral,

$$E_d = \int_{t_o}^{t_o+T} A_p \sigma_{zz}(\dot{w} - \dot{w}_s)\ dt$$

in which t_o is any time large enough so that the system is in steady-state motion and T is the period of motion.

In Fig. 9, the variation of η with amplitude of substrate acceleration is shown with and without nonlinear viscous damping present. That is, with both strain-rate independent and dependent stresses present, and with only strain-rate independent stresses present. In the latter case, the energy dissipation is due only to hysteretic losses attributable to pad friction. Both curves exhibit similar trends and approach constant values at large amplitudes of substrate motion. For high amplitudes it appears that the energy loss due to strain-rate independent stresses alone accounts for about 30 percent of the total energy loss; thus, both dissipation mechanisms are important.

Parametric Resonance

At certain combinations of the vertical substrate acceleration amplitude and the frequency, the system may become unstable laterally. This is demonstrated analytically in Fig. 10(a) where the substrate is oscillating vertically in steady state motion at 80 Hz with an acceleration amplitude of 30 g's. If the system is perfectly symmetric, as is assumed here, no lateral motion occurs and the normal stress, σ_{zz}, exhibits the typical nonlinear high peaked response history seen in Fig. 7, while the shear stress is zero. However, in reality there always exists some perturbing disturbance to excite an instability if one exists. Hence, to excite the lateral motion analytically, a small oscillatory disturbing shear stress is externally applied to the tile with a magnitude of 0.003 psi and oscillating at 80 Hz; the same frequency as the vertical motion. (This is equivalent to 0.03 g's of lateral acceleration on the tile.) After a few cycles the lateral stress grows from 0.001 psi to about 0.5 psi and takes on a frequency about half that of the vertical substrate and tile frequency. Such behavior is classically referred to as parametric response. Figure 10(a) also shows that as the shear stress and hence lateral motion grows, the normal stress decreases as energy leaves the vertical motion and goes into lateral motion.

Using the analysis herein, similar results can be generated for other combinations of amplitude and frequency to produce the stability boundary shown in Fig. 10(b). The stability boundary is derived using average pad properties and thus other tile/pad specimens may have somewhat different boundaries from what is shown here. However, general statements about its character can be safely made.

The figure illustrates that for low amplitude motion the system is always stable, but becomes unstable above a critical value of excitation amplitude which for the pad properties used herein is 16 g's. The instability occurs over a specific frequency band; the width of the band growing slowly with increasing amplitude. Further, for the tile/pad combination under examination here, there does not appear to be any instability possible at frequencies below 40 Hz independent of amplitude.

Also shown in Fig. 10(b) is a duplicate of the experimental and analytical resonant frequency variation of Fig. 8. As is seen, the analytically predicted resonant frequencies, for the pad properties used herein, lie outside of the unstable range for values of excitation amplitude less than 32 g's. Above this value the resonant frequency will have little significance unless the tile is restrained from lateral motion. All but one of the experimental resonant frequencies lie outside of the predicted unstable region and above 16 g's of excitation the test data generally lie above the unstable region. Thus, in performing sine sweep tests to locate resonant frequencies, the unstable region may be entered temporarily. Indeed this has been the experience in experimental investigations, where the parametric resonance of the system was first observed. Parametric resonances were observed to occur in torsional as well as lateral modes.

Although lateral instabilities were observed experimentally and analytically under sinusoidal substrate excitation they have not been observed under the random loads of the actual dynamic environment. Nevertheless the lateral instability does indicate a strong coupling between vertical and lateral motion. Since the tile will also rock during lateral motion an inertial moment on the tile due to coupling must be accounted for as has been done in determining equivalent static loads for the system stress analysis [2].

Gain Values for Random Substrate Excitation

Random spectral tests and nonlinear analysis were performed at different substrate peak g^2/Hz levels on 0.454 and 0.844 Kg (1.0 and 1.86 lb) tile/pad configurations. These tile masses are high for typical Shuttle tiles but were selected specifically for test-analysis correlation. For both test and analysis system gains based upon rms tile acceleration to rms substrate acceleration and the peak tile acceleration to peak substrate acceleration were determined and plotted against the substrate rms acceleration level in Fig. 11. Considering the variation of pad properties from specimen to specimen, the correlation is very good using average pad properties.

In performing the nonlinear analysis, the power spectral density (PSD) associated with substrate excitation used in the test is employed to derive an appropriate substrate acceleration history using a random number generator subject to the constraint of a Gaussian probability density distribution.

If the system was linear, the curves of Fig. 11 would show no variation with substrate rms acceleration level and the gains based upon rms and peak ratios would be identical. Inasmuch as both test and analysis gains based on rms ratios display little variation with substrate acceleration level, gains based on rms ratios could be predicted using a linear analysis with the appropriate amount of damping. However, this is not true for gains based on peak ratios. Both test and analysis gains based on peak ratios become considerably higher than those based on rms ratios at higher substrate acceleration levels. The result is strictly a nonlinear phenomenon.

Probability of Occurrence for Positive Peak Pad Stresses Due to Random Gaussian Substrate Acceleration

In predicting the fatigue life of the thermal protection system, it is first necessary to predict the probability of occurrence of positive pad stress peaks. It is often convenient to assume that this follows a Rayleigh distribution. In a linear system where the excitation positive peaks follow a Rayleigh distribution, the assumption is completely valid. The rms pad stress completely characterizes the assumed Rayleigh distribution and the probability of occurrence for positive pad stress peaks exceeding three times the rms pad stress or 3-SIGMA value is about 3.3 percent. Therefore, the purpose of this section is to address the validity of the Rayleigh distribution using the nonlinear analysis.

In the nonlinear analysis, it is first necessary to generate random Gaussian substrate acceleration histories which have the proper PSD's. These substrate acceleration histories are then used as transient excitations in the nonlinear analysis. The predicted nonlinear pad stress history is then calculated and the data reduced (this includes counting and ordering positive peak stresses) to provide the probability density of positive peak pad stresses as shown for example in Fig. 12. Also shown is the tile weight, PSD input spectrum used, linear and nonlinear predicted rms tile response and pad stress. A comparison of the nonlinear predicted probability density of positive peak pad stresses with the assumed Rayleigh distribution is normalized on the basis of a linear predicted rms stress. The linear analysis assumes 35 percent of critical damping and a linear stiffness of 1368 N/cm (781 lb/in.). The comparison indicates that, in general, there is little difference between the linear and nonlinear predicted rms stress values; the same conclusion reached previously. As a consequence, the Rayleigh distribution generally provides a good approximation for the occurrence of pad stresses near the rms stress value which has the greatest probability of occurrence. However, as the pad stresses get higher, the Rayleigh distribution becomes more inaccurate, with a much higher percentage of peaks occurring beyond three times the rms stress value. It is these higher stresses which are most damaging to the life of the thermal protection system. They exceed the Rayleigh distribution prediction due to the presence of nonlinearities in the pad behavior which have more influence when higher pad stresses are present. Similar results show that the greater the substrate motion, the higher the pad stress and hence the greater the exceedance of the Rayleigh distribution at its high end, while for lighter tiles the exceedance decreases [6].

Summary of Nonlinear Dynamic Analysis Results

In view of the test data scatter due to the variation of material properties from test specimen to specimen, the dynamic analysis is in good agreement with the experimental results. Both test and analysis show an amplitude dependent resonant frequency and gain ratios based on peak values. Gain ratios based on rms values appear to be predictable from a linear analysis when appropriate linear viscous damping values are chosen since the rms based gains show little variation with amplitude. Gain ratios based on peak values are seen to be higher than those based on rms values. However, it is believed that the design loads are sufficiently conservative so that the lower rms based gains can be safely used rather than the higher peak based gains.

Although the dynamic analysis produced useful general information on the system behavior, gave added confidence that the system was understood, and could be exercised on specific individual tiles, it was not feasible to perform a dynamic analysis on each of thousands of tiles. Thus, a static nonlinear analysis using equivalent static loads from the dynamic environment [2] was developed and applied. The dynamic analysis also aided in defining an unanticipated load for the static analysis in the form of a moment due to vertical-lateral coupling.

STATIC ANALYSIS AND DATA MANAGEMENT SYSTEM

Scope

Assessment of the integrity of the thermal protection system required that a stress analysis be performed on each of thousands of tiles as shown in Fig. 13. A stress analysis program [7-9] was developed for this purpose. The analysis accounts for the nonlinear material properties of the strain isolator pads used to attach the tiles to the metal surface of the Orbiter. This analysis requires geometry definition, aerodynamic and vibroacoustic loads, Orbiter surface deflections, and materials data for each tile (see Fig. 14). For example, the material properties of the pad and filler bar depend upon the proof test level used on each individual tile inasmuch as this causes the pad filaments to realign themselves [1]; thus, making the pad under each tile unique. The geometry, loads and material data existed in many forms in various engineering reports. The gathering and preparation of input data for the analysis of a single tile was a time-consuming process (required approximately one man-day per tile) when done by hand. Therefore, there was a need for the capability for automatic storage and retrieval of data needed for analysis so that large numbers of tiles could be analyzed in a timely manner.

To incorporate an advanced engineering data management system with a static nonlinear stress analysis use was made of the Relational Information Management (RIM) system [16] which was developed as part of the NASA-sponsored IPAD project. The interactive query language of the RIM system is used to make selected on-line retrievals of any stored data. A FORTRAN interface, which is a set of user callable RIM subroutines, is used extensively by other computer programs needed for communication of data between the nonlinear analysis program and RIM. This analysis/data management system served to automate the entire tile assessment process beginning with access of tile data from RIM through execution of the nonlinear stress analysis program and display of results. This significant analysis effort was performed in a timely manner (less than a day) and is typical of the studies performed to aid in flight-readiness certification of the tiles for the first Orbiter flight.

Capabilities

The capabilities of the static analysis are schematically illustrated in Fig. 14 and are similar to those of the dynamic analysis. However, there are certain significant differences.

Configuration.- To provide capability to analyze all tile configurations, the pads are defined with an arbitrary boundary made up of linear segments including cutouts for instrumentation or other penetrations. Since the analysis process requires integration of stresses over the pad, the pad and/or filler bar surfaces are divided into triangular regions each containing a mesh of subtriangles as shown in Fig. 14(c). The integrated stress is the sum of contributions of assumed linear stress distributions over each subtriangle. The mesh refinement can be varied to give any desired solution accuracy.

Material Properties.- In statically treating the nonlinear material properties of the pad and filler bar, it is assumed that the tile experiences no load reversals in arriving at a given load state. Thus the modeling of the hysteretic nature of the material as required in the dynamic analysis is eliminated. With this complication removed it becomes feasible to model the softening of the pad which occurs at high stress levels as shown in Fig. 14(d). For accurate stress analysis, this may have a significant effect.

Tile Loads.- Stresses in the strain isolator pad are caused by pressures acting on the tile which result from the aerodynamic environment, inertia forces from vibratory motion of the tile, and deflections of the substrate to which the pad is attached. The vibratory inertia loading on the tiles and corresponding dynamic substrate deflections are collectively referred to as vibroacoustic loads.

The various tile loading sources considered are shown in Fig. 14(e). The parameters needed to define the steady aerodynamic loads include the pressure change across a shock for both separated and unseparated flow, aerodynamic pressure gradients in the streamwise and transverse directions, and a reference pressure which is related to the ambient pressure. Aerobuffet loading is given as forces and moments measured from wind-tunnel tests. The load on the tile caused by a lag in venting the interior tile pressure during Orbiter ascent is taken to be a constant value for all tiles. The skin friction on the external surface is a function of the distance of the tile from the leading edge of the Orbiter planform, a quantity that is calculated and stored in the data management system for each tile. The substrate deformation for vibroacoustic loading has a specified amplitude and wavelength corresponding to the structural panel width. The static substrate deflection corresponds to deformation of the skin between stiffeners on the panel caused by a combination of in-plane loads and pressure differentials across the skin. In the analysis procedure, the deflections of the substrate are positioned relative to the tile to give maximum stress. The maximum positive amplitude of the long wavelength is positioned at the center of the tile while the maximum negative amplitude of the short wavelength is positioned under the front corner of the tile. These substrate deflection positions were guided by results presented in Ref. [17].

The data needed to describe this load environment are defined in relation to aerodynamic and structural panels defined on the surface of the Orbiter. The aerodynamic load parameters are taken to be constant within each of the aerodynamic panels shown in Fig. 14(f). The boundaries of the wing panels are located at constant fraction of semispan locations and constant percent chord locations, the usual nondimensional coordinates used by aerodynamicists. Only two aerodynamic panels, corresponding to the MF-5 and MF-6 tile regions of the Orbiter are used for the fuselage.

The static substrate deflection is defined in relation to the structural panels shown in Fig. 14(g). The boundaries of the wing structural panels are along ribs and spars and along frames and stringers on the fuselage. The vibroacoustic tile loading is a function of distance from the panel boundary.

Stress Analysis

In the baseline or original configuration, the tiles had uniform properties through the thickness (undensified tiles). During early testing of the undensified tiles under externally applied loads, failure was found to occur in the tiles adjacent to the plane where they were bonded to the pad. Based on this observation, it is assumed that the integrity of the system depends upon the normal stress at the pad/tile bondline. If this calculated normal stress exceeded a specified allowable stress, the tile was removed and densified (strengthened by a thin layer of impregnated material at the tile's inner surface).

A tile analysis program based on the above considerations was developed to calculate these normal stresses in the pad [8,9]. The analysis procedure is a generalization and extension of the basic method described in Ref. [7] and is the static counterpart of Eqs. (8), but with assumed small deflections. External loads are applied to the tile as concentrated forces, pressures, and/or inertially equivalent accelerations (g-load). The substrate under the pad can be given a prescribed shape to represent mismatch from the manufacturing process, warpage of the tile, and/or deformations of the external surface of the structure such as those caused by buckling.

A Newton iteration procedure is used to calculate the displacements and rotations of the rigid tile for which the reaction forces from stresses in the pad and filler bar material are in static equilibrium with the applied loads. Once equilibrium is established, the maximum stress and its location in the pad are calculated. The uniqueness and stability of the nonlinear solution as well as the convergence of the Newton iteration is addressed in Ref. [7].

Data Handling

The use of the RIM system for managing the Orbiter tile data was greatly facilitated by its efficient, flexible, easy-to-use capabilities for data retrieval. The capabilities provided ready access to the tile engineering data for display in a user selected form. The methods used to retrieve, manipulate, and display the tile data are discussed in this section.

A relational query language, which contains Boolean conditional clauses for selecting desired data, is available in RIM. This language has the flexibility to support retrieval of data to satisfy a variety of conditions many of which were not anticipated during the organization of the tile data base. The syntax of the query language statements makes them self-explanatory. In general, the statements specify an operation to be performed, specify the location of the data within the data base, and define conditions to be satisfied by data values. Data manipulation commands are available in RIM to change the contents and organization of the data base.

Graphical displays of the tile data were important for validating or correcting the data after it was loaded into the data base. A separate plotting program was developed for this purpose. This program generates a planform view of tile geometry with each tile annotated with any related data which can be displayed on an interactive terminal and/or offline plotter. Such a display is illustrated by the planform view of tiles in Fig. 13.

Automated Data Management/Analysis System

The data management system RIM together with the analysis programs were combined into a system which was used to calculate, display, and interpret tile analysis results. The resulting automated data management/analysis system is a collection of computer programs and data files needed for data communication between the nonlinear stress analysis program and RIM. This system can be used in three different modes as indicated in Fig. 15. The first mode is to use the RIM interactive Executive as a stand-alone system and access any of the desired engineering data. This capability is usually accessed from an interactive terminal with keyboard input and printed output. In the second mode, graphical displays of selected data are generated on an on-line terminal and/or off-line plotter using the separate program developed for this purpose. The third user mode is to perform automated stress analysis. This mode requires use of pre- and post-processors containing several computer programs and data files to connect the stress analysis program with the RIM data files. The development of the pre- and post-processors was a significant task requiring the same level of effort as the creation of the tile data base itself. Neither the stress analysis program nor RIM were modified during development of the automated system.

User-prepared input data are required to select the tiles and to specify load conditions to be used in a particular analysis. This information is used by the preprocessor to extract all data from the RIM data files which are required for a stress analysis and to generate an analytical model of the tile and its applied loads.

The preprocessor makes extensive use of the RIM FORTRAN interface subroutines. These subroutines are used to support repetitive queries that are tailored to extract all data necessary to analyze the selected tile part numbers at the specified Mach number selected from a prescribed Shuttle Orbiter flight trajectory. The resulting analytical model is in the form of a card image input file which is used by the nonlinear stress analysis program. The maximum interface stress for each tile/pad combination is computed for each load case that is specified, thus completing the automated stress analysis process. This calculated stress information is usually subsequently processed to determine the load case which produces the largest stress for each tile. These stress values are compared with the allowable stresses and then all pertinent stress data are stored in the RIM data files using a postprocessor. Various user initiated queries are then made to assess the calculated stress data.

Because of computing time requirements for the nonlinear stress analysis procedure, interactive use of the system is effective when only a few cases are to be analyzed. For the analysis of a large number of tiles and/or load cases, operation of the system in a batch mode is desirabl

The automated data management/analysis system required a 10 man-month effort for development. Approximately 60 percent of the effort was required to gather, organize, and store the data into RIM and the other 40 percent involved the development of computer programs to serve as an interface between the stress analysis program and the RIM data base. The data base contains approximately 600,000 words of engineering data necessary to analyze the 8,000 tiles on the lower surface of the wing and fuselage (Fig. 13). An additional 250,000 words of data are used for schema descriptions and inverted files that are retained so that a total of 850,000 words of disk storage are required.

The largest application of this system was the analysis of all 3,137 undensified tiles on the lower surface of the Orbiter. A nonlinear stress analysis performed for each of these tiles required approximately 9.5 hours of central processing time on CDC CYBER 175 computers. This analysis was divided into several individual runs, each involving approximately 100 tiles. This division into smaller runs was a precautionary measure to minimize the effect of a software or hardware malfunction. It also allowed an opportunity for incremental review of results while taking advantage of the multiprograming capabilities of the CYBER computer. Over 3,000 tiles were analyzed in one day in contrast to the previous manual analysis which required one man-day per tile. A typical analysis of 100 tiles required 0.8 minute for execution of the data access and analytical model generation programs and 20.0 minutes for the nonlinear stress analysis program. Thus, the data access and model generation time is minor compared to the time required for stress analysis. Accordingly, it is cost-effective to regenerate the analytical models of the tiles for input into the stress analysis program each time an analysis is made rather than save the models on auxiliary storage.

During the tile study, graphic displays were used to assess the calculated stress data. Although data for each tile zone were stored in a separate data base, it was sometimes desirable to have composite pictures of the calculated results. For this purpose, the data in all pertinent relations were combined in a common data base. Such a common data base was used to create the display of 1,000 undensified tiles on the lower surface of the Orbiter in Fig. 16. These tiles are annotated with an integer 1-10. Each integer indicates a group of 100 tiles for a table sorted in order of decreasing criticality of their calculated stresses.

During the development of an automated analysis system to access the data, many changes in data organization and data content were made. These changes reflected the evolutionary nature of an engineering analysis process. For example, during development of the system, there was a continuing modification of the loads data as various wind-tunnel tests were completed accompanied by changes in criteria used to apply these loads to the tiles in combinations to give realistic design conditions. Hence, an important feature of an engineering data management system is the flexibility for changing the contents, not only addition or deletion of data items but also reorganization or restructuring of the data base schema.

The integrity of the software system and security of the data was manifested by the fact that no data were inadvertently destroyed or lost because of system malfunction during development and use of the tile analysis system. The use of the automated system proved to be successful in producing analysis results for large numbers of tiles in a timely manner. These results aided in the flight-readiness certification of the tiles for the first Orbiter flight and aided in determining which tiles should be removed and densified between the first and second Orbiter flights.

Summary of Data Management/Analysis System

The application of an engineering data management system was found to be very effective for the stress analysis of Space Shuttle Orbiter tiles. By use of this system, thousands of tiles can be analyzed in one day in contrast of the one man-day of effort per tile required when input was prepared manually. Thus, the system permitted the efficient analysis of thousands of unique tile/pad combinations, produced reliable data handling and effected easy alteration of material, load and geometry data.

CONCLUDING REMARKS

Dynamic and static nonlinear analysis procedures have been developed and applied to study and assess the integrity of the tile/pad thermal protection system of the Shuttle Orbiter. The experimental results are in reasonably good agreement with analysis. These procedures gave added confidence that the thermal protection system was understood and permitted the appropriate calculation of risks for flight. The stress analysis results influenced the densification and rebonding of many tiles and were used to establish the flight readiness certification of the tiles.

REFERENCES

1. Cooper, P. A.: Structural Characteristics of the Shuttle Orbiter Ceramic Thermal Protection System. Shock and Vibrations Bulletin, 1982.
2. Muraca, R. J.: Shuttle Tile Environments and Loads. Shock and Vibration Bulletin, 1982.
3. Sawyer, J. W.; and Rummler, D. R.: Room Temperature Properties of Shuttle Thermal Protection System Materials. NASA TM 81786, April 1980.
4. Housner, J. M.; Edighoffer, H. H.; and Park, K. C.: Nonlinear Dynamic Response of a Uni-Directional Model for the Tile/Pad Space Shuttle Thermal Protection System. NASA TM 81901, Nov. 1980.
5. Housner, J. M.; Edighoffer, H. H.; and Park, K. C.: Nonlinear Dynamic Phenomena in the Space Shuttle Thermal Protection System. AIAA SDM Conf., Atlanta, GA, April 6-8, 1981, AIAA Paper No. 81-0565.
6. Edighoffer, H.: Parametric Analytical Studies for the Nonlinear Dynamic Response of the Tile/Pad Space Shuttle Thermal Protection System. NASA CR 165707, Oct. 1981.
7. Housner, J. M.; and Garcia, R.: Nonlinear Static TPS Analysis. NASA TM 81785, March 1980.
8. Giles, G. L.; and Vallas, M.: Computer Program for Nonlinear Static Stress Analysis of Shuttle Thermal Protection System. Users Manual. NASA TM 81856, May 1981.
9. Giles, G. L.; and Vallas, M.: Use of an Engineering Data Management System in the Analysis of Space Shuttle Orbiter Tiles. AIAA Computers in Aerospace 3rd Conference, San Diego, CA, Oct. 26-28, 1981.
10. Giles, G. L.: Substructure Procedure for Including Tile Flexibility in Stress Analysis of Shuttle Thermal Protection System. NASA TM 81864, August 1980.
11. Sawyer, J. W.; and Waters, W. A., Jr.: Room Temperature Shear Properties of the Strain Isolator Pad for the Shuttle Thermal Protection System. NASA TM 81900, Jan. 1981.
12. Fung, Y. C.: Foundations of Solid Mechanics. Prentice Hall, Inc., Englewood Cliffs, New Jersey, 1965, pp. 436-439.
13. Timoshenko, S.: Vibration Problems in Engineering. D. Van Nostrad Co., Inc., New York, 2nd Edition, 1937, pp. 57-61.

14. Miserentino, R.; Pinson, L. D.; and Leadbetter, S. A.: Some Space Shuttle Tile/Strain-Isolator-Pad Sinusoidal Vibration Tests. NASA TM 81853, July 1980.

15. Miserentino, R.; Pinson, L. D.; and Leadbetter, S. A.: Some Vibration Characteristics of a Space Shuttle Tile/Strain-Isolator Pad System. Presented at the 1980 SAE Aerospace and Exposition, October 13-16, 1980, Los Angeles, CA.

16. Erickson, W. J.: User Guide: Relational Information Management (RIM). Report No. D6-IPAD-70023-M, Boeing Commercial Airplane Company, Seattle, Washington, 1981.

17. Shore, Charles P.; and Garcia, Ramon: Effects of Substrate Deformation and SIP Thickness on Tile/SIP Interface Stresses for Shuttle Thermal Protection System. NASA TM 81855, July 1980.

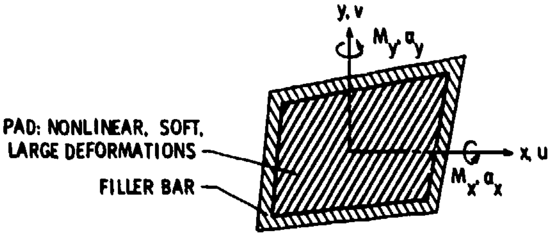

Tile/pad contact area

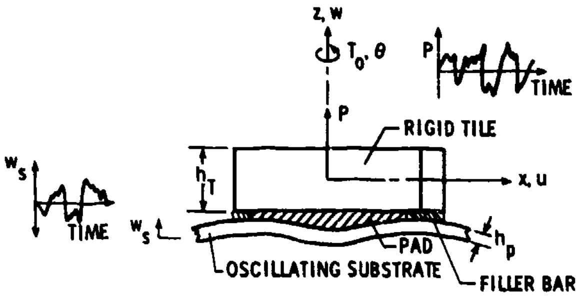

Tile/pad/substrate profile

Fig. 1 - Tile/pad geometry and loads

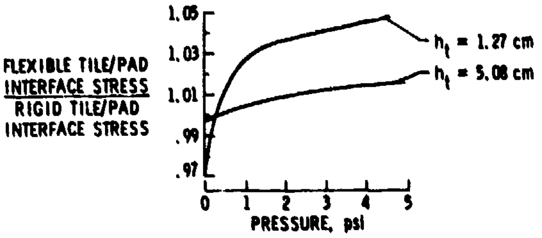

Fig. 2 - Comparison of tile/pad interface tensile stress for flexible and rigid tiles subject to uniform pressure

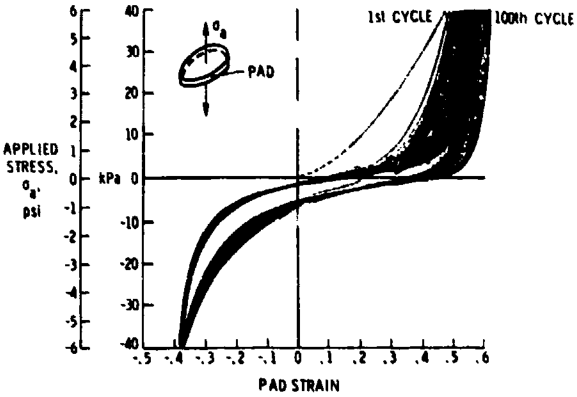

(a) Vertical loading

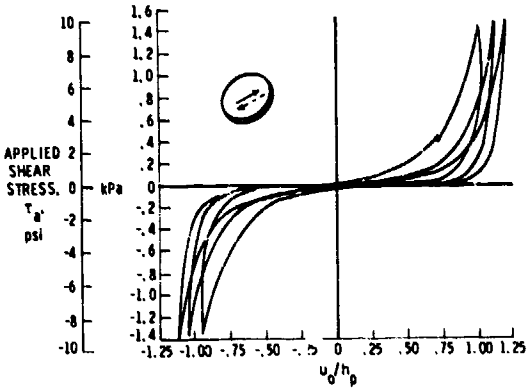

(b) Lateral loading

Fig. 3 - Effect of cyclic loading on pad material properties

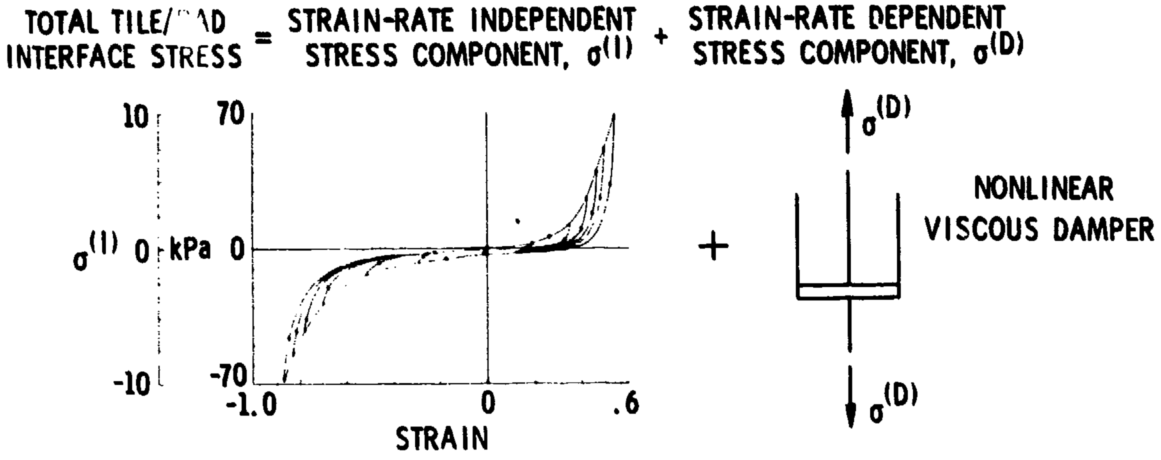

Fig. 4 - Schematic depiction of the summation of strain-rate independent and dependent stresses

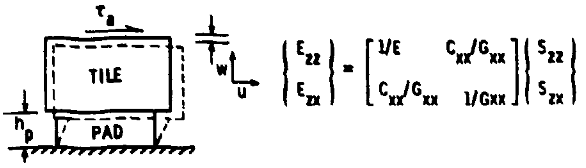

(a) Geometric coupling

(b) Material coupling

Fig. 5 - Schematic depiction of the two mechanisms of vertical-lateral coupling

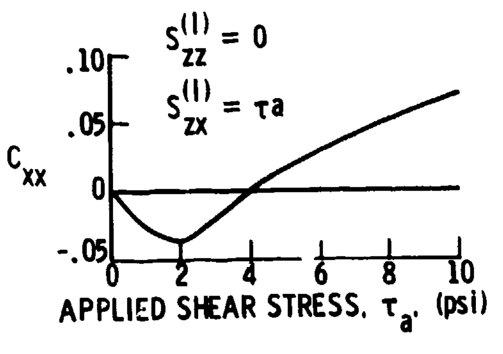

Fig. 6 - Variation of material coupling effect with applied shear stress

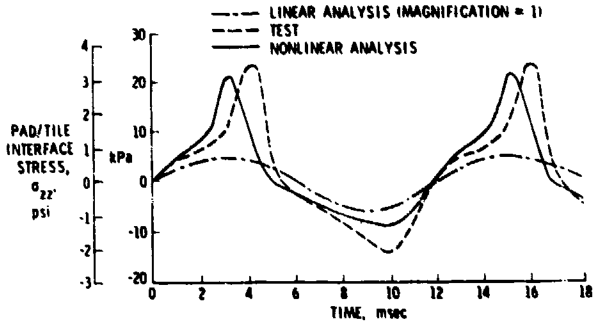

Fig. 7 - Nonlinear wave shape due to vertical sinusoidal substrate acceleration of 30 g's at 80 Hz

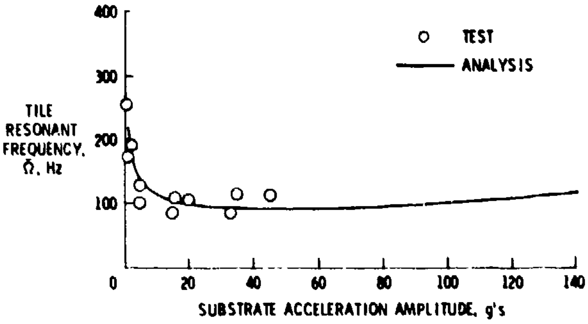

Fig. 8 - Variation of tile-pad resonant frequency with amplitude of vertical sinusoidal substrate excitation

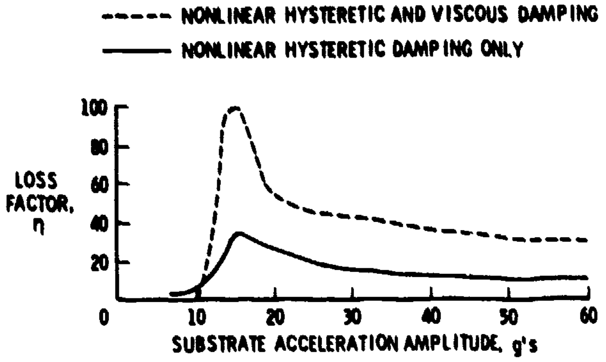

Fig. 9 - Variation of loss Factor with amplitude of vertical sinusoidal substrate excitation at resonant frequency

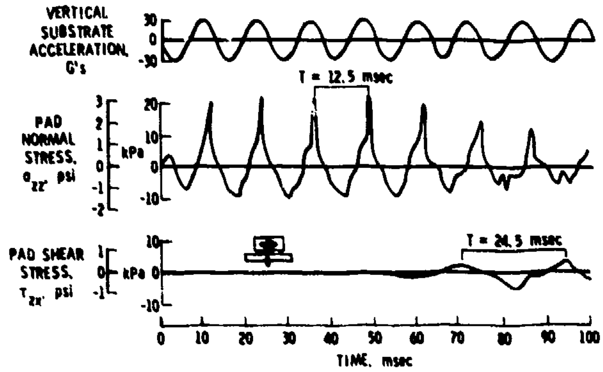

Fig. 10(a) - Development of parametric resonance during vertical sinusoidal substrate motion

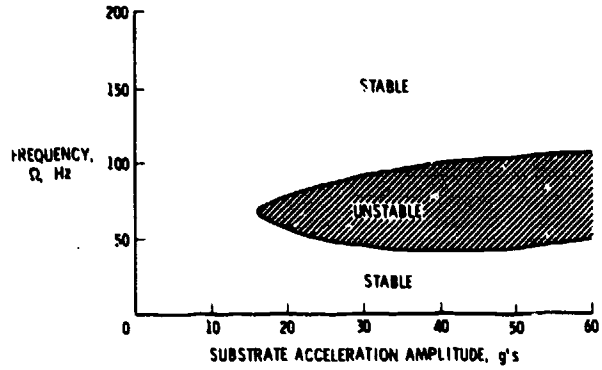

Fig. 10(b) - Parametric resonance stability boundary for vertical sinusoidal substrate excitation

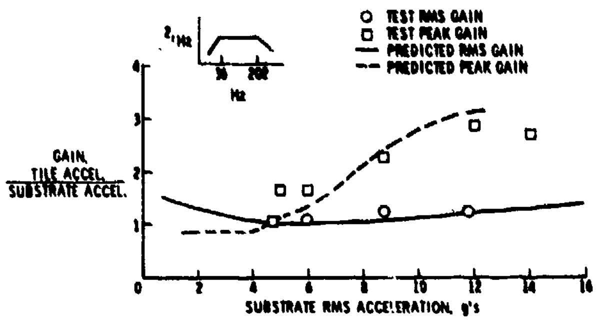

Fig. 11 - Comparison of tests and nonlinear analysis for gains based upon rms and peak tile accelerations under random substrate excitation

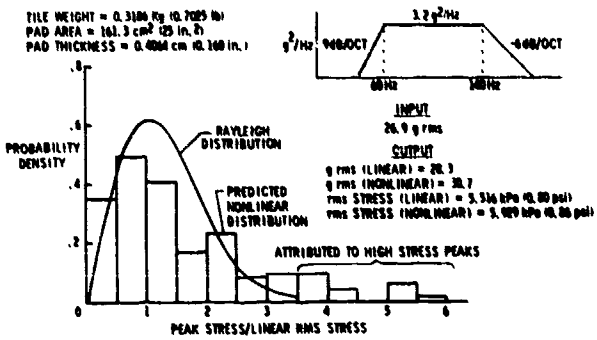

Fig. 12 - Comparison of Rayleigh and nonlinear probability distribution predictions for peak tensile bondline stress

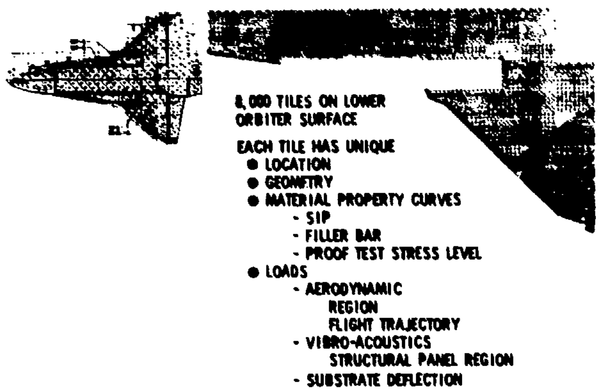

Fig. 13 - Scope of required static tile analysis

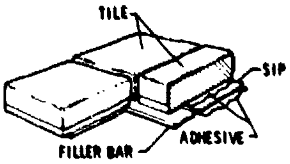

Fig. 14(a) - Typical TPS installation

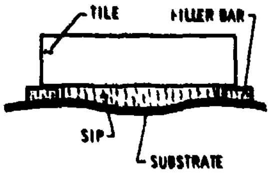

Fig. 14(b) - TPS arrangement

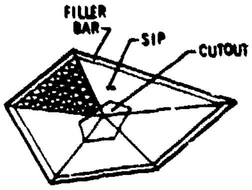

Fig. 14(c) - Nonlinear modeling

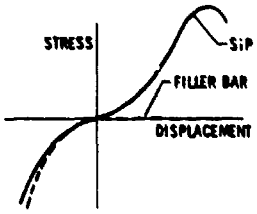

Fig. 14(d) - Material properties

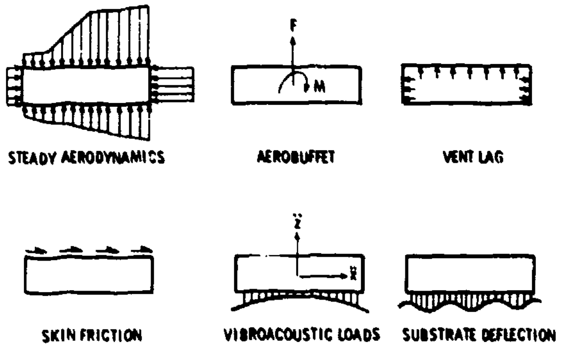

Fig. 14(e) - Loads

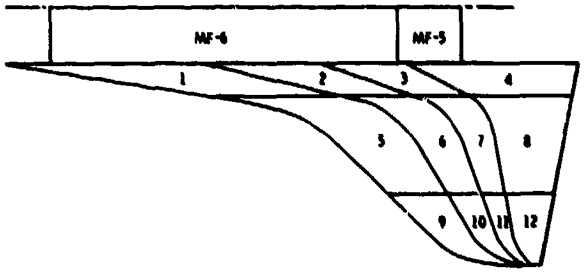

Fig. 14(f) - Load regions

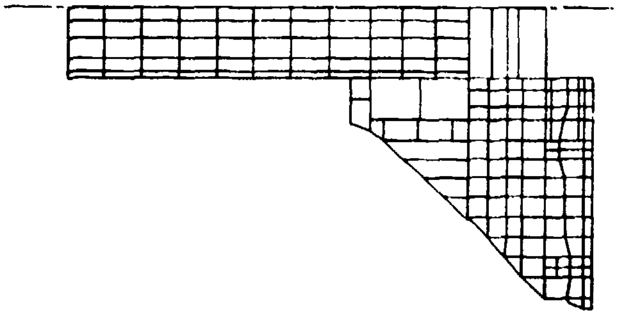

Fig. 14(g) - Orbiter structural panels

Fig. 14 - Static analysis capabilities: geometry, material properties and loads

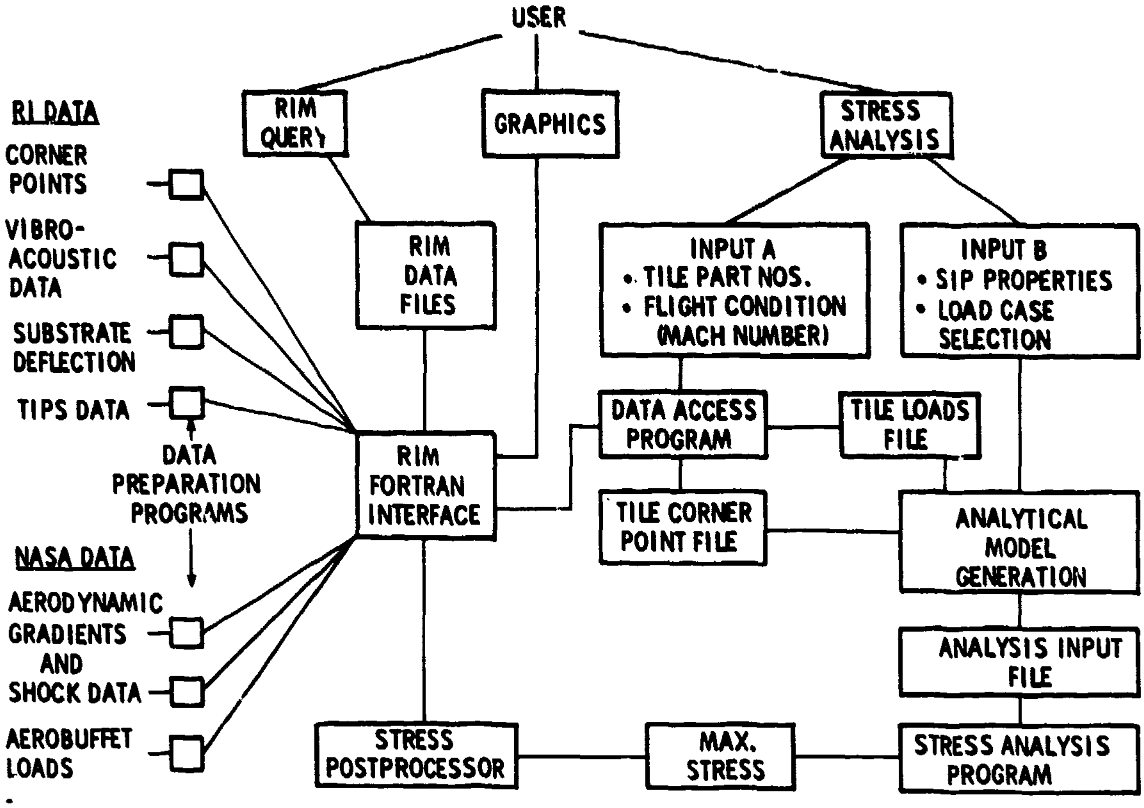

Fig. 15 - Automated data/management static analysis system

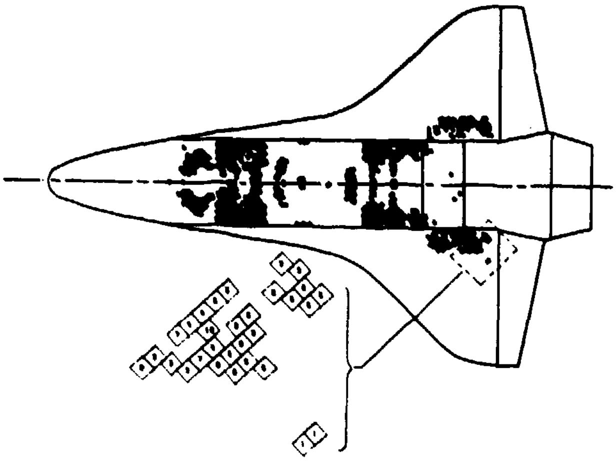

Fig. 16 - Sample output from automated stress analysis

BUFFET LOADS ON SHUTTLE
THERMAL-PROTECTION-SYSTEM TILES

Charles F. Coe
NASA, Ames Research Center
Moffett Field, California

This paper presents results of wind-tunnel and acoustic tests to investigate buffet loads on Shuttle Thermal-Protection-System (TPS) tiles. It also describes the application of these results to the prediction of tile buffet loads for the first shuttle flight into orbit (STS-1). The wind-tunnel tests of tiles were conducted at transonic and supersonic Mach numbers simulating flow regions on the Orbiter where shock waves and boundary-layer separations occur. The acoustic tests were conducted in a progressive wave tube at an overall sound pressure level (OASPL) approximately equal to the maximum OASPL measured during the wind-tunnel tests in a region of flow separation. The STS-1 buffet load predictions yielded peak tile stresses due to buffeting that were as much as 20 percent of the total stress for the design-load case when a shock wave was on a tile.

INTRODUCTION

This paper addresses the problem of evaluating the aerodynamic buffet loads on Shuttle Orbiter TPS tiles. The buffet loads of concern are dynamic loads resulting from pressure fluctuations that occur on tiles in regions of shock waves and separated flows during transonic and supersonic flight (Fig. 1).

SHOCK AHEAD OF TILE, AERO SEPARATION

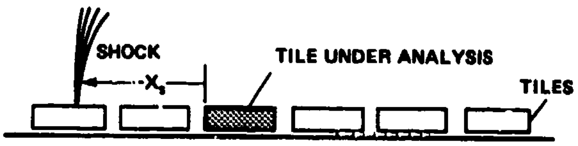

SHOCK ON TILE, AERO SHOCK

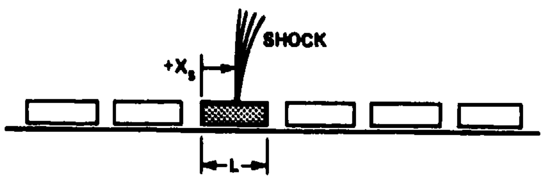

Fig. 1 - Tile buffet-load cases

There are many variables that affect the buffet loads on the more than 30,000 tiles on the Orbiter. The exterior-surface pressure fluctuations are the fundamental source of the excitation; however, the resultant excitation of each tile depends upon the difference between external and internal pressure fluctuations. The reactive surfaces to the excitation are the very thin nonporous glaze on the outer surface and edges of the tile and the adhesive at the bond line. (See preceding paper by Cooper for description of tiles and bonding method.) The tile interior vents only around the periphery of the tile at the base of the gaps between tiles. The magnitude of the internal pressure fluctuations therefore depends on the pressure fluctuations at the base of the gaps and the time constant associated with the porosity of the tile material and the vent area. Gap pressure fluctuations are an important variable that depends upon the tile thickness and the gap dimensions, which can vary with load due to the elasticity of the Strain Isolation Pad (SIP) and substructure. Because of this complexity and impossible scaling of models that could include Orbiter geometry, the only practical approach to the investigation and estimation of buffet loads has been via wind-tunnel tests of full-scale tiles using special fixtures in the wind tunnels to create the desired shock wave and separated-flow environments. Some buffet load tests were also conducted in an acoustic progressive wave tube to determine the differences in loading due to aerodynamic and acoustic environments.

NOTATION

$\tilde{C}_{M_b}$ = buffet pitching-moment coefficient, $\tilde{M}_b/q_\infty S$

$\tilde{C}_{N_b}$ = buffet normal-force coefficient, $\tilde{F}_b/q_\infty S$

$\tilde{C}_p$ = fluctuating pressure coefficient, $\tilde{p}/q_\infty$

$\tilde{F}_b$ = buffet normal force

L = length of tile

$\tilde{M}_b$ = buffet pitching moment

M = Mach number

OASPL = overall sound pressure level

PSD = power spectral density

$\tilde{p}$ = fluctuating pressure

q_∞ = free-stream dynamic pressure, $(1/2)\rho V^2$

rms = root mean square

S = tile surface area

X_s = distance from shock wave to tile leading edge

α = angle of attack

β = angle of sideslip

ρ = free-stream density

WIND-TUNNEL TESTS

Apparatus and Instrumentation

Several wind-tunnel (and also flight) tests have been conducted by the Shuttle contractor, Rockwell International (RI), and by NASA that relate to the buffet problem. Generally, the tests by RI were proof tests with some measurements of tile and substructure dynamic response. Examples of tile dynamic response tests that were conducted at Ames Research Center are shown in Fig. 2. (Also see accompanying paper by Shuetz, Pinson, and Thornton that describes a combined loads test, OS-53, conducted at Langley Research Center.) In most tests of this type, the arrays of tiles (like those shown) were mounted on elastic substrates that simulated the structure of the Orbiter at selected locations. Special test fixtures were also designed to simulate the shock wave and separated flow regions on the Orbiter where high dynamic loads would occur. The photograph at the upper left of Fig. 2 shows a tiled panel (test OS-36) installed in a fixture designed for the Ames 11-Foot Transonic Wind Tunnel. This fixture has

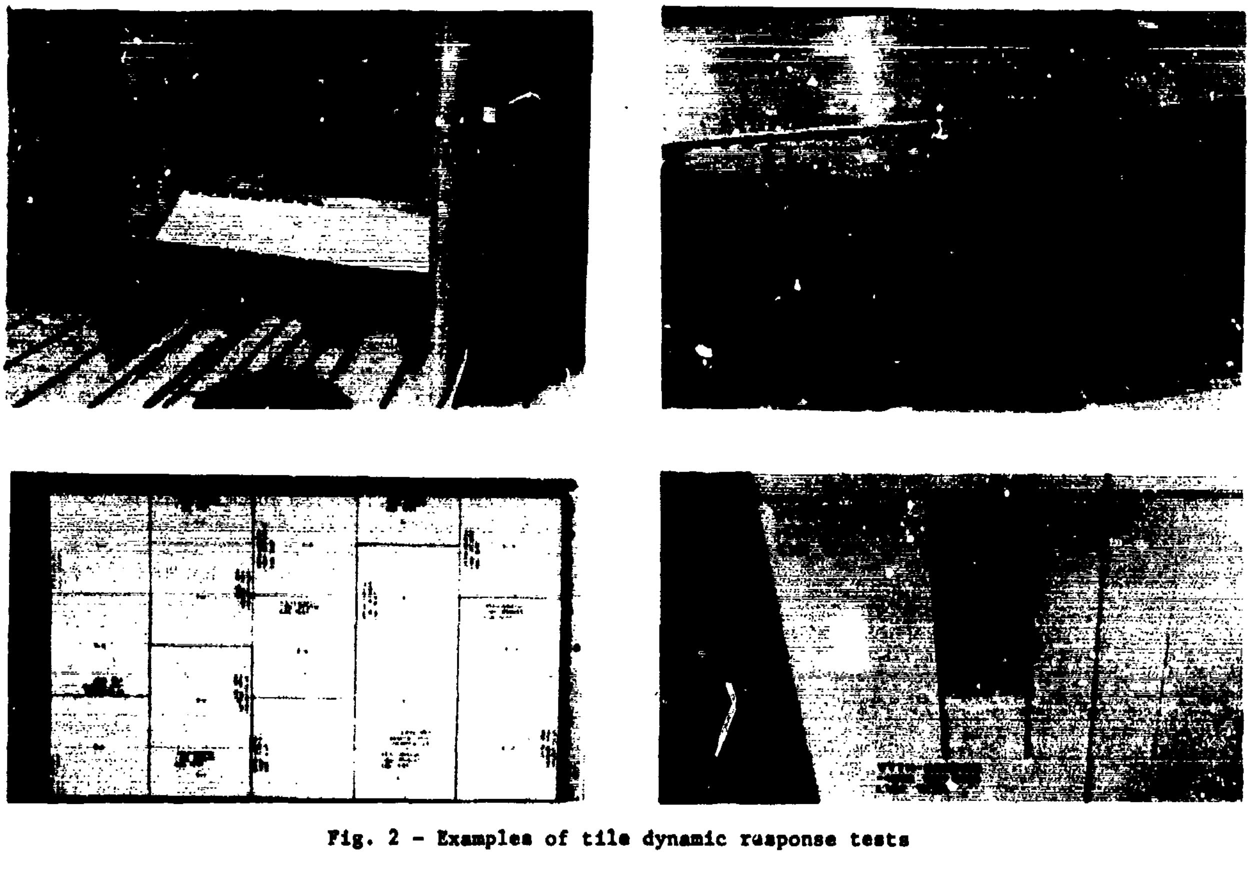

Fig. 2 - Examples of tile dynamic response tests

a hydraulically activated leading-edge flap that produces a transonic recompression shock wave and separated flow on the panel when the flap is deflected. The upper right photograph shows the same panel mounted in a ceiling fixture in the Ames 9- by 7-Foot Supersonic Wind Tunnel. In this case, a hydraulically actuated flap is downstream of the panel to produce a supersonic compression shock and separated flow on the tiles. This photograph shows the tiles after testing, and some minor damage can be seen near the tile edge, a result of tile vibration. The photo at the lower left shows an array of thin tiles with several cracks that resulted from the test loads; on the lower right, a panel is shown where there was a bond-line failure of diced tiles. The load environment and the failure was similar to the STS-1 tile failures on the Orbital Maneuvering System (OMS) pods that could be seen on the television pictures of the Orbiter in space.

The instrumentation used for the tile-response tests included Scani-valves, fluctuating-pressure transducers, and accelerometers. Each test arrangement included a calibration panel that was thoroughly instrumented to establish the environment, and a test panel with a few sideline pressures to confirm a repeat of the test environment. The accelerometers were installed on the test-panel substrate and in some test-panel tiles. The results of the tile dynamic response tests indicated that the buffet loads could be significant, but quantitative forces and moments were not obtained that would support the development of a tile loads model (see preceding paper by Howsner). Additional tests, designated OS-52, were therefore conducted, in this case by NASA, to obtain measurements of both the steady and dynamic tile airloads.

OS-52 tests were carried out in the Ames 11-Foot Transonic Wind Tunnel using the OS-36 panel-test fixture with the leading-edge flap. For OS-52 a special tile-balance load-measurement system was constructed to test single tiles of various thicknesses. Photographs of the wind-tunnel installation and airloads instrumentation are shown in Fig. 3. Figure 4 shows additional details of the instrumentation. The tile under tests was bonded conventionally with SIP to a 6.35×10^{-3}-meter-thick (1/4-inch) aluminum plate, which in turn was supported by four strain-gage beams attached at the corners of the balance frame. Each strain-gage beam contained foil gages for low drift and semiconductor gages for higher output from dynamic loads. The tiled plate contained nine strain-gaged diaphragms that responded to the local loads at the SIP/plate bond line. The diaphragms were milled directly into the plates by an initial machine cut and by a final electrodisplacement process to yield a thickness of 7.62×10^{-5} meter (0.003 inch). The instrumentation for these tests also included non-contacting displacement probes for measuring in-plane and out-of-plane displacements and instrumentation for measuring steady-state and fluctuating pressures. To preserve the steady-state and dynamic elastic properties of the

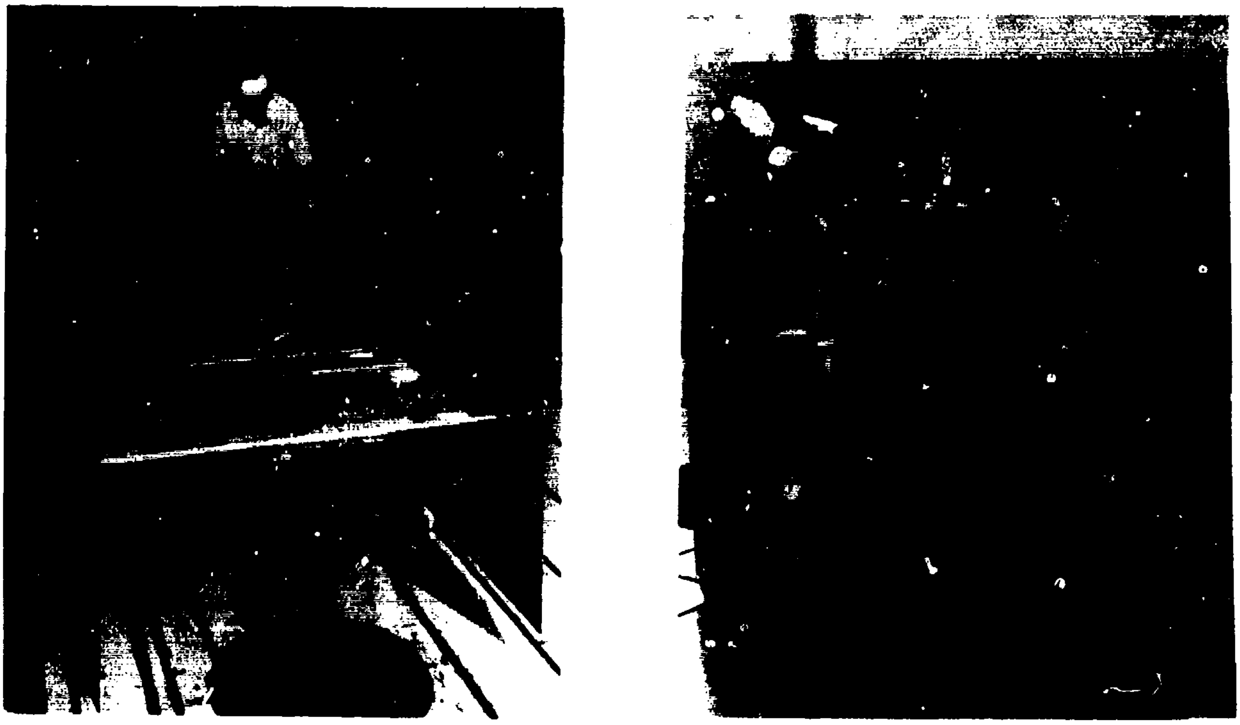

Fig. 3 - Tile airload tests in Ames 11-Foot Transonic Wind Tunnel

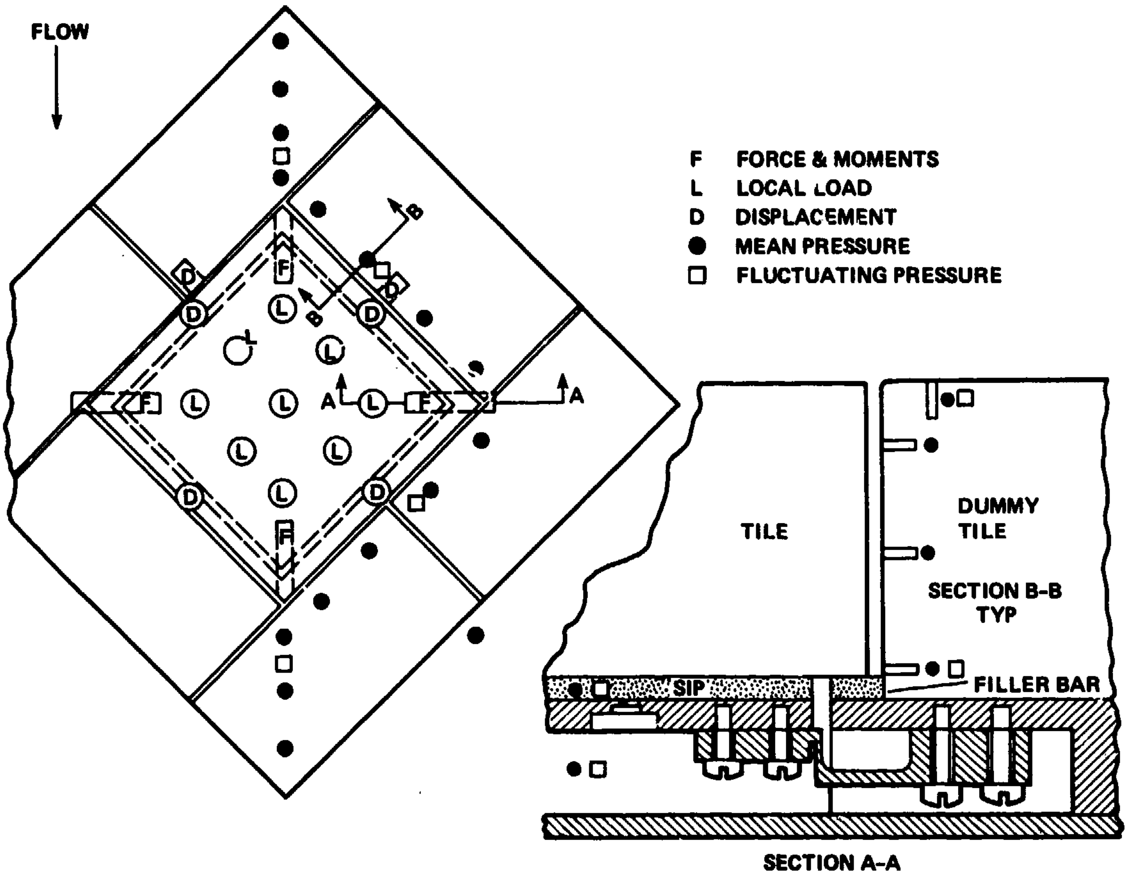

Fig. 4 - Instrumentation for tile airload tests

tile/SIP combination for OS-52, no instrumentation was placed in the tiles under test. Section A-A, Fig. 4, shows the cross section of one of the strain-gage beams, the tile, SIP, tile plate with a diaphragm load sensor, and the cavity beneath the tile plate. This cavity, which was necessary for this instrumentation approach, was vented only around the boundary of the tile plate, through a 3.18×10^{-3}-meter (1/8-inch) gap corresponding to the gap between the SIP and filler bar. (The filler bar is a piece of SIP material at the base of the tile gaps that is not bonded to the tiles.) It is obvious from this sketch that differences in either steady-state or dynamic pressure between the SIP and cavity would affect the airload measurements. Pressures were therefore measured in the SIP and cavity that showed, fortunately, that the pressure differences across the plate were negligible relative to the accuracy of the force and local load measurements.

Tile Buffet Load Measurements

The measured buffet normal force coefficients, $\tilde{C}_{N_{b_{rms}}}$, versus the shock position on the tile, X_s/L, are presented in Fig. 5. For these tests, the position of the shock wave was controlled by varying Mach number while the

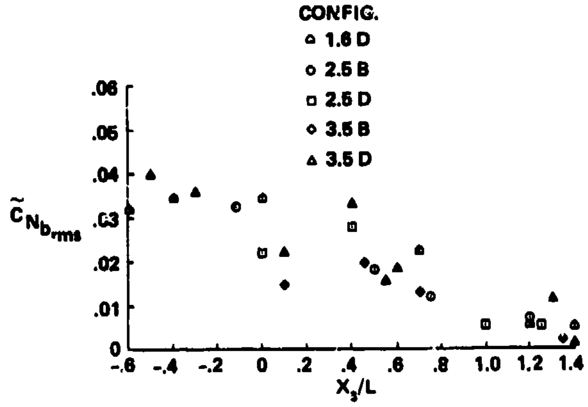

Fig. 5 - OS-52 aero-buffet normal-force coefficients

leading-edge flap deflection was held constant at 20°. The strength of the shock wave and corresponding buffet excitation was controlled by varying the free-stream dynamic pressure, q_∞, to correspond with the nominal launch conditions of STS-1. Overall sound pressure levels (OASPL) on the tiles under test were approximately 161 db ($\tilde{C}_{p_{rms}} = 0.077$) when the flow was separated and 168 dB ($\tilde{C}_{p_{rms}} = 0.171$) when the shock wave was on the tile. The tile material was LI 900, which has a density of 144 kg/m^3 (9 lbs/ft^3) The tile test configuration is identified in Fig. 5 by various symbols that designate the tile thickness in inches (1.6 to 3.5) and whether the tile was densified at the bond line (D) or a baseline tile (B, undensified). The results show that the highest buffet normal forces occurred when the flow over the tile was separated, $X_s/L < 0$. For the case when the shock wave was on the tile, $0 < X_s/L < 1$, there is an apparent peak in the buffet normal-force data at $X_s/L = 0.4$. The fact that the buffet loads were higher for the separated-flow case than for the shock-wave case is accountable to the wider frequency range of the pressure fluctuations from the separated flow.

Figure 6 shows the variation of the buffet pitching-moment cofficients, $\tilde{C}_{M_{b_{rms}}}$, with shock position. As would be expected the buffet response in terms of pitching moment or normal force have similar characteristics. The data in both forms show relatively large scatter of the plotted points for the various configurations tested. The scatter in both normal-force and pitching-moment points results from several factors relating to the tile bonding and SIP. For example, SIP properties varied significantly among the configurations tested. In most cases the SIP was sufficiently elastic to allow the tiles to touch adjacent dummy boundary tiles. The scatter, unfortunately, indicates that more data are needed to establish, statistically, the effects of dependent parameters.

PROGRESSIVE WAVE TUBE TESTS

Four tile configurations from the OS-52 wind-tunnel tests were also tested in a progressive wave tube at the Johnson Space Center Acoustic Test Facility. The acoustic tests were conducted to determine if tile buffet loads resulting from aerodynamic or acoustic environments are significantly different. A photograph in Fig. 7 shows a tile installation in the progressive wave tube. The same force balance hardware and load sensors were used for both the wind-tunnel and acoustic tests. In addition, for the acoustic tests, accelerometers (ATxx) were mounted on the tile surface and a microphone (M1) was suspended within the progressive wave tube. The tile was positioned with its leading edge normal to the progressive wave propagation. For OS-52 (Fig. 3), tiles were oriented diagonally to the airstream.

The OASPL and frequency content of the acoustic excitation was adjusted to conservatively simulate the aerodynamic separated-flow excitation. Figure 8, which shows the power spectra of the two excitations,

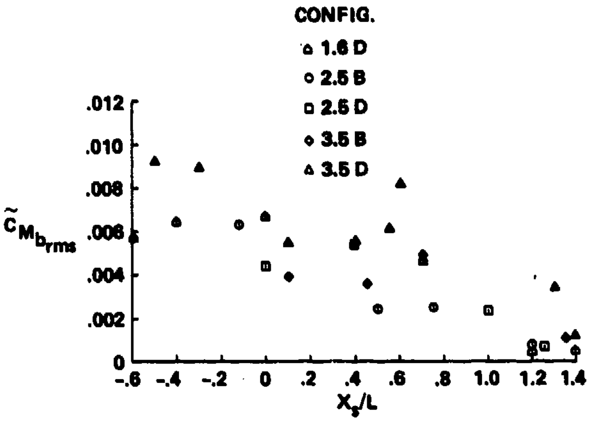

Fig. 6 - OS-52 aero-buffet pitching-moment coefficients

Fig. 7 - Tile installation in JSC Acoustic Test Facility

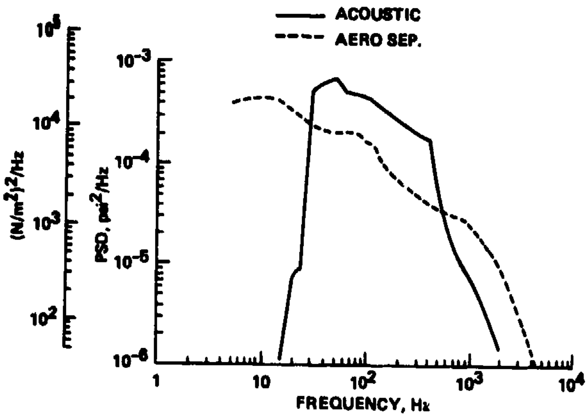

Fig. 8 - Power spectra of acoustic and aero-separation excitations

indicates that the shaping of the acoustic spectrum compares with the aero-separation spectrum within the frequency range of the acoustic driver; however, within this range the acoustic excitation was higher than the aero-separation excitation. The OASPLs of the acoustic excitation was 163 dB and the aerodynamic excitation was 161 dB.

Examples of power spectra of buffet normal forces resulting from acoustic and aerodynamic excitations are shown in Fig. 9. The first normal-mode resonant frequency of this tile on SIP is about 100 Hz. No resonant peaks occurred at 100 Hz, which is indicative of the high damping of SIP; to some extent the rubbing of the tile on an adjacent dummy tile would also cause high damping. The relatively undamped resonant peaks at about 700 Hz are from the strain-gage balance beams. As noted in Fig. 9 the buffet force resulting from the acoustic excitation was significantly higher than that resulting from the aerodynamic excitation. The incremental diffence between the two buffet spectra is larger than the corresponding difference in the excitation spectra. The higher buffet forces would be expected from the acoustic excitation because acoustic pressure fluctuations are more highly correlated spatially than aerodynamics pressure fluctuations. Also aerodynamic damping may significantly reduce aerodynamic buffet forces.

ESTIMATION OF TILE BUFFET LOADS ON STS-1

The data obtained from OS-52 were used to predict the tile buffet loads on STS-1 as part of an independent NASA effort to check tile loads and stresses. (All the various environments and loads and the approach taken by NASA to combine the loads are discussed by Muraca in a preceding paper.)

The method for estimating the tile buffet loads on STS-1 is given in Fig. 10. The approach taken was to multiply the measured ratios of buffet forces and moments to surface-pressure excitation from OS-52 by the predicted surface-pressure fluctuations for the STS-1 tiles. Such a simple method was justified because the OS-52 tiles were full scale. Also the environmental conditions for the OS-52 tests were near full scale, with exception of the OASPL ($\tilde{p}_{rms}$) of the excitation.

Estimation of Surface-Pressure Fluctuations on STS-1

As mentioned in the Introduction, there were two tile buffet-load cases of concern (Fig. 1). For one case the aerodynamic flow at the tile of interest is separated, and for the second case a shock wave impinges on the tile.

The tile excitation on STS-1 was determined from two sources. The primary source was the pressure-fluctuation measurements obtained from RI and NASA tests, IS-2, which were conducted in the Ames 11-Foot Transonic Wind Tunnel and 9- by 7-Foot Supersonic Wind Tunnel. The tests extended over a Mach-number range from 0.6 to 2.5. A photograph of the model in the 9- by 7-Foot Supersonic Wind Tunnel is shown in Fig. 11. The model, which was 3.5-percent

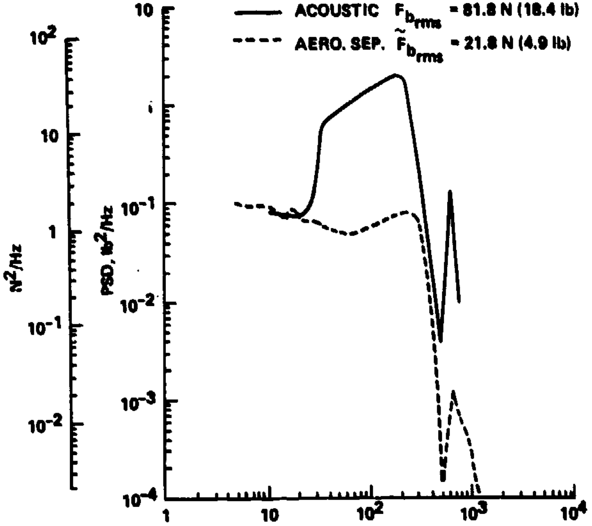

Fig. 9 - Power spectra of buffet normal forces due to acoustic and aero-separation excitations, LI 900, 2.5B.

$$\left(\tilde{F}_{b_{rms}}\right)_{STS\text{-}1} = \left(\frac{\tilde{F}_b}{\tilde{p}}\right)_{OS\text{-}52} \times \left(\tilde{p}_{rms}\right)_{STS\text{-}1}$$

$$\left(\tilde{M}_{b_{rms}}\right)_{STS\text{-}1} = \left(\frac{\tilde{M}_b}{\tilde{p}}\right)_{OS\text{-}52} \times \left(\tilde{p}_{rms}\right)_{STS\text{-}1}$$

Fig. 10 - Method for estimating tile buffet loads on STS-1

Fig. 11 - IS-2 aero-noise model in Ames 9- by 7-Foot Supersonic Wind Tunnel

scale, contained 237 dynamic-pressure transducers. The frequency range of the recorded pressure fluctuations was from 5 Hz to 40,000 Hz, which corresponds to full-scale frequencies from 0.2 Hz to 1400 Hz. Examples of the variation with Mach number of projected overall sound pressure levels (OASPL) on the Orbiter are shown in Fig. 12. Orbiter transducer No. 83 was located on top of the fuselage over the crew compartment. High OASPLs caused by separated flow are indicated up to $M = 0.857$, and the effect of the shock wave oscillating over the transducer can be seen at $M = 0.885$. Orbiter transducer No. 6 was located on the bottom of the fuselage upstream of the forward bipod strut that attaches to External Tank (ET) to the Orbiter. In this case, the effects of supersonic-flow separation can be seen.

Data like those in Fig. 12, which were compiled by RI, were converted to the excitation, $\tilde{p}_{rms}$, for the various aerodynamic subzones on STS-1 as described by Muraca. In some cases, however, the IS-2 data were judged to be insufficient to detect the shock wave. In these cases, the strength of the shock waves that had been determined for the idealized shock model (see paper by Muraca) was used to estimate the $\tilde{p}_{rms}$ resulting from the shock wave. The value of $\tilde{p}_{rms}$ was estimated to be 1/6 of the static-pressure difference across the shock wave. A substantial amount of other experimental data exists that confirms the validity of this ratio.

Buffet Excitation of OS-52 Tiles

The excitation, $\tilde{C}_{p_{rms}}$, used to calculate the ratio of buffet loads to excitation was based on measurements of pressure fluctuations that were obtained during the OS-36 and OS-52 tests. Since the same installation fixture was

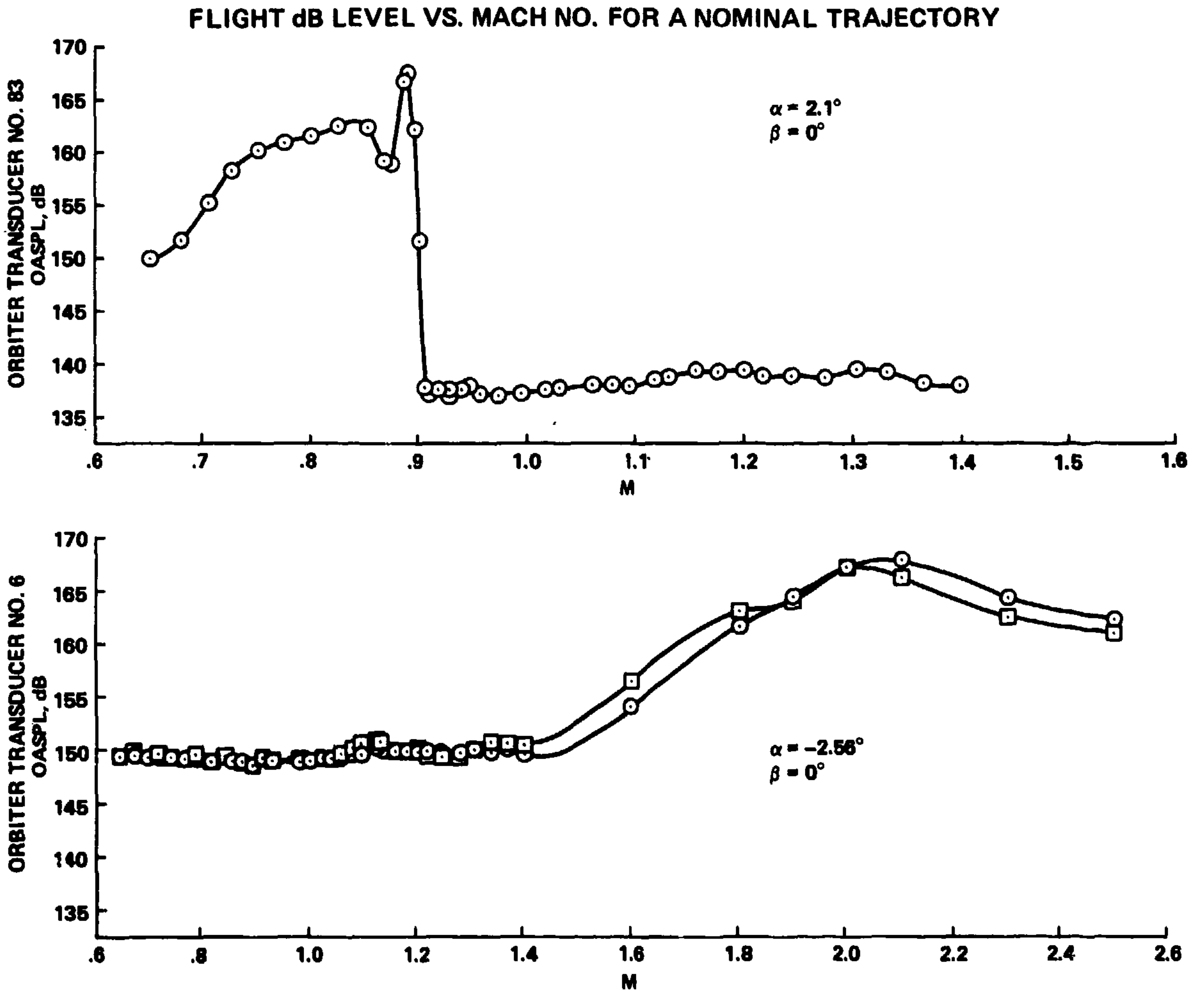

Fig. 12 - Examples of overall sound pressure levels on Orbiter

used for both tests, the data could be combined to yield good longitudinal distributions of $\tilde{C}_{P_{rms}}$ in the vicinity of the OS-52 tiles. $\tilde{C}_{P_{rms}}$ levels were established from these data for separated flow and for the center of the shock oscillation. These two values of $\tilde{C}_{P_{rms}}$ were then adjusted to account for the position of the shock wave on the tile as shown in Fig. 13. This excitation model designated a constant $\tilde{C}_{P_{rms}} = 0.077$ when the flow was separated with the shock ahead of $X_s/L = -0.2$. When the shock wave oscillations started to touch the tile at $X_s/L = -0.2$ the $\tilde{C}_{P_{rms}}$ was increased to the measured maximum $\tilde{C}_{P_{rms}} = 0.170$ at $X_s/L = 0.5$. The $\tilde{C}_{P_{rms}}$ was then allowed to decrease to the level of the attached boundary layer at $X_s/L = 1.2$.

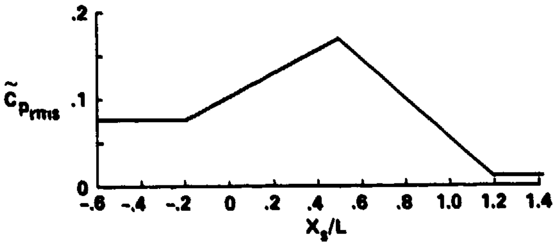

Fig. 13 - Buffet excitations of OS-52 tiles

Buffet Excitation on STS-1

The buffet excitation on STS-1 tiles was based on the aforementioned estimation of surface pressure fluctuations on STS-1. For the separated-flow case, the buffet excitation applied in the equations of Fig. 10 was taken directly from the IS-2 data that had been projected to STS-1 flight conditions, as illustrated in Fig. 12. For the aero-shock case, the pressure fluctuations that were obtained from IS-2 or the aero-shock model were adjusted to account for the position of the shock, X_s/L, by the same approach described for the estimation of buffet excitation of OS-52 tiles. The STS-1 aero-shock pressure fluctuations were simply multiplied by the ratio of buffet excitation to shock pressure fluctuations versus X_s/L shown in Fig. 14; this ratio was obtained by normalizing the OS-52 buffet excitation (Fig. 13). For both cases, when IS-2 data were used, the upper bound of the IS-2 data was taken when there was more than one measurement within an aerodynamic subzone.

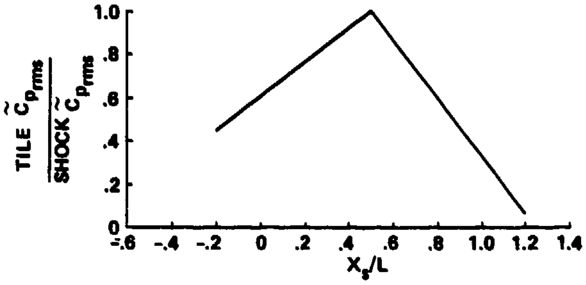

Fig. 14 - Ratio of buffet excitation to $\tilde{C}_{P_{rms}}$ of shock wave at center of tile on STS-1

Ratios of Buffet Forces and Moments to Excitation

The ratios of buffet forces and moments to excitation that were applied to the prediction of STS-1 tile buffet loads are shown in Figs. 15 and 16. These ratios were obtained by dividing the forces and moments from OS-52 (Figs. 5 and 6) by the OS-52 buffet excitation (Fig. 13). The dashed lines, which approximate the nominal trends of the data, are the ratios used in the loads model. The upper bounds of these data were not used in the loads model in order to avoid conservatism. Some confidence in the loads model is provided, however, by the good correlation of some independent buffet loads data that were obtained from test OS-53A (filled symbols in Figs. 15 and 16). OS-53 is described in an accompanying paper by Shuetz, Pinson, and Thornton.

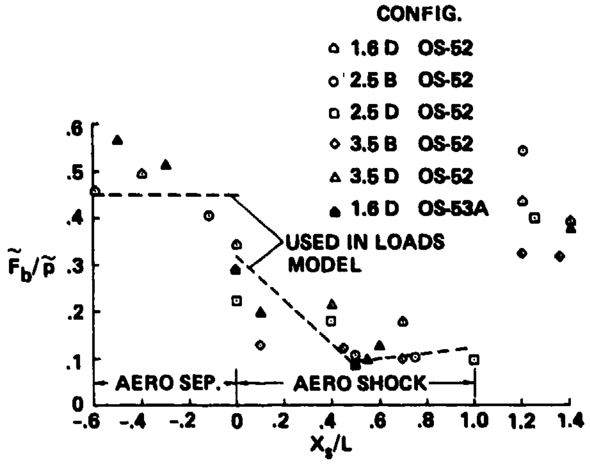

Fig. 15 - Ratio of buffet normal force to excitation

Peak Buffet Loads and Stresses

The buffet loads on STS-1 were estimated by applying the equations in Fig. 10. The ratios $\tilde{F}_b/\tilde{p}$ and $\tilde{M}_b/\tilde{p}$ were represented by the dashed lines in Figs. 15 and 16.

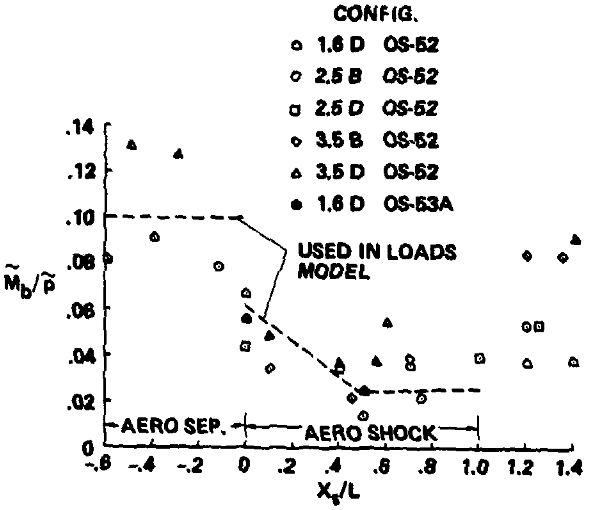

Fig. 16 - Ratio of buffet pitching moment to excitation

The peak buffet loads were taken to be 4 times the rms load. The appropriate peak-to-rms ratio for this application was evaluated from both OS-52 and OS-53 test data. Examples of peak-to-rms measured from OS-53 data are shown in Table 1.

TABLE 1
Peak-to-rms Ratios of OS-53 Tile Buffet Normal Forces

Run	Max	Min	Mean	St. Dev.	$\frac{\text{Max-mean}}{\text{St. dev.}}$
1	20.0	-7.9	6.7	3.50	3.80
3	32.8	-5.7	11.6	4.50	4.61
5	22.1	-3.4	9.7	3.40	3.65
7	37.4	7.0	23.9	3.35	4.03
					$\overline{16.09} \div 4 = 4.02$

As previously discussed by Muraca, the design load case for STS-1 was the load combination when a shock wave was on a tile. Some typical peak buffet normal forces ($\tilde{F}_{b_{pk}}$), pitching moments ($\tilde{M}_{b_{pk}}$) and stresses ($\tilde{S}_{b_{pk}}$), resulting from the combination of forces and moments when a shock wave was on a tile, are as follows:

$$\tilde{F}_{b_{pk}} = 44 - 54 \text{ N } (10 - 12 \text{ lbs})$$

$$\tilde{M}_{b_{pk}} = 1.6 - 1.8 \text{ N-m } (14 - 16 \text{ in-lbs})$$

$$\tilde{S}_{b_{pk}} = 9{,}600 - 10{,}300 \text{ N/m}^2 \ (1.4 - 1.5 \text{ lbs/in}^2)$$

These buffet loads were estimated for the undensified tiles that were on STS-1 in under-wing and under-mid-fuselage subzones. Stresses due to tile aero buffet were about 20 percent of the total estimated tile stresses.

CONCLUDING REMARKS

This paper has described the method used by NASA to estimate TPS tile aerodynamic buffet loads on STS-1. The method was based on a simple buffet-loads model, which was developed from tile dynamic force and moment measurements obtained in wind tunnels. The model established the buffet loads versus the position of the shock wave on a tile as a function of the buffet excitation. The paper also described the estimation of the buffet excitation on STS-1.

The buffet-loads model was established from a relatively small amount of wind-tunnel data which had substantial scatter. The model represented the approximate nominal trends of the data rather than upper bounds, to avoid undue conservatism in the predicted STS-1 buffet loads. Additional tests of tile buffet loads, to establish the effects of important parameters and to improve the confidence of future buffet-load predictions, have been recommended.

UNSTEADY ENVIRONMENTS AND RESPONSES OF THE SHUTTLE COMBINED LOADS ORBITER TEST

P. H. Schuetz
Rockwell International
Downey, California

L. D. Pinson and H. T. Thornton, Jr.
NASA Langley Research Center
Hampton, Virginia

Both separate and combined wind tunnel and vibration shaker tests were conducted on two structural panels representative of the Shuttle orbiter in the NASA LaRC 8-foot transonic pressure tunnel (TPT) to determine the effects of combined loads on the thermal protection system (TPS). The primary objective of this test was to provide a combined full-scale load environment and realistic time history of the dynamic pressures, Mach numbers (through transonic), and dynamic structural responses of these panels. The panels were selected from orbiter locations where interactive load sources such as aerodynamic shock waves, turbulent boundary layers, strut-induced vorticity, and substrate deformation combined to provide high bonding loads between the TPS and the orbiter structure.

The test panels for this program were highly instrumented with static and dynamic pressure gages, accelerometers, deflectometers, strain gages, Schileren and high speed photography, and special instrumentation necessary to determine TPS/structure interface loads and tile motions. Two test specimens of each orbiter panel were utilized. Both were high-fidelity representations of the selected orbiter location. The first panel (calibration panel) for each test was utilized to calibrate the tunnel and shaker system as well as provide a data-gathering source for applied static and dynamic loads. The second panel (test panel) for each test was subjected to flight time exposures only so that TPS characteristics as a function of flight mission exposure could be determined. These tests were the last in a series that was successfully completed and necessary to certify the TPS prior to the first launching of the Shuttle.

INTRODUCTION

The combined loads orbiter test (CLOT) program was part of the TPS flow test program that was initiated after flow-induced TPS problems were found during the ferry flight of Orbiter 102 from California to Florida. The problems included migration of the filler material in wide tile gaps, lifting of mini-tiles, and loosening of tiles with small bonding surface areas. The objectives of the flow test program were to obtain detailed steady and unsteady aerodynamic pressure data for TPS analyses, obtain TPS failure modes data, and to demonstrate the ability of the TPS to endure the most severe pressure gradients and aerodynamic turbulence expected on the orbiter surfaces. Areas from which TPS configurations were selected for flow tests are shown in Fig. 1. Flow tests were conducted in wind tunnels at NASA Ames Research Center, USAF Arnold Engineering Development Center, and NASA Langley Research Center (LaRC), as well as on F-15 and F-104 aircraft at NASA Dryden Flight Research Center.

The CLOT program consisted of wind tunnel tests of two full-scale panels designated CLOT 20-A and CLOT 20-C. These panels represented locations on the orbiter forward fuselage underbody as shown in Fig. 1. They were subjected to realistic time histories of the dynamic pressure and Mach numbers that they would be subjected to during the period of highloading in actual flight. Both panels were of high-fidelity structural skin and tile configuration. These panels were selected because of high combined tile loads. CLOT panel 20-A, located downstream of the forward orbiter/external tank (ET) attachment (bipod), was selected because of the structural flexibility and large pressure gradients in this area during the maximum Q period of ascent flight. The pressure gradients and highly turbulent flow aft of the bipod made this a prime candidate for a combined loads

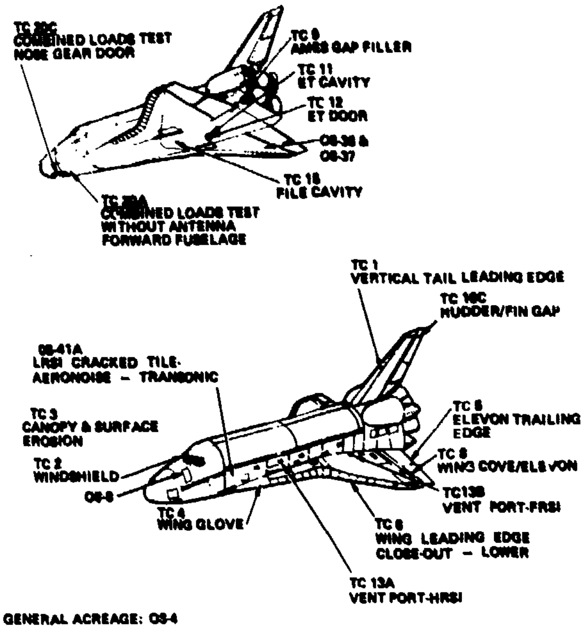

Fig. 1 - TPS flow test program; test article locations

test specimen. CLOT panel 20-C, located ahead of the bipod, was selected because of the unusual tile footprints on the nose landing gear door and the high aerodynamic shock load associated with a compression shock that forms in front of the attachment during ascent supersonic flight.

The primary objectives of the CLOT test program were to verify that the tiles remained attached during exposure to the aerodynamic environments, and that the surface roughness (step and gap) remained within the specification following the test. Additional objectives were to obtain test data of static and dynamic pressure, loads, and deflection, which would support on-going analysis and math models.

TEST FACILITY

The LaRC 2.44 m (8 ft.) transonic wind tunnel facility was utilized to test both CLOT panels. This facility has the capability to provide a time history simulation of the Q and Mach numbers (Fig. 2) that are experienced during orbiter flight. The tunnel Mach numbers were varied from approximately Mach equals 0.6 to Mach equals 1.3 with dynamic pressures up to approximately 815 psf to meet the total objectives of this test program. Tunnel Mach numbers were controlled by adjusting the tunnel diffuser flaps to follow the desired Q on the panel. Local Mach and Q values varied over the panels; however, the tests were controlled by measurements located on tiles in the center of the tile test area. A hydraulic shaker system was installed beneath the tunnel test section (Fig. 3) to provide a dynamic forcing function to the panel (CLOT 20-A) during the wind tunnel operation.

TEST PANEL CLOT 20-A

The CLOT 20-A test panel consisted of a replica section of the structure from the orbiter lower forward fuselage just aft of the bipod. The panel measured 1.66 m (65.3 in.) in the stream-wise direction (X-axis) and 1.24 m (49 in.) in the crosswise direction (Y-axis). Basic construction consisted of 0.18 cm (0.071 in.) aluminum skin with hat section stringers in the stream-wise direction, located on 9.85 cm (3.88 in.) centers. Two major frames and one mini-frame in the crosswise direction completed the panel construction, which was mounted in an I-beam box frame. Most of the panel was covered with higher strength densified tiles having a weight density of 9 pcf and mounted on strain isolator pads (SIP) having a thickness of 0.041 cm (0.16 in.), which were then bonded to the skin using flight vehicle installation and inspection procedures. Foam tiles of the same density covered the remainder of the test panel.

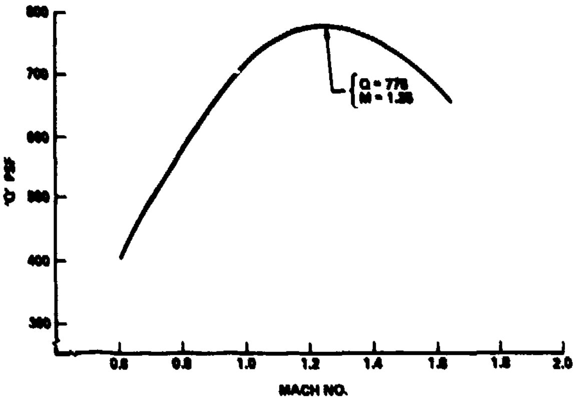

Fig. 2 - Flight Q versus Mach no. design limit

Except for the tiles, a CLOT 20-A calibration panel of identical configuration was also constructed. This panel had all but one selected tile made of foam and was utilized to calibrate the tunnel to ascertain aerodynamic and instrumentation checkout. This eliminated unnecessary life cycles being applied to the test panel during calibration and checkout.

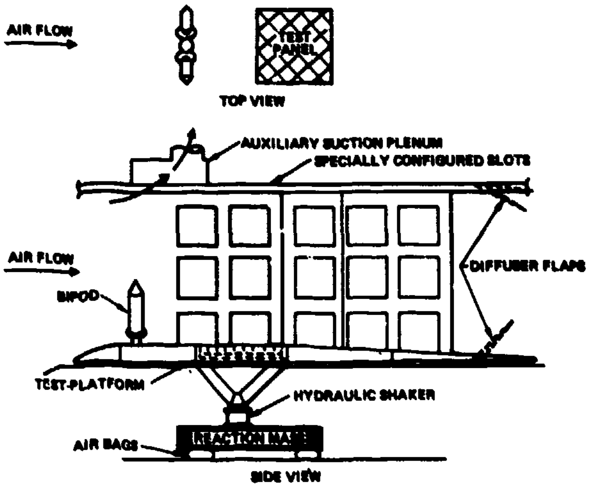

Fig. 3 - Wind tunnel test configuration for panel aft of external tank to orbiter connection; CLOT 20-A

There was also a large amount of instrumentation to define the applied static and dynamic loads as well as response parameters. To avoid interference between measurements, it was decided to install load instrumentation on the calibration panel and response instrumentation on the test panel. A picture of the test panel installed in the wind tunnel is shown in Figs. 4 and 5. Fig. 6 shows panel tile configuration and instrumentation. The size of the wind tunnel test section by necessity limited the size of the CLOT test panels. As a result, significant lower frequency vibration responses were not excited by the pressure fluctuations in the aerodynamic flow, unlike the lower forward fuselage of the orbiter, which the test panel purported to represent. If no further action were taken, the lack of lower frequency panel response would cause undertesting of the tiles. The test panel had a fundamental natural frequency of approximately 75 Hz while the orbiter structure exhibited significant responses down to below 25 Hz.

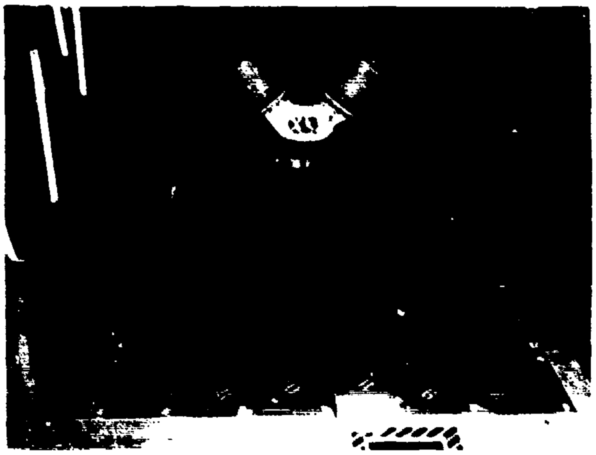

Fig. 4 - CLOT 20-A installation in LaRC 8 foot TPT

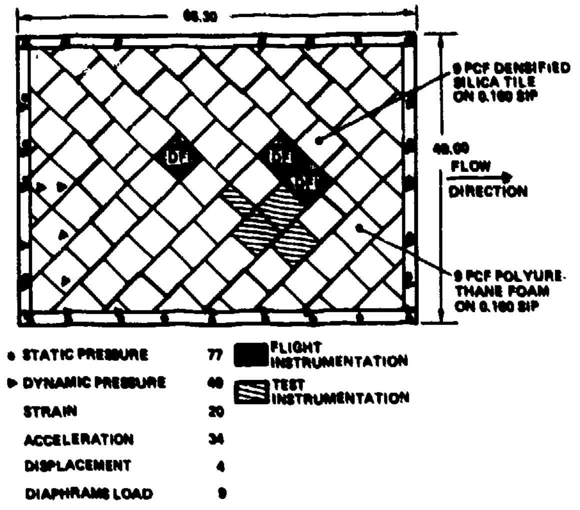

Fig. 6 - Test configuration for CLOT 20-A test panel

To avoid the undesirable undertest of the tiles, it was decided to utilize a shaker system to simulate the low frequency response of the orbiter (Fig. 7). The low frequency vibration was determined from the vibration response of a larger forward fuselage panel (FFA-04) in a reverberant acoustic test and from modal surveys conducted on both FFA-04 and Orbiter 101 (see Ref. [1 and 2]). The modal data were compared to determine which modes of FFA-04 were unrealistic, i.e., fixture or facility related, compared with the orbiter. These responses were then omitted and a total adjusted rms acceleration (12.5 grms) below 75 Hz was determined. To avoid double driving the fundamental mode of the CLOT 20-A panel, which would already be driven by the wind tunnel environment, the shaker system was designed to provide excitation up to 55 Hz. Because the vibration below 55 Hz provided nonresonant loading to the tiles, it was only necessary to simulate the rms

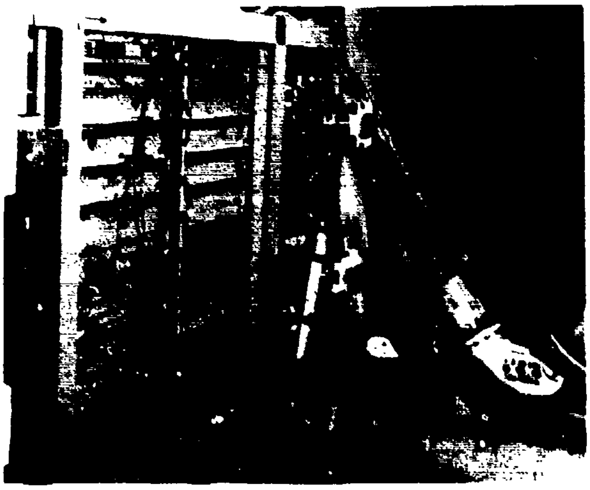

Fig. 5 - CLOT 20-A being installed in LaRC 8 foot TPT

Fig. 7 - Hydraulic shaker system for CLOT 20-A

acceleration and not necessarily the spectrum shape. (The first mode of the tiles on SIP was expected at approximately 160 Hz, so redistributing lower frequency vibration had no appreciable effect on their response.) Random vibration was applied by the shaker to duplicate the peak distribution that would be encountered in flight. To avoid an unrealistic interaction between the random vibration displacement of the panel and the boundary layer, the shaker system input was limited to frequencies above 35 Hz. This limited panel peak displacement to less than 0.51 cm (0.2 in.), compared with a boundary layer thickness of 2.54 cm (1.0 in.).

The test panel was mounted flush to the floor of the test section of the 2.44 m (8 ft) LaRC transonic wind tunnel (as shown in Fig. 3). The test panel was supported by a fixture attached to a hydraulic shaker, which was in turn reacted by a 50,000 pound mass supported on air bags. (See Fig. 7.) The fixture was guided by a set of four bearings.

A bipod was mounted upstream of the test panel (Fig. 3) to provide the shock and separated flow on the test panel in simulation of the orbiter environment. To conduct each test cycle the tunnel airspeed was increased to a Mach number of approximately 0.6. Then the shaker was brought up to full level and the tunnel cycled up to Mach 1.4 and back to Mach 0.6. Then the shaker and air flow were shut down. This cycle produced the desired Mach number versus Q curve shown in Fig. 2. Because only one test panel is exposed to the combined wind tunnel and shaker loads, some accounting must be made for the statistical scatter in fatigue life that might have occurred if several panels had been tested. Using the precedent set by DOD in Ref. [3], the orbiter contract specified that a scatter factor of 4 be used for fatigue-type loading on one specimen, thus four exposure cycles were determined to constitute one flight mission.

Instrumentation for the CLOT 20-A test and calibration panels consisted of static pressures, dynamic pressures, strain gages, accelerometers, deflectometers, and load measuring diaphragms. Each panel had in excess of 200 measurements that were recorded on either FM tape or digital computer.

The calibration panel that was used to establish the desired wind tunnel operating conditions was instrumented with surface dynamic pressures (94) and surface static pressure measurements (28). In addition, 25 static pressure measurements and 10 dynamic pressure measurements were located beneath and between the tiles. Six additional dynamic pressures were potted inside the one real tile located on the calibration panel. Fifteen strain gages were located on the structure to monitor and evaluate the surface strains that contribute to SIP/tile loadings. Sixteen accelerometers were also located on the structure to evaluate the dynamic response.

The test panel was instrumented with 28 surface dynamic pressure and 28 static pressure measurements. An additional 50 static pressure measurements and 21 dynamic pressure measurements were made beneath, between, and inside the tiles. Absolute dynamic pressure instruments were utilized on all internal tile measurements to avoid a reference pressure tube across the SIP interface. Small wires with a loop at the SIP interface were utilized on accelerometers and dynamic pressure within the tiles to minimize stiffness characteristics across the SIP interface. Eighteen accelerometers were buried in four different tiles to define total dynamic motion. An additional 16 accelerometers were utilized to monitor and evaluate the structural responses. Four proximity measuring devices were located under one tile with small metal targets located on the tile to determine the relative motion between the tile and the structure. The same tile was also instrumented with internal accelerometers. Another tile area was instrumented with load diaphragms to measure the tensile force between the SIP and the structure. The calibration of these nine measurements was such that moments and normal forces could be determined on that specific tile. Fig. 5 shows the instrumentation wiring beneath the panel prior to installation in the tunnel. A summary of all instrumentation is shown in Fig. 6.

TEST PANEL CLOT 20-C

The CLOT 20-C panel consisted of a replica of the aft 1.02 m (40 in.) of the orbiter nose gear door (located just forward of the bipod), bipod (reduced to half size), and associated tiles and fuselage structure between the bipod and door. (See Fig. 8.) The bipod was movable from approximately 5.1 cm (2 in.) upstream (nearer to the panel) to approximately 25.4 cm (10 in.) downstream. This allowed for proper location of the compression shock on the test specimen. The highest shock load was predicted to occur at Mach 2.4, but the tunnel was only capable of providing Mach 1.4. Proper shock strength was controlled with tunnel Q conditions, and shock location was controlled with bipod size and location.

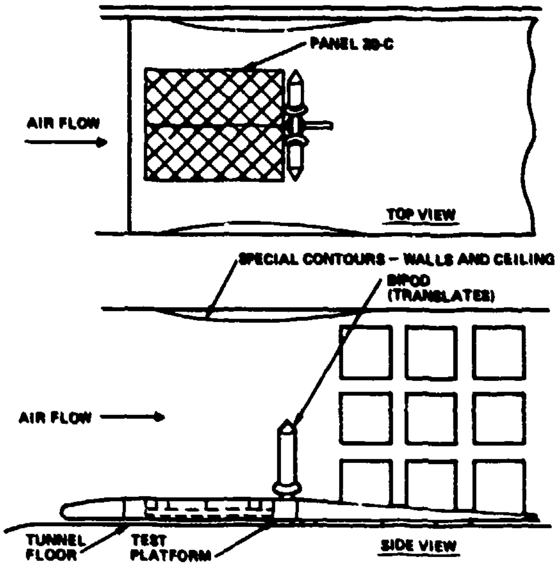

Fig. 8 - Nose wheel door panel test configuration; CLOT 20-C

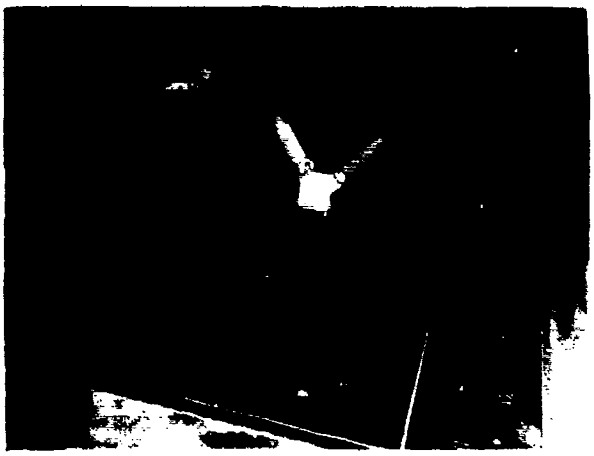

Fig. 9 - CLOT 20-C installation in LaRC 8 foot TPT

The CLOT 20-C doors were constructed from 10.16 cm (4 in.) thick aluminum honeycomb. To this were bonded skewed densified tiles of approximately 15.34 cm by 10.16 cm by 4.45 cm (6 in. by 4 in. by 1.75 in.), using flight vehicle installation and inspection procedures. Eleven tiles were made of 22 pcf silica and bonded on 0.229 cm (0.090 in.) SIP. Ten tiles were made of 9 pcf silica and bonded on 0.41 cm (0.160 in.) SIP. This test panel was also mounted flush to the wind tunnel floor. Foam tiles covered the remainder of the panel. Figs. 8, 9, and 10 show the test setup and instrumentation. Because of the rigidity of this panel, only the aerodynamic shock presented a loading problem to the tiles. Predicted vibration levels for the doors during flight were low, thus eliminating the need for a shaker to simulate low frequency loading. A wooden calibration panel was installed prior to the test panel to calibrate the tunnel and to verify aerodynamic shock locations and shock strengths. During this phase a procedure to position the bipod was developed to maintain the shock at its proper location. During testing the tunnel was cycled through a Mach number range, similar to that used for CLOT 20-A, so that the shock strength and location duplicated that predicted for the orbiter in flight.

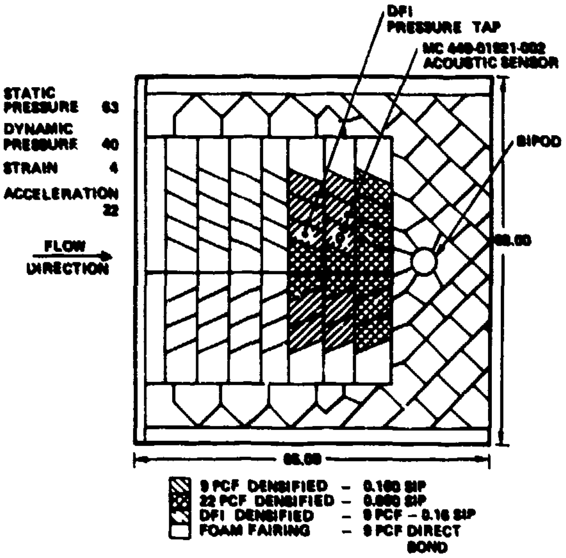

Fig. 10 - Test configuration for CLOT 20-C test panel

Instrumentation for the CLOT 20-C test panel consisted of static and dynamic pressure gages, strain gages, and accelerometers (approximately 130 total measurements). These were recorded on either FM tape or digital computers. Nineteen static pressure measurements were located around or on the test specimen while an additional 44 were mounted beneath and between test tiles to determine loads. Twenty-four dynamic pressure gages were located around the perimeter or on the test specimen, and 16 additional were mounted beneath in the SIP and between the tiles. Two tiles were instrumented with seven accelerometers each, which were potted internally to measure tile response in six rigid body degrees of freedom. Eight accelerometers and four strain gages were located on the structure to monitor structural response.

A flight-type microphone was also installed that protruded through the tile and was flush with the exterior surface of the tiles. Also a flight-type pressure measurement was installed beneath one test tile in SIP.

TEST RESULTS – CLOT 20-A

Worst-case aerodynamic flight environments for the lower forward fuselage aft of the bipod were conservatively simulated in the CLOT 20-A test. The TPS demonstrated the ability to withstand these environments without serious degradation or damage.

The first Shuttle flight, STS-1, followed a relatively benign trajectory. The maximum dynamic pressure was limited to 610 psf. This was well below the maximum Q of 775 psf used in the CLOT 20-A tests. It is expected that future flights will approach these higher dynamic pressures. Because of the difference in Q between CLOT 20-A and STS-1, comparisons between test panel and flight vehicle dynamic responses should be scaled by the difference in Q of 2.3 dB. As can be seen in Fig. 11, the STS-1 acoustic data would agree with CLOT 20-A above 65 Hz if it was adjusted by this 2.3 dB difference. CLOT 20-A would show some conservatism below 65 Hz; however, if a flight microphone on the orbiter had been located closer to the region represented by the CLOT 20-A test band, some of this conservatism may have disappeared. Fig. 12 shows a distribution of dynamic rms pressures over the CLOT 20-A panel. These are consistent with predicted values from IS-2 model tests of approximately 164 dB for this area.

The CLOT 20-A control point was at approximately X_O450 and the STS-1 microphone was at X_C500. A typical structural vibration measurement on the CLOT 20-A panel is

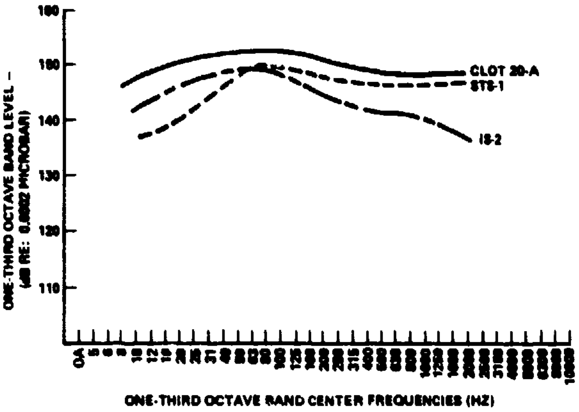

Fig. 11 - Surface acoustic levels for CLOT 20-A versus STS-1 and predicted (IS-2)

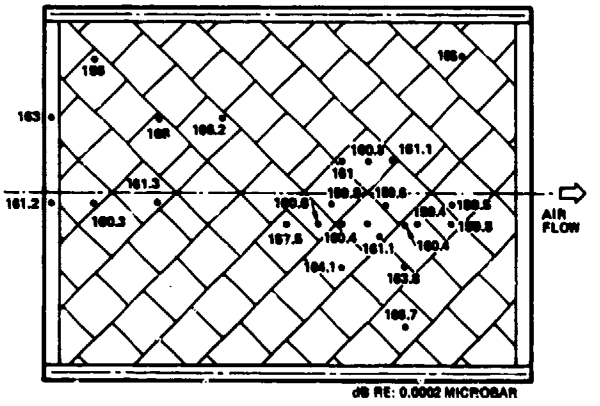

Fig. 12 - RMS pressure distributions panel aft of bipod; CLOT 20-A

shown in Fig. 13 along with an STS-1 measurement from a similar location. The CLOT 20-A response below 65 Hz was primarily from the excitation applied by the shaker system, while the response above 65 Hz was primarily caused by the aerodynamic environment. The STS-1 vibration data should also be scaled up by approximately 2.3 dB, as previously explained, for comparison to CLOT 20-A. This would still show conservative responses except in the 100 Hz to 130 Hz range; however, as mentioned previously, only the rms value below the first mode of the tile at 160 Hz is considered important. Comparison shows that the CLOT 20-A rms value below 160 Hz exceeds that for the orbiter in flight when scaled for Q.

The structural integrity of the SIP and tiles were verified for 25 missions under the conservative test conditions. Additional testing was not considered useful since the tiles and SIP were not being exposed to other environments such as moisture and heating. The tile surface roughness (step and gap) remained essentially constant after the first mission (four cycles). Some chipping of the tile coating did occur following the first mission and some erosion of the tiles did occur in these areas. Erosion appeared more severe in the crack areas between tiles than on surface areas. This erosion was not considered a serious problem because this type of anomaly can easily be found by inspection and the tiles replaced before any danger exists. Fig. 14 shows a picture of these surface chips on the CLOT 20-A test panel after 25 missions. Because chipping is not a fatigue phenomenon, the 100 cycles (25 missions) would most likely represent 100 missions as far as chipping and erosion were concerned.

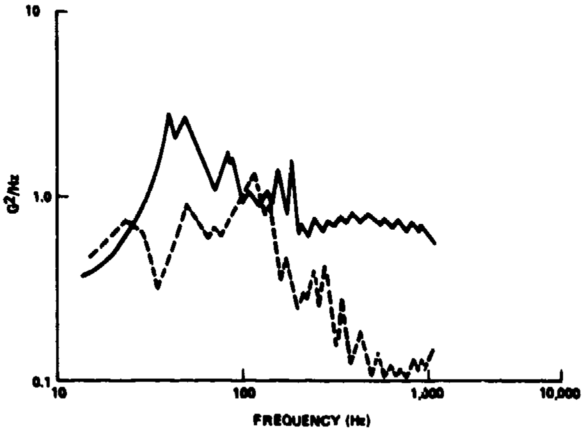

Fig. 13 - Panel vibration response for CLOT 20-A versus STS-1

TEST RESULTS – CLOT 20-C

The test environment for this test panel was adequately duplicated, as shown in Fig. 15. IS-2 model test data were utilized as a criteria in addition to other calculated aero parameters. Fig. 15 presents the IS-2 model data and one STS-1 flight data point that compare favorably with the CLOT 20-C environment. Again, it should be noted that the STS-1 flight maximum Q was lower than nominal, which would have the effect of lowering the one flight data point.

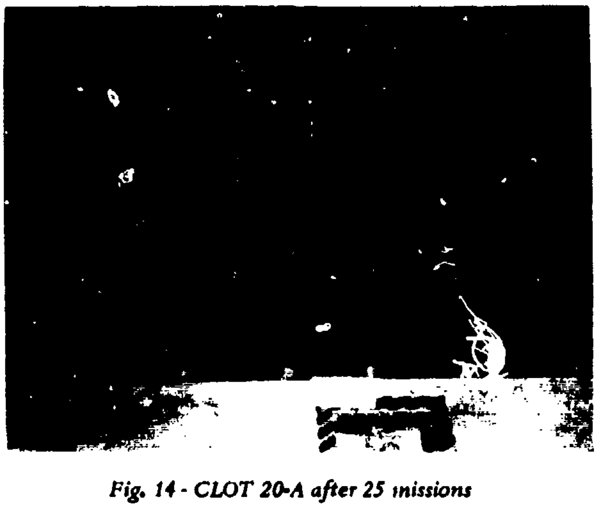

Fig. 14 - CLOT 20-A after 25 missions

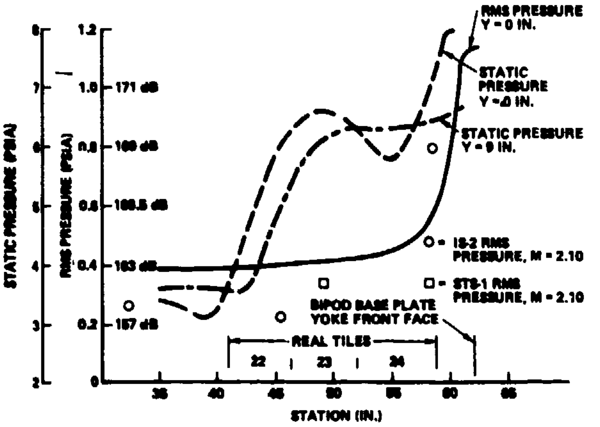

Fig. 15 - CLOT 20-C test panel pressure distributions (Po = 1 ATM, Mα = 1.655)

Fig. 16 was photographed after 25 missions of testing. Although no damage is visible in the photograph, some small chips were found on the tile where they had apparently contacted each other. This damage was minimal. The tile surface roughness remained essentially constant after the first mission (four cycles).

Fig. 16 - CLOT 20-C after 25 missions

CONCLUSIONS

The test program met the major test objectives in that no tiles were lost and that surface roughness remained within limits required for thermal entry requirements. All test levels were considered adequate or conservative. The additional data obtained from this test program to support analysis and math models have been in part reviewed by various disciplines and in general have verified that the math models have predicted conservative loads. These data are still being utilized in developing and verifying analytical approaches to certifying the TPS system.

REFERENCES

1. R. A. Stevens, "Engineering Analysis Report Foward Fuselage Underbody (FFA-04) Acoustic Fatigue Certification Test," Rockwell SOD 80-0496, Dec. 1980

2. Structural Dynamics Research Corporation, "Final Report for Modal Testing of Space Shuttle Enterprise (OV-101) Forward and Mid-Fuselage and Wing Panels to Identify Critical Modes and Boundary Condition Effects," Structural Dynamics Research Corporation – Western Operations, Feb. 6, 1981

3. Anonymous, "Airplane Strength and Rigidity Reliability Requirements," Military Specification MIL-A-008866A, Mar. 31, 1975, par. 3.1.1.1

SPACE SHUTTLE MAIN ENGINE DYNAMICS

VIBRATION MATURITY OF THE SPACE SHUTTLE MAIN ENGINES

Edward W. Larson and Earl Mogil

Rockwell International/Rocketdyne Division
Canoga Park, California

The initial structural design of the Space Shuttle Main Engine was capable of withstanding all known shock and vibratory loads to be encountered during its useful life. However, during the development stage, some unexpected dynamic loads were uncovered that required redesign. The successful incorporation of the knowledge of shock and vibration loads gained during the development of these engines led directly to the first successful flight, and will ensure future successful flights of the Space Shuttles. This paper is a review of the development of the Space Shuttle Main Engine zonal vibration criteria, laboratory vibration tests using zonal criteria to verify life of engine components, and the resolution of unexpected structural problems in turbine blades and in the main injector liquid oxygen post due to hot-gas flow. Hardware modifications were made to resist the dynamic loads associated with the vibration environments and the hot-gas flow phenomena until long lead time redesigns could be incorporated. This experience and knowledge will add to the data base of information useful to the design of future liquid rocket engines.

INTRODUCTION

The Space Shuttle Main Engines (SSME) were designed and developed by the Rocketdyne Division of Rockwell International under contract to NASA's Marshall Space Flight Center. One of the many essential aspects of the design is to provide structural adequacy to withstand the numerous shock and vibration loadings and still maintain a light, flightweight configuration. Therefore, it was essential that shock and vibration loads be considered part of the structural dynamic effort in four areas that were influenced by dynamic considerations during the development phase of the program and changed the structural configuration of the engine:

1. Development of zonal vibration criteria--initially, criteria predictions were based on previous rocket engine experience and subsequently modified as actual SSME test data became available.

2. Design verification specification (DVS) test programs that identified weaknesses in a few components that did not lend themselves to detailed structural analysis.

3. Analysis of the high-pressure fuel turbopump (HPFTP) turbine blade that was extended through the use of 3-D finite element modeling and experimental analysis. This analysis was used to explain airfoil cracks that were appearing, even though vibration dampers were incorporated to control the resonant amplification of the stresses. Laboratory testing of the turbine blades and complete wheel assemblies with blades rotating at full speed were utilized to optimize the damper design.

4. Liquid oxygen (LOX) posts in the main injector had been designed with spoilers to eliminate vortex shedding as an input load. However, an unexpected combination of separated flow, mechanically induced vibration, and acoustically induced pressure oscillations combined to cause fatigue failures. LOX post shields and a change in material were used to provide an interim fix to meet the immediate flight requirements.

ZONAL VIBRATION CRITERIA

The initial design of the SSME accounted for certain expected vibration environments based on the experience gained in the design and development of engines for the Saturn program. Of particular importance was the knowledge gained from the J-2 engines that used the LOX/hydrogen as propellants. Recognizing that the vibration levels generated by liquid rocket engines are a function of many variables, the initial criteria, jointly agreed upon by Rocketdyne and NASA, was based on an extrapolation of all available data using the Barrett* relationship. This accounted

---

*Barrett, R. E., Techniques for Predicting Localized Vibratory Environment of Rocket Vehicles, NASA TN D-1836, October 1963.

for the more important known variables, such as thrust, weight, exit gas velocity, etc.

Vibration Zones

Vibration zones were established as a means of describing the vibration environment experienced by various components in different areas of the SSME. The zonal vibration criteria specified for these zones consisted of random vibration power spectral density curves augmented by superimposed sinusoids; a typical criteria is presented in Fig. 1. These criteria are utilized any time the dynamic environment for a given component is required. Principal uses are analytical model excitation forces and vibration input during laboratory tests.

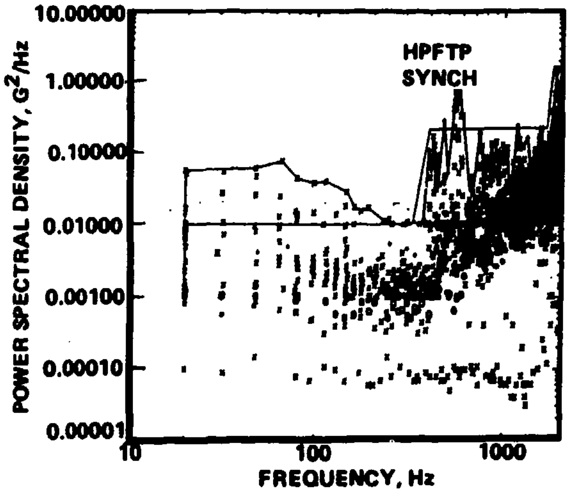

Fig. 1. Typical SSME zonal vibration criteria

The SSME vibration zones have been divided into two categories--source zones and response zones. Source zones contain the major areas of vibration generation and include all turbomachinery and combustion devices. In all, nine source zones have been defined and they are designated as Zones A through I (Table 1).

Response zones contain passive components, such as valves, actuators, and sensors. To date, 14 response zones have been specified and they are designated zones J through W (Table 1).

The zonal vibration criteria were developed by acquiring hot-fire test data and enveloping the maximum random vibration levels across the 20- to 2000-Hz spectrum. Where turbomachinery generated sinusoids appear above this random floor, superimposed sinusoids are utilized to account for them.

Source Zones

Evolution of the SSME zonal vibration criteria followed the growth of the SSME from early design phase through rated-power level (RPL) development (initial hot-fire tests, RPL operation, and flight certification) to current effort of full-power level (FPL) development. The process of updating, as new data became available, ensured that the most recent knowledge of the environment was being used to verify the design--whether analysis or by test.

A typical example of the initial zonal vibration is shown in Fig. 2. The basic characteristics include a random base level that varies in intensity across the frequency range from 20 to

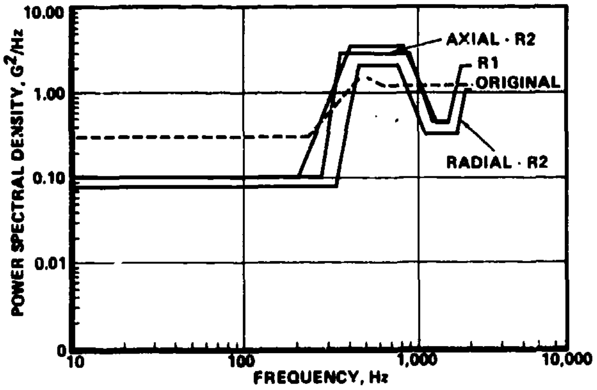

Fig. 2. Typical zonal vibration criteria

Table 1. SSME Zonal Vibration Criteria Source and Response Zone Designations

Source Zone	Contents	Response Zone	Contents
A	Main Combustion Chamber (MCC)	J	Main Fuel Valve (MFV)
B	MCC Throat and Engine Controller	K	Main Oxidizer Valve (MOV) and Actuator
C	Thrust Chamber Nozzle	L	Pneumatic Control Assembly
D	Oxidizer Preburner	M	Chamber Coolant Valve (CCV) and Actuator
E	Fuel Preburner	N	Fuel Preburner Oxidizer Valve (FPOV)
F	Low-Pressure Oxidizer Turbopump (LPOTP)	O	Oxidizer Preburner Oxidizer Valve (OPOV) and Actuator
G	High-Pressure Oxidizer Turbopump (HPOTP)	P	Oxidizer and Fuel Bleed Valves
H	Low-Pressure Fuel Turbopump (LPFTP)	Q	Vehicle Attach Panel
I	High-Pressure Fuel Turbopump (HPFTP)	R	Pressure Sensors
		S	Anti-Flood Valve
		T	Check Valve
		U	Not Used
		V	Pogo Accumulator and Valves
		W	Turbine Temperature Sensors

2000 Hz, plus superimposed sinusoids that are functions of specific phenomena such as pump blade wake frequencies (speed dependent) and combustion frequencies.

The first engine, known as Integrated Systems Test Bed (ISTB) was first hot-fire tested in May 1975. Many early ISTB tests were of very short duration and only at lower power levels. By January 1977, a limited amount of data had been acquired at power levels between 85 and 95 percent RPL. These data were used to issue a revision to the original source zone criteria. This revision identified as the "interim" or "R1" criteria utilized Barrett's scaling techniques to ratio these lower power level data to projected RPL and FPL levels. This R1 criteria produced levels generally lower than the original estimate criteria in the lower frequency ranges, essentially equal in the middle ranges, and slightly higher in the upper frequency range. The structural dynamic adequacy of all major SSME components was verified by analyses utilizing these R1 criteria.

As flight configured SSME engines were tested and data gathered, a second revision ("R2" criteria) was published in October 1978. This revision was based on a larger data base including many tests on different components, engines, and test stands. This large data sample increased the confidence in the criteria as the likelihood of any one factor (engine, test stand, etc.) significantly biasing the data was significantly reduced. Engine operation during these tests ranged between 70 and 100 percent RPL. These data were closely enveloped using the maximum random vibration vibration levels in conjunction with superimposed sinusoids to establish the best estimate of FPL environments. The original R1 and R2 criteria for a typical zone are compared in Fig. 2. This figure shows how the random vibration levels have been generally lowered with each revision, which indicates the conservatism in the original estimates of the vibration environments. As had been done with the previous revision, the structural adequacy of all major SSME components was verified by analyses using the R2 criteria. These criteria did not utilize the Barrett technique for scaling the 100 percent RPL data to projected FPL levels, as was done in the previous revisions. Experience with the R1 criteria had shown that rocket engine component random vibration levels do not scale with power level, and therefore this technique was not considered suitable for use with the latter criteria revision.

Inspection of the nine source zones included in the R2 criteria shows the highest vibration levels to be found in Zone C. This is to be expected since it is adjacent to the largest source of energy, the combustion zone, produced by the engine. The original R1 and R2 criteria for this zone are compared in Fig. 2.

Some minor revisions to the R2 criteria have been made since its publications. Each time revisions are made, the designation is also changed. The next revised criteria will be designated as R3. Both low pressure turbopumps exhibited increased vibration spectra during operation when operated at low inlet pressures. Thus, special criteria for these two zones were generated to describe these special environments, and the structural adequacy of the affected hardware was verified by a combination of analysis and straingage measurements made during hot-fire tests.

This revision process used during the SSME development program has provided an accurate and timely source of vibration information data for the nine source zones, which in turn, has been utilized to demonstrate the structural dynamic adequacy of major SSME components.

Response Zones

The vibration response zones differed somewhat from that of the source zones in that an initial prediction was not made. Hot-fire data was acquired from early engine tests to support laboratory tests and special analytical tasks. Where only limited amounts of data were available, conservative envelopes were used to ensure that valid results were obtained. However, analytically predicted criteria were generated for the main propellant valve actuators during the design phase of the program. These criteria were used by the actuator vendor to vibration test the actuators prior to ISTB hot-fire testing.

As hot-fire test data were acquired, criteria were generated for the components shown in Table 1. In many instances, criteria were generated for both the vibration input to a given component as well as the response at a given location on the component. These data were used primarily to ensure valid vibration testing in the laboratory, where it is frequently difficult to duplicate component boundary conditions as seen on the engine. As new data were generated, criteria were updated only when the validity of existing criteria was in question.

FPL Data Comparison

All existing criteria were based on data taken at a maximum of 100 percent RPL operation. Full power level (109 percent RPL) development of the SSME has recently been undertaken and new data are being acquired and compared to the existing source and response zones. To date, only minor increases over the established level for RPL have been noted.

Figure 3 (Zone G) shows a typical FPL power spectral density (PSD) compared to the R2 criteria. The data are clearly below the criteria throughout the spectrum. The spikes protruding through the random floor are covered by sinusoids.

---

*Barrett, R. E., Techniques for Predicting Localized Vibratory Environment of Rocket Vehicles, NASA TN D-1836, October 1963.

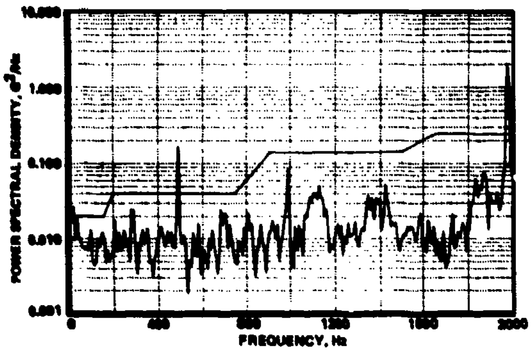

Fig. 3. Zone G HPOTP vibration criteria

Figure 4 shows Zone D, where the data exceeds the R2 criteria in specific frequency bands. If subsequent FPL tests produce similar PSDs, the R2 Zone D criteria will be revised for final FPL use, such as design verification specification (DVS) testing or analysis. It is important to note that the R1 criteria in most cases covered the FPL levels; therefore, the structural adequacy of engine hardware based on analysis using R1 levels is not in question.

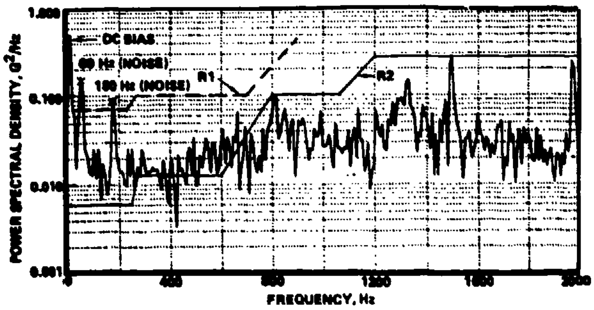

Fig. 4. Zone D oxidizer preburner vibration criteria

The complete SSME zonal vibration criteria is not given in the paper as it would be too voluminous.

Vibration Considerations Not Accounted for by the Zonal Criteria

Whereas the zonal criteria was extremely useful in designing the overall engine system, fuel ducts, connections, etc., and establishing the requirements for the design verification tests, it could not ensure freedom from other vibration phenomena, such as:

1. Subsynchronous whirl - turbopumps
2. Hot-gas, flow-separation instabilities - fuel feed line transient vibrations
3. Flow-induced whistles - main oxidizer valve
4. Turbine blade vibration and cracking
5. Impellers
6. Vortex shedding and random excitations of main injector LOX posts
7. Sheet metal fatigue

Some of the more significant vibration phenomena that generated problems during the development testing will be discussed in a subsequent section.

SSME DVS VIBRATION TESTING

To ensure that the SSME major components can withstand the vibration environment associated with long term reusable operation, DVS tests were conducted. This included both the transient and steady-state vibration environment generated during ground handling and flight operations.

Components tested during the DVS vibration program included those components that would not be analyzed in significant detail to verify that adequate life was available when subjected to the transients and steady-state vibration conditions. These components typically contained moving parts that were subject to wear, electronic systems, nonlinear elements and/or those components too structurally complex to adequately model (multi-ply bellows or braided hoses). Table 2 lists the components that were tested in the DVS Program.

Table 2. Components Tested in the DVS Program

- PROPELLANT VALVES
  - MAIN OXIDIZER
  - MAIN FUEL
  - OXIDIZER PREBURNER OXIDIZER
  - FUEL PREBURNER OXIDIZER
  - CHAMBER COOLANT
- PROPELLANT VALVE ACTUATORS
  - MOV/MFV
  - OPOV/FPOV
- POGO SYSTEM VALVES
  - RECIRCULATION ISOLATION
  - HELIUM PRECHARGE
  - GASEOUS OXYGEN CONTROL
- ENGINE FLEX JOINTS
  - LPFTP PUMP DISCHARGE
  - FPFTP TURBINE DISCHARGE
  - OXIDIZER TANK PRESSURIZATION LINE
  - LPOTP PUMP DISCHARGE
  - FUEL BLEED LINE
- ENGINE - VEHICLE INTERFACE LINES (6 BRAIDED HOSES)
- ANTI-FLOOD VALVE
- PNEUMATIC CONTROL ASSEMBLY
- PURGE CHECK VALVES
- PREBURNER SPARK IGNITER
- MCC SPARK IGNITER
- ENGINE CONTROLLER
- FASCOS BOX
- ENGINE SENSORS
  - PRESSURE
  - TEMPERATURE
  - FLOW
  - SPEED
- ELECTRICAL CONNECTORS

The vibration environments for the DVS vibration program were derived from measurements made during engine hot-fire tests. These criteria and their development were discussed earlier in this paper. The criteria represents test conditions of engine power levels from 65 to 109 percent of rated thrust. Individual power spectral density data plots were obtained at each power level, combined and subsequently enveloped to define the steady-state vibration environment. To obtain the transient conditions, shock spectra analysis was performed for the engine start and shutdown sequence and used to define the necessary shock tests to satisfy the DVS requirements.

Test Procedure

DVS vibration tests were conducted in two segments. Initially, testing was conducted to satisfy First Man Orbital Flight (FMOF) certification. This testing consisted of transient shock tests representing 60 engine starts and 60 engine starts and 60 engine shutdowns, plus 1-1/2 hours of steady-state random vibration representing engine operation at power levels between 65 and 102 percent of rated thrust. The second part consisted of extended life DVS testing for full power level certification (FPLC) consisting of an additional 6 hours of steady-state vibration to demonstrate a total of 7-1/2 hours design life required by the SSMEs. This latter testing incorporates any vibration amplitude changes associated with operation at 109 percent power level (FPL). A typical DVS vibration test procedure consists of:

- Vibration and shock tests of the components on each of three orthogonal axes in the following sequence:
  - A 2-g peak sinusoidal sweep test to determine specimen resonant frequencies
  - 120 transient shock spectra pulses to simulate the 60 engine starts and 60 engine shutdowns
  - 1-1/2 hours of steady-state random vibration is conducted with superimposed sinusoids representing vibration components generated by the rotating machinery to demonstrate the required FMOF operational life; there are four turbopumps on the SSME.
  - Finally, 6 hours of steady-state random vibration is conducted with superimposed sinusoidal frequencies to demonstrate component stability to fulfill the original 7-1/2 hour design life goal.

The superimposed sinusoids during the 1-1/2 hour random vibration test are performed to cover the conditions that represent engine throttling and represent pump-generated frequencies. These sinusoids are caused by pump blade wake conditions, struts in the flow path, and turbine blade pulsations.

Failures and Fixes

One of the derivatives of the DVS Program was identifying weaknesses in component designs. During the DVS vibration program weaknesses were encountered with the main engine controller, the recirculation isolation valve (RIV), and the anti-flood valve (AFV).

Controller. Early in the program, the main engine controller was subjected to a predicted random vibration environment of 22 g rms. This controller was to be hard mounted on the SSME; therefore, it was hard mounted in the laboratory vibration tests. Results indicated that the attachment fittings could not survive the long-term, high-vibration environment. Galling of the shear pins and the spherical bearings were evident early in the test (Fig. 5). Also, it appeared that the electronic components in the controller would not survive the high level of transmissibility through the hard mounts. Therefore, a soft viscoelastic mount system was designed for the controller. The design constraint was that the position of the controller relative to the engine should not change, i.e., the envelope would remain the same. A quick review of "off-the-shelf" isolator mounts revealed that bushing type mounts such as those used by off-road vehicles could be accommodated in the envelope. These off-the-shelf units were initially evaluated and later a high-temperature silicon compound isolator mount of similar configuration was developed to be used for final application (Fig. 6). The test setup is shown in Fig. 7.

Figure 8 shows a comparison of the controller responses with or without the shock mounts. Subsequently, the SSME controller passed all specified shock and vibration requirements successfully. The design of the mount system provided a natural frequency between 20 and 40 Hz

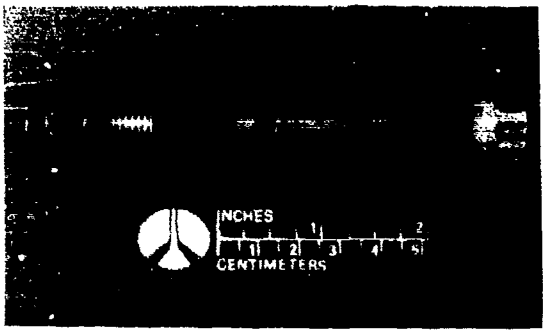

Fig. 5. Controller forward bolt showing galling after vibration

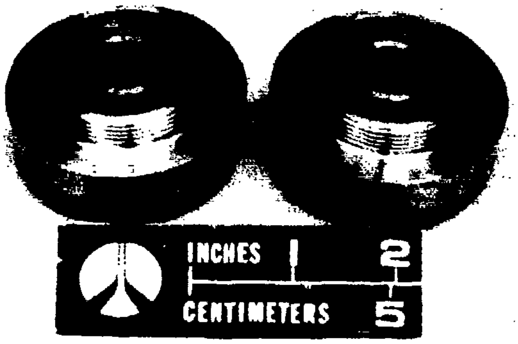

Fig. 6. Controller silicone isolator mount

Fig. 7. SSME controller mount on vibration slip table

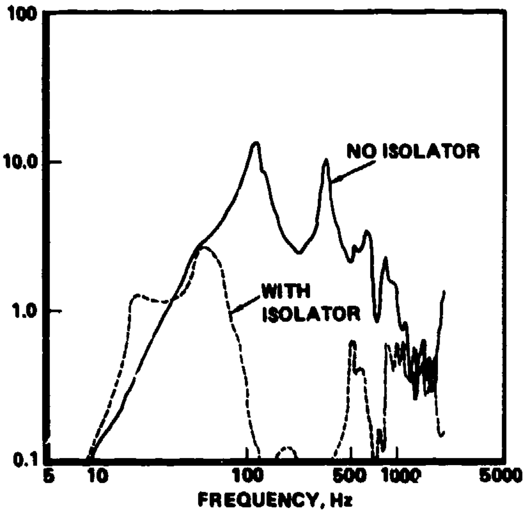

Fig. 8. SSME controller with and without isolators - laboratory sine sweep tests

in the soft axis. In the cross axis, the stiffness was to be twice the soft axis. The first resonant design verification of the effectiveness of the controller isolator system shown in Fig. 9 displays the DVS random vibration criteria, the engine measured environment (at 75 percent power level) and the controller response on the engine. As can be seen, the laboratory tests, when data is enveloped, is quite conservative.

Recirculation Isolation Valve. The recirculation isolation valve (RIV) prevents a "short circuit" (through the Pogo accumulator) in the engine oxidizer system during the propellant conditioning mode of engine start preparation. The normally open RIV is actuated closed by the same pneumatic pressure that opens the normally closed oxidizer bleed valve.

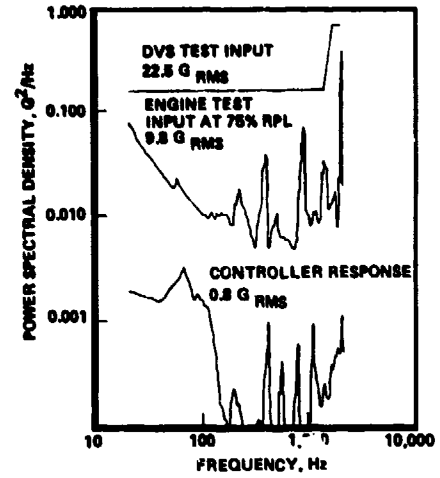

Fig. 9. Controller vibration data - engine hot-fire test

A malfunction of the recirculation isolation valve (Fig. 10) occurred during the DVS vibration program. The armature extension of the linear variable displacement transducer (LVDT) failed during random vibration portions of these tests as shown in Fig. 11. A redesign of the armature with an improved radius was incorporated at the high stress concentration point, and the unit subsequently passed its DVS vibration successfully.

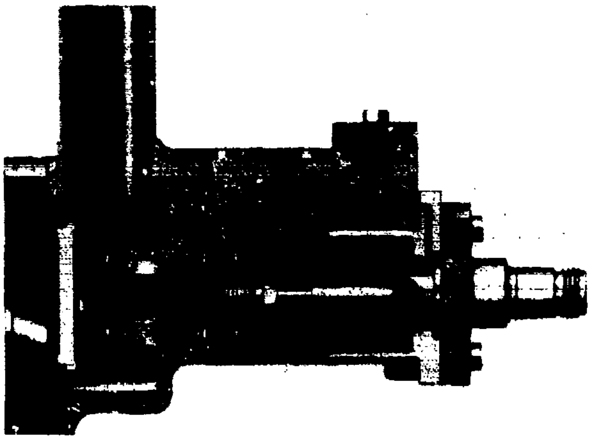

Fig. 10. Recirculation isolation valve

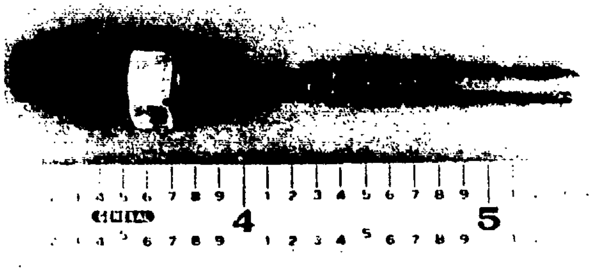

Fig. 11. LVDT extension arm fracture.

Anti-Flood Valve. The anti-flood valve (AFV) is a spring-loaded, normally closed poppet type valve that prevents the flow of liquid oxygen into the heat exchanger until there is sufficient head applied to the heat exchanger during engine start to convert the liquid oxygen to gaseous oxygen.

The anti-flood valve LVDT developed an electrical connector feed-through malfunction during vibration testing, which was analyzed to be due to poor potting compound (Fig. 12). An improved potting compound and application technique was utilized to correct this weakness. In addition, support was provided to the attaching wire, and the valve subsequently passed its DVS vibration test successfully.

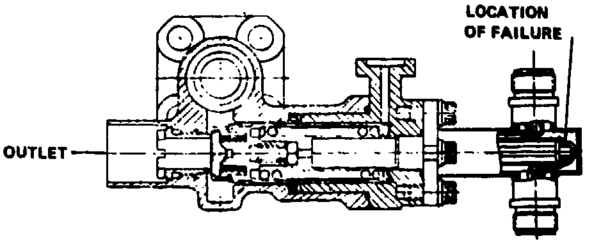

Fig. 12. Heat exchanger anti-flood valve

HPFTP TURBINE BLADES

The high-pressure fuel turbopump (HPFTP) is a three-stage centrifugal pump that is directly driven by a two-stage, hot-gas turbine. The pump receives fuel from the low-pressure fuel turbopump (LPFTP) and supplies it at increased pressure through the main fuel valve (MFV) to the thrust chamber assembly coolant circuits. The turbine is powered by hot gas (hydrogen-rich steam) generated by the fuel preburner.

During 1977, Rocketdyne encountered two known incidents of HPFTP, first-stage, turbine-blade cracking and a third probable incident. The common denominator between the incidents and the suspected failure cause was loss of turbine-blade damping. In the first incident, the turbine blades had nickel-plated dampers and gold-plated blade platform mating surfaces. During operation, an "over-temperature" condition effectively brazed the dampers to the blades producing a locked-up condition. Two cracked blades were discovered during posttest inspection. The unit had experienced 8 tests for a total of 330 seconds of operation. The two failure locations were an airfoil root leading edge fillet crack and a trailing edge airfoil crack approximately 1/3 the blade height from the airfoil foot.

During the second incident, the turbine blades had nickel-plated dampers but no gold plating on the blade platform mating surface. The blade failure occurred after 38 tests and a total of 2973 seconds of operation. Examination of the hardware revealed that the nickel plating on the damper had extruded radially outward, as illustrated in Fig. 13. It was postulated such that the nickel effectively locked the blades together producing a condition similar to that incurred on the prior unit.

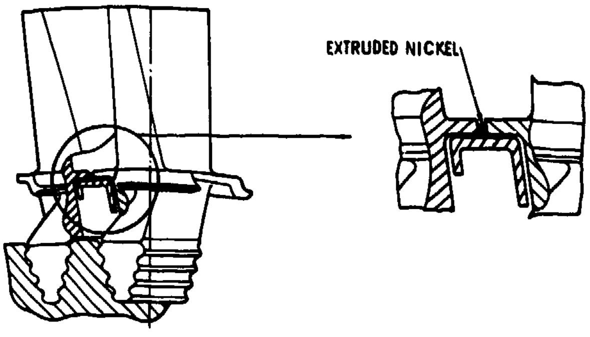

Fig. 13. HPFTP turbine blades

The third failure occurred after 4325 seconds of operation and a total of 21 tests. Extensive hardware damage precluded actually identifying a blade failure as a cause.

To identify the cause of the turbine failures, first-stage blades were subjected to blade evaluation laboratory tests consisting of structural, dynamic, and fatigue tests.

A unique test technique known as whirligig testing* was utilized to study the effectiveness of dampers in the turbine-blade critical modes. This test technique utilized the actual rotating blade disk combination, instrumented with strain gages and excited by a series and air jets, to force the frequencies expected during engine operation. A comparison was made of the modal strains of each damping system for each excitation frequency under identical force excitation. An output of this testing technique produces a Campbell diagram directly, requiring only a correction to engine operating temperatures.

Test Program (Whirligig). The Rocketdyne test program consisted of five different blade-damper combinations:

Group No.	
1	No damper
2	As-designed damper, 0.92→1.14 grams
3	Platforms brazed together (locked-up blades)
4	Precision damper, 0.52→0.54 grams
5	Chem-milled damper, 0.51→0.67 grams

---

*Developed through the assistance of the General Electric Corporation, Jet Engine Division, Cincinnati, Ohio.

The layout of the blade groups is shown in Fig. 14. A total of 48 strain gages and 2 thermocouples was applied to the five groups of blades. Each blade type was in groups of ~12 blades with only the center five blades being instrumented. Each instrumented blade had a strain gage in two of the four following locations:

1. Leading-edge airfoil root
2. Trailing-edge airfoil root
3. Midchord airfoil root
4. Trailing edge 1/4-inch upward from airfoil root

The gage locations were governed by three considerations:

1. Known failure locations during engine testing
2. Locations that would provide a significant strain level for the maximum number of natural frequencies. The relative strain levels were determined experimentally by vibrating instrumented blades in the laboratory at each of their frequencies
3. Locations with small strain gradients such that the strain gage position was not critical

Since the whirligig provides only comparative data, only the strains within a particular test may be compared. Additionally, the strains should be compared only for common harmonics of the forcing function.

The test program consisted of 4 test runs. The initial test run utilized 19 nozzles as excitation and was performed to limit the maximum rotational speed to 28,000 rpm. The 19 per revolution excitation did not correspond to any known engine forcing function, but was selected to excite the blade first-frequency at a low-rotational speed, thus permitting a check of the rotating assembly and to give maximum information. The principal modes of vibration excited during this test were the first-bending mode and first-torsion mode. A comparison of the relative amplitudes of strain for the five test groups for the various harmonics of the forcing function is shown in Tables 3 and 4. The first-bending mode strains clearly indicate that the locked-up blade configuration (Group 3) is the most responsive. This is consistent with both analytical predictions as well as the hypothesis that the turbopump failures were due to locked-up blades.

The various damped configurations, as well as undamped configurations (Group 1) are not separable, although Groups 2 and 4 seem to be somewhat better than Group 4.

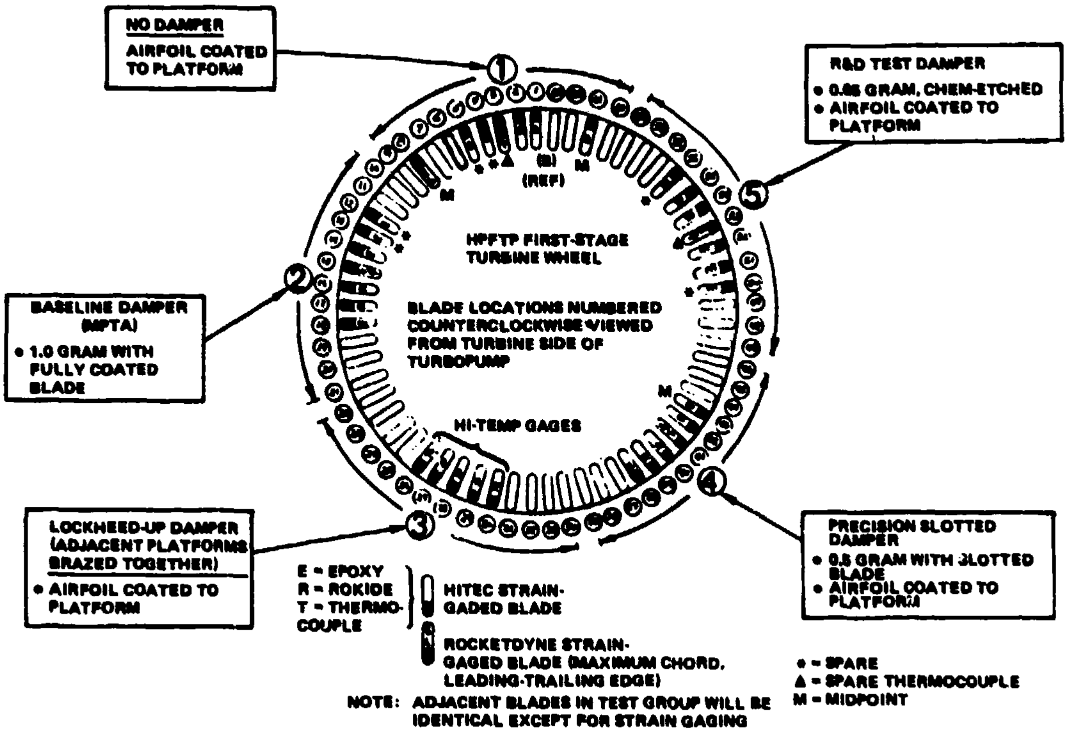

Fig. 14. First-stage wheel blade/damper assignment whirligig testing

Table 3. First-Flex Mode Strains (Test 1)

	STRAIN, μIN./IN.	
GROUP	1ST HARMONIC	2ND HARMONIC
1	30	--
2	4	9
3	128	86
4	10	6
5	33	26

Table 4. First-Torsional Mode Strains (Test 1)

	STRAIN, μIN./IN.		
	HARMONIC		
GROUP	2	3	4
1	60	90	48
2	70	15	48
3	127	82	27
4	43	17	22
5	64	14	8

The second harmonic of the forcing function exciting the first-torsional mode also indicates that the locked-up configuration (Group 3) is the most responsive. Higher harmonics indicate little difference between the damped configurations, but all are superior to the locked-up and undamped configurations.

The torsional mode was particularly responsive because of the method of excitation. The disk was rotating in the normal direction with the gas flow being directed against the suction surface of the airfoil on the trailing edge. The imparted force from the gas jet produces a torsional moment about the airfoil cross section center of gravity (Fig. 15).

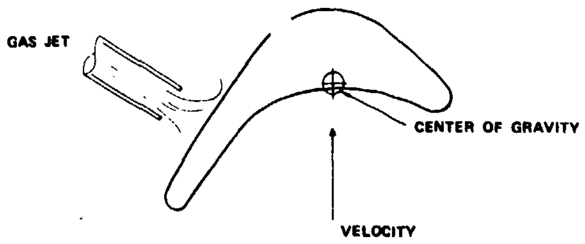

Fig. 15. Relative force on turbine blade

The conclusion from the first test was that the locked-up platform was the most probable cause for the engine turbine blade failures. However, the relative merit of the various damper configurations could not be assessed from this test. Therefore, testing at higher rotational speeds with nozzle excitation consistent with turbopump operation was required.

The second series of tests was run to 38,000 rpm and utilized 13 nozzles as excitation. This was representative of the 13 struts upstream of the first-stage nozzle in the turbopump. These tests showed response at the first harmonic of the 13 per revolution excitation for the first-flex mode. The undamped configuration showed a discernible strain about 105 μin./in. peak to peak and all damper configurations were effective in suppressing this mode.

A summary of the measured strains for the various configurations for the first-torsional model is shown in Table 5. The maximum strains generally occurred on the trailing edge.

Table 5. Turbine Blade Strains Due to First-Torsional Mode

	HARMONIC	
GROUP	2	3
1	421	211
2	263	126
3	--	--
4	305	205
5	300	205

The result of the torsional mode strain data was similar to Test 1, showing that the damper is relatively ineffective in damping the torsional mode.

The final test series utilized 41 nozzles simulating the number of nozzles in the actual design. The test served to indicate that there were no unexpected responses to this high-frequency excitation.

The method used to present the data gathered from the whirligig testing is illusrated in the Campbell diagram (Fig. 16). The Campbell diagram presents a plot of blade frequency vs shaft speed and the blade strain response. The natural frequencies of the blades are shown by the almost horizontal appearance of the data and the frequencies of the forcing functions are clearly evident by the diagonal lines. At the intersection of these lines, the high amplitude of the strain response is easily observed. Most importantly, this diagram forms the basis for interpretation of similar diagrams obtained during turbopump operation during engine tests (Fig. 17).

The multiples of shaft speed exciting the blade during turbopump operation are shown in the right margin of Fig. 17. These multiples of shaft speed are expected excitations associated with the 13 inlet struts in the turbines

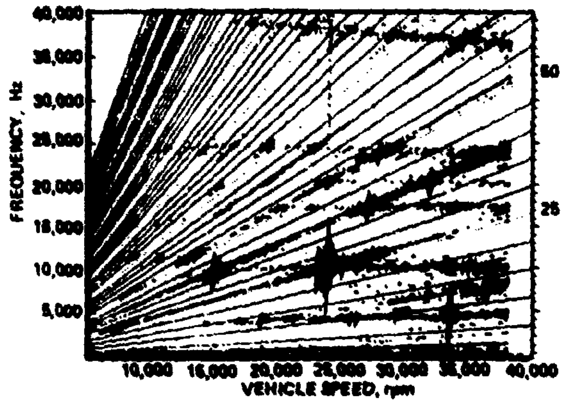

Fig. 16. HPFTP first-stage turbine blade Campbell diagram (whirligig)

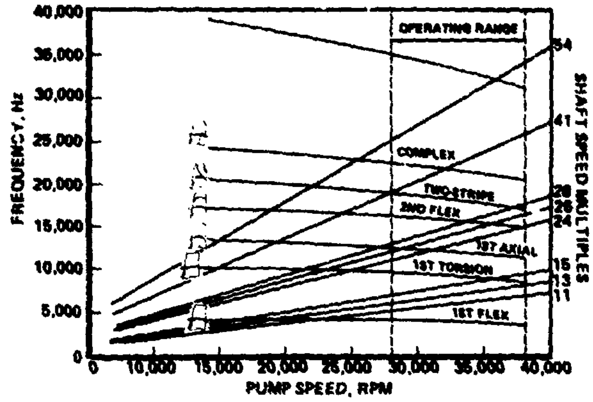

Fig. 17. HPFTP first-stage turbine blade Campbell diagram (operation)

and their irregular spacing, and also due to the first stage-nozzles. Examination of this figure indicates that the following modes of turbine blade vibration are in the engine operating range:

Mode	Rpm
1st Torsion	/ 36,000
1st Axial	28,000 to 31,000
2nd Flex	33,000 to 37,000
2 Stripe	37,000
Complex	32,000

Based on the results of the whirligig testing, it was concluded that the turbine blade failures incurred during testing were directly attributable to locked-up blades. Although the whirligig testing did not provide a clear ranking of the dampers tested, all dampers appeared to function well.

SSME MAIN INJECTOR OXIDIZER POST

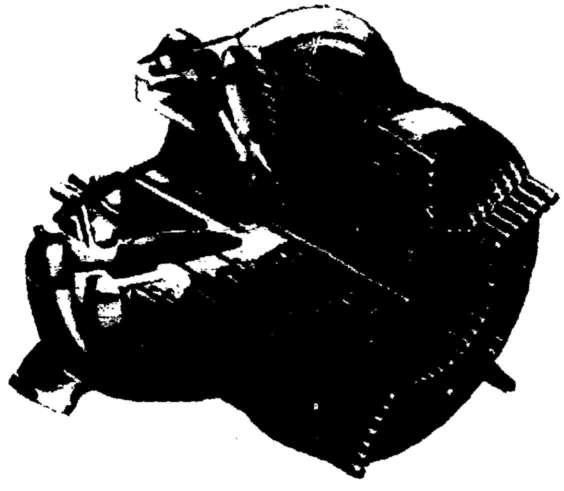

Fig. 18. Main injector assembly

The SSME main injector (Fig. 18) consists of 600 concentric posts, each of which allows liquid oxygen (LOX) to flow through a center passage and hot hydrogen gas from the turbines to flow through the outer concentric passage. The posts are arranged in 13 rings (rows), and the hot hydrogen gas impinges directly on the outer row os posts as it discharges from the five transfer ducts. Structurally, the LOX posts (Fig. 19) are welded to the interpropellant plate at the upper end, are laterally restrained at the secondary face plate, and are cantilevered below the secondary face plate, except for three guide vanes in the fuel sleeve which limit the lateral motion.

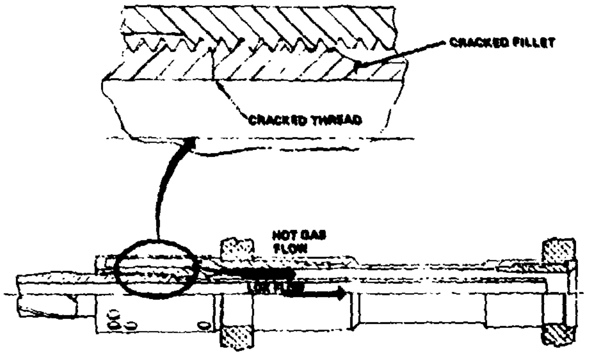

Fig. 19. LOX post thread and fillet crack locations

The outer posts (row 13) were subjected to the most severe loading conditions. The steady state loads included a bending moment due to the deflection of the interpropellant plate, thermal loads due to differential temperature, a drag force due to the flow of hot hydrogen gas, and the direct loads due to the differential pressure across the face plates. Dynamic loads are induced by the structural vibration of the powerhead, vortex shedding in the hot-gas flow stream, and random excitation from the hot-gas flow stream. Recognizing these potential excitation sources and resulting loads were extremely difficult to assess quantitatively, steps were taken during the initial design to minimize the dynamic loads, i.e., helical strakes on the LOX posts to reduce the vortex shedding induced vibrations.

The location of the highest alternating stress, most critical in fatigue, are the threads where the fuel filter attaches and the fillet directly below these threads (Fig. 19). The location of the maximum stresses depends on the degree of tightness in these threads. It is not possible to torque the filter tightly on these threads because they are used to adjust the support for the secondary face plate. In addition, experimental verification of the maximum stress levels could not be measured due to their local nature and inaccessibility.

Although it was thought that a conservative approach had been taken in the design of these posts, two engine tests were terminated after 780 seconds of equivalent rated power level testing. Thus, the engine development program had uncovered higher load conditions than had been predicted.

Analysis of the failed hardware showed permanent bending deformation in the direction of the hot gas flow, indicating higher drag loads than had been anticipated. In addition, several of these posts showed fatigue cracks in the threaded area, and one showed a fatigue crack in the fillet below the threads. Model studies showed a nonuniform flow distribution between the transfer ducts, with the outer ducts on the HPFTP side carrying twice the flow of the center duct.

Since it was not practical to quickly redesign the turbine and transfer ducts to reproportion the flow and increase the fatigue strength of the posts, flow shields (Fig. 20) were added to pairs of posts in row 13. These shields reinforced the posts in the outer row, modified the flow distribution, and kept the posts cooler. However, since the shields did not shield two posts in Row 12, these posts were plugged to ensure a minimum injector fatigue life of 14,500 seconds of RPL. Further engine testing showed that a predicted life of 20,000 seconds of equivalent RPL could be obtained by plugging nine additional posts in Row 12.

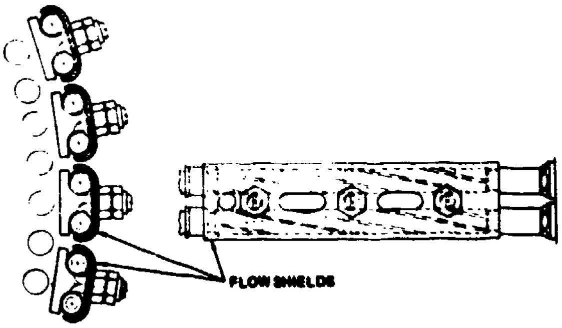

Fig. 20. Main injector design modification

To further improve the predicted life of existing injectors, a modification (Fig. 21) was developed that replaces the tips of the LOX posts with material having improved properties (316L material was replaced with Haynes 188). This replacement increases the fatigue strength in the most critical areas, the threads and the fillet below the threads. This redesign gives 28,000 seconds of life at RPL.

The long-range redesign calls for the entire LOX post to be changed to Haynes 188 material, and will provide an infinite fatigue life at RPL and at FPL (109% RPL).

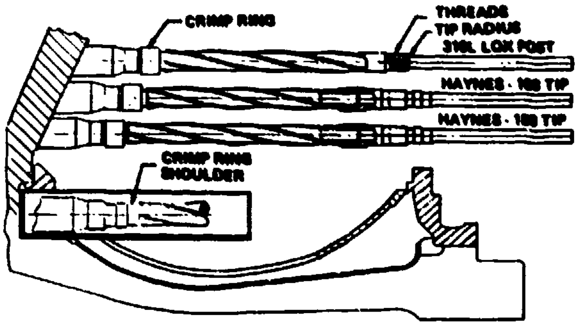

Fig. 21. LOX post configurations

CONCLUSIONS

As has been discussed, the SSME has undergone design changes as a result of engine development testing. Failures have occurred, have been evaluated, and fixes have been implemented. The engine environment has gone through several criteria definition changes and now represents more accurately the current environment. The engine has matured and is expected to meet its operational life requirements for RPL and eventually FPL. The dynamic data base has been established and can be used for upgrading the SSME and for future engine designs.

ACKNOWLEDGEMENT

The authors wish to take this opportunity to acknowledge the contribution to the paper by Messrs. John Haworth, Tom Henderson, and Fred Nitz who provided text inputs and to Bob Sutton who directed the whirligig test hardware design and test effort and to D. D. Cicii for his design effort on the whirligig hardware. Also to the numerous Rocketdyne and NASA engineers who contributed to the analysis and solution of the development problems associated with the SSME.

DISCUSSION

Mr. Himelblau (Rockwell Space Transportation Group): I thought you also had some whirl and instability problems from time to time. Are those also included in your paper?

Mr. Mogill: No. There is a seperate paper on whirl and instability, written by Bernie Rohen, which was published about six months ago. It is an excellent paper. There is also another paper that was written by Matt Eck, our chief engineer, who is the head of the original whirl team. So there are two excellent papers on that whirl phenomena that we ran into on the high pressure fuel pumps.

STRUCTURAL RESPONSE TO THE SSME FUEL FEEDLINE TO UNSTEADY SHOCK OSCILLATIONS

Edward W. Larson, Gary H. Ratekin,
and George M. O'Connor

Rockwell International/Rocketdyne Division
Canoga Park, California

The Space Shuttle Main Engine flight nozzle experiences unexpectedly large accelerations during engine start and cutoff transients. Two fuel feedline failures occurred during separate engine tests. To define the forcing function causing high nozzle accelerations, experimental air flow tests using a subscale model were performed with high-frequency pressure instrumentation such that pressure oscillation amplitude, frequency, and spacial characteristics could be determined. The test results led to the conclusion that the SSME was experiencing pressure oscillations at 38 psi at a frequency of approximately 100 Hz occurring over the last 3 feet of the nozzle. Results of this investigation yielded an understanding of the cause of the failures and led to a redesign that exceeds life requirements.

BACKGROUND

Hardware Description

The SSME uses a high-performance, large-area ratio, bell-contour nozzle to maximize the engine performance at altitude. The expansion area ratio, ϵ, of 77.5 achieves this altitude performance and also allows the nozzle to flow full at sea level. The sea level operation results in the nozzle flowing in a highly overexpanded condition, that is the wall exit pressure, P_e, is much lower than the ambient pressure, P_a.

The nozzle assembly attaches to the main combustion chamber at an area ratio of 5, as shown in Fig. 1.

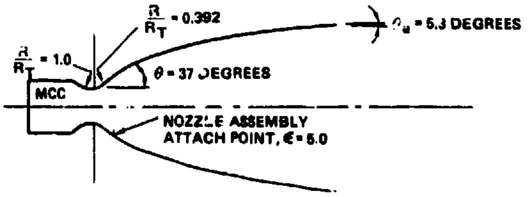

Fig. 1. Nozzle assembly attach point

The nozzle expands the gases along the wall to a maximum flow angle of 37 degrees relative to the axis of symmetry. The remainder of the contour then turns the flow back toward the axis, ending with a wall exit angle of 5.3 degrees. The SSME nozzle is a regeneratively cooled bell chamber made of 1080 tubes attached to upper and lower manifolds (Fig. 2). Liquid hydrogen enters at the coolant inlet and flows to the lower distribution manifold through three fuel feedlines and branching connecting ducts referred to as the "steerhorns." The coolant then flows up the tubes that form the nozzle wall and into the collection manifold.

Two steerhorn failures occurred during two separate engine development tests. The fracture locations were at steerhorn welds near the distribution manifolds and the tee where the fuel feedline branches. The steerhorn is made of Inconel 718 tubing that is 1.625 inches in diameter with a 0.049-inch nominal wall thickness and is welded using Inconel 718 filler wire.

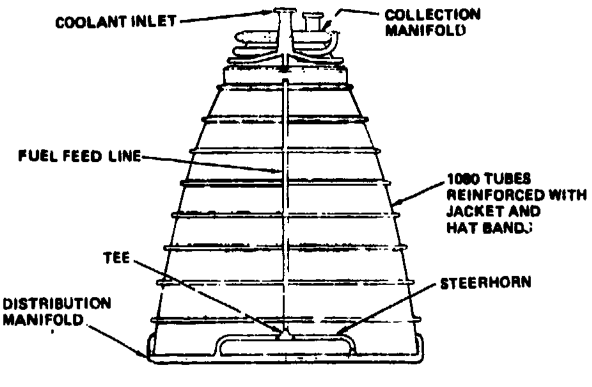

Fig. 2. Nozzle/steerhorn assembly

The assembly is solution treated at 1900 F as part of the nozzle braze cycle and aged for 10 hours at 1400 F.

Description of Incidents

Test 750-041 on Engine 0201 was terminated at 4.27 seconds by a redline limit. During the shutdown transient, at 5.15 seconds, approximately 0.9 seconds after cutoff, a steerhorn ruptured. At the time of failure, the main chamber pressure was 1350 psi as compared with 2800 psi at the time of test termination (Fig. 3). The failed hardware showed fractures at both the tee weld and the aft manifold, accompanied by extensive fragmentation.

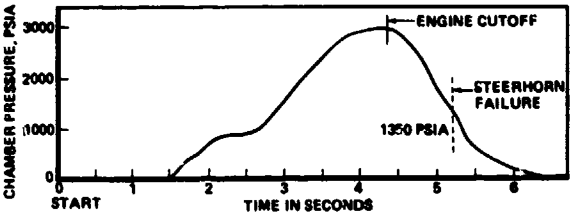

Fig. 3. Main chamber pressure during engine test 750-041

A metallurgical analysis of the failure surfaces determined that the fracture was initiated by fatigue. Fatigue striations found in the fracture surface adjacent to a weld are shown in Fig. 4. This type of failure was completely unexpected. The structural design analysis had shown factors of safety on ultimate strengths of greater than 2 for transient loads, and 1.5 for steady-state conditions. The calculated stresses during both transients and steady-state resulted in zero predicted fatigue damage and a corresponding infinite life.

Fig. 4. Fatigue striations on fracture surface

The second incident occurred at about 0.9 seconds after cutoff during the engine main propulsion test article, Test SF6-003. Again, the steerhorn ruptured at welds near the tee and aft manifold.

The metallurgical examination did not show signs of fatigue striations; however, it did uncover soft low-strength welds. Thus, a combination of high-transient strains and the low-strength weld were sufficient to cause failure.

A detailed description of the hardware analyses, the tee reinforcement of soft welds that allowed development testing to continue, and the steerhorn redesign for future engines is contained in Ref. 1 and 2. Experimental verification of the adequacy of the redesign was obtained through full-scale vibration testing of both steerhorn designs at the Marshall Space Flight Center (Ref. 3). The reinforced tee configuration was used on all three engines in the successful first launch of Columbia.

ANALYSIS OF ENGINE DATA

Accelerometer Data

The first indication of the cause of the vibration leading to the fatigue failure was obtained from accelerometer data. Vibration data showed two short periods of transient vibration, one at approximately 2.8 seconds after start and another at approximately 5.12 seconds or 0.9 seconds after engine cutoff (Fig. 5). The latter period was coincident with the time of failure, and showed frequencies in the 250 to 400 Hz range. Movies of the nozzle exit at start and cutoff showed normal and oblique shocks near the exit at the time accelerometers were showing the high-amplitude transients. Therefore, a series of engine tests were run using strain gages, movies, and accelerometers to further define the structural behavior and fluid dynamics during both of the nozzle transients.

Strain Gage Data

Strain gage measurements obtained during the start and cutoff transient also showed high amplitudes at the tee in the 200- to 400-Hz regime. This transient was shown to be a shock pulse with a few cycles of high-amplitude strain that rapidly decayed to low levels. These transient strains

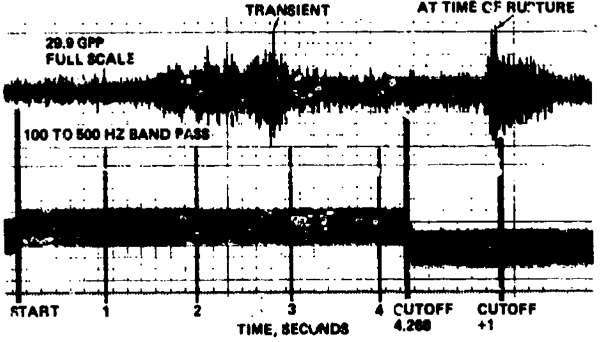

Fig. 5. Acceleration on oxidizer preburner

were significantly higher than those correspondign to the design stresses and could explain a low cycle fatigue failure, but the strains are not large enough to explain an overload-type failure in a normal weld.

An expanded trace of the data during the transient period is shown in Fig. 6. Here the data were filtered to separate the contribution of strain due to side loads, breathing modes, and shock transients. Approximately 95 percent of the total peak-to-peak strain shown on the unfiltered trace is contained in the 100- to 500-Hz frequency band. This figure also shows the low amplitude of strain range contributed by the breathing and pendulum modes.

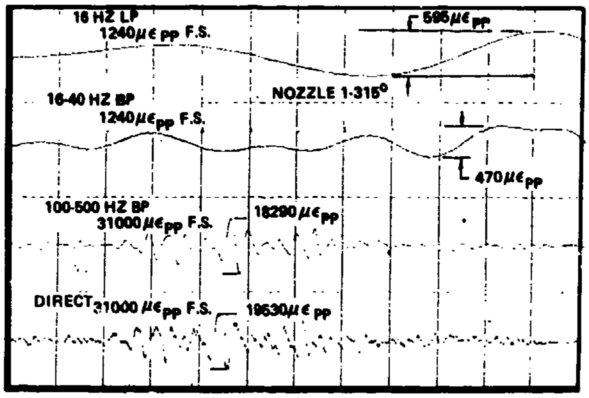

Fig. 6. Test 902-160 strain gage during start transient

There was considerable variation in the maximum strain range from test to test, and usually only one cycle at this peak strains occurs in each test. The magnitude of the peak-strain range occurring in each of the 41 tests is plotted in Fig. 7 in the order in which the tests were run. Generally, the peak-strain range is below 7000 microinches/inch, a value that contributes very little to low-cycle fatigue damage.

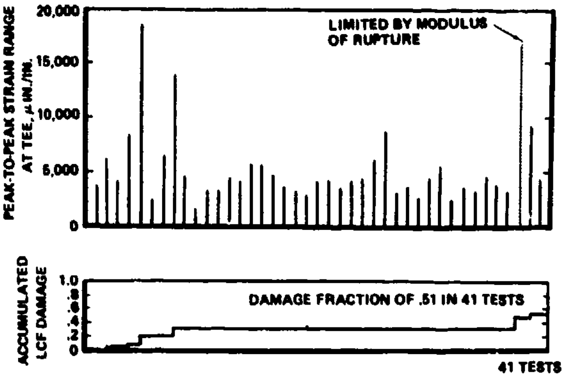

Fig. 7. History of maximum strains

Cause of Failure

The cause of the failure was traced to a period of unsteady flow separation during start and cutoff. Operation of the SSME at sea level results in an overexpanded situation where the nozzle exit pressure is less than ambient. This effect is increased during the startup and shutdown sequences when the engine is operating below full-chamber pressure. Figure 8 depicts such a situation during the shutdown transient observed in subscale cold-flow testing. As the chamber pressure, P_c, is decreased relative to ambient pressure, P_a, the formation of a λ shock at the nozzle exit can be seen in the Schlieren photographs (Fig. 8A). As the chamber pressure is decreased further, the shock system moves into the nozzle and the downstream leg of the λ shock appears to intersect the nozzle wall at the exit (Fig. 8b). The flow becomes unsteady at this pressure ratio, and large pressure oscillations occur on the nozzle wall with the flow attaching and detaching from the wall as shown in Fig. 8B and 8C. With a further decrease in the chamber pressure, the flow remains detached, and the large pressure oscillations cease.

- UPSTREAM SHOCK LEG INSIDE NOZZLE
- DOWNSTREAM SHOCK LEG OUT OF NOZZLE
- NO PRESSURE OSCILLATIONS

- DOWNSTREAM SHOCK LEG AT NOZZLE EXIT
- PULSE EXPANDING AND CONTRACTING APPROXIMATELY 20 PERCENT IN DIAMETER
- LARGE PRESSURE OSCILLATIONS NEAR NOZZLE EXIT

Fig. 8. SSME subscale nozzle pulse during periods of high-pressure oscillations

The shock transients discussed above resulted in dynamic motion of the aft manifold where the steerhorns attach. These shocks excited a natural frequency of the steerhorn with a mode shape having high strains at the tee welds. To further evaluate the loading dynamics, a series of subscale air flow tests were carried out.

EXPERIMENTAL TESTING AND ANALYTICAL RESULTS

Subscale Air Tests

The tests were conducted with a 1/9 scale model of the SSME nozzle, $\epsilon = 77.5$. High-frequency static pressure instrumentation was installed as shown in Fig. 9, in addition to low-frequency static pressure taps.

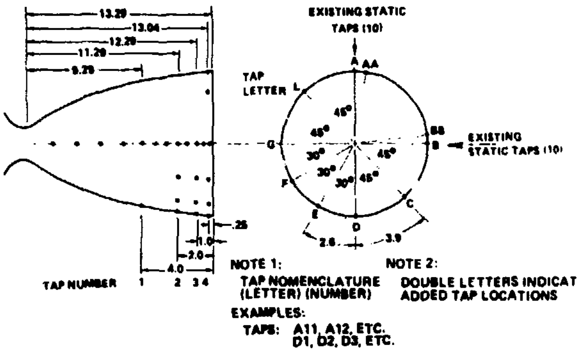

Fig. 9. SSME nozzle model high-frequency pressure instrumentation tap locations

Startup and shutdown sequences were simulated by varying the pressure ratio P_c/P_a. A typical test cycle is presented in Fig. 10, which shows a compressed oscillograph record of the test cycle (Fig. 10A) along with expanded portions of the same cycle. The portion noted as 10B shows the wall pressure while the nozzle is flowing full ($P_c/P_a > 1000$). As the pressure ratio is decreased, the shock moves into the nozzle, and several strong pressure oscillations occur (Fig. 10C). This simulates the SSME during shutdown. The pressure ratio is decreased further (Fig. 10D), and only small oscillations are measured. To complete the cycle, the pressure ratio is then increased and as the shock system passes through the nozzle exit, the strong pressure oscillations occur again (Fig. 10E). Finally, the pressure ratio is high enough to result in a full flowing nozzle once again (Fig. 10F).

The high-frequency pressure transducers were located axially, as well as circumferentially, to determine the extent of area over which the loading was occurring. Data obtained from the tests indicated a circumferentially uniform distribution. The axial distribution is shown in Fig. 11. This figure shows that the pressure fluctuation is axially in phase but varies in amplitude. The amplitude of the pulse initially increases moving toward the throat and then decreases to a very small value.

(A) COMPRESSED OSCILLOGRAPH RECORD OF TEST CYCLE

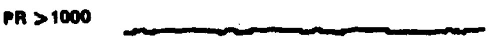

(B) OSCILLOGRAPH RECORD EXPANDED IN TIME.
NOZZLE FLOWING FULL – NO PRESSURE OSCILLATIONS

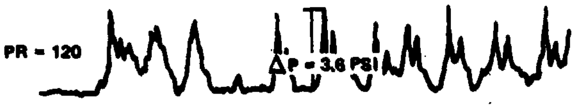

(C) SHOCK SYSTEM ENTERS NOZZLE AND FLAPPING OCCURS.
SEVERAL STRONG PRESSURE OSCILLATIONS

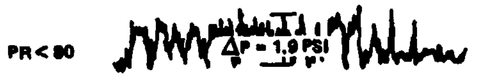

(D) SHOCK SYSTEM FURTHER UP NOZZLE,
NOT RESTRICTED TO NOZZLE EXIT

(E) SHOCK SYSTEM NEAR NOZZLE EXIT. FLAPPING OCCURS; STRONG PRESSURE OSCILLATIONS

(F) SHOCK SYSTEM DOWNSTREAM OF EXIT; NOZZLE RESUMES FULL FLOW

Fig. 10. Typical test cycle (location D3)

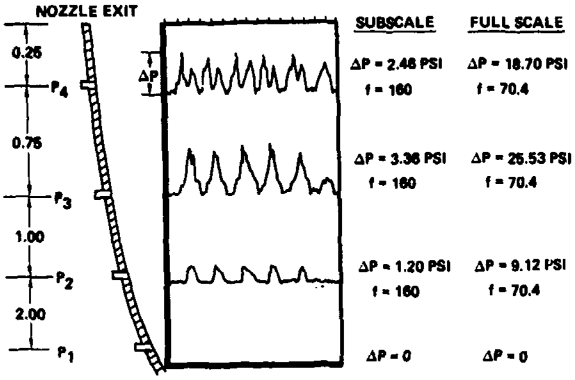

Fig. 11. Pressure pulses during period of jet oscillations (PR = 105)

A possible mechanism for this phenomenon is shown in Fig. 12. The downstream leg of the λ shock impinges on the nozzle wall, resulting in pressure buildup at the wall, which forces the flow off the wall. The flow then acts like a free jet pump and lowers the wall pressure,

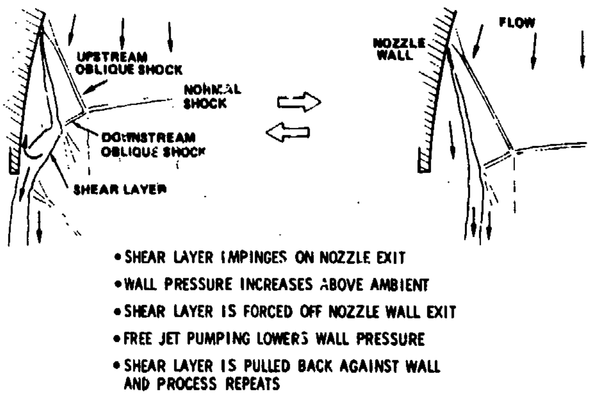

Fig. 12. Primary candidate driver mechanism of high nozzle strains (nozzle unsteady flow separation)

causing the jet to impinge on the wall again, and the cycle repeats itself.

Analytical Model

A computational model was also developed during this study, the results of which are shown in Fig. 13. This figure illustrates a velocity vector field near the nozzle exit and the entrainment of ambient air by the free jet. The flow has been forced off the wall by the high ambient pressure as shown by the degraded boundary layer profile. The vector length represents the magnitude of the velocity. As can be seen by the boundary layer profile near the upstream portion of the flowfield, the velocity at the wall is zero then approaches the free-stream velocity in the classical manner. Further downstream, degradation of the boundary layer begins, shown by the steepening of the gradient. Backflow than occurs as well as entrainment of ambient air. Flow turning as a result of the oblique shock is also apparent. The large arrow shows the flow of ambient air into the free jet.

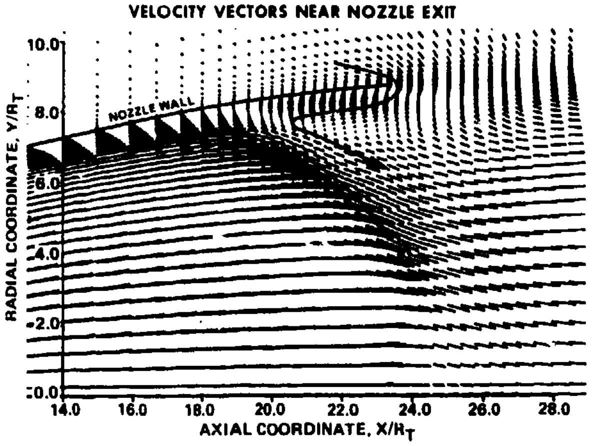

Fig. 13. Analytical prediction of SSME nozzle flow (P_C = 735 psia)

Full-Scale Nozzle Loading

From the several test cycles conducted, a statistical survey was performed to determine a characteristic pulse frequency, amplitude, and number. The results of this survey are shown in Fig. 14. The values shown have been scaled from the air flow tests to SSME full-scale conditions. The scaled results indicate pressure pulses as high as 38 psi occur in the SSME nozzle at a frequency of the order of 100 Hz. The last 30 to 36 inches of the nozzle experience approximately 7 pulses during start and 3 pulses during cutoff. This corresponds to an outward oscillating load on the structure of the order of 200,000 lbf.

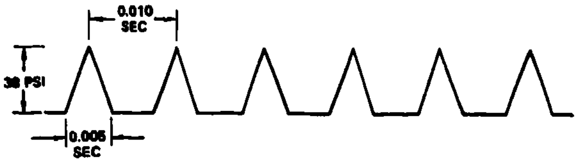

Fig. 14. Representative shock pulses for dynamic model

The pulse series input was used as a forcing function for a finite difference structural model of the nozzle. The results indicated high levels of stress in the fuel feedline, and were in good agreement with strain gage measurements.

IMPROVED FEEDLINE DESIGN

Two fuel feedline redesigns were developed to reduce the stress levels that the steerhorns were experiencing during engine start and shutdown. The first redesign consisted of nickel plating the existing design to reinforce the weld area. This design was selected because it could readily be implemented on the engines.

A second redesign was developed that would provide a 50-percent reduction in the stress levels. Since it was not possible to modify the shock behavior within the existing nozzle, a more dramatic design change was incorporated. In this configuration, the horizontal run of the steerhorn is supported by the ninth hatband (Fig. 15). A thermal expansion loop is provided in the vertical feedline. The redesigned configuration of the fuel feedline was also modeled and excited with the same pulse series as before. The redesign showed a much lower level of response than the initial design, and has been incorporated into the SSME.

Forty-one samples of strain data had been gathered during the engine testing of the original design, and it was shown that fatigue occurred in only a few tests. Based on this data, it was desirable to obtain a similar number of samples of both the reinforced tee design and the final redesign. Fifty-seven samples of data from the reinforced tee configuration were obtained, and showed maximum strains only 56 percent of those of the original configuration.

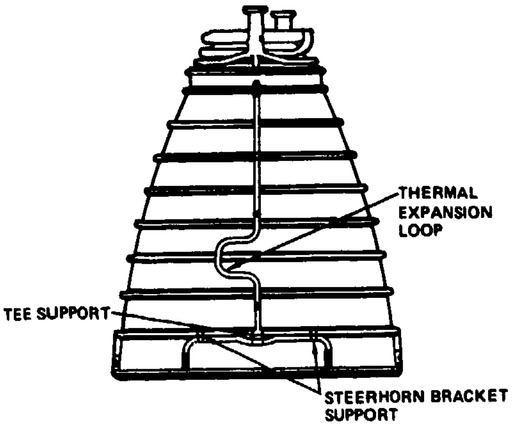

Fig. 15. Redesigned nozzle

Thirty-one samples of data from the final design have been accumulated, and the maximum strain is only 14 percent of the original design. This is significantly below the fatigue damage limit and results in infinite predicted life. A comparison of the engine test data is shown in Fig. 16.

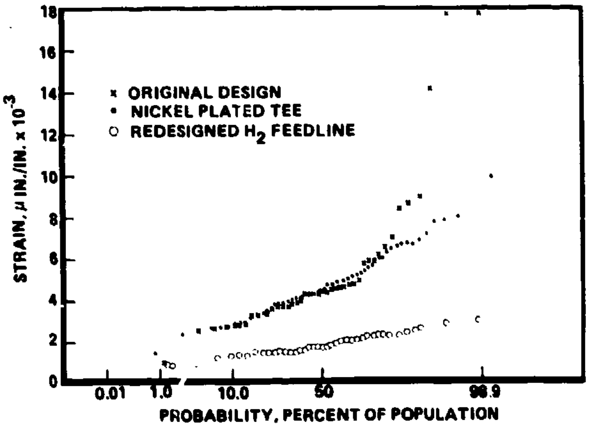

Fig. 16. Nozzle steerhorn strain measurements

CONCLUSIONS

The SSME nozzle experiences on overexpanded situation during the start and cutoff transients, at sea level, that results in periods of unsteady flow separation. A time-dependent solution to the viscous Navier-Stokes equation was developed to analyze the complex flowfield.

Experimental air flow tests indicated that the SSME nozzle was experiencing peak pressure oscillations of 38 psi at a frequency of approximately 100 Hz occurring over the last 3 feet of the nozzle.

Pressure pulses input to the dynamic structural response model showed excellent correlation with data measured during engine testing.

Finally, engine test data show both the reinforced tee design and the redesign have life capability for the planned flights of the Space Shuttle Vehicle.

REFERENCES

1. E. W. Larson, "Investigation of the Fuel Feed Line Failures on the Space Shuttle Main Engine," AIAA Paper No. 80-1309.

2. D. J. Sanchini and H. I. Colbo, "Space Shuttle Main Engine Development, AIAA Paper No. 80-1129.

3. L. Kiefling, "Space Shuttle Main Engine Nozzle-Steerhorn Dynamics," AIAA Paper No. 81-0505-CP.

4. S. Chakravarthy, S., Personal communication with and unpublished work, Rockwell International Science Center, 1980.